ABSTRACT

Title of Document:	DEVELOPMENT OF A SIMPLIFIED, MASS PRODUCIBLE HYBRIDIZED AMBIENT, LOW FREQUENCY, LOW INTENSITY VIBRATION ENERGY SCAVENGER (HALF-LIVES)
	Michael Tawfik Khbeis, Doctor of Philosophy, 2010
Directed By:	Professor Reza Ghodssi, Department of Electrical and Computer Engineering, Institute for Systems Research

Scavenging energy from environmental sources is an active area of research to enable remote sensing and microsystems applications. Furthermore, as energy demands soar, there is a significant need to explore new sources and curb waste. Vibration energy scavenging is one environmental source for remote applications and a candidate for recouping energy wasted by mechanical sources that can be harnessed to monitor and optimize operation of critical infrastructure (e.g. Smart Grid).

Current vibration scavengers are limited by volume and ancillary requirements for operation such as control circuitry overhead and battery sources. This dissertation, for the first time, reports a mass producible hybrid energy scavenger system that employs both piezoelectric and electrostatic transduction on a common MEMS device.

The piezoelectric component provides an inherent feedback signal and pre-charge source that enables electrostatic scavenging operation while the electrostatic device provides the proof mass that enables low frequency operation. The piezoelectric beam forms the spring of the resonant mass-spring transducer for converting vibration excitation into an AC electrical output. A serially poled, composite shim, piezoelectric bimorph produces the highest output rectified voltage of over 3.3V and power output of 145μW using ¼ g vibration acceleration at 120Hz. Considering solely the volume of the piezoelectric beam and tungsten proof mass, the volume is 0.054cm^3, resulting in a power density of 2.68mW/cm^3.

Incorporation of a simple parallel plate structure that provides the proof mass for low frequency resonant operation in addition to cogeneration via electrostatic energy scavenging provides a 19.82 to 35.29 percent increase in voltage beyond the piezoelectric generated DC rails. This corresponds to approximately 2.1nW additional power from the electrostatic scavenger component and demonstrates the first instance of hybrid energy scavenging using both piezoelectric and synchronous electrostatic transduction. Furthermore, it provides a complete system architecture and development platform for additional enhancements that will enable in excess of 100μW additional power from the electrostatic scavenger.

DEVELOPMENT OF A SIMPLIFIED, MASS PRODUCIBLE HYBRIDIZED
AMBIENT, LOW FREQUENCY, LOW INTENSITY VIBRATION ENERGY
SCAVENGER (HALF-LIVES)

By

Michael Tawfik Khbeis

Dissertation submitted to the Faculty of the Graduate School of the
University of Maryland, College Park, in partial fulfillment
of the requirements for the degree of
Doctor of Philosophy
2010

Advisory Committee:
Professor Reza Ghodssi, Chair
Professor Pamela Abshire
Professor Christopher Cadou
Professor Martin Peckerar
Professor Gang Qu

Preface

Recent industrialization of developing nations and economies is driving global energy demands to unprecedented levels. Meanwhile, the United States is facing economic hardships paralleling the great depression, in large part, due to unbounded increases in the demand and in direct response the cost of energy. Despite this, the US remains the largest waster of energy. On 18 April 1977, Jimmy Carter, the 37th President of the United States, recognized this in his address to the Nation stating,

> "Ours is the most wasteful nation on Earth. We waste more energy than we import. With about the same standard of living, we use twice as much energy per person as do other countries like Germany, Japan, and Sweden."

In over 30 years, little has changed. In 2003, the U.S. Department of Energy projected an annual increase of 1.5 percent in energy consumption between 2001 and 2020. Based on these projections, it is clear that efforts to conserve energy will only solve a portion of the energy crisis. New sources of energy must be explored. On 24 February 2009, in his address to the joint session of Congress, Barack Obama, the 44th President of the United States, reiterated the need for new sources of energy,

> "We have known for decades that our survival depends on finding new sources of energy. Yet we import more oil today than ever before."

Clearly, to facilitate sustained global growth it is vital to discover or harness new forms of energy, apart from fossil fuels, as well as optimizing the operation of existing infrastructure to curb gross consumption and wasted energy. To this end, this work seeks to initiate the study of harnessing environmental sources of vibration energy for zero overhead distributed critical infrastructure monitoring, using a mass producible system with the smallest possible form factor.

Dedication

To my wife, Jessica for her enduring patience and tolerance and my precious daughter, Madison who is my inspiration and motivation. Also, to my father, Tawfik for his guidance in all things electrical and practical, and in remembrance of my mother, Joan who in our short time together taught me to be creative and contemplative. Finally, to my brother, David, who still thinks I am a nuclear physicist.

Acknowledgements

First, I would like to thank my advisor, Professor Reza Ghodssi for his guidance, support, and at times directed motivation over the past six years that kept me working toward the goal. Second, I thank my Dissertation Committee, Professors Marty Peckerar, Pamela Abshire, Gang Qu, and Chris Cadou for their guidance and consideration to set and reach attainable goals.

Next, I thank my superiors, colleagues, and peers at the Laboratory for Physical Sciences for supporting this work both financially and logistically. Specifically, I thank Bill and Norm for pushing me to keep working, Barry for encouraging me that I am not the only one to take six years to complete a PhD, and Cathy for helping me find hiding places to write my proposal. Notably, I want to thank Jonathan McGee for guidance and innumerable discussions of all things theoretical, and John Sugrue for aiding me in machining the critical components and realizing ideas for improving the mechanical components of the system and test apparatuses.

I must acknowledge my colleagues at the MEMS Sensors and Actuators Laboratory (MSAL) for the fruitful discussions, peer reviews, and tolerance during the testing phase; especially Nathan Siwak, Konstantinos Gerasopoulos, and Xiao "Mike" Fan for their critiques of my written works. Additionally, I am grateful to the Laboratory for Physical Sciences cleanroom staff and George de la Vergne for being my cohorts in new, sometimes bizarre processes. Last, but certainly not least, I want to thank my family, Jessica and Madison for being patient with my absences so I could complete this work.

Michael Khbeis, 2010

Table of Contents

List of Tables

List of Figures

1 Chapter 1: Introduction

1.1 Background and Motivation

Recently, significant interest in providing long-term energy for autonomous wireless sensor networks has driven development of both piezoelectric and electrostatic vibration energy scavengers [1]. However, while research to date has shown macroscopic (on the order of several cm^3) examples of energy harvesting devices, the capability to provide usable energy does not scale well as harvester dimensions are reduced since available excitation is generally low frequency. This research effort will explore a means of scavenging energy at the millimeter-scale while increasing the energy density in a fixed volume.

1.1.1 Smart Dust Networks Application

The initial motivation of this research is to provide long-term, useable energy from the ambient environment without dominating the size of the wireless sensor nodes that comprise Smart Dust networks. For expansive or long-term sensor network deployments, utilization of battery operated nodes is not feasible; therefore, to overcome wireless communication overhead, successful systems need to exploit environmental energy over the extended life of the network.

Several institutions are working toward miniature autonomous wireless sensor networks, commonly denoted as Smart Dust, for a myriad of sensing applications. While a few demonstrations of Smart Dust technology have been presented in academia, most of the sensor networks are comprised of macro-scale devices that are

powered by batteries [1]. While battery power is acceptable for short term, proof-of-concept applications, the limited energy supply is prohibitive for long term deployments in the field. Furthermore, most critical Smart Dust sensing applications will require a high density of nodes in remote locations that will rule out the possibility of performing battery changes.

This work was initiated as part of a multidisciplinary research group at the University of Maryland (UMD) that was pursuing Smart Dust networks for discrete event detection. An example of discrete event detection is proximity sensing and tracking of a particular object travelling through a Smart Dust network. Movement of the object activates the nearest nodes and will either provide a real-time transmission, providing notification of the event to a monitoring system or record the event with a respective timestamp for delivery to a collection point at a later time.

The exact implementation of Smart Dust network operation is dictated by the availability of ambient energy as wireless communication power requirements dominate the transmission distance and frequency in which events are passed to the monitoring system. In addition, as mentioned previously, large scale sensing networks will prohibit battery changes. Finally, it is desirable to enable this event driven sensor network to function in multiple operational environments. As a result the Smart Dust nodes will require a multidisciplinary approach to scavenging energy from multiple environmental sources.

1.1.2   Hybrid Energy Scavenging

Macro-scale environmental energy scavenging for power generation, such as harnessing wind energy, has been utilized for decades. The provision of wind power

in industrialized nations is an augmentation to the main power grid. However, in remote locales the harnessing of environmental power may be the only source of available energy. One such case is reported in the literature in which a hybridized system is employed [2]. This hybrid system uses wind power for primary generation, but has a biogas supply for secondary power when the wind supply is insufficient.

Analogously, the UMD Smart Dust will employ a hybrid system for cogeneration of power as illustrated in Figure 1.1. In this specific example, radio frequency (RF), solar/thermoelectric, and vibration energy sources will be utilized as they become available. Typically, the devices used for energy conversion can double as sensor elements even if sufficient excitation is not available for power generation.

For example, in a remote outdoor environment where vibration sources are not commonly available, solar or RF energy becomes the dominant power source while the vibration scavenger device can be used as an acoustic sensor.
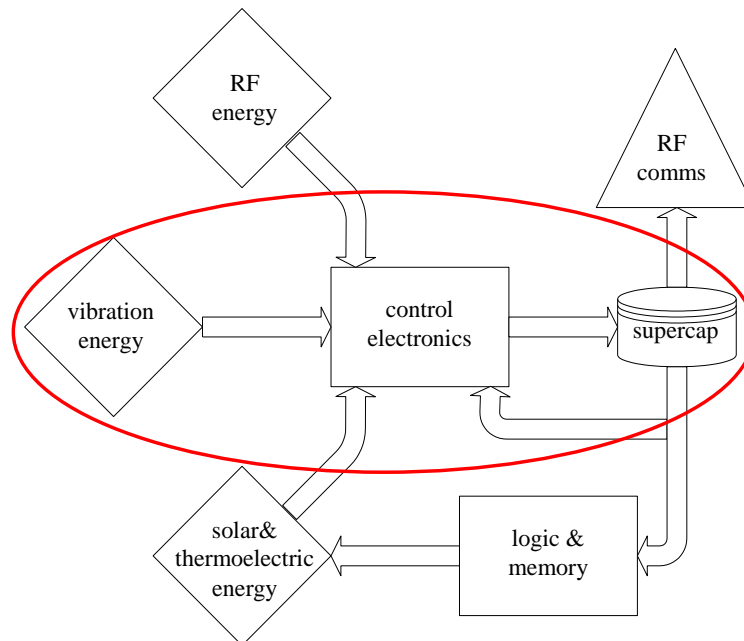
Figure 1.1 Source energy flow diagram for Smart Dust node

1.1.3 Critical Infrastructure Applications

As energy demands continue to grow while fossil fuel supplies are being depleted or controlled to increase costs, alternative energy sources are becoming critical. Large-scale environmental energy scavenging, such as wind, solar, and geothermal, will be the dominant sources of primary environmental generation. However, essential electromechanical systems, such as heating, ventilation, and air conditioning (HVAC), induce energy losses in the form of heat, light, and vibration. The availability of small-scale, low cost, ubiquitous hybrid environmental energy scavengers has the potential of recycling wasted energy by converting these losses back into electrical energy for operation of remote sensor systems. While the recaptured energy is a fraction of the wasted energy, due to inefficiencies of the scavenging systems, the aggregate impact of prolific availability of such systems could have substantial impact on curbing energy waste by providing data for optimization of systematic performance. For example, monitoring systems would impact the Smart Grid by detecting environmental conditions or predicting critical equipment failure so the grid can adapt to changing conditions. For these applications, it is vital to obtain a systematic balance between cost and volume, to ensure adoptability, and sufficient energy generation. To this end, this work focuses on development of low cost, mass-producible systems while simultaneously maximizing energy density by improving the transduction in a fixed volume.

1.2 Summary of Accomplishments

The main contribution of this dissertation is the design, development and characterization of a mass-producible hybrid energy scavenging system that converts

commonly available environmental vibration energy via simultaneous piezoelectric and electrostatic transduction in a shared volume. While vibration scavengers have been widely reported, cantilever-based piezoelectric scavengers require a large proof mass to resonate at the low frequencies that are dominant in the environment. Furthermore, electrostatic scavengers require either an asynchronous electret configuration or dynamic operation using storage of a pre-charge and synchronization with the mechanical oscillation to operate properly [1]. Both scenarios result in lower power densities due to the volume occupied by non-transducing components. Furthermore, implementations of synchronized electrostatic scavengers generally utilize a significant fraction of the scavenged energy to power elaborate timing and control circuits.   In this dissertation, a system-based approach to couple both piezoelectric and electrostatic energy scavenging mechanisms simultaneously is presented to increase energy density in a minimal volume while focusing on low-cost.

1.2.1   Design and Fabrication of Mass-Producible Hybrid Transducer

Typical piezoelectric energy scavengers are comprised of a mass-beam cantilever system. The mass and spring (beam) must be appropriately sized to ensure resonance at the frequency of the anticipated environmental excitation. Piezoelectric material is stiff and thus for low frequency (sub-kHz) operation, either a large proof mass or scaling of the beam is required. Generally, the proof mass is comprised of a high density material to minimize the volume while obtaining desired resonance; however, it still reduces the energy density of the scavenger.

For the first time, in this dissertation, the proof mass is utilized as an electrode to enable electrostatic transduction by creating a variable capacitor, denoted C_{VAR},

within the volume of the piezoelectric (PZT) scavenger, as depicted in Figure 1.2. Furthermore, the hybrid transducer is comprised of low cost, commercially available materials and produced using simple MEMS microfabrication processing and assembly to ensure mass producibility.
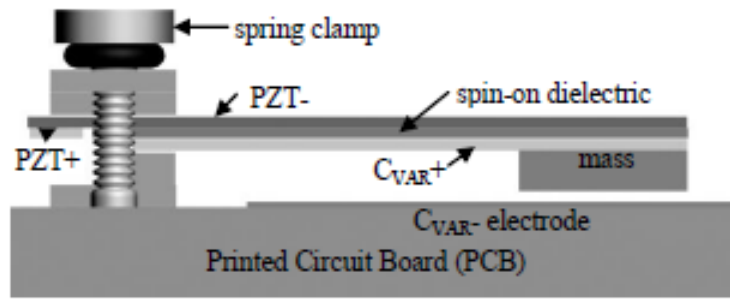
Figure 1.2 Cross-section diagram of hybrid energy scavenger

1.2.2   Use of Piezoelectric for Electrostatic Charge Control

As described in detail in Section 2.4, two types of electrostatic energy scavenger architectures exist; one type relies on the integration of an embedded electret for asynchronous operation while the other requires synchronous charge control at the peaks of the capacitance cycle. Electrets are difficult to produce with low cost methods and are susceptible to leakage/depolarization over long periods and thus are undesirable for widely distributed energy scavenger platforms.

In contrast, charge controlled systems are cheap to produce but require active circuits, such as voltage-controlled oscillators (VCOs), to obtain synchronous charging at the maximum capacitance and discharging at the minimum capacitance [3]. These types of synchronization schemes are shown to consume as much as 85 percent of the scavenged energy and require a battery to provide energy to the control circuit and provide a pre-charge. Over long periods of inactivity, the battery may become depleted thereby preventing long term operation.

This dissertation addresses these deficiencies by exploiting the coexistence of the piezoelectric scavenger to generate the required energy to operate control electronics and provide the electrostatic pre-charge voltage, thus eliminating the need for a battery. Furthermore, the piezoelectric voltage signal is exploited to provide information on the displacement of the oscillating beam, reflecting the inherent change in capacitance, and is utilized for synchronization by implementing low power peak detector circuits in lieu of power hungry VCOs.

1.2.3 Demonstration of Hybrid Energy Scavenging

This dissertation details the first demonstration of hybrid scavenging of vibration energy by simultaneous transduction of both piezoelectric and electrostatic devices in a shared volume. In support of this dissertation, a vibration energy test bed that includes an isolated electrodynamic shaker and analytical equipment is established for laboratory characterization of the system. Additionally, several iterations of printed circuit boards (PCBs) are designed, simulated, and assembled using commercial-off-the-shelf (COTS) components to provide rapid prototyping of hybrid scavenger systems. Included in the system are on-board diagnostics circuits for characterization of the isolated constituent components in addition to power management and signal conditioning for operation of the overall system.

Using these capabilities, several types of piezoelectric beams of differing configurations are characterized to identify optimal commercial beam material and verify beam resonance calculations and simulation. Furthermore, a correlation between the piezoelectric voltage signal and displacement is demonstrated and utilized for synchronous electrostatic charge control, facilitating hybrid scavenging.

7

1.3   Literature Review – Environmental Energy Scavenging

This section reviews relevant collaborations, discussions, and published works that are used to establish the context of the dissertation. First, a joint collaboration documenting the measurement and analysis of environmental energy is summarized. Next, a selection of differing approaches to environmental energy scavenging is presented. Finally, traditional vibration energy scavenging and recently published hybrid scavenging approaches are discussed.

1.3.1   Environmental Energy Survey

For proper design of an energy scavenging platform, it is vital to understand the most common expected input excitation from the operational environment. This enables design for optimal operation during the most common conditions and provides essential data on extreme conditions that must be accounted for to ensure a robust design. Ambient vibration conditions in a limited selection of operating environments were initially catalogued and are detailed in Table 1.1[4]. For the bulk of resonant vibration scavenging, it is critical to observe the amplitude and frequency of vibration; however, this study does not report other sources (e.g. light and heat).

Table 1.1 Summary of initial vibration source study[4].

Vibration Source	Amplitude (m/s^2)	Frequency (Hz)
Car engine compartment	12	200
Base of 3-axis machine tool	10	70
Blender casing	6.4	121
Clothes dryer	3.5	121
Person nervously tapping their heel	3	1
Car instrument panel	3	13
Door frame just after door closes	3	125
Small microwave oven	2.5	121
HVAC vents in office building	0.2-1.5	60
Windows next to a busy road	0.7	100
CD on notebook computer	0.6	75
Second story of busy office	0.2	100

In order to understand the available power in the environment, a parallel study by a graduate researcher is commissioned in support of this effort [5]. This study uses a common platform to measure environmental light, heat, and vibration to estimate the available energy density that would be obtained using commercially available or published photovoltaics, thermoelectric, and vibration scavengers respectively and is summarized in Table 1.2.

From the table, it is clear that given differing conditions either photovoltaics or tuned vibration scavengers dominate in performance. However, the photovoltaics are only viable during lit conditions. Therefore, vibration energy is clearly a viable source of energy. Despite this, the vibration power density is closely coupled to amplitude, as evidenced by differentiation between hot days (when AC is operating) and cold days (AC idle) on a HVAC duct, and tuning the of the resonant frequency to match the dominant excitation; shown in the engine compartment of an automobile.

Table 1.2 Summary of UMD environmental energy survey [5].

Vibration Source	Static Vibration Pwr Density	Tuned Vibration Pwr Density	Dominant Frequency	Thermoelectric Power Density	Photovoltaic Power Density
Automobile (Engine Block)	1.0 mW/cm^3	3.0 mW/cm^3	57.3 Hz	370 μW/cm^3	-
Automobile (Engine Compartment)	648 μW/cm^3	2.9 mW/cm^3	90 Hz	2.03 μW/cm^3	33.1 nW/cm^2
Automobile (Rear Window)	223 μW/cm^3	345 μW/cm^3	1.72 Hz	3.97 μW/cm^3	9.4 mW/cm^2
Clothes Dryer ("Closet" Indoor Lighting)	185 μW/cm^3	191 μW/cm^3	149 Hz	14.7 μW/cm^3	100-170 nW/cm^2
Clothes Washing Machine ("Closet" Indoor Lighting)	27 μW/cm^3	32 μW/cm^3	7.15 Hz	1.74 μW/cm^3	100-170 nW/cm^2
HVAC vents (Hot Day)	1.3 μW/cm^3	1.3 μW/cm^3	120 Hz	-	9-370 nW/cm^2
HVAC vents (Cool Day)	100 nW/cm^3	100 nW/cm^3	50 Hz	-	9-370 nW/cm^2
Roadway	1.2 nW/cm^3	3.1 nW/cm^3	1.89 Hz	7.2 μW/cm^3	23 nW - 7.2 mW/cm^2

The remainder of this subsection briefly discusses key published results of varying methods of extracting environmental energy. First, commercially available methods such as photovoltaic and thermoelectric are presented. Next, custom devices extracting energy from radioisotope materials and radio frequency (RF) signals are presented. Finally, a detailed overview of vibration energy scavengers is provided.

1.3.2 Photovoltaics

Solar energy is a significant source of environmental power; however, the source is periodic and affected by the intensity and wavelength of light impinging on the surface. Photovoltaic (PV) cells generally consist of *pn*-junctions on which photon impingement induces electron-hole pair generation producing a photocurrent.

Figure 1.3 illustrates the technology roadmap for photovoltaic cells. Crystalline silicon has dominated the PV industry due to the economic impact of the widespread availability of crystalline silicon for the microelectronics industry. Despite this, silicon has significant drawbacks. Silicon PVs are most efficient when the photon energy is close to the bandgap. If the impinging excitation is below the bandgap, the silicon is transparent and little energy is converted. Conversely, if the energy is above the silicon PV bandgap, the excess energy is turned into heat. To mitigate this, multilayer PVs have been created to capture differing energies at the cost of increased cost of production, yield, and complexity. As a result, silicon is undesirable in comparison to materials such as gallium arsenide (GaAs) because while 90 percent of photons are captured in the top 1μm of a GaAs PV. Since the *pn*-junction is at the surface of the device, the photogenerated carriers need to have a significant diffusion length and thus require a very high quality crystal [7].
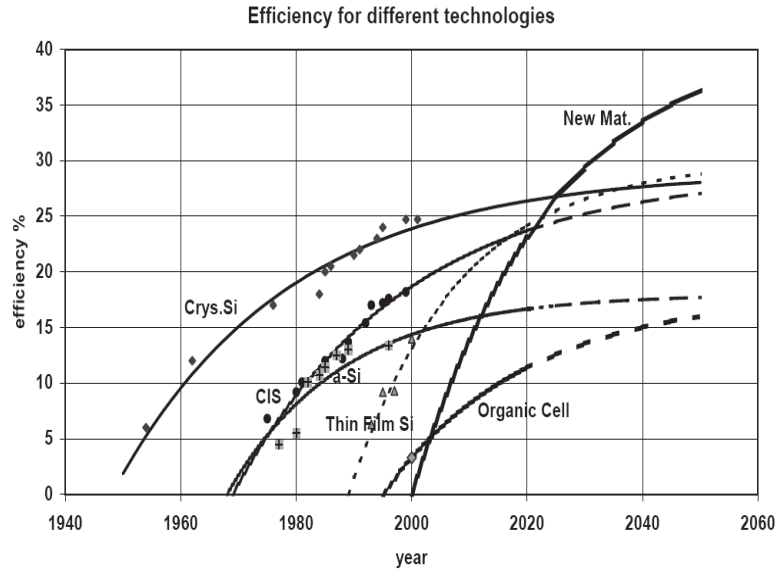
Figure 1.3 Photovoltaic conversion efficiencies roadmap [7]

Currently, through significant research and development in the PV industry, conversion efficiencies of crystalline silicon are approaching 30-40 percent well ahead of the roadmap, but rely on concentrating the light [8]. Given 30 percent conversion efficiency, Table 1.3 provides an approximation of solar cell areas required to produce enough power to operate a digital IC. As shown, as source light intensity is reduced, the required area increases significantly. In this example, PVs limited to the Smart Dust node area of 25mm^2 will only provide noticeable power in light intensity conditions that exceed 16000 lux and therefore cannot be used as the sole source of environmental energy.

Despite these limitations, as per the PV technology roadmap, conversion efficiencies are increasing as breakthroughs in materials research are made. An ideal PV material is environmentally compatible (e.g. non-toxic), direct bandgap, and cost effective while providing high conversion efficiencies. Recently, the Russian Joint Institute of Nuclear Research (JINR) announced a nanoparticle-based PV, dubbed the

star battery, that can convert luminance as low as starlight into useable energy [9]. In the star battery, the nanoparticles are suspended in a high-*k* polymer matrix and form many nano-scale *pn*-junctions. These structures are referred to as metamaterials. In theory, the high dielectric constant of the metamaterial facilitates the absorption and conversion of visible and infrared wavelengths. While the results remain to be validated by academic publications and peer review, initial data indicates a visible light conversion efficiency of 54 percent, an infrared conversion efficiency of 71 percent, and photocurrents that are four times that of silicon PVs [9].

Table 1.3 Required dimensions to provide 60µW to a node [10]

Light Sources	Luminance (lux)	Solar Cell ($\mu W/cm^2$)	Power (μW)	Area (cm^2)	Linear dimension (cm)
outdoor high	102000	1649.514849	60	0.036374332	0.190721
television stage	25000	404.292855	60	0.148407273	0.385237
skylight alone	16000	258.7474272	60	0.231886364	0.481546
dull day	1000	16.1717142	60	3.710181818	1.926183
reading light	500	8.085857101	60	7.420363636	2.724034
moonlight	0.4	0.006468686	60	9275.454545	96.30916
starlight	0.002	3.23434E-05	60	1855090.909	1362.017

1.3.3 Thermoelectrics

Thermoelectric generators (TEGs) exploit the Seebeck effect, the direct conversion of a temperature gradient into an electrical potential. This effect is primarily due to charge carrier diffusion. A temperature gradient causes carriers to diffuse from the hot side of a thermoelectric element to the cold side. When two dissimilar thermoelectric elements, such as a *p*-type and *n*-type polysilicon rods, are connected, a thermocouple is formed [11]. Equation 1.1 describes the open circuit voltage of a thermocouple in which S_A and S_B are the Seebeck coefficients of the two materials and T_1 and T_2 are the hot and cold side temperatures.

Equation 1.1 $V = \int_{T_1}^{T_2} \left(S_B(T) - S_A(T) \right) dT$

A basic TEG is comprised of a multitude of thermocouples connected in series (thermopile) to maximize volume utilization. Ideal thermoelectric materials have high Seebeck coefficients, low electrical resistance and low thermal conductivity [11]. Since semiconductors exhibit a high Seebeck coefficient and are compatible with microelectronics production, the development of silicon-based TEGs is emerging in commercial markets. Unfortunately, TEGs do not scale well for micro-scale devices. As dimensions become small, the thermal resistance of a micro-scale TEG is significantly reduced and thus thermal stability of the hot and cold junctions becomes a critical issue.

Figure 1.4 illustrates the calculated effect of scaling of conventional silicon-based TEGs. Complementary metal oxide semiconductor (CMOS) fabrication of micro-scale TEGs has been realized and demonstrated as measured in Figure 1.5. This result indicates that a power density of $1\mu W/cm^2$ is achieved with a 5K temperature differential.
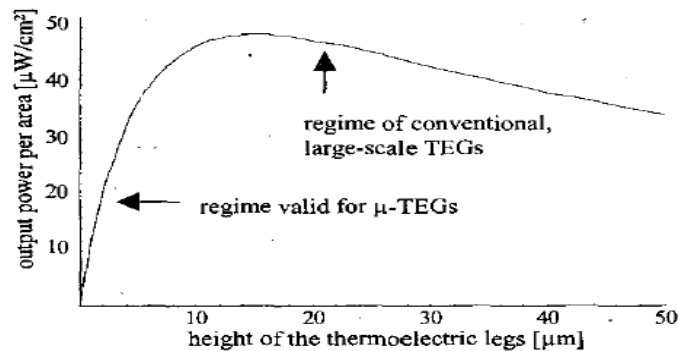
Figure 1.4 Calculated power density vs. leg thickness for ideal CMOS TEGs [11].
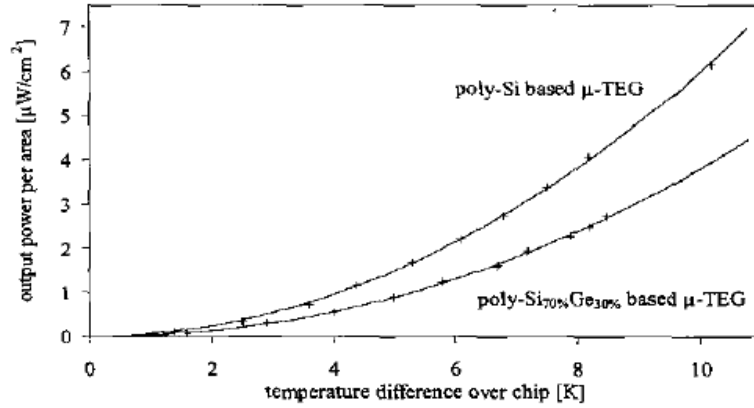
Figure 1.5 Measured output power for CMOS TEGs [11].
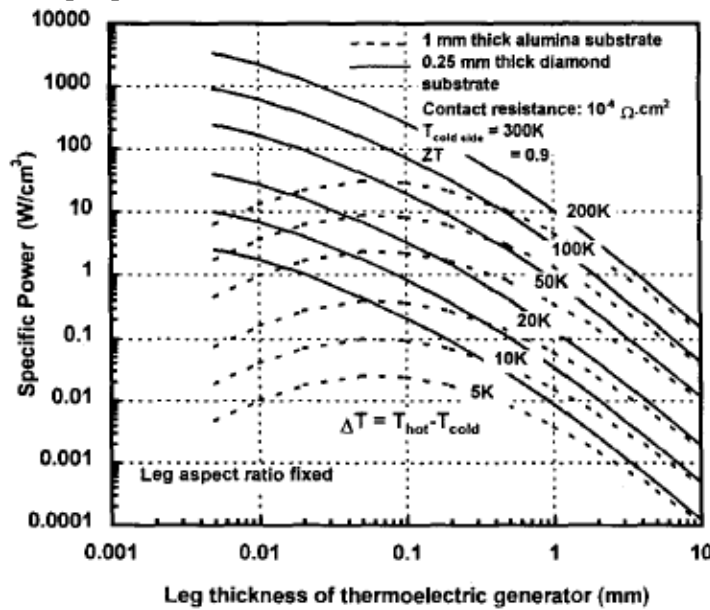
Figure 1.6 Power density vs. leg thickness for Bi2Te3 TEGs [12].

While CMOS compatibility is a desirable characteristic of an energy scavenging device, the CMOS TEGs exhibit conversion efficiencies well below 5 percent. As a result, efforts in materials engineering to realize more efficient TEGs are underway. Bismuth telluride (Bi_2Te_3) is an example of a compound semiconductor material that increases efficiency by reducing thermal conductivity. As shown in Figure 1.6, Bi_2Te_3 power densities are much higher than CMOS micro-TEGs; however, materials

integration issues and fabrication costs are much higher and thus at this time this technology is undesirable for mass production [12].

Despite the robustness of TEGs, the use of the devices in ambient environmental conditions is severely limited. A significant, constant temperature difference must be maintained to provide steady-state power. Lawrence *et al* studied the feasibility of using a macro-scale TEG buried in soil, with the top temperature junction exposed to air [13]. As depicted in Figure 1.7, the performance is periodic on a 24 hour time interval and therefore cannot provide high levels of continuous power. Furthermore, TEGs have to be optimized in design and fabrication using pre-determined temperature differences and therefore will not operate efficiently in scenarios where the temperature drifts significantly. However, if an environment with a constant temperature is defined as the target operational environment then TEG use is warranted.
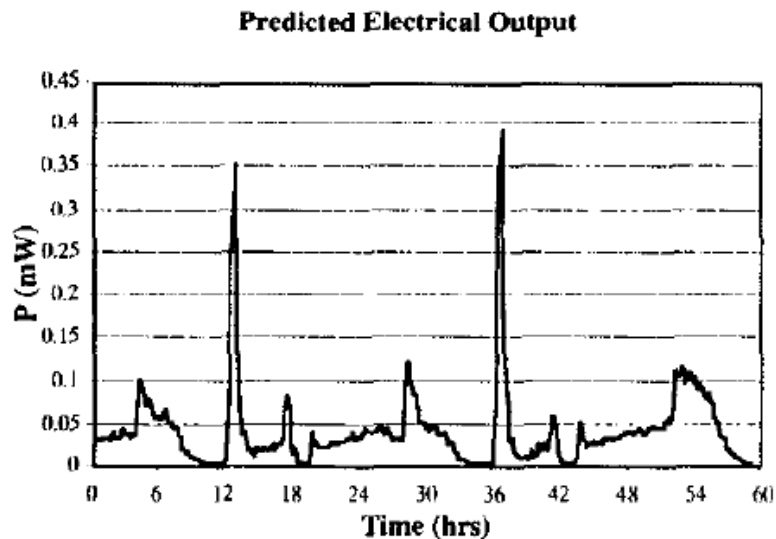
Figure 1.7 Predicted output power from soil to air TEG [13].

1.3.4 Radioisotopes

One of the most promising, yet most controversial forms of energy scavenging is radioisotope scavenging. By coupling energy from radioactive decay, long term power can be provided. Since these devices require ionizing radiation they should not be classified as environmental energy scavengers, but should instead be considered long life batteries. Blanchard describes a direct conversion method using a liquid ^{63}Ni source emitter of beta particles that impinge on micro-fabricated *pn*-junctions which then conduct a current when excited [14]. Figure 1.8 demonstrates the I-V characteristics of this direct conversion battery, commonly referred to as a betavoltaic. It should be noted that the peak current of this device is 1.31nA with a maximum power generation of 0.07nW. While many researchers are striving toward higher energy direct conversion methods, high energy beta particles (maximum of 66.7keV) cause irreparable damage to the semiconductor material by embedding themselves into the semiconductor lattice, posing long-term reliability concerns [15].
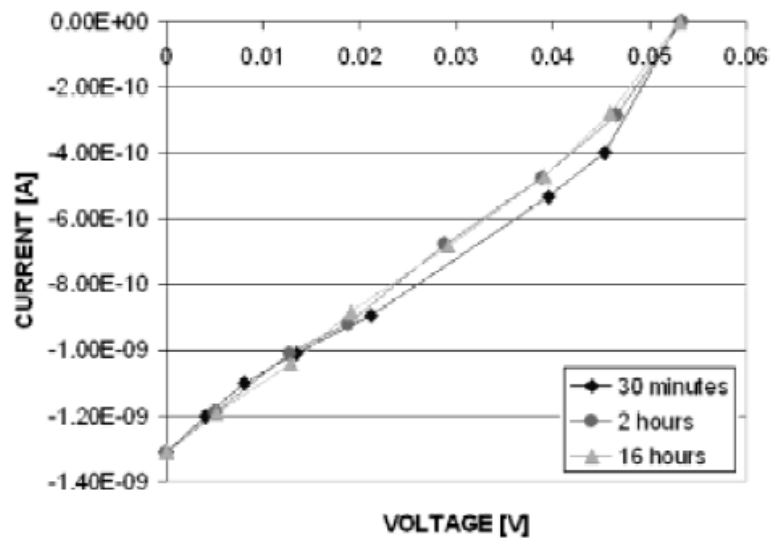
Figure 1.8 I-V characteristics for a 63Ni direct conversion nuclear battery [14].

Recent work using liquid-based semiconductors to encapsulate radioisotope materials simultaneously improves electrical conversion efficiency and prevents degradation and failure found in solid semiconductor betavoltaics [15]. Conversion efficiency is improved because electron-hole pair generation from beta emissions is omni-directional as the radioisotope is interspersed with the liquid semiconductor; whereas, solid semiconductor betavoltaics, as single-sided devices, generally collect only a fraction of the emissions. The tested device produces an open circuit voltage of 899mV and short circuit current of 0.107μA, with a maximum power generation of 16.2nW with a calculated efficiency of 1.24 percent [15].
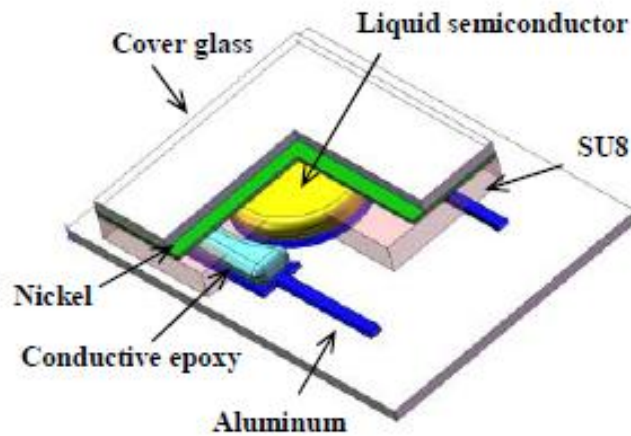
Figure 1.9 Drawing of liquid-semiconductor betavoltaic cell [15].

Radioisotope thermal generators (RTGs) have been extensively used in satellite and deep space probe applications. RTGs use radioactive decay to heat thermocouple elements, exploiting the Seebeck effect. While these devices are highly reliable, the most common ionizing source on macro-devices is Plutonium (^{238}Pu) which is highly radioactive and limited in availability. At best these systems have a conversion efficiency of 8 percent. A similar, indirect approach to nuclear-induced harvesting is the radioisotope energy conversion system (RECS) [16]. Proposed RECSs use an

ionizing source to charge a fluorescing media that emits light which is captured and converted by PV cells. The RECS approach claims to have a potential of achieving 20 percent efficiencies; however, this device will still use ^{238}Pu.

For obvious reasons, highly ionizing sources are undesirable for widespread use in ambient environmental conditions. Beta emitters, such as Americium or Tritium are preferred because beta emissions are blocked by the human epidermis and thus pose a much lower health risk to the general population. Despite this, as mentioned earlier, direct conversion of beta emissions results in low current and power generation. Blanchard describes a MEMS device that utilizes a beta emitter source [17],[18]. Figure 1.10 depicts the four stages of operation including the ionizing charging of copper sheet that results in electrostatic attraction of the cantilever until it contacts the bottom electrode and releases causing a ringing of the cantilever. The cantilever is covered with a piezoelectric element that generates an AC voltage during the ringing phase of operation. While this device has been demonstrated to operate for long periods, the power output is on the order of 20nW [18].
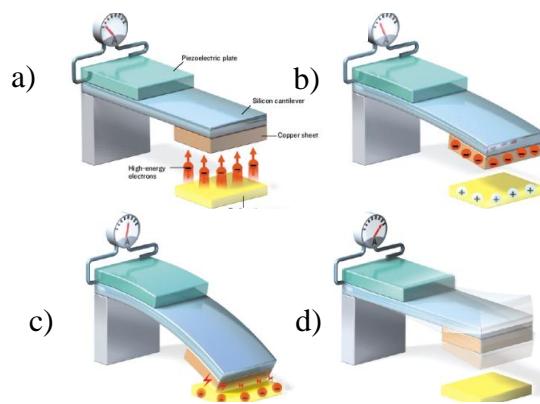
Figure 1.10 Indirect radioisotope conversion mechanism using cantilever a) ionizing charge of copper sheet, b) electrostatic attraction, c) shorting of electrodes and ringing that bends a piezoelectric [18].

Overall, there is significant effort required to make radioisotope scavenging a practical technology. While introduction of liquid semiconductors has mitigated lifetime concerns of lattice damage, the power density is low compared to the high energy density due to long half-lives of radioisotopes. Even though the technical challenges may be surmountable, political and practical challenges to overcome public concern regarding exposure and related health risks of prolific radioactive devices persist.

1.3.5 Electromagnetic/Radio Frequency

Electromagnetic power delivery is used in commercial applications for powering radio frequency identification (RFID) tags and bio-medical implants. Ghovanloo and Najafi detail a system for RF powering of medical implants that provides insight to common issues in this technology [19].

In general, the use of electromagnetic power delivery is used in close proximity to the source since electromagnetic radiation power falls off as a function of the radial distance squared. Furthermore, if the source and receiver are located on the ground, the radiation power falls off by the fourth power of the radius. Finally, the Federal Communications Commission (FCC) limits the transmit power of unlicensed band (2.4-2.485GHz) to a maximum power of 1W. Using this source limitation, the expected power at a node that is five meters from the source will be 50μW [1].

Recent work at the University of Maryland demonstrates the capability to extract directed 900MHz, 3W radiation using an efficient rectifying antenna (rectenna) system [23]. The measured power delivered to a load resistor was measured to be

212µW at 27m from the source. However, the extracted power is dependent on the availability of efficient antennas that do not scale well.

Given the promising delivery of RF energy, one might consider an effort to scavenge common cellular, radio frequencies and other ambient radiation. To investigate the feasibility of this, an accurate assessment of the ambient electromagnetic radiation is desired. Government studies and assessments of ambient radiation have been performed globally to ensure the general population is not over exposed to radiation [20],[21],[22]. The consensus of the studies, regardless of the diversity of the study geography, is that ambient environmental electromagnetic energy densities are usually below $1µW/cm^2$.

Utilizing ambient electromagnetic radiation, a group from University of Maryland reported generation of 0.9V with a power output of 162nW across a 5MΩ load from as little as 2.5µW of RF energy [23]. At these levels, it is essential that the devices are in close proximity to the RF source. Furthermore, numerous bands cannot be scavenged simultaneously because each targeted band requires a dedicated antenna and tuned receiver that further decreases energy density. In summary, directed electromagnetic power delivery, using an optimized receiver antenna with a dedicated band, which is in close proximity to the emanating source, is currently the only viable scenario for wireless powering of small systems. Therefore, it should not be considered viable for general purpose ambient scavenging technology without predefined, proximal, and persistent RF sources.

1.3.6   Vibration

Roundy pioneered small scale energy scavenging for wireless sensor networks developed at UC Berkeley [1]. Ambient measurements indicate that the majority of high intensity vibrations are low frequency, harmonics of 60Hz noise from machinery as shown in Figure 1.11. As a result, ambient vibration energy scavengers should be designed for low frequency (60-120Hz) resonant operation with an acceleration amplitude of 1-3m/s^2.
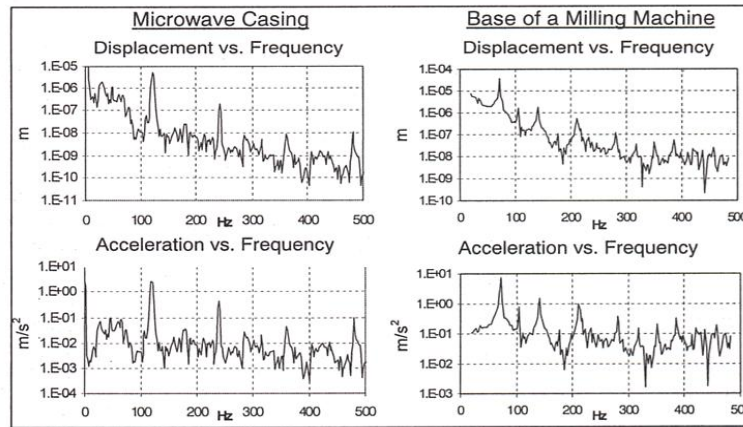
Figure 1.11 Commonplace excitation measurements [1].

Three types of vibration scavengers have been documented. These vibration-based energy scavenger types include electromagnetic (inductive), piezoelectric, and electrostatic (capacitive).

1.3.6.1   Electromagnetic

Williams *et al* describe the first demonstration of a millimeter-scale (4mm x 4mm x 1mm) vibration scavenger. The device is electromagnetic and consists of an electrical conductor that passes back and forth through a magnetic field. The device is capable of generating 0.3μW. However, it was actuated at 4.4kHz with an input acceleration of 380m/s^2 which is not commonly found in ambient conditions [24].

Additionally, Roundy extrapolates that the output voltage of the device is on the order of 8mV which is too low to operate basic power conditioning electronics like a full wave rectifier [1].

While large-scale electromagnetic scavengers with volumes in excess of $3.7cm^3$ are demonstrated to produce an average power of 39.5µW with 1g excitation at 10Hz, the dominant challenge is scaling of the devices below $1cm^3$, as it is challenging to microfabricate coils with low internal resistance and numerous windings [25]. Miniature windings down to 100µm have been realized; however, these only contain a maximum of 15 windings and generate 1mT. Using arrays of 1mm diameter micro-coils with 7 windings, 1.4mV was produced with 300kHz excitation; however, amplitude of excitation and total volume and energy production was not reported [26]. Overall, to date, miniaturized electromagnetic scavengers have been unable to produce sufficient voltages or energy to be effective with commonly available ambient vibration.

1.3.6.2   Piezoelectric

Piezoelectric generators use either film or ceramic piezoelectric benders that undergo flexure due to mechanical vibrations. The resultant change in the piezoelectric material stress generates an AC voltage. Lu *et al* reports a simulated power output of an out of plane piezoelectric generator to be 16µW and 64µW for 5µm and 30µm displacements respectively at a frequency of 2.94kHz [27]. The piezoelectric dimensions are given to be 1mm x 0.5mm x 5mm; however, the dimensions of the seismic mass are not provided for consideration so accurate energy density metrics cannot be ascertained.

While this kHz regime excitation would not be suitable for ambient environments, Roundy *et al* report the performance of a piezoelectric generator actuated at 120Hz [1]. As discussed in Section 2.3, low frequency resonant operation requires either large proof masses or compliant springs. Since piezoceramics are stiff, the volume is dominated by a tungsten alloy mass as shown in Figure 1.12. The results of several designs indicate a peak power of 180μW delivery to a capacitive load for a 1cm^3 volume. This documents the first known demonstration of a vibration scavenger powering a RF transceiver system. Simultaneously, the same group developed a low frequency electrostatic scavenger for comparison purposes.
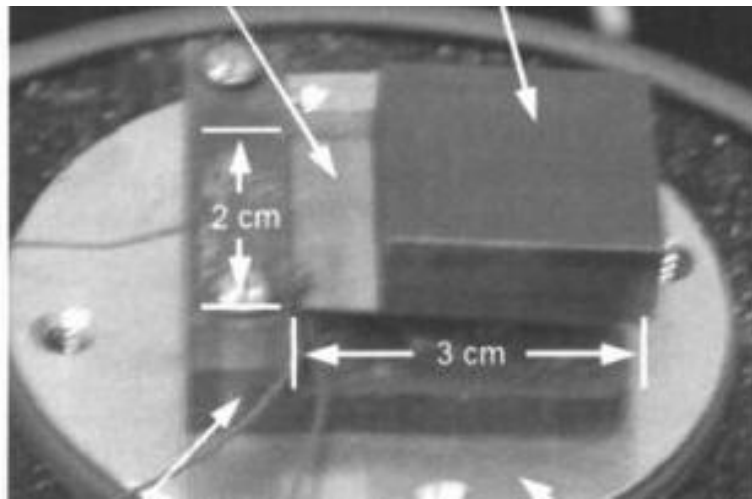
Figure 1.12 Piezoelectric scavenger with tungsten proof mass [1].

A common failure mode for PZT scavengers is micro-fracturing and inelastic deformation within the piezoceramic. To address this limitation, research in polymer-based piezoelectrics such as poyvinylidene fluoride (PVDF) has been conducted; however, this material has a considerably lower coupling coefficient. A 8mm x 20mm bimporph of PVDF only generates 4.13V with 15mm of displacement and was not characterized for output power generation [28]. Despite this, in specific

applications such as integration within the soles of shoes, polymer-based piezoelectric are effective in macro-scale applications and are reported to generate peak voltages in excess of 130V (regulated to 4.5V) with 2.6mW of power [29]. Irrespective of these results, the energy density is low due to the large volume of material and large displacements (from biped locomotion) required.

Other methods exploit striking of piezoceramics but engineer the scavenger to avoid stress induced fracturing. One such impact-based design generates up to 600μW, but requires 10cm displacement amplitude at 10Hz to achieve this metric and cannot be driven by commonplace excitation [30].

Recent work in optimizing PZT scavengers focuses on shape optimization to obtain uniform strain distribution and results in a 30 percent improvement in output power over rectilinear beams [31]. Another attempt to improve PZT performance requires special materials integration to achieve miniaturization, but operates in an unrealistic regime with 0.39g at 528Hz with little improvement in power density over competing standard PZT beams [32]. Both optimizations impose significant challenges in the manufacturing process which limits mass producibility and compatibility with CMOS processing.

1.3.6.3   Electrostatic

Of all vibration energy scavenging implementations, electrostatic scavenging has the highest potential for mass producibility by exploiting economies of scale and is capable of co-fabricated monolithic integration with CMOS electronics. As discussed in Section 2.4, traditional electrostatic scavengers exploit a change in capacitance in a variable capacitor structure due to mechanical displacement to scavenge vibration

energy. Two types of traditional electrostatic conversion mechanisms exist. The voltage constrained energy conversion cycle starts when the variable capacitor is at the maximum capacitance and is charged to a set voltage value. As the plates of the capacitor move apart, charge flows to maintain the fixed voltage. Meninger *et al* describes voltage constrained conversion as the maximum limit of electrostatic conversion; however, this is at the cost of additional control and voltage sources to force a fixed voltage on the device [33]. A much simpler conversion cycle is charge constrained energy conversion in which a fixed charge is applied to the variable capacitor at the maximum capacitance which is then disconnected. The voltage on the variable capacitor increases as the capacitance decreases and is connected to a reservoir at the minimum capacitance thus resulting in a charge pump behavior. Either cycle has two critical requirements: at least one external energy source and either diode connections or active timing control to ensure the charge cycle coincides with the variable capacitance extrema [1],[34],[35]. Roundy *et al* report a MEMS electrostatic scavenger of 1.2mm x 0.9mm x 0.5mm, as shown in Figure 1.13. However, output power is low (337nW) due to parasitic capacitance and diode leakage. Meninger *et al* report a system with active control that could provide 8.66μW. However, control electronics consume 50 percent of scavenged power and require an 8V external source. The significant drawbacks of traditional electrostatic scavenging are the requirements of synchronization and pre-charge supply that retard efficiency.
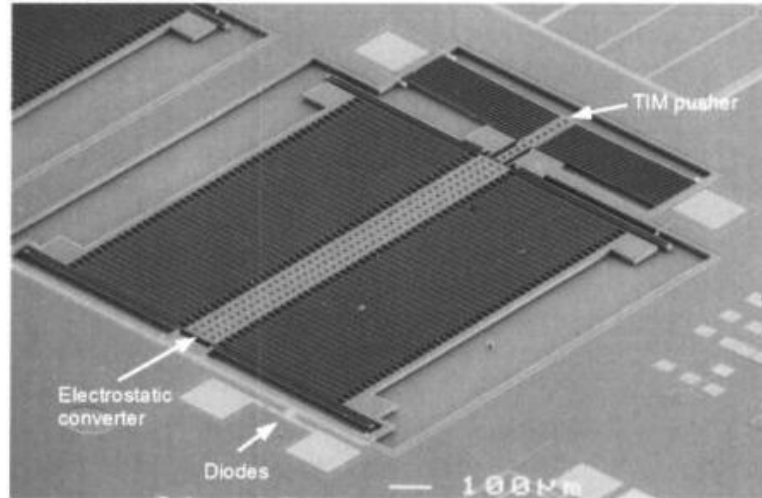
Figure 1.13 Silicon-based electrostatic harvester [1].

Incorporation of electrets, permanently charged structures, seeks to overcome the deficiencies of traditional electrostatic scavengers at the cost of increased fabrication complexity and potential for long-term degradation. Electret-based vibration energy scavengers pass a moving electrode through the electric field of the electrets to induce an alternating current flow due to induced charge displacement [36],[37],[38]. Standard electrets can store up to 150V as a quasi-permanent charge and are known to leak charge over time. An energy scavenger with standard CMOS fabrication materials is demonstrated to produce 1μW with an in-plane resonance of 600Hz and can generate 4V peak-to-peak voltage at excitation amplitude of 4g [36]. A mm-scale electret-based system was shown to generate a 170pA current at resonance operation of 1166Hz with 1 m/s^2 amplitude; however, no power data was reported [37]. Using materials engineering to improve electret performance yields a cm-scale capable of producing 0.7mW of power at 20 Hz. It uses an amorphous perfluroinated polymer CYTOP as the electret material that is charged to -545V [38]. Despite this data, the literature contradicts itself and claims a maximum output of 13.7μW at optimal load

with a displacement of 1.2mm. No data on excitation amplitude to achieve this displacement is reported. In summary, while electrets are promising for enabling miniaturization of vibration scavengers and alleviate the requirement for charge control and pre-charge; reported sub-cm devices to date have only been demonstrated using high vibration levels that are not readily available in the ambient environment.

1.3.6.4 Hybrid Systems

In order to operate within commonly available excitation, vibration energy scavengers must resonate at low frequencies, usually at harmonics of 50-60Hz from operation of large-scale electromechanical systems. Further constrained by availability of structural materials and critical mechanical properties, the design space and resulting limitations on scaling are well defined as discussed in Chapter 2. Since scaling impacts the resonance frequency of a harmonic vibration scavenger, the only way to increase the power density of the device is to improve the energy transduction. Transducer optimization is one path toward increasing energy density. However, if additional transducers can be integrated in the same volume, the energy density also increases. To date, efforts to increase the power density of piezoelectric scavengers by hybridization with either electrostatics (this work) or electromagnetics are reported [39],[40],[41].

1.3.7 Summary of Scavengers

A summary of energy scavengers are provided in

Table 1.4. Despite these results, it should be noted that, power density data does not account for the input excitation energy required to produce the power. A more

accurate metric is power density that is normalized to excitation amplitude and should be measured in power per volume per gravitational acceleration ($W*cm^{-3}*g^{-1}$).

Table 1.4 Comparison of energy scavenging techniques

Technology	Dependence on External Source	Power Density (W/cm^3)	Energy Density (J/cm^3)	Comments
Photovoltaic – High	Yes	1.65E-03	-	Sunlight [10]
Photovoltaic – Moderate	Yes	8.00E-06	-	Indoor [10]
Thermoelectric	Yes	1.00E-02	-	ΔT=5K Bi_2Te_3 [12]
Radioisotopes	No	2.00E-08	1.60E+8	^{63}Ni [18]
Electromagnetic / RF	Yes	1.62E-07	-	2.5μW RF in [23]
Vibration - Electromagnetic	Yes	3.95E-05	-	[25]
Vibration – Piezoelectric	Yes	1.80E-04	-	[1]
Vibration – Electrostatic	Yes	6.24E-04	-	[36]
Vibration – Electret	Yes	1.35E-05	-	[38]
Vibration – Hybrid PZT/Electrostatic	Yes	2.68E-03	-	[39],[40]
Vibration – Hybrid PZT/Electromagnetic	Yes	1.35E-04		[41]

1.4   Structure of Dissertation

Chapter 1 introduced the motivation and current work in the field of environmental energy scavengers. Next, Chapter 2 details the basic theory and design principles used for the piezoelectric and electrostatic transducers as well as the system circuit. Then, Chapter 3 discusses the fabrication and materials selection for a mass-producible hybrid energy scavenger. Chapters 4 and 5 discuss the testing and characterization of the piezoelectric and electrostatic transducers respectively. Finally, Chapter 6 summarizes the results, limitations, and discusses key future work.

2   Chapter 2: Theory of Operation and Design

2.1   Introduction

As discussed in Chapter 1, this dissertation combines two transducers within a shared volume to improve energy density of a mass producible system by utilizing previously non-functional structures. This chapter introduces the principles of operation, design, and simulation of the piezoelectric and electrostatic vibration energy scavenger components independently, followed by a detailed description of their physical integration and interaction in the hybrid system circuit. Originally, an in-plane hybrid energy scavenger was the intended design; however, several factors proved this design infeasible for both operating conditions and fabrication challenges that will be discussed in Chapter 3. The full analytical models for the original in-plane design can be referenced in the Appendices.

2.2   Generic Vibration Harvesting Model

At the most basic level, resonant vibration energy scavengers are modeled as damped mass-spring oscillators. Williams and Yates present a generic vibration harvester model using a spring, mass, dash-pot system [47]. The basic model is expanded by Roundy *et al* to

Equation 2.1 $-m\ddot{x} = m\ddot{y} + f_e + f_m + ky$

where x is the input displacement, y is the internal displacement, m is the internal proof mass, k is the spring constant, and f_e and f_m are the electrical (scavenged energy) and mechanical loss functions (also referred to as damping) respectively [1]. The loss functions must simultaneously incorporate all damping mechanisms of both

piezoelectric and electrostatic components as discussed in the appendices in Chapters 7 and 8. These loss functions are presented individually and then combined in the system lumped model to provide the most accurate model possible. Mechanical damping should be minimized where possible to enable the maximal electrical damping that includes driving the load, control electronics and storage capacitors. Analytical models for the piezoelectric springs, proof mass and electrostatic charge pump for both in-plane and out-of-plane designs are introduced.

2.3 Piezoelectric Transducer

The piezoelectric transducer is the primary enabler of the hybrid vibration energy scavenger system as it provides the mechanical resonator structure, the primary voltage source, and the feedback signal. This section will describe the mechanical structure, a brief synopsis of the phenomenon of piezoelectricity, theory of operation for piezoelectric vibration energy scavenging, critical design parameters, and an overview of analytical modeling and simulation techniques utilized to obtain an experimental starting point.

2.3.1 Device Structure

The piezoelectric transducer (generator) is a rectilinear beam that is comprised of at least a single layer of piezoelectric material clad on top and bottom by a thin nickel metal coating. Multi-layer transducers include a center shim layer that is either a metal or conductive composite that provides the internal wiring. Wiring configuration, referred to as poling, determines the electrical performance of the material. Shown in Figure 2.1, series connected (X-poled) 2-layer piezoelectric

beams use the internal shim to connect two oppositely poled beams to produce higher supply voltages (approximately 2x the single layer). In contrast, the parallel connected structure uses the shim as the central electrode to extract more current. This work, considers only single layer and series connected 2-layer piezoelectric beams because the 3-wire requirement of parallel configurations adds unnecessary complexity to the fabrication.
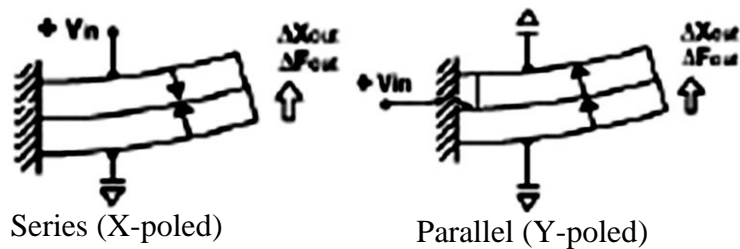
Figure 2.1 Polling configurations for 2-layer piezoelectric beams [42].

Initial design work was focused on the in-plane scavenger, shown in Figure 2.2 that would be monolithically integrated with CMOS ICs. In this design, the piezoelectric elements are folded flexures that would stretch and compress as the center proof mass oscillated in the plane. This design was abandoned for three primary reasons, out-of-plane overstress concerns, low expected piezoelectric flexure voltage, and complexity of fabrication.
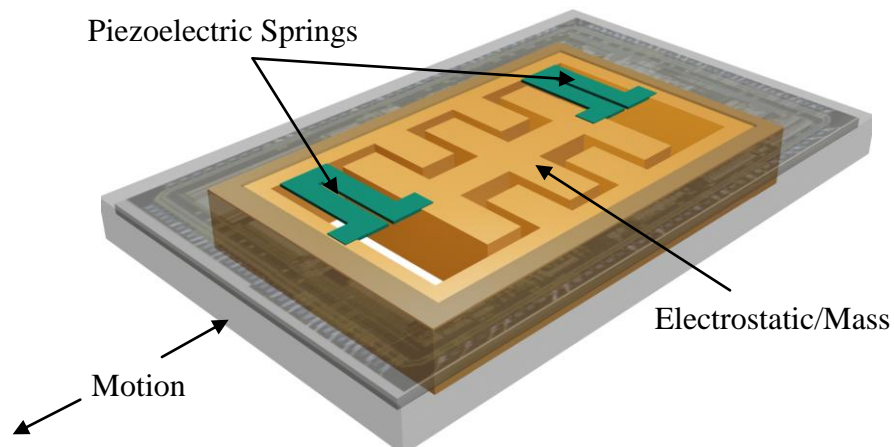
Figure 2.2 Initially proposed in-plane hybrid energy scavenger.

The simpler design shown in Figure 2.3 utilizes a single piezoelectric beam in an out-of-plane configuration. This design substantially reduces modeling and fabrication complexity while simultaneously improving piezoelectric performance and long-term reliability. The piezoelectric beam is attached to the proof mass at the tip and mechanically clamped to form a resonator beam. Electrical connections to the piezoelectric are made by physical contact by the clamp on the top side (denoted PZT-) and by a wire connection on the bottom (shown as PZT+).
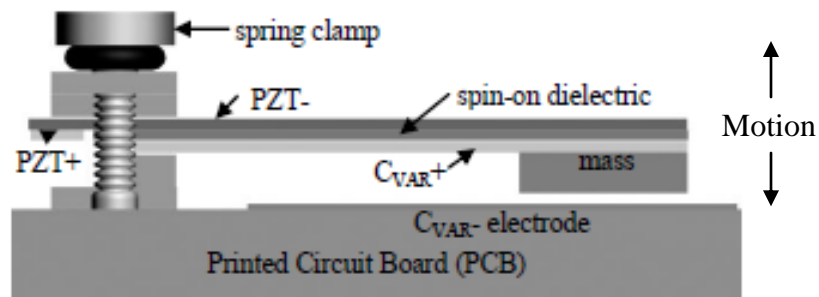
Figure 2.3 Out-of-plane, simplified hybrid energy scavenger.

2.3.2   Theory of Operation

Piezoelectricity is the phenomenon exhibited by a certain class of materials to generate an electric potential in response to applied mechanical stress. Their behavior is linked to the change of polarization density within the material. Piezoelectric materials like Lead Zirconate Titanate (PZT) have crystal lattices with an asymmetric charge distribution that result in electric dipole moments. Collocated dipoles tend to be aligned in regions called Weiss domains. These are generally randomly oriented, but a strong electric field (2kV/mm) applied at high temperatures (poling process) will cause the Weiss domains to align [1]. When a poled piezoelectric material is used as the dielectric of a capacitor, the applied strain changes the polarization

32

density which induces an electric potential that tries to return the material to the equilibrium state. This is represented mathematically using constitutive equations:

Equation 2.2 $\qquad \delta = \dfrac{\sigma}{E} + dE_{field}$

Equation 2.3 $\qquad D = \kappa_{pzt}\, \varepsilon_0\, E_{field} + d\sigma$

where δ is strain, σ is average stress, d is the piezoelectric coupling coefficient (d_{31}), E_{field} is the electric field, D is electrical displacement, κ_{pzt} is the dielectric constant of the piezoelectric, and ε_0 is the permittivity of free space.

When connected in a circuit, sinusoidal stress excitation results in an alternating current (AC) that can be rectified to produce a direct current (DC) voltage across a capacitor. The AC voltage signal is proportional to the amplitude and frequency of the applied sinusoidal stress and consequently to the displacement. Additionally, it should be noted that the electrical performance of the system is dependent on the average stress only covered by the electrodes.

2.3.3   Critical Electromechanical Parameters

While average stress under the piezoelectric electrode is important for estimating the electrical performance of the piezoelectric, as a practical matter the peak stress is the most critical parameter to consider as the piezoelectric material is a brittle ceramic and incapable of experiencing more than approximately 100MPa without risking permanent damage in the form of inelastic deformation or micro-scale fracturing. Secondarily, it is also critical to ensure that the beam's resonant frequency matches the expected dominant excitation frequency. Since the piezoelectric cantilever is a stiff beam, the quality factor (Q) is relatively high and thus small variations between

the dominant vibration excitation frequency and the beam's resonant frequency dramatically degrades electrical performance. Finally, the overall volume is important to ensure that systems are not obtrusive.

2.3.4   Modeling and Simulation

Combinations of analytical, numerical, and finite-element modeling (FEM) techniques were employed to estimate performance and feasibility prior to attempting to fabricate the hybrid energy scavenger system. The initial comprehensive in-plane analytical and numerical modeling is complex and misses critical design flaws that are found using FEM. This FEM simulation result eliminates the feasibility of the in-plane design. In contrast, out-of-plane modeling is simpler, using beam theory, and is used to establish basic piezoelectric beam geometries for experimental analysis.

2.3.4.1   In-plane Hybrid Energy Scavenger – Piezoelectric Analytical Modeling

This section briefly mentions key equations in modeling the piezoelectric springs for the initial hybrid scavenger system design. A detailed derivation of these equations can be found in appendix B in Chapter 8.

Simple folded piezoelectric elements function as both mechanical springs as well as electrical pre-charge and voltage representation of the electrostatic shuttle position. A simple 3-D mechanical model, as illustrated in Figure 2.4, is essential to determine the 3-D displacement and associated stress within the bending element. The use of the 3-D displacement model is critical since the weight of the electrostatic shuttle will induce bending out of the plane of interest and thus must be considered to affect the operation of the system. In this model of a single spring element, point *A* is tethered to the device frame, while point *D* is connected to the electrostatic shuttle.

Most simple mechanical beam models only depict 2-D bending; however, Steward provides a detailed application of Castigliano's 2nd theorem and internal strain energies to determine the 3-D displacement of the beam spring element due to movement of a proof mass by an applied force [43].
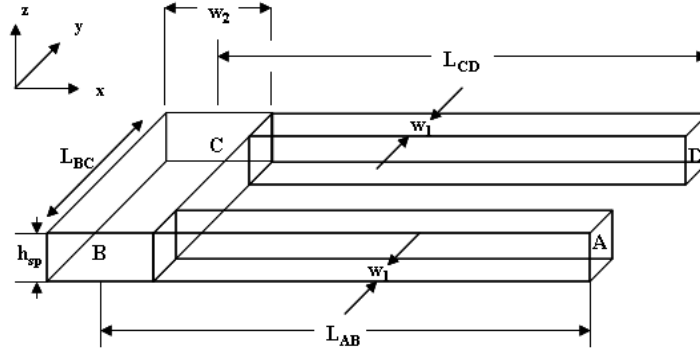
Figure 2.4 Simple 3-D model of piezoelectric folded spring.

Although designs for hybrid scavenger devices with 3 DOF exist, for simplicity a design with only 2 DOF is analyzed and presented.

The *x*-displacement in a 2 DOF system is negligible and represented by

Equation 2.4
$$\Delta_{Dx} = F_x \left[\frac{L_{BC}^{\,3}}{3EI_{cz}} + \frac{L_{BC}^{\,2} L_{AB}}{EI_{bz}} + \frac{6L_{BC}}{5GA_c} + \frac{L_{CD}}{A_b E} \right] + F_y \left[\frac{L_{BC}^{\,2} L_{CD}}{2EI_{cz}} - \frac{L_{BC}}{2EI_{bz}} \left(L_{AB}^{\,2} - 2L_{CD} L_{AB} \right) + \frac{L_{AB}}{A_b E} \right]$$

In such a system, the primary displacement of interest for energy conversion is the *y*-displacement defined by,

Equation 2.5
$$\Delta_{Dy} = F_x \left[\frac{L_{BC}^{\,2} L_{CD}}{2EI_{cz}} - \frac{L_{BC}}{2EI_{bz}} \left(L_{AB}^{\,2} - 2L_{CD} L_{AB} \right) \right] + F_y \left[\frac{1}{3EI_{bz}} \left(L_{AB}^{\,3} - 3L_{CD} L_{AB}^{\,2} + 3L_{CD}^{\,2} L_{AB} \right) \right]$$
$$+ F_y \left[\frac{L_{CD}^{\,3}}{3EI_{bz}} + \frac{L_{CD}^{\,2} L_{BC}}{EI_{cz}} + \frac{6L_{CD}}{5GA_b} + \frac{L_{BC}}{A_c E} + \frac{6L_{AB}}{5GA_b} \right]$$

while displacement in the *z*-direction due to gravity is defined by,

Equation 2.6
$$\Delta_{Dz} = F_z \left[\frac{L_{CD}^{\,3}}{3EI_{by}} + \frac{L_{CD}^{\,2} L_{BC}}{GJ_c} + \frac{6L_{CD}}{5GA_b} + \frac{L_{BC}^{\,3}}{3EI_{cx}} + \frac{L_{BC}^{\,2} L_{AB}}{GJ_b} + \frac{6L_{BC}}{5GA_c} + \frac{6L_{AB}}{5GA_b} \right]$$
$$+ F_z \left[\frac{1}{3EI_{by}} \left(L_{AB}^{\,3} - 3L_{CD} L_{AB}^{\,2} + 3L_{CD}^{\,2} L_{AB} \right) \right]$$

In these equations, F_i is the respective force in direction i, E is the modulus of elasticity, A is the cross-sectional area, I is the second moment of area, G is the shear modulus, and J is the polar moment of inertia.

These displacements result in a bending stress in the piezoelectric spring element. Bending stress in the plane of the spring is approximated by considering the Euler-Bernoulli beam equation and axial strain along the beam, resulting in

Equation 2.7 $\qquad \sigma_x(x, y, z) = \dfrac{F_x(x)}{A} + \dfrac{M_y(x)z}{I_y} + \dfrac{M_z(x)y}{I_z}$

where σ is stress, F_x is the axial force, M is the bending moment, y and z are the displacements on the associated axes from the beam neutral axis.

For simplicity, the piezoelectric springs can be modeled as a lumped transformer model that converts from the mechanical to electrical domain as shown in Figure 2.5.
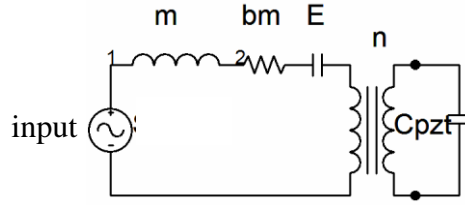
Figure 2.5 Piezoelectric converter lumped model

On the mechanical side of the model, the analogous voltage parameter is stress while the parameter analogous to current is the derivative of strain.

The input stress is a composite of the stress due to displacement, as described in Equation 2.7, and is defined by

Equation 2.8 $\qquad \overline{\sigma_{in}} = \left(\dfrac{m\ddot{x}}{n_{sp}} \left(\dfrac{2}{A_b} + L_{BC} \left(\dfrac{w_1}{I_{bz}} - \dfrac{w_2}{2I_{cz}} \right) \right) + \dfrac{m\ddot{y}}{n_{sp}} \left(\dfrac{1}{A_c} + \dfrac{w_1}{2I_{bz}}(L_{CD} - L_{AB}) - \dfrac{w_2 L_{CD}}{I_{cz}} \right) + \dfrac{m(g+\ddot{z})}{n_{sp}} \left(\dfrac{h}{2I_{by}}(3L_{CD} - L_{AB}) - \dfrac{hL_{BC}}{2I_{cx}} \right) \right)$

where m is the mass, g is the gravitation constant, and n_{sp} is the number of springs.

36

The inertial loss term is due to gravitational forces and is represented by the inductor, denoted m, and is defined by.

Equation 2.9
$$\overline{\sigma_m} = \frac{m\ddot{z}}{n_{sp}} = \frac{m}{n_{sp} b_z^{**} b_z^{*}} \ddot{\delta}$$

where δ is strain and b^{*} as well as b^{**} are geometric constants described in Appendix B.

The mechanical damping term is represented by a resistor, denoted b_m, includes both electrostatic and piezoelectric mechanical damping, and is defined by

Equation 2.10
$$\overline{\sigma_{bm}} = \frac{b_{mx}}{b_x^{*}} \dot{\delta} + \frac{1}{b_y^{*}} \left(b_{my} + \frac{\mu L_s W_s}{d_s} + 16 N_g \mu L_o h^3 \left(\frac{1}{(d-y)^3} + \frac{1}{(d+y)^3} \right) \right) \dot{\delta} + \frac{b_{mz}}{b_z^{*}} \dot{\delta} \quad,$$

where b_m is the mechanical damping coefficient.

Finally, the stiffness term is represented by the capacitor, denoted E in Figure 2.5, and is Hooke's Law and the electrical damping force of the electrostatic component defined in

Equation 2.11
$$\overline{\sigma_E} = \left(E + \frac{1}{b_y^{*}} \frac{Q^2}{2 N_g \varepsilon_0 L_o h \left(d + 2 w_d \left(\frac{1 - \kappa_{SiO_2}}{\kappa_{SiO_2}} \right) \right)} \right) \delta \quad,$$

where E is the elastic (Young's) modulus.

The transformer represents the mechanical to electrical conversion. Assuming the electrodes cover the top and bottom of the spring structure, the current and voltage of the primary (mechanical) side of the transformer are defined by

Equation 2.12
$$\dot{q}_t = -dEa \left(w_1 (L_{AB} + L_{CD}) + w_2 L_{BC} \right) \dot{\delta} \quad,$$

Equation 2.13
$$\sigma_t = \frac{-dEa}{2 h_{sp}} V \quad,$$

where *a* is equal to 1 if the electrodes are in series and 2 if in parallel. These key equations are solved using the numerical modeling with a focus on the electrical side of the lumped model that are discussed in the Appendix. However, the analytical models require validation via FEM.

2.3.4.2   In-plane Hybrid Energy Scavenger

Simulation using a FEM suite (COMSOL Multiphysics® 3.3) is performed to validate the complex analytical models for the piezoelectric spring structures. In addition, since analytical models neglect critical mechanical parameters, such as peak stresses, the use of FEM is warranted before proceeding to a full system model. This section discusses FEM results and findings that show infeasibility of in-plane design.

A comparison between FEM and the displacement equations presented in the previous section validates the use of Castigliano's method for 3-D displacement. The displacement equations are implemented in MATLAB for time domain simulations using a specified mass, piezoelectric material properties, and spring dimensions. The same spring structure is modeled in COMSOL Multiphysics® 3.3 for detailed analysis. The piezoelectric material used for simulation purposes is commercial grade lead zirconate titanate 502 (PZT-502 commonly known as Navy Type-II) due to high coupling coefficients and yield strength.

As depicted in Figure 2.6, the analytical model matches the FEA simulation well (within 15 percent). As a result, the analytical model can be used in the complete system model without a significant amount of error.
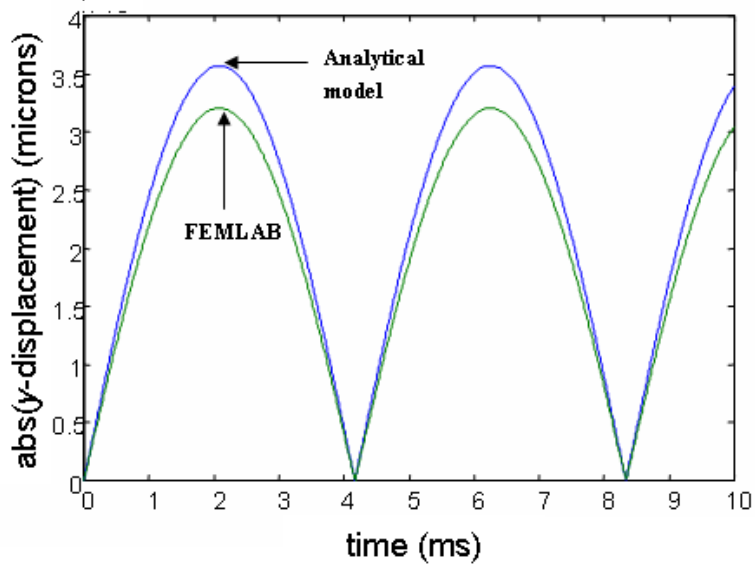
Figure 2.6 Comparison of analytical model and FEA simulation for y-displacement.

As mentioned previously, for simplicity and ease of fabrication, the use of bulk, commercial piezoelectric materials has been chosen, specifically PZT-502. This material has high piezoelectric coupling coefficients; however, the FEM identified a critical design flaw that would not be readily identified by analytical and numerical modeling.

The sum of the integrals of Equation 2.7 along each element of the folded spring provides average principle stress. This value closely approximates the von Mises stress, a composite scalar value representing stress magnitude, provided via FEM. However, it should be noted that the average stress represents the effects of a piezoelectric bender covered completely by a single pair of electrodes and thus the peak stresses cancel. In reality, electrodes would be placed to optimize and extract the localized induced voltage at areas of high stress; however, this would dramatically increase fabrication complexity. However, stress concentration points must be considered for reliability purposes.

Analytical models for bending stress miss critical artifacts such a stress concentration points at sharp corners. Primary simulation results, Figure 2.7, showed a peak stress in the piezoelectric springs on the order of 590MPa. Unfortunately, typical bulk ceramic piezoelectric materials have yield strengths of less than 100MPa. While these stress concentrations were limited to corners and are mitigated by implementing a bulbous spring structure as depicted in Figure 2.7. This design resulted in a maximum stress below 80MPa without affecting the displacement of the system. In spite of this, the elimination of peak stress concentrations results in lower piezoelectric voltage that generates too little voltage to forward bias rectifier diodes.

2.3.4.3 Out-of-Plane Hybrid Energy Scavenger – Piezoelectric Analytical Modeling

Given the complications of engineering a balance between high peak stresses and poor electrical conversion that would preclude rectification for in-plane hybrid scavenger as well as immense fabrication challenges discussed in Chapter 3, the design was abandoned for a simple out-of-plane configuration, shown in Figure 2.8.

590M

80Mpa
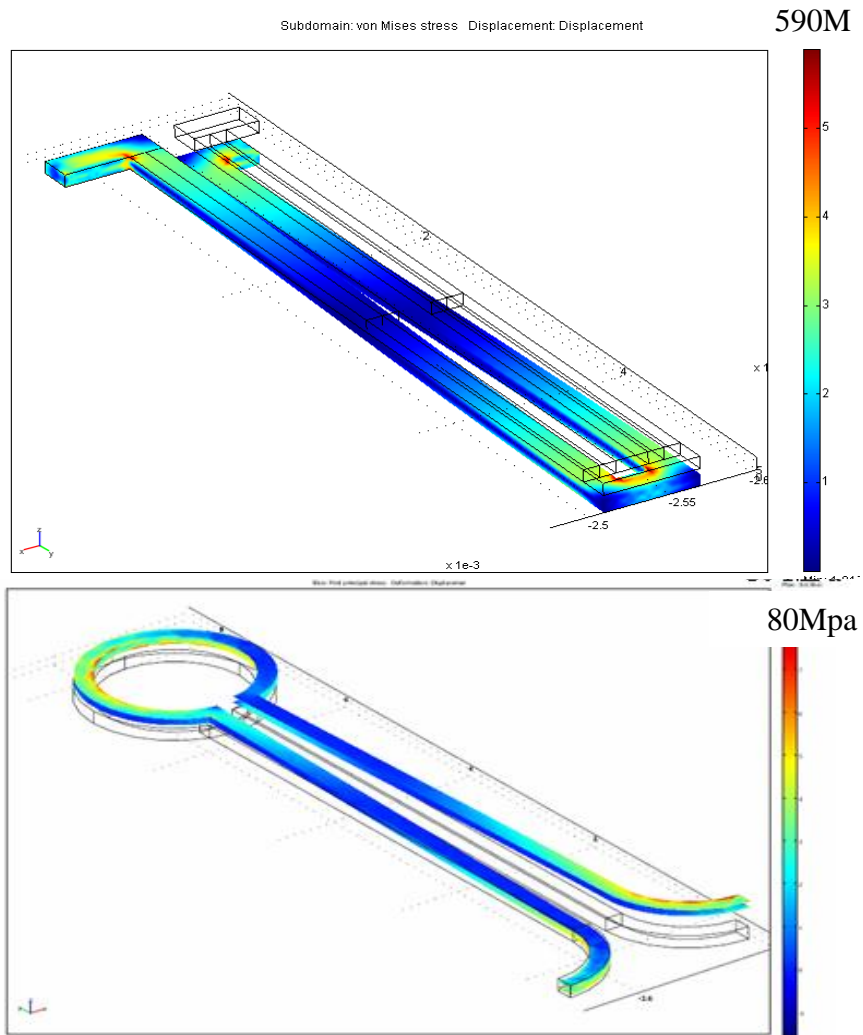
Figure 2.7 FEA simulation of a rectilinear versus bulbous spring to eliminate stress concentration points.

w_b

l_b

t_m

w_m

l_m
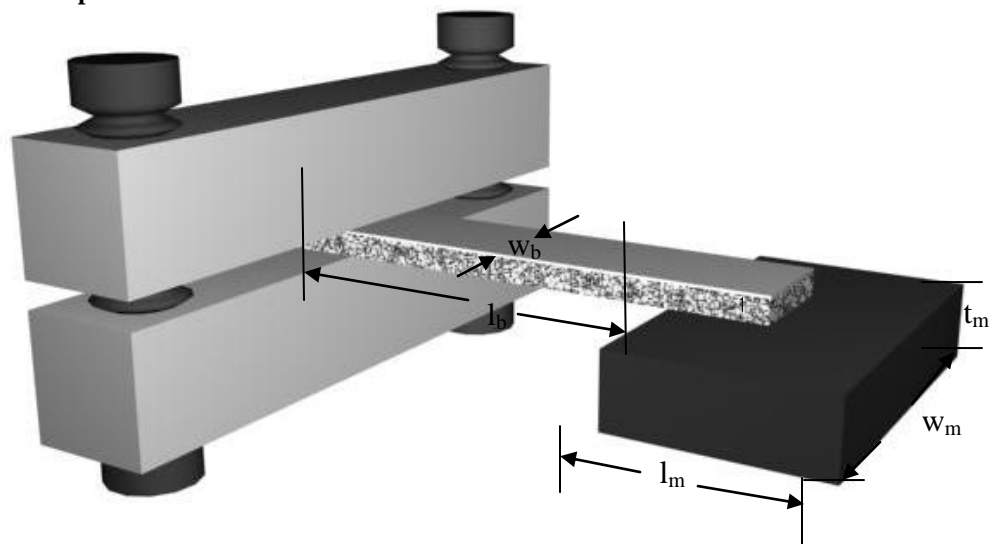
Figure 2.8 Diagram of out-of-plane piezoelectric for analytical modeling.

This dramatically simplifies the analytical modeling as the Euler-Bernoulli (classical) beam theory can be utilized to examine the mechanical behavior of the system. Furthermore, a realization that the intended use of the lumped model shown in Figure 2.5 is not complete as the electrical side of the circuit would not only be loaded by the storage capacitors, but would also be affected by the not-yet-determined rectifier and feedback signal processing circuits that are described in Section 2.5. As a result, the comprehensive system modeling was abandoned in lieu of an approach to design a sustainable mechanical system with experimental analysis and evolution of the electrical system following fabrication and characterization of the piezoelectric transducer.

Classical (Euler-Bernoulli) beam theory is used to provide a fabrication starting point by providing beam and mass dimensions with three primary goals, peak stress below the yield strength of the piezoelectric material, resonance at a fundamental frequency of 120Hz, and a total volume of less than 0.25cm^3. Limitations of this theory are the assumptions that shear stresses are negligible and stresses are only linear when the total stress is below the yield strength of the material.

Euler-Bernoulli beam theory describes deflection $u(x)$ of a one-dimensional beam in terms of a distributed load $w(x)$ (force per unit length) by

Equation 2.14 $\dfrac{\partial^2}{\partial x^2}\left(EI\dfrac{\partial^2 u}{\partial x^2}\right) = w(x)$

and bending stress as

Equation 2.15 $\sigma = \dfrac{M(x)b}{I}$

where $M(x)$ is the bending moment, I is the second moment of area, and b is the position from the neutral axis.

The bending moment is defined by

Equation 2.16 $M(x) = F_Z(l_b + \frac{1}{2}l_m - x)$

and the second moment of area for a rectangular beam is

Equation 2.17 $I = \dfrac{w_b\, t_b^3}{12}$

where F_z is the force perpendicular to the beam, l_b, w_b, t_b are the length, width, and thickness of the beam respectively, and l_m is the length of the proof mass. For a single layer beam let $b = t_b$ and the electrodes cover both top and bottom surfaces by $l_b = l_e$, then the average stress is defined by

Equation 2.18 $\bar{\sigma} = \dfrac{1}{l_e}\int_0^{l_e} \dfrac{M(x)t_b}{I}\,dx = \dfrac{F_z t_b}{2I}(2l_b + l_m - l_e) = \dfrac{6F_z(l_b+l_m)}{w_b t_b^2}.$

Euler-Bernoulli approximates deflection at the point of attachment to the proof mass, z by integrating

Equation 2.19 $\dfrac{\partial^2 u}{\partial x^2} = \dfrac{M(x)}{EI} = z = \dfrac{F_z l_b^2}{2EI}(\frac{2}{3}l_b + \frac{1}{2}l_m).$

The fundamental frequency ω of the beam as

Equation 2.20 $\omega = \sqrt{\dfrac{k}{m}} = 2\pi f,$

where m is the mass and defining the spring constant (stiffness) k as

Equation 2.21 $k = \dfrac{F_z}{z} = \dfrac{2EI}{l_b^2(\frac{2}{3}l_b+\frac{1}{2}l_m)} = m(2\pi f)^2$

and F_z as a product of mass and acceleration, the substitution of Equation 2.21 into Equation 2.18 to produce

Equation 2.22 $m = \rho l_m w_m t_m = \dfrac{E w_b t_b^3}{6(2\pi f)^2 l_b^2(\frac{2}{3}l_b+\frac{1}{2}l_m)},$

where ρ is the density of the proof mass material, f is the desired fundamental frequency in hertz, and l_m, w_m, t_m, are the dimensions of the proof mass.

43

The modulus E, proof mass density ρ, thickness of beam t_b are material properties that are constrained by available off-the-shelf materials that are discussed in Chapter 3. Furthermore, the dimensions of the proof mass are constrained by the volumetric specifications and frequency is set by the expected environmental conditions (120Hz for this work), thus only the width and length of the piezoelectric beams can be arbitrarily set, with regard to the volumetric limitations. Furthermore, chosen values can be inserted into Equation 2.18 to ensure the average stress does not exceed the yield strength of the material. Despite this, average stress values can miss peak stresses, analogous to the scenario with the in-plane device described in Section 2.3.4.2; therefore, COMSOL Multiphysics® 3.3 is used to ensure stresses in excess of the yield strength were not expected for extracted beam dimensions. Piezoelectric beam dimensions that were simulated, fabricated, and tested will be detailed in Chapters 4 after a discussion of fabrication induced non-idealities in Chapter 3.

2.4 Electrostatic Transducer

Vibration-based electrostatic energy scavengers are comprised of a variable capacitor structure that uses mechanical vibration to change the capacitance and thus the energy stored in the capacitor to change. This energy change can be applied at optimal times to charge an energy reservoir or power circuits. This section will discuss the basic structure, theory of operation, critical parameters, and design and simulation of both in-plane and out-of-plane charge-based electrostatic scavengers.

2.4.1 Device Structure

The initially proposed in-plane design, shown in Figure 2.2, consists of an interdigitated, high aspect ratio (HAR) structure with the goal of maximizing capacitance values, furthermore, the mechanical displacements would allow two energy conversion cycles per mechanical excitation cycle. Despite this goal, fabrication challenges, namely the formation of molds and deposition of high density materials for the interdigitated electrodes that are discussed in Chapter 3, preclude the implementation of this design in a hybrid system. In lieu of this, the simpler out-of-plane design, shown in Figure 2.3, employs the required proof mass for the harmonic piezoelectric transducer and base electrode on a printed circuit board (PCB) to form a variable capacitance structure. While not optimized, the single parallel plate structure inherent in this design is sufficient to demonstrate the underlying theory of the hybrid vibration energy scavenging within the volume of the piezoelectric transducer. The remainder of this section will present theory of operation for dynamic charge-based (non-electret) electrostatic energy scavengers, and simple models to predict energy scavenging performance.

2.4.2 Theory of Operation

Basic electrostatic scavenging theory is well defined in the literature and will be briefly discussed in this section [33],[44]. Dynamic electrostatic scavengers can undergo either one of two energy conversion cycles, voltage or charge constrained. Figure 2.9 depicts energy conversion cycles for both voltage (A-C-D-A) and charge (A-B-D-A) constrained approaches. For voltage constrained conversion, when the variable capacitor is at the maximum capacitance value, C_{max}, the control system

45

charges the system to the initial voltage, V_{max}. As the capacitance decreases, the mechanical force pushes charge back into the energy reservoir. When the capacitance is minimized to C_{min}, the remaining charge is recovered. Net energy gained is the area of the triangle ACD; however, this approach, while appearing to have considerably more energy conversion requires an additional voltage supply to hold a constant voltage across the variable capacitor during the capacitance change.
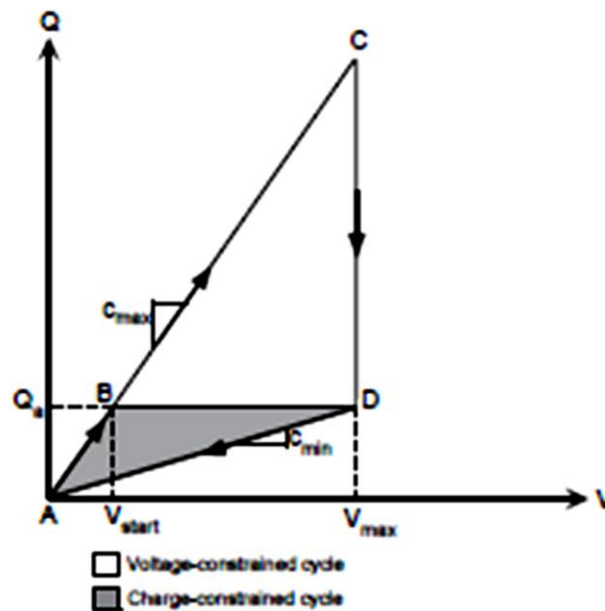
Figure 2.9 Diagram of dynamic electrostatic energy conversion [44].

Charge constrained conversion, charges the variable capacitor to an initial voltage, such as the rail voltage, V_{start} and then is disconnected from the circuit during the capacitance change. Since charge is fixed, the mechanical force that pulls the plates apart induces a voltage increase. At C_{min} the voltage is maximized and the variable capacitor discharges to the energy reservoir. The inherent advantage of this approach is the reduction of essential voltage sources and simplicity of the charge control circuitry. Regardless, of conversion cycle chosen, energy is maximized as the

change in capacitance is increased and thus requires critical timing to ensure the extrema are captured for synchronizing charge transfer.

2.4.3   Critical Electromechanical Parameters

The parallel plate architecture that comprises the variable capacitor of the electrostatic energy scavenger requires several design considerations. As described in the following section, the capacitance magnitude dominates the energy conversion and most significantly affects performance; however, mechanical considerations are vital to ensure proper behavior and long term resilience. In order to maximize capacitance, overlapping surface area should be maximized while minimizing gap at the displacement peaks.   In contrast, the parallel plate configuration with large overlap and small gaps induce squeeze film damping that adversely affects the system behavior by exerting an opposing force. Despite this, squeeze film damping may be exploited to help preserve the device in an overdrive scenario since shock damage fractures the piezoelectric beam material. These design factors are presented in the following section, in the form of analytical modeling for both in-plane and out-of-plane configurations.

2.4.4   Modeling and Simulation

In the hybrid energy scavenger, the proof mass doubles as the moving electrode of a variable capacitor that provides electrostatic transduction. This section describes the analytical models for both in-plane and out-of-plane architectures.

2.4.4.1 In-Plane Hybrid Energy Scavenger – Proof Mass Analytical Modeling

For in-plane configuration, the electrostatic energy conversion component is a proof mass shuttle that is comprised of interdigitated electrodes forming a variable capacitor structure as shown in the three-dimensional (3-D) model in Figure 2.10. As described previously by Equation 2.1, the mass is utilized to couple vibration acceleration in turn inducing a sinusoidal excitation force. The total mass of the electrostatic shuttle, m_{total} is

Equation 2.23 $m_{total} = \rho_s h \left[L_s \cdot W_s + \left(N_g + 2 \right) \left(L_f \cdot W_f \right) \right]$

where ρ_s is the material density, h is the electrode height, L_s and L_f are the center shuttle and finger lengths, W_s and W_f are the corresponding widths, and N_g is the number of gaps between electrodes with complete derivation in Appendix A.
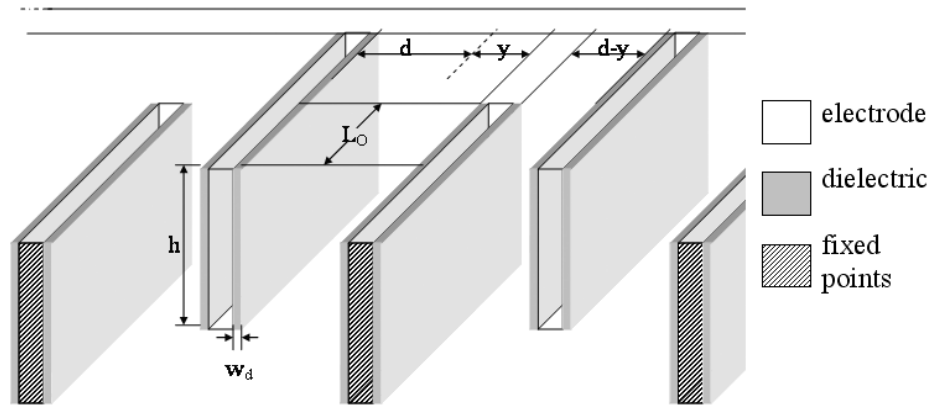
Figure 2.10 Geometry of proof mass/electrostatic electrode structure

2.4.4.2 In-Plane Hybrid Energy Scavenger – Electrostatic Analytical Modeling

This section briefly mentions key equations in modeling the electrostatic transducer for the hybrid scavenger system. A complete derivation of these equations can be found in Appendix A.

Ideally the system pre-charges the temporary storage capacitor to V_{IN}, roughly equal to peak-to-peak voltage of the piezoelectric (V_{PZT}) less the rectifying diode voltage drop. At the maximum displacement, that coincides with the maximum capacitance, C_{max}, the control circuit charges the variable capacitor resulting in a fixed charge. At the neutral point, which corresponds with the minimum capacitance, C_{min}, the capacitor is at its maximum output voltage, V_{OUT}, and is discharged to a capacitor reservoir. The primary figure of merit for the HALF-LIVES system is the energy transfer per half cycle to the capacitor, ΔE is then

Equation 2.24 $\quad \Delta E = \dfrac{1}{2} V_{IN} V_{OUT} \left(C_{max} - C_{min} \right).$

For the HALF-LIVES system to be effective, every effort must be made to scavenge the maximum amount of energy. Using the definition of energy transfer, it is clear that the change in capacitance is important. Typically, mechanical stops are used to prevent shorting of the electrodes. Due to fabrication limitations inherent to large aspect ratio devices, the minimum feature size for these mechanical stops is on the order of a few microns. Using mechanical hard stops, the maximum capacitance, C_{max} is

Equation 2.25
$$C_{max} = 2 N_g \kappa_{air} \varepsilon_0 L_o h \left(\dfrac{d}{2 d w_{stop} - w_{stop}^2} \right),$$

where N_g is the number of gaps, κ_{air} is the dielectric constant of air, ε_0 is the free space permittivity, L_o is the length of electrode overlap, h is the height, d is the initial gap and w_{stop} is the width of the mechanical stop shown in Figure 2.10.

Leveraging from the developments in the micro-fabrication of supercapacitors, the use of a dielectric sidewall coating is possible. For the electrostatic shuttle, a sub-

micron dielectric coating can be used to prevent shorting and eliminate the need for an external mechanical hard stop. This allows the electrodes to come into intimate contact thereby increasing the maximum capacitance. The variable capacitance of this configuration is defined by

$$C_{var} = 2N_g \varepsilon_0 L_o h \left(\frac{d + 2w_d \left(\frac{1-\kappa}{\kappa} \right)}{d^2 - y^2 + 4w_d \left(\frac{1-\kappa}{\kappa} \right) \left(d + w_d \left(\frac{1-\kappa}{\kappa} \right) \right)} \right),$$

Equation 2.26

where y is the displacement, κ is the dielectric constant and w_d is the thickness of the insulating coating, resulting in maximum and minimum capacitances as described by

Equation 2.27 $\quad C_{max} = N_g \varepsilon_0 L_o h \left(\frac{1}{\frac{2w_d}{\kappa}} + \frac{1}{2d + 2w_d \left(\frac{1 - 2\kappa}{\kappa} \right)} \right),$

Equation 2.28 $\quad C_{min} = 2N_g \varepsilon_0 L_o h \left(\frac{1}{d + 2w_d \left(\frac{1-\kappa}{\kappa} \right)} \right).$

   Using this model, the mechanical and electrical damping functions can be defined. The mechanical damping function caused by the electrostatic component is dominated by Couette and squeeze film damping that is collectively described by

Equation 2.29 $\quad f_{m_{electrostatic}} = \left[\frac{\mu L_s W_s}{d_s} + 16 N_g \mu L_o h^3 \left(\frac{1}{(d-y)^3} + \frac{1}{(d+y)^3} \right) \right] \dot{y},$

where μ is the viscosity of air [1].

   In this case, the electrical damping function,

Equation 2.30 $\quad f_{e_{electrostatic}} = \frac{Q^2}{2N_g \varepsilon_0 L_o h \left[d + 2w_d \left(\frac{1-\kappa}{\kappa} \right) \right]} y,$

is dominated by the electrostatic attraction force between the charged electrodes, where Q is the charge on the interdigitated capacitor structure. Using these analytical models, the mechanical properties, including mass and fluid damping functions, as well as the electrical properties, including the capacitance and electrostatic damping have been defined and are used for numerical modeling of the electromechanical system described in Section 2.5.2.

2.4.4.3 Out-of-Plane Hybrid Energy Scavenger – Analytical Modeling

Modeling of the proof mass and electrostatic parameters of the out-of-plane architecture is trivial as a simple block is used for the proof mass and thus the variable capacitor is a single parallel plate. Based on Figure 2.8, the mass is

Equation 2.31 $\quad m = \rho_s t_m l_m w_m$

where ρ_s is the density of the block material.

Due to the shock damage mechanism of piezoelectric material, mechanical hard stops are not used with the exception of the fixed electrode, and thus an initial gap should be utilized to prevent striking but allow maximum capacitance, defined by

Equation 2.32 $\quad C_{max} = \dfrac{\kappa_{air} \, \varepsilon_0 \, l_m \, w_m}{d - \dfrac{z}{2}},$

where κ_{air} is the dielectric constant of air, ε_0 is the free space permittivity, z is the displacement described in Equation 2.19, and d is the initial gap. Minimum capacitance is then

Equation 2.33 $\quad C_{min} = \dfrac{\kappa_{air} \, \varepsilon_0 \, l_m \, w_m}{d + \dfrac{z}{2}}.$

Mechanical damping for the out-of-plane system only includes squeeze film mechanisms and is described by

Equation 2.34 $f_{m_{electrostatic}} = \left[\dfrac{16\, \mu l_m\, w_m{}^3}{\left(d - \dfrac{z}{2} \right)} \right] \dot{z}$,

where μ is the viscosity of air.

Electrostatic force that opposes the squeeze film damping is defined by

Equation 2.35 $f_{e_{electrostatic}} = -\left(\dfrac{\partial U}{\partial z} \right) = \dfrac{Q^2 \left(d - \dfrac{z}{2} \right)}{2 \kappa_{air}\, \varepsilon_0\, l_m\, w_m}$;

however, these are negligible in comparison to the vibration driving and piezoelectric spring forces. Given this, fortunately stiction from electrostatic attraction is not a primary concern. Unfortunately, squeeze film damping is not sufficient to prevent shock behavior in overdrive conditions.

In the out-of-plane configuration, per cycle (versus half cycle of in-plane) energy generation of the electrostatic harvester is also given by Equation 2.24. Since energy is directly dependent on the total change in capacitance and the simple block configuration is area limited, the effective gap of the variable capacitor plates is critical and should be sub-micron at maximum displacement as shown in Figure 2.11.
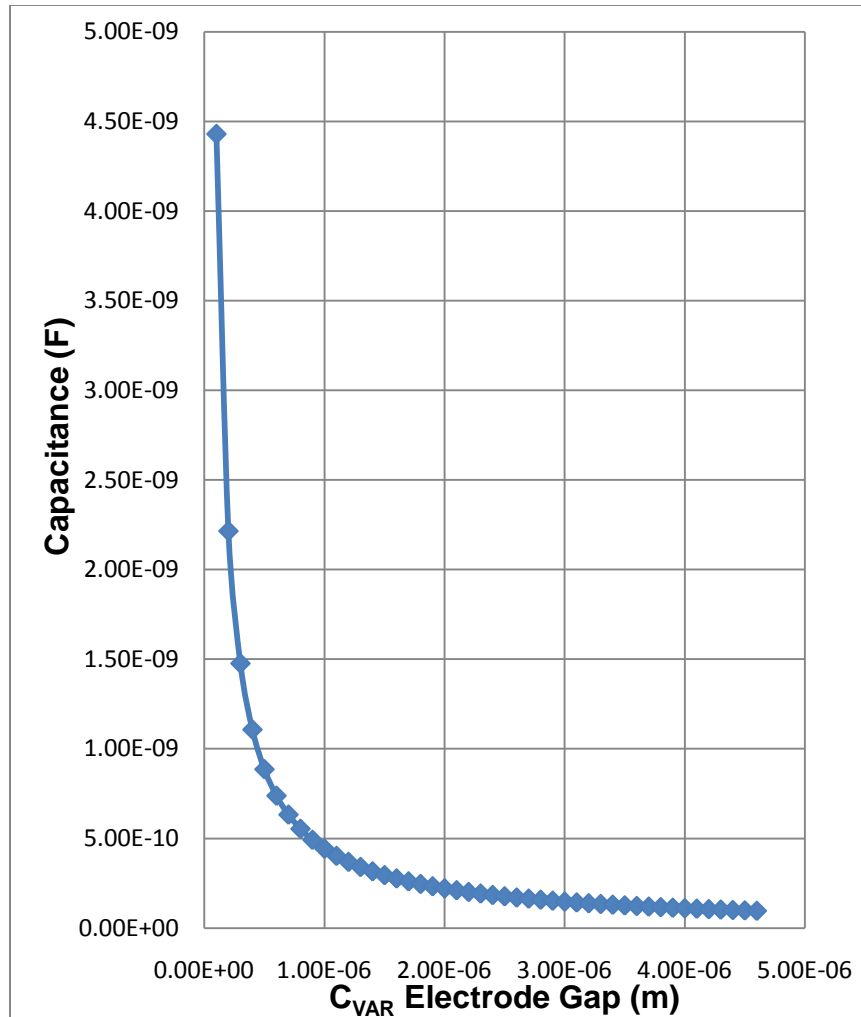
Figure 2.11 Capacitance versus C_{VAR} electrode gap for 5mm x 10mm x 1mm proof mass.

Given both in-plane and out-of-plane models for the piezoelectric spring, proof mass, and electrostatic transducer, these components are coupled mechanically and electrically. While modeling of the mechanical coupling is relatively straightforward, the electrical coupling is complicated due to the dynamic behavior of the electrical system and is described in the following section.

53

2.5   Hybrid Energy System and Circuit

The cornerstone of the hybrid energy scavenger system is the circuit that provides coupling between the piezoelectric and electrostatic transducers and connection to the energy reservoir and load. This section describes desired circuit operation at a high level with an introduction of critical sub-components and modeling using a custom numerical model in MATLAB as well as Simulation Program with Integrated Circuit Emphasis (SPICE). Additionally, printed circuit board (PCB) design methodologies and evolution of the system are discussed.

2.5.1   <u>Theory of Operation</u>

A high-level, block diagram of the basic out-of-plane system is shown in Figure 2.12. In the system, the piezoelectric element generates a voltage, denoted V_{pzt}, when excited by vibration. This voltage is rectified by diodes to charge two storage capacitors that generate positive and negative DC rail voltages, denoted V_{EE} and V_{SS} respectively. These rails are used for a pre-charge for the variable capacitors where

Equation 2.36 $V_{IN} = V_{EE} - V_{SS},$

as well as operating control and conditioning electronics as needed. The most essential control sub-component is the peak detector system. Using the inherent relationship between the piezoelectric voltage and displacement, a feedback circuit that correlates capacitance extrema is built into the system with little overhead. By using a simple comparator as a peak detector, the system can synchronously charge and discharge the electrostatic transducer at optimal points. This provides two advantages over other published synchronous charge-based electrostatic energy scavengers as 1) no battery is required to generate pre-charge voltage, and 2) no

sophisticated, high energy consumption electronic sub-systems (such as phase locked loops) are required for charge control synchronization. However, the system modeling is complicated by dynamic switching behavior and is not trivial as there are multiple states of operation. Furthermore, analytical, numerical, and SPICE modeling provide ideal results and thus the necessity for additional electronics for signal conditioning (e.g. active noise filtering) could not be pre-determined. Nevertheless, the circuit modeling of both in-plane and out-of-plane systems prior to physical implementation is discussed.
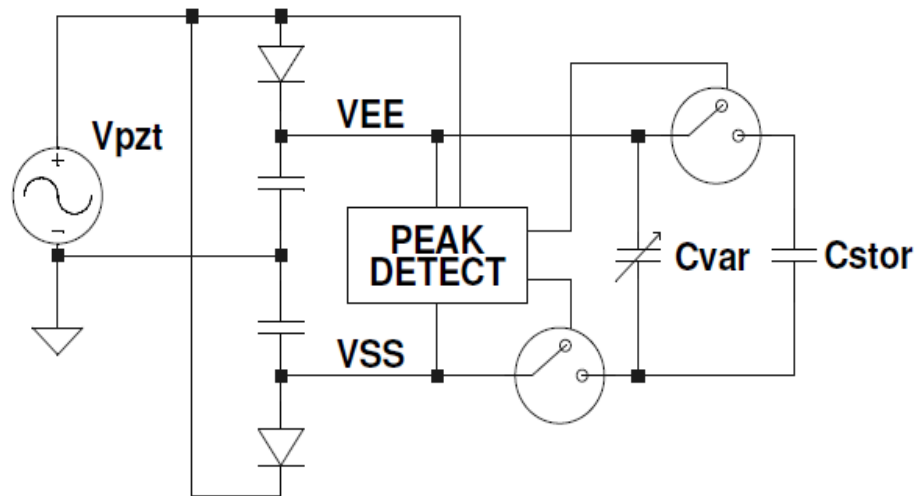
Figure 2.12 High-level circuit diagram for hybrid energy scavenger system.

2.5.2   Modeling and PSPICE Simulation

In the design evolution and evaluation of feasibility several modeling techniques were used in parallel as necessary. Using analytical models derived in the previous sections for an in-plane system, a numerical simulator was developed in MATLAB to observe system behavior based on lumped electromechanical model; however, the implementation of the simulation misses the dynamic effect of control electronics loading on the system. When abandoned for the out-of-plane system due to

mechanical limitations, the modeling was moved wholly to SPICE using vendor models of real commercial-off-the-shelf (COTS) components to ensure that the control and conditioning electronics impact on system operation could be pre-determined prior to PCB fabrication. Furthermore, SPICE is utilized to design implementations of control and conditioning electronics for a future low power ASIC using Bi-CMOS technology.

2.5.2.1   Numerical Modeling of In-Plane System

Numerical modeling is utilized to describe the entire hybrid scavenger system to provide validation of expected operation and identification of effects from singular parametric changes on the global system. This section discusses the numerical model implementation, assumptions, and optimal system behavior.

The entire electromechanical system is implemented in MATLAB code to obtain a numerical solution for the analytical models. The electrical side of the piezoelectric lumped model has a dynamic nature and switches depending on state of operation within the system. The full wave rectifier and peak detector circuits determine which stage of operation the system is in. On the electrical side, the system operates in five distinct stages that are represented by Figure 2.13(a-d).

In stage 0, the piezoelectric voltage is less than the voltage on temporary storage capacitor, C_{st}, thus the rectifying diodes are all off, leaving the piezoelectric component unloaded. In this case, there is no transfer of charge. In stages 1 and 3 the input voltage exceeds C_{st}, thus the rectifying diodes are conducting and charging C_{st} to provide the pre-charge voltage. While the displacement is at a peak point, the

variable capacitor is maximized, and the control electronics signal the first switch to conduct, denoted stage 2. In this stage, there is a charge transfer from C_{st} to C_{var}. Finally, in stage 4, when the displacement is equal to the neutral point and the variable capacitor is minimized, the control electronics close the second switch to allow energy transfer to C_{sup}, the supercapacitor reservoir and is the key figure of merit for system simulation results.
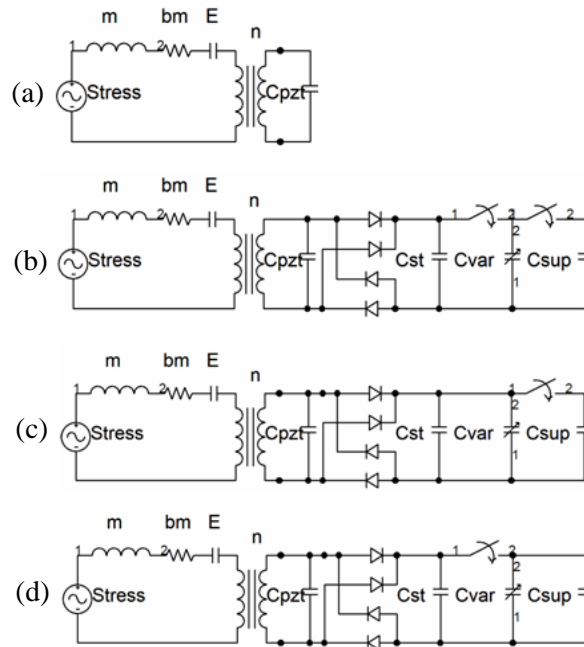
Figure 2.13Multi-stage lumped system model (a) Stage 0 – disconnected, (b) Stages 1/3 – charging Cst, (c) Stage 2 – charging Cvar, and (d) Stage 4 – charge transfer to Csup

This complete system was implemented and simulated in MATLAB programming language. Mechanical and electrostatic domains are modeled using the derived analytical models while the control electronics and MOS switches were modeled as ideal components and implemented as a series of conditional statements. As a result, due to history dependence and discontinuities in the transitions between stages, the standard Runge-Kutta-based MATLAB ordinary differential equation

(ODE) solvers could not be used. For simplicity, a finely-stepped Euler method was used to solve the system of differential equations.

Behavior of the system and indication of stages of operation from a MATLAB solution is provided in Figure 2.14(a-d). By observing the graphs for the in-plane system, it is clear that the capacitance reaches its maximum value at the displacement extrema and its minimum at the neutral points.
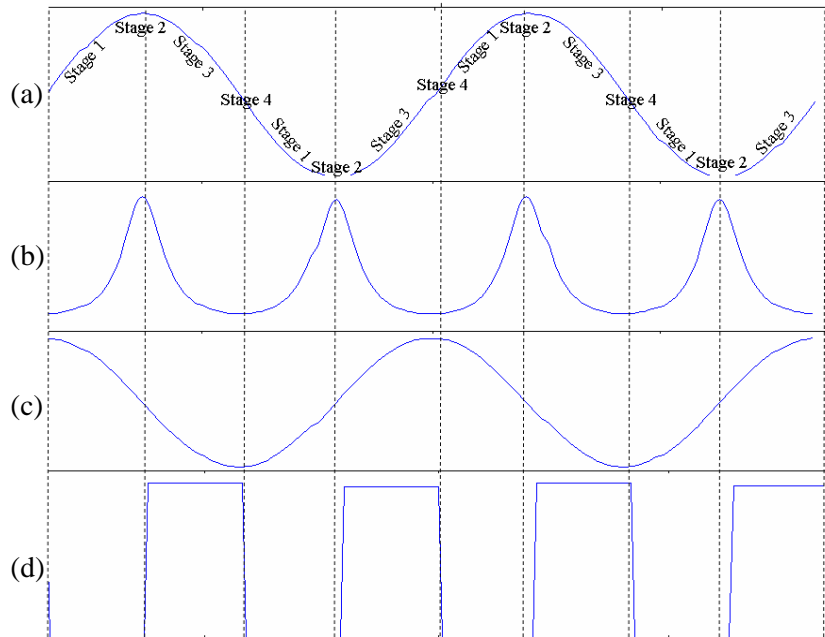
Figure 2.14 MATLAB solution of system behavior (a) displacement, (b) variable capacitance, (c) piezoelectric voltage, and (d) charge on Cvar

The piezoelectric voltage operation also functions as expected and is the derivative of the displacement. As shown in Figure 2.14(c-d), the piezoelectric voltage is used by the control electronics to signal the charging of C_{var} at the zeros and discharges at the voltage extrema.

This system model demonstrates the dynamic behavior of the full hybrid scavenger system, which is used for validation of the expected operation as well as

providing transient operation. By observing the transient behavior, one can monitor the transition from startup to steady state operation. While the numerical model indicates theoretical operation, the ideal modeling of the control systems results in unrealistic operating conditions as the dynamic behavior and loading of the control architecture significantly impacts performance. When FEA modeling precluded in-plane operation due to overstress or low voltage conditions, numerical modeling was also abandoned in lieu of SPICE system modeling to capture control circuit loading effects.

2.5.2.2   SPICE Modeling of Out-of-Plane System

COTS components are the basis for rapid prototyping of a test system for hybrid energy scavenging. After abandoning numerical modeling, experimental testing of electromechanical components with rapid prototypes of control circuits with PCB system implementations enabled rapid progression in realization of a functional hybrid scavenger system. LTSPICE IV is a freeware SPICE program from Linear Technology Corporation (www.linear.com). This software permits the simulation of complex circuits, such as the COTS hybrid scavenger model shown in Figure 2.15, since there is no limitation on component count and custom models can be created.
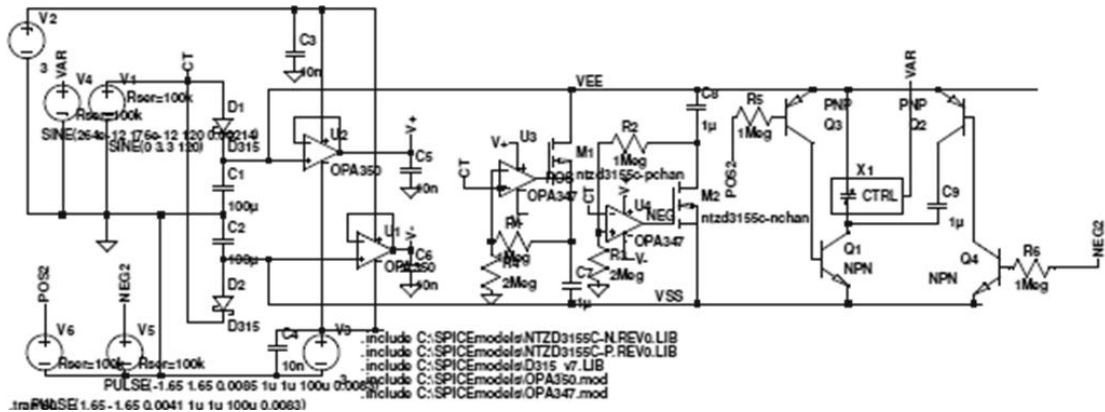
Figure 2.15 LTSPICE simulation layout of COTS scavenger system.

59

SPICE modeling aided in design of proper electrical control architecture by identifying a flaw in CMOS-based charge control switches. A CMOS-based charge control is desirable from the perspective of reducing switching induced losses; however, when the NMOS switch experiences drain-source inversion, due to the floating node of the variable capacitor exceeding the negative V_{SS} rail during energy scavenging, the transistor conducts and thus will not permit voltage increase beyond the pre-charge rails, as shown in Figure 2.16.
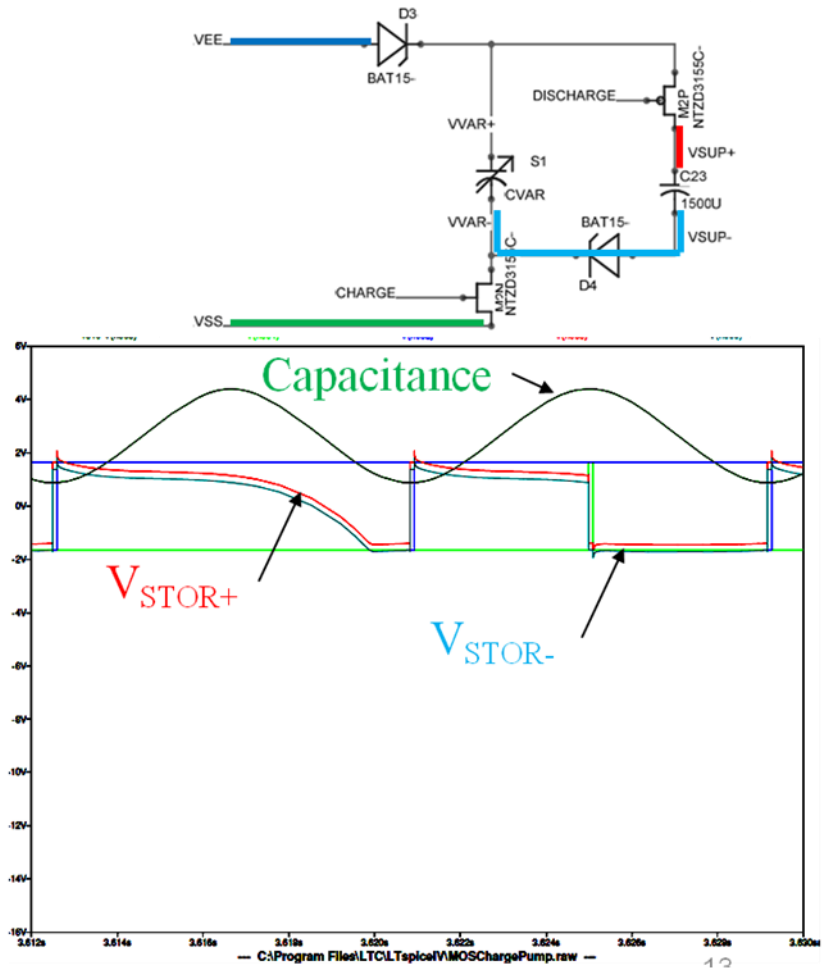
Figure 2.16 SPICE modeling and simulation results showing CMOS charge control design defect.
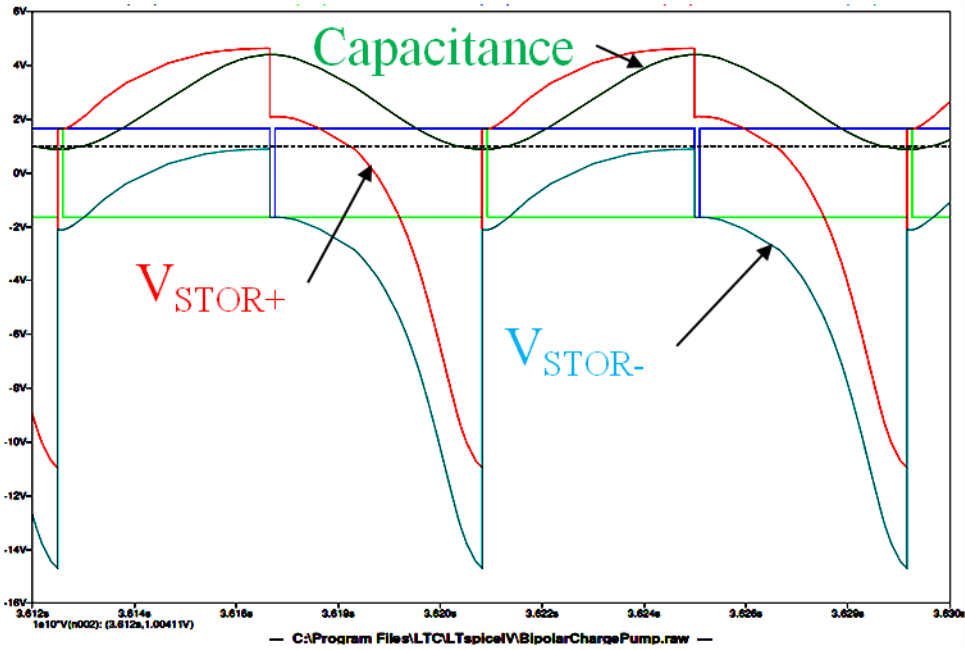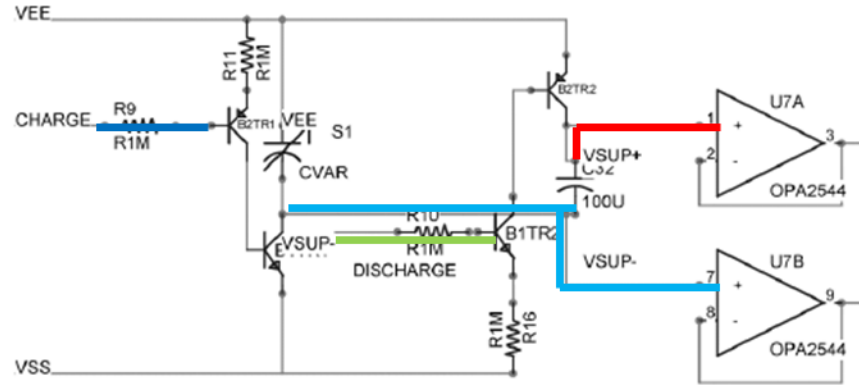
Figure 2.17 BJT architecture SPICE simulation results indicating proper scavenging operation.

This flaw was accounted for by utilizing bipolar junction transistors (BJTs) in lieu of MOS components. Since BJTs are charge controlled devices, the floating node of the variable capacitor can change without inducing inadvertent conduction as shown in Figure 2.17. Use of BJTs facilitates proper operation, but introduces additional current paths in the circuit that must be controlled to ensure proper operation and will be discussed further in Chapters 4 and 5.

61

2.5.2.3   SPICE Modeling of Low Power Sub-Circuits

SPICE was further utilized to design low power sub-circuits that could be implemented into a Bi-CMOS ASIC component to enhance overall system performance in contrast to the utilization of COTS components. Several sub-circuits have been custom designed and simulated to reduced control overhead but have not yet been realized.

For the in-plane design, an efficient full wave rectifier circuit that generates a relatively stable DC supply is simulated and essential for optimized operation. These full wave rectifiers have been used for some time in rectenna circuits for RFID tags and biomedical applications [19].

The literature describes the minimization of losses in this type of rectifier circuit. Special considerations must be made to account for the fact that the AC voltage swing will possibly exceed the established V_{DD}. Ghovanloo and Najafi describes an enhanced full wave rectifier circuit that minimizes the current leakage to the body and minimizes the possibility of latch up due to input fluctuations beyond DC rails as shown in Figure 2.18. In this enhanced version of the rectifier circuit, the additional PMOS FETs bias the body voltage to match the highest voltage between the V_{PZT} and V_{DD}. Likewise, the NMOS transistors set the body to the minimum between *GND* and V_{PZT}.

For the SPICE simulation, some general parameters, such as transistor widths and length (*W* and *L*) as well as capacitor values were chosen by sweeping the parameters for a fixed input voltage and frequency until an optimum parameter set was determined. It should be noted that the power FET widths did not dramatically affect

the power delivered to the capacitor, but does impact the capacitor voltage for small values of V_{PZT}. SPICE simulation indicates that large power FET widths, on the order of 100µm, are necessary for improving the voltage on the capacitor for relatively short charging times (<1 minute). Furthermore, simulations show that the use of the enhanced rectifier over a standard rectifier increases voltage on the capacitor, V_{DD}, by 20 percent.
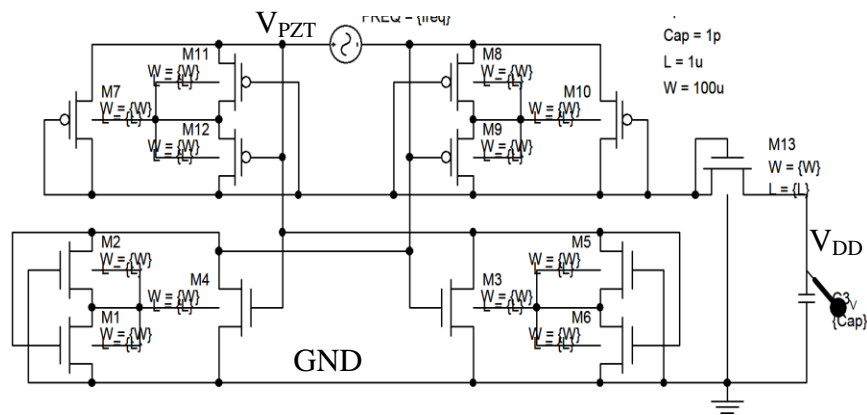
Figure 2.18 SPICE model of Ghovanloo and Najafi full wave rectifier circuit [19].

The COTS-based peak detector depends on multiple operational amplifiers (opamps) and at best consumes 10-20 milliwatts of constant power. In the COTS implementation, an opamp voltage follower is used to track the piezoelectric generated DC rails but provides the high current required to run the COTS components in the circuit. In reality, these architectures are not feasible since the voltage rails will be dependent on input vibrations and sufficient surplus power will not likely be available. For energy scavenging applications, it would not be possible to run the detector circuit alone. Therefore, sacrifices in accuracy must be made to save power. To this end, every effort was made to minimize the power consumption of the peak detection circuit for an ASIC design.

As shown in Figure 2.19, the simplified peak detector circuit consists of a differential pair, a single PMOS transistor, and a reference capacitor. The rectified input voltage from the piezoelectric springs is fed into the inverting input of the amplifier. The top rail feeding the current uses the V_{DD} voltage from the temporary storage capacitor. Diode connected transistors are used to reduce the voltage feeding the current source bias and the inverting input, thereby minimizing current through the differential pair. In this arrangement, the feedback capacitor does not require an initial charge. Therefore a positive input causes the capacitor to charge up to the peak voltage over many cycles. Once at steady state, as the input voltage peaks to the common mode input, at the maximum voltage, the differential pair inverts the output signal and turns on the PMOS device that keeps the reference capacitor charged up to the peak value at each cycle. The differential output can be tapped to feed the input of an inverter pair as depicted in Figure 2.19. This provides a buffered output with a positive clocking mechanism, denoted a V_{CLK}.
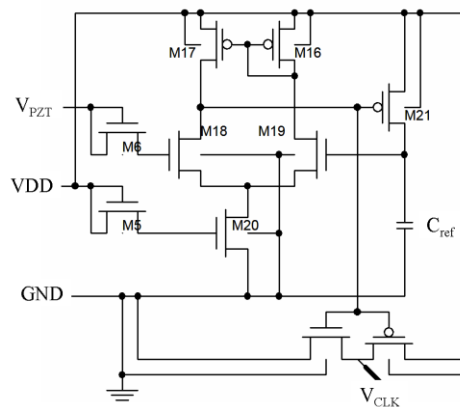
Figure 2.19 SPICE model of a simple, self-starting, low power peak detector circuit

When the energy scavenging device produces a sufficient DC voltage rail, when V_{DD} is approximately 2V, the peak detector starts to operate properly as shown by the

64

steady state output of the SPICE simulation shown in Figure 2.20, with peak power

consumption of 600nW and maintains operability of the system with minimal control

overhead.
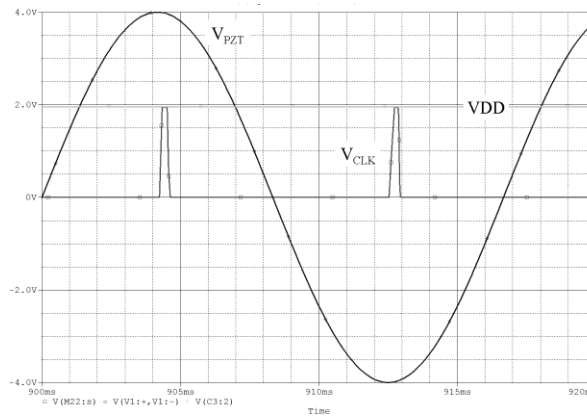
Figure 2.20 SPICE simulation demonstrating a functional output of the low power peak detector.

2.5.3   Test Printed Circuit Board (PCB) Design

Given operability validation via SPICE simulation, a COTS-based test platform

on PCB platform is the next progression in realization of hybrid energy scavenger

prototype. Easily Applicable Graphical Layout Editor (EAGLE) software package is

used to generate a system schematic, COTS and custom parts libraries, and custom

PCB layout for generation of a test platform design. The work flow consists of

generating a parts library, then creating a system-level schematic as depicted in the

sample of the peak detector sub-circuit, shown in Figure 2.21. Finally, a PCB is

manually floor planned and routed in the PCB editor resulting in a completed design

as shown in Figure 2.22.
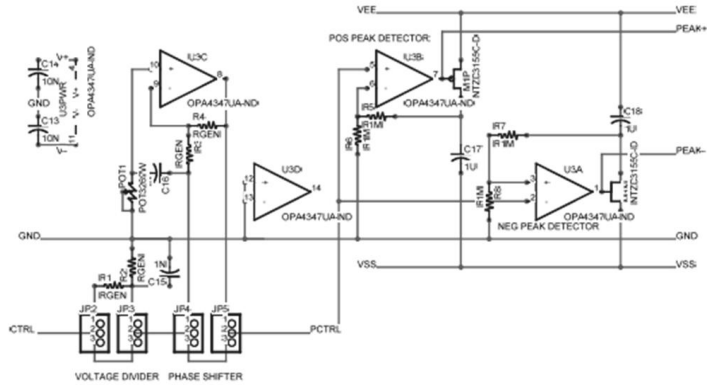
Figure 2.21 Eagle schematic of COTS peak detector and conditioning circuits.
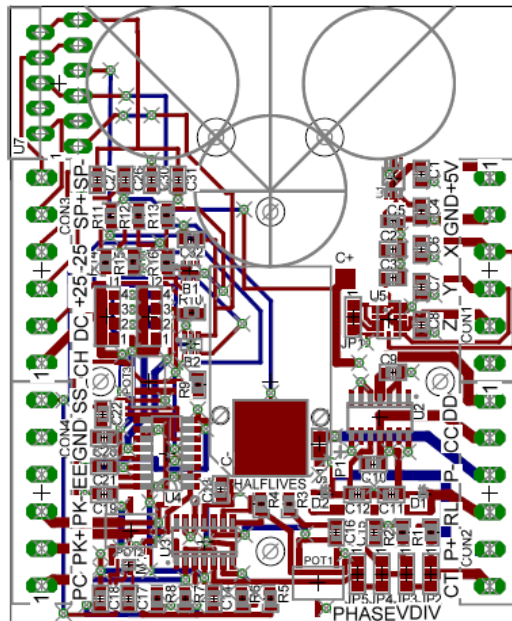
Figure 2.22 Eagle PCB layout of test system for hybrid scavenger.

2.6 Summary

The hybrid energy scavenger system has been modeled analytically and numerically, simulated for overall behavior as well as detailed sub-circuit performance for both COTS and ASIC designs. Finally, a test platform has been developed and designed using a custom parts library, schematic, and PCB layout and is ready for fabrication that is detailed in Chapter 3.

3 Chapter 3: Fabrication

3.1 Introduction

Successful adoption of any prolific MEMS device hinges on the ability to produce the device with low fabrication overhead by exploiting economies of scale in mass production. In order to deploy copious quantities of the system designed and modeled in Chapter 2, low cost materials and fabrication with short production cycle time is critical. This chapter discusses materials selection criteria, fabrication process flow and parameters utilized to realize low cost components that comprise the hybrid MEMS energy transducer.

3.2 Mass Production Considerations

Commercially successful MEMS devices historically leverage bulk silicon semiconductor fabrication and processing equipment technologies to realize economies of scale without inducing significant technological overhead. For fabrication of this system, commercially available starting materials are obtained and processed with a minimal amount of semiconductor back-end-of-line (BEOL) packaging, and machining technologies to fabricate extremely low cost devices. The goal is absolute minimization of process overhead while obtaining robust devices that meet the design criteria. The goal of fabrication simplicity thereby naturally promotes high throughput and enables mass production of energy scavenging devices for prolific distribution.

3.3 Piezoelectric Cantilever

The piezoelectric cantilever is the crux of the hybrid energy scavenger as an electromechanical transducer and the platform for wiring both piezoelectric and one of the electrostatic electrodes. Commercially available bulk piezoelectric material is chosen for both performance and cost and preferred over the option of depositing and polling piezoelectric material in-house due to the infrastructure requirements. All subsequent processes are performed in-house using common semiconductor and packaging technologies.

3.3.1 Choice of Materials

Due to a wide application space, COTS piezoelectric materials are readily available at extremely low cost. For fabrication of energy scavenging transducers, bulk sheets of commercial piezoelectric materials are processed using low cost semiconductor manufacturing; however, there is a balance of material cost, performance, and compatibility with all process steps. This section briefly details the motivation of materials selection for the piezoelectric beam.

3.3.1.1 Piezoelectric

Prefabricated commercial grade piezoelectric sheets from Piezo Systems, Inc. were selected to enable wafer-level processing (WLP) for amortization of the processing overhead over many beams. Piezo Systems produces two grades of piezoelectric material whose properties are shown in Table 3.1. PSI 5A4E is Industry Type 5A (Navy Type II) with a strain coupling coefficient (d_{31}) of -190E-12 m/V and PSI 5H4E is Industry Type 5H (Navy Type VI) with d_{31} of -320E-12 m/V. PSI 5H4E is chosen for higher coupling to compensate for low expected displacements, even

though it suffers from higher capacitance and a lower Curie temperature. The Curie temperature induces processing limitations as a thermal budget constraint ensures that the material does not depolarize during fabrication.

Three variants of PSI 5H4E were utilized for fabrication and characterization described in Chapter 4. A single layer sheet (T105-H4E-602) with a thickness of 127μm was ordered for making the thinnest possible beam for maximum deflection. For higher voltages, two variants of 2-layer, series poled, 380μm thick piezoelectric stacks were ordered with brass and composite shim materials (T215-H4-503X and T215-H4CL-503X respectively). The manufacturer states that the composite shim provides higher motion, force, and response without increasing form factor and thus should have better performance as discussed in Chapter 4.

Table 3.1 Piezoelectric material properties from Piezo Systems Inc.

PIEZOELECTRIC & MATERIAL PROPERTIES OF PSI-5A4E SINGLE SHEETS

PIEZOELECTRIC

Composition		Lead Zirconate Titanate	
Piezo Systems Material Designation		Type 5A4E (Industry Type 5A, Navy Type II)	
Relative Dielectric Constant (@1KHz)	K^T_3	1800	
Piezoelectric Strain Coefficient	d_{33}	390×10^{-12}	meter/Volt
	d_{31}	-190×10^{-12}	meter/Volt
Piezoelectric Voltage Coefficient	g_{33}	24.0×10^{-3}	Volt meter/Newton
	g_{31}	-11.6×10^{-3}	Volt meter/Newton
Coupling Coefficient	k_{33}	0.72	
	k_{31}	0.35	
Polarization Field	Ep	2×10^6	Volt/meter
Initial Depolarization Field	Ec	5×10^5	Volt/meter

MECHANICAL

Density	ρ	7800	Kg/meter³
Mechanical Q		80	
Elastic Modulus	Y^E_3	5.2×10^{10}	Newton/meter²
	Y^E_1	6.6×10^{10}	Newton/meter²

THERMAL

Thermal Expansion Coefficient		$\sim 4 \times 10^{-6}$	meter/meter °C
Curie Temperature		350	°C

ROHS   Compliant. Piezoceramic exempted from requirements of Article 4(1).

PIEZOELECTRIC & MATERIAL PROPERTIES OF PSI-5H4E SINGLE SHEETS

PIEZOELECTRIC

Composition		Lead Zirconate Titanate	
Piezo Systems Material Designation		Type 5H4E (Industry Type 5H, Navy Type VI)	
Relative Dielectric Constant (@1KHz)	K^T_3	3800	
Piezoelectric Strain Coefficient	d_{33}	650×10^{-12}	meter/Volt
	d_{31}	-320×10^{-12}	meter/Volt
Piezoelectric Voltage Coefficient	g_{33}	19.0×10^{-3}	Volt meter/Newton
	g_{31}	-9.5×10^{-3}	Volt meter/Newton
Coupling Coefficient	k_{33}	.75	
	k_{31}	.44	
Polarization Field	Ep	1.5×10^6	Volt/meter
Initial Depolarization Field	Ec	3.0×10^5	Volt/meter

MECHANICAL

Density	ρ	7800	Kg/meter³
Mechanical Q		32	
Elastic Modulus	Y^E_3	5.0×10^{10}	Newton/meter²
	Y^E_1	6.2×10^{10}	Newton/meter²

THERMAL

Thermal Expansion Coefficient		$\sim 3 \times 10^{-6}$	meter/meter °C
Curie Temperature		230	°C

ROHS   Compliant. Piezoceramic exempted from requirements of Article 4(1).

A drawback of using commercial prefabricated sheets of piezoelectric material is the fragility of the sheets. The sheets, especially single layer, are brittle and easily fractured by stress concentrations. The double layer sheets are slightly more robust but are still susceptible to fracture with little induced mechanical force. The fabrication process flow must be adapted to address this fragility for transport, automated equipment handling, and essential deposition process conditions such as ultra high vacuum for metal evaporation.

3.3.1.2 Dielectric

For proper operation, it is critical to electrically decouple the electrostatic electrode from the piezoelectric. As shown in Figure 2.3, nickel electrodes cover the entire piezoelectric beam (PZT+/-), the overlapping electrode (C_{VAR+}) for the electrostatics is susceptible to capacitive coupling that may induce asynchronous charging as the piezoelectric voltage swings. While using the adjacent piezoelectric electrode (PZT+) as the ground reference helps mitigate inadvertent charging, capacitance between electrodes needs to be minimized and thus a suitable dielectric material is required.

The dielectric material must be sufficiently thick and preferably low-k to minimize the capacitance and free of pinhole defects to prevent shorting. Furthermore, the material must be low stress to minimize impact on the mechanical performance of the beam. Finally, the dielectric deposition process must be below the thermal budget of the 230ºC Curie temperature of the piezoelectric to avoid depolarization.

Standard plasma enhanced chemical vapor deposition (PECVD) silicon dioxide depositions are normally used for insulating multi-layer metallization; however, deposition process temperatures of 300-350ºC are common for extended periods. Lower temperature processes at 100ºC were attempted but resulted in high stress and porous films that cause electrical shorts once the electrodes are deposited and are unsuitable for this application. Additionally, the use of PECVD films requires photolithography and etch processing for pattern definition that increases the fabrication overhead.

In lieu of PECVD films, spin-on dielectrics were pursued because they can achieve thicker, continuous films with minimal processing. Unfortunately, common spin-on dielectrics like polyimide and benzocyclobutane (BCB) require high temperature curing processes to achieve stability. Alternative films are pursued, namely SU-8 and KMPR 1050 from Microchem. These materials exhibit low-*k* (3.2) properties and can be spun up to 150µm with a single step. Furthermore, they are photodefinable thereby reducing fabrication overhead. For this work, KMPR 1050 is utilized due to on-hand availability and the lack of hard curing requirement. The only drawback of KMPR is that, due to its recent introduction to the market, little is known regarding mechanical and electrical properties and must be characterized.

3.3.1.3 Metallization

The commercial piezoelectric comes with a 100nm thick nickel (Ni) coating for electrical contacts. This layer is easily absorbed during soldering; therefore, additional metal is required to form the piezoelectric contact in addition to the electrostatic electrode. For the piezoelectric contact, the material choice is limited to

solderable films, so aluminum can be excluded, leaving copper and gold as common materials. Since the electrostatic contact is made via physical connection, it is vital that the surface does not readily oxidize, so copper is excluded, leaving gold as the only suitable choice for both structures. Gold (Au) does not oxidize readily and can be deposited with a low thermal budget using electron-beam thermal evaporation. However, the non-reactive nature of gold that prevents oxidation also makes adhesion a challenge; requiring a thin layer of titanium (Ti) to provide good adhesion between Ni/Au and KMPR/Au interfaces.

3.3.1.4 Wire

Two of the three electrodes use physical compression contacts for making electrical connection from the transducer to the system circuit. The remaining contact, denoted PZT+ utilizes a wire connection from the transducer to the printed circuit board (PCB). Since the piezoelectric beam is fragile and the contact area is small, a fine single strand wire is needed. Constantan wire is selected due to its inherent low resistivity (500 nΩ·m) that limits electrical parasitic effects. Furthermore, Constantan has desirable mechanical properties. The wire is highly ductile, with over 45 percent elongation before fracture; providing a resilient and robust contact for assembly and long term operation by resisting fatigue.

3.3.1.5 Solder

Thermal budget restrictions to avoid exceeding the Curie temperature preclude the use of standard eutectic tin-lead solder (63/37 Sn/Pb) because it has a melting point of 185ºC and requires reflow oven or hotplate temperatures in the range of 230-250ºC to achieve the liquidous solder state. In lieu of eutectic Sn/Pb solder, an Indium-Lead

solder paste is utilized. The melting point of In-Pb ternary allows is as low as 114ºC, enabling a hotplate reflow at 150ºC. One impact of this material choice is weaker solder joints that are susceptible to mechanical separation if not handled carefully.

3.3.2   Fabrication Process Flow

An emphasis of process overhead minimization is paramount for integrating the required materials into the desired transducer structure to simultaneously obtain high yield and low cost. The process flow, depicted in Figure 3.1 shows the streamlined process after significant development. Processing is split in two major sections, batch and singulated beam fabrication. All cost sensitive steps are emphasized in batch fabrication for maximum cost amortization, while final assembly of the individual beams is completed post dicing.

3.3.2.1   Batch Beam Fabrication

Due to the fragility of the commercial piezoelectric sheets, the first step is bonding of the sheet to a 150mm silicon carrier wafer. This step provides a robust backing for mechanical processes and enables the utilization of standard automated
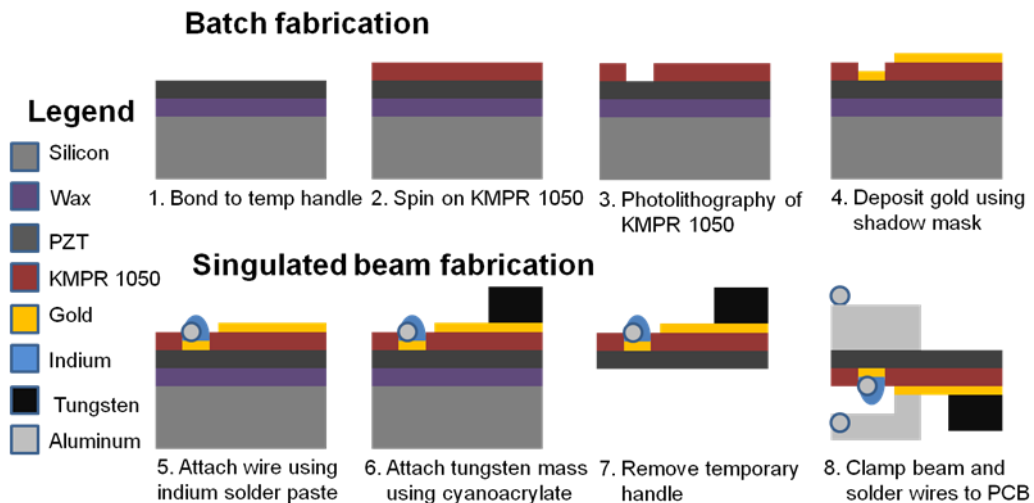
Figure 3.1 Fabrication process flow for the hybrid piezoelectric/electrostatic transducer.

73
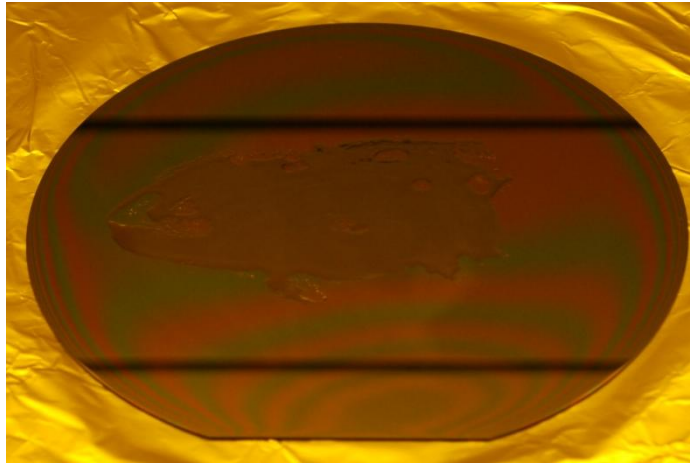
Figure 3.2 Melted Aquabond 80 thermoplastic for bonding piezoelectric sheet.

machine handling and process fixtures. Shown in Figure 3.2, a low temperature thermoplastic, Aquabond 80 is applied by heating the carrier wafer to 90ºC. Aquabond 80, in the form of a solid ingot is applied directly to the wafer like a crayon. The Aquabond 80 kept at temperature for a period of 10 minutes to facilitate degassing of the material; thereby reducing the probability of bubble formation in the bond interface from trapped gasses. Bubble formation is most problematic during metal deposition when the exposed surface is subject to ultra high vacuum conditions. If sufficiently large bubbles exist in the bond layer, the piezoelectric sheet behaves as a membrane and induces fracturing of the sheet. After degassing, the piezoelectric sheet is gently placed on top of the molten thermoplastic and scrubbed to squeeze out excess material. Then a beta wipe and weight are placed on top of the piezoelectric sheet to absorb excess thermoplastic material and provide bonding force to obtain a thin and uniform bond line. The sample is then allowed to cool while the weight is applied. Excess thermoplastic is removed from the exterior surface of the

piezoelectric by a triple rinse of acetone/methanol/isopropanol followed by nitrogen gun drying; thereby readying the surface for KMPR application.

KMPR 1050 is a highly viscous (13000 cSt) negative photoresist material analogous to SU-8 but has improved clarity for better photolithographic feature definition. The material is too viscous to deposit using standard resist pumps or pipettes. The material is decanted for the native 1L bottle into small sterile amber bottles with an approximate volume of 10mL. These amber bottles are kept in cryogenic storage until time of use to prolong the shelf-life of the material beyond the 1 week room temperature lifespan. Bottles are removed from cold storage and kept at room temperature 12 hours prior to use. Approximately 1 hour prior to use, the bottles are placed on a 50ºC hotplate to reduce viscosity and bubble formation, and ease pouring for dispense. The carrier wafer with piezoelectric sheet is loaded onto a semi-automatic handler of a Karl Suss RC8 spinner platform, as shown in Figure 3.3.
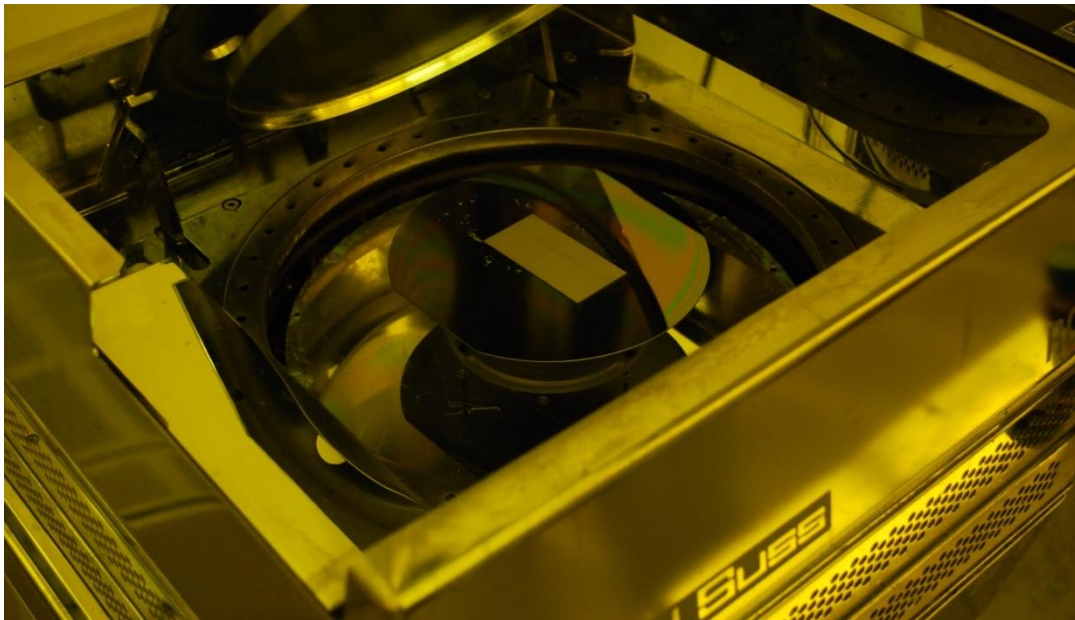
Figure 3.3 Piezoelectric sheet on carrier ready for spin coating.

This system ensures the sample is centered during spinning. Hexylmethyldisilizane (HMDS) is dispensed, via pipette, onto the sample that is spun dry at 1krpm for 60 seconds. Warm KMPR is then poured onto the wafer center straight from the amber bottle while trying to minimize bubble formation. The wafer is spun at 500rpm for 20 seconds with an open lid for spreading, followed by a closed-lid spin at 3krpm for 30 seconds to obtain a 35µm thick film (post-cure measurements). Due to the thickness of KMPR 1050, a two-stage pre-exposure (soft), shown in Figure 3.4, bake is necessary. The primary stage is 65ºC on a hotplate for 30 minutes. This step facilitates gradual evaporation of solvent carrier and prevents micro-bubble or ripple formation. The second step ensures solvent removal at 90ºC for 60 minutes. While the bake times appear excessive, the bonding thermoplastic is a thermal barrier and slows the heating rate and time to get thermal equilibrium on the outer piezoelectric surface.
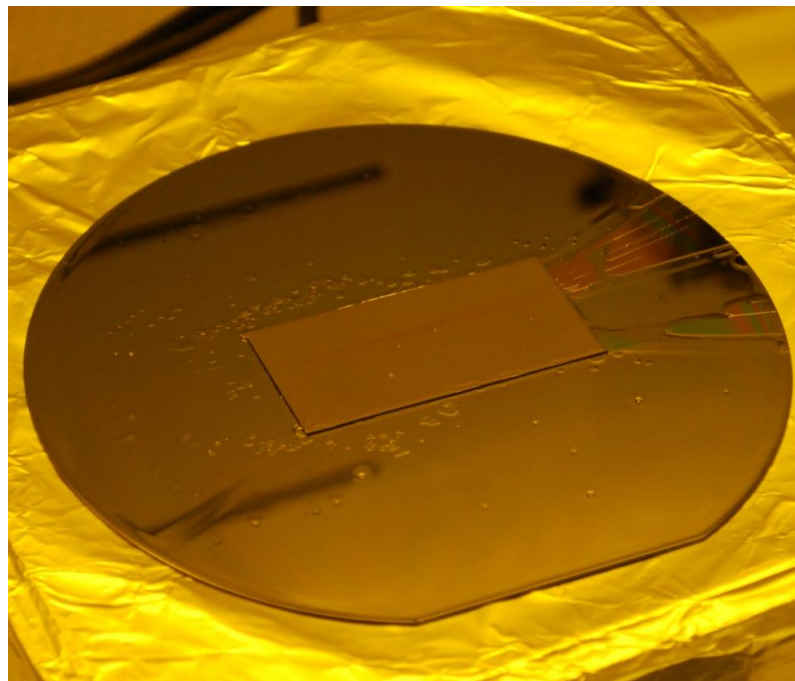
Figure 3.4 Pre-exposure extended soft bake.
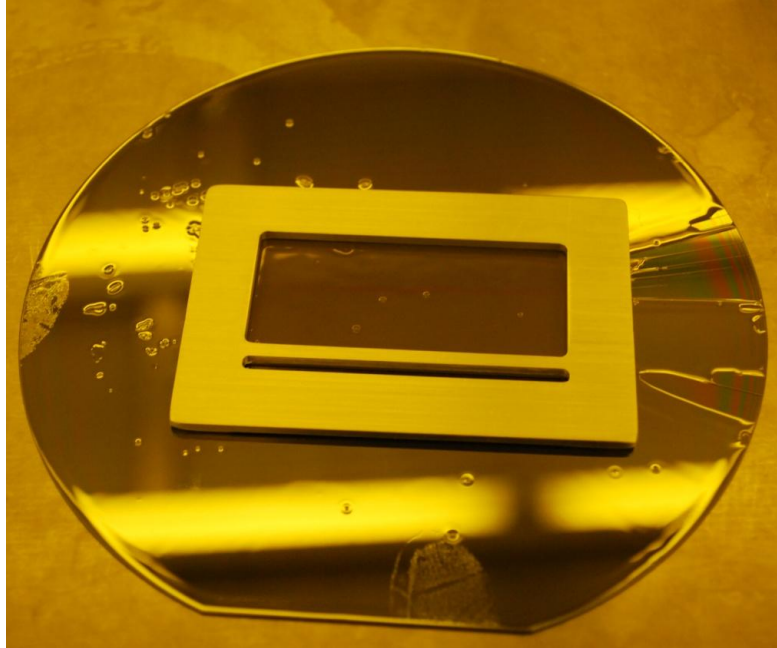
Figure 3.5 Simple shadow mask for lithography and metallization.

Upon photo-activation, KMPR forms a strong acid and uses thermal processing to drive cross-linking to form the resist pattern. After pre-exposure bake, the wafer is ready for exposure. Shown in Figure 3.5, a metal shadow mask defining the electrode patterns is placed over the piezoelectric sheet and grossly aligned using the edge of the piezoelectric sheet. The carrier wafer is placed onto the chuck of a Karl Suss MA-6 contact aligner and pushed into the exposure position without using the semi-automatic loading sequence. No mask contact plate is loaded as it would interfere with the shadow mask during the WEC (wafer touches mask to determine height and travels to alignment gap as predetermined in recipe) operation. Shown in Figure 3.6, the LAMP TEST sequence is used for exposure without the contact plate. Ultraviolet light exposure is set for 10mW/cm^2 at 365nm (i-line). Microchem recommends an exposure dosage of 665-1055 mJ/cm^2, so the exposure time is set to the lower end at 70 seconds.

Figure 3.6 KMPR exposure sequence using LAMPTEST on Karl Suss MA-6 aligner.

Following exposure, a prolonged post-exposure bake is performed at 100ºC for 5 minutes. The wafer is then allowed to cool before developing the pattern. SU-8 developer, a proprietary solvent-based developer, is used to obtain the desired pattern via puddle develop in a 200mm diameter beaker using 250mL until the patterned electrode is cleared visually. The sample is then rinsed in isopropyl alcohol (IPA) and dried manually using a nitrogen gun and ready for metallization. A continuity test using a handheld digital multi-meter (DMM) is conducted to ensure the developed piezoelectric electrode is cleared of KMPR and to verify discontinuity with the KMRP surface. The pre-metal structure is shown in Figure 3.7.
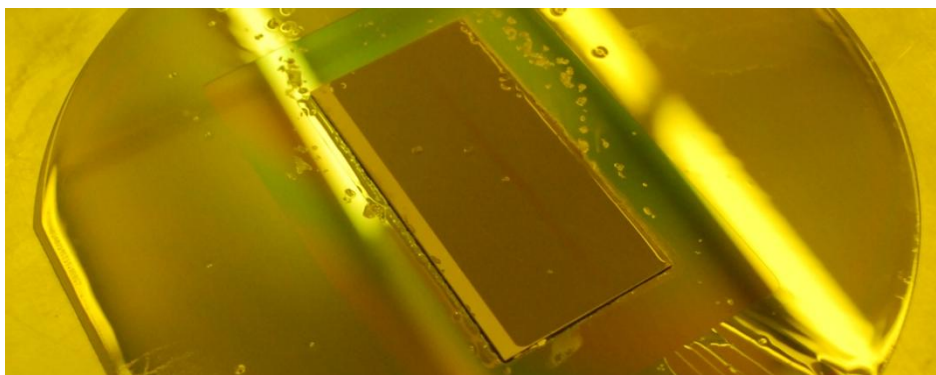
Figure 3.7 Tested piezoelectric sheet prior to metallization.

As mentioned earlier, gold (Au) is used for the electrode material. To promote adhesion of the gold layer, a 25nm thick layer of titanium (Ti) is deposited as an intermediate layer. Prior to metal deposition, the piezoelectric plate is re-bonded using the Aquabond thermoplastic to ensure good bonding due to thermal cycling of the photolithography process. The shadow mask that is used for exposure is shifted and re-used for defining gap between electrostatic and piezoelectric electrodes. The shadow mask is secured using the Aquabond and additional Kapton (polyimide) tape to ensure it remains in place during metal deposition. A Charles Herman and Associates (CHA) Mark-40 evaporator is used to deposit the 25nm Ti/ 500nm Au electrode stack under ultra high vacuum (5E-6 Torr) conditions. The requirement of UHV deposition conditions reduces the probability of metal oxidation; however, if voids in the thermoplastic bonding interface exist, the piezoelectric sheet will rupture. After deposition, the shadow mask is removed; leaving the metalized piezoelectric sheet is shown in Figure 3.8.
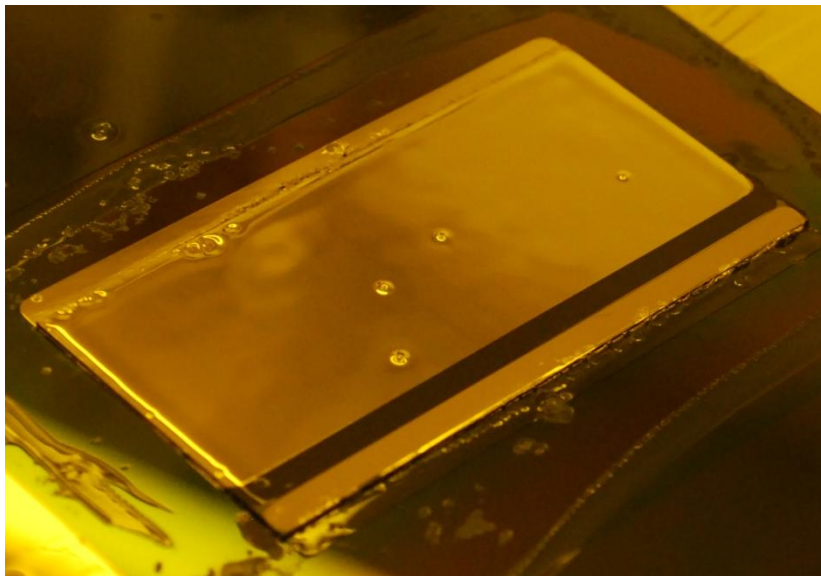
Figure 3.8 Metallized piezoelectric sheet with 25nm Ti/ 500nm Au.

Figure 3.9 Dicing of piezoelectric sheet and carrier wafer on Disco DAD321 dicing saw.

Following metal deposition, a protective non-photoactive resist layer (Microposit FSC-M) is spin coated to protect the devices during the mechanical dicing process. A 50µm thick blue adhesive dicing tape is manually applied on the backside of the carrier to hold the singulated beams together during the dicing process. Shown in Figure 3.9, dicing is performed in a Disco DAD-321 automatic dicing saw system using a 4000-grit CX-90 (Dicing Blade Technologies) blade that is traditionally used for silicon dicing. Dicing parameters use 30krpm blade rotation with a 3mm/s feed rate. Dicing dimensions are set as desired (1.5mm x 20.25mm for composite bimorphs), with an additional 250µm to account for the kerf of blade (results in 1.25mm x 20mm beam for composite bimorph), shown in Figure 3.10. Blade height is set to 50µm to keep the dicing tape intact while separating the silicon carrier thereby providing backing on the individual beams for robust handling through the duration of the singulated beam assembly process, shown in Figure 3.11.
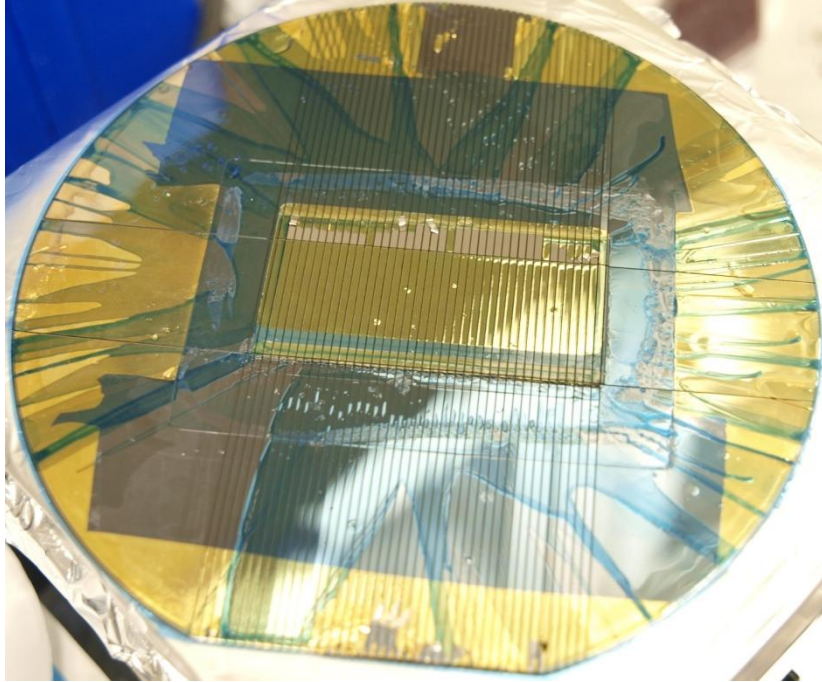
Figure 3.10 Diced carrier wafer with singulated composite bimorph piezoelectric beams.
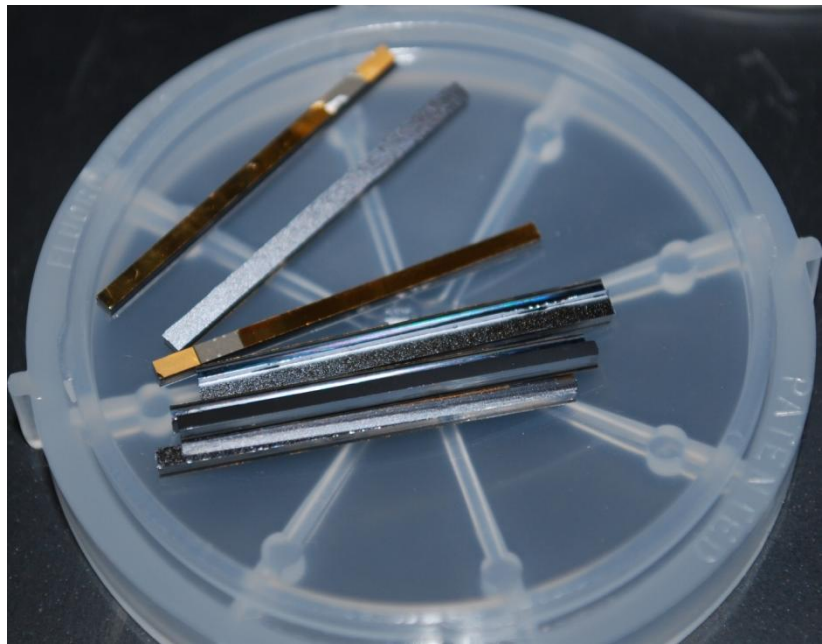
Figure 3.11 Triple rinse cleaned piezoelectric beams, post dicing, with silicon backing intact.

3.3.2.2   Singulated Beam Fabrication

After dicing to form singulated beams, the protective Microposit resist coating is removed using acetone/methanol/IPA triple rinse and dry. A bead of either pure Indium (melting point of 150ºC) or eutectic 52In/48Sn (melting point of 128ºC) solder paste is applied to the exposed piezoelectric electrode. Constantan wire is placed laterally in the bead of solder paste. The entire assembly is carefully transferred to a pre-heated 150ºC hotplate to reflow the solder paste and permanently attach the wire, shown in Figure 3.12. At this point, the silicon backing may be removed by sliding the piezoelectric beam off with a pair of tweezers while on the hotplate. The beam is then cleaned with the solvent triple rinse. Backing removal is acceptable for thicker, robust beams prior to attachment of the electrostatic proof mass, described in the next section; however, for fragile single-layer beams, the backing can remain intact until the time of use.

Figure 3.12 In/Sn solder reflowing of piezoelectric beam to secure constantan wire.

3.4   Electrostatic Proof Mass

The electrostatic proof mass is a combination of physical high density mass for coupling vibration energy and a movable single side of the variable capacitor used for electrostatic energy scavenging. To address the need for high change in capacitance values the surfaces should have a large overlapping surface area with the counter electrode and minimal gap; however, it is also essential for the electrode to have as large of a mass as possible in the allotted volume. This section describes initial work and challenges in fabricating a high aspect ratio interdigitated electrode structure, followed by a description of materials selection, fabrication, and assembly of the simplified, low cost, proof mass/electrode in the prototype system used for testing.

3.4.1   Initial Fabrication Plans – In-Plane Proposal

The initially proposed fabrication plan included the fabrication of high aspect ratio (HAR) interdigitated electrodes for lateral in-plane displacement. Due to the challenging nature of the fabrication, initial work toward realizing HAR interdigitated electrodes was performed in parallel to modeling of the initial in-plane design. Ultimately, as the infeasibility of the in-plane architecture due to the piezoelectric flexures became apparent, this challenging and cost-prohibitive effort was halted. This section discusses the initially proposed fabrication plan while the following section discusses completed work toward HAR electrodes.

3.4.1.1   Flip-chip Integration Plan

A flip-chip based assembly and fabrication plan was developed to facilitate a lower-risk realization of the scavenging system. This plan will result in a device that

is integrated with control electronics via a solder flip-chip assembly as depicted in Figure 3.13.

This fabrication methodology requires high aspect ratio electroplating. The depth of plating is reduced by the use of iterative process steps. This process requires the patterning of SU-8, or a similar thick (>100µm) photoresist, that is used to define the electroplating mold. The resist is inherently non-conducting; thereby facilitating bottom-up electroplating. After plating, excess metal is removed via chemical mechanical polishing (CMP) after which the patterning and plating processes are repeated until the desired thickness is achieved. Denoted Damascene processing, as performed in planar integrated circuit fabrication, the electrode fabrication process can be completed as shown in the cross-section diagram in Figure 3.14(a-e).

Once the electrodes are completed, the piezoelectric springs are fabricated by bonding commercial grade material to the plated MEMS structure. This bonded material is then patterned by chemical etching. MEMS fabrication is completed by the removal of SU-8 in between electrodes and conformal dielectric deposition. The packaging is complete by solder ball attach of the controller ASIC and sacrificial etching of the silicon handle as depicted in Figure 3.14(h).

While lower risk than the proposed silicon-based process discussed in the next section, the iterative HAR plating and Damascene processing approach is plagued by several prohibitive issues. Assuming a well established process can be obtained, the fabrication overhead is on the order of 2-3 man days per iteration; furthermore, cost overhead of maintaining plating infrastructure is high. Finally, the cost and quantity requirements of sacrificial SU-8 material would drive up raw material overhead.
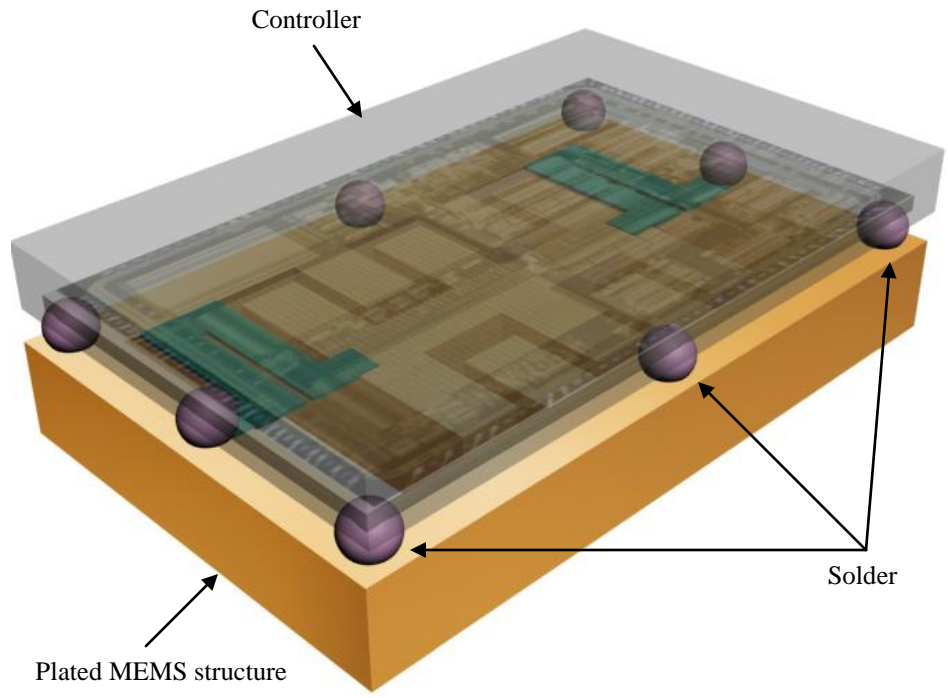
Figure 3.13 Flip-chip based assembly of the MEMS device and controller ASIC
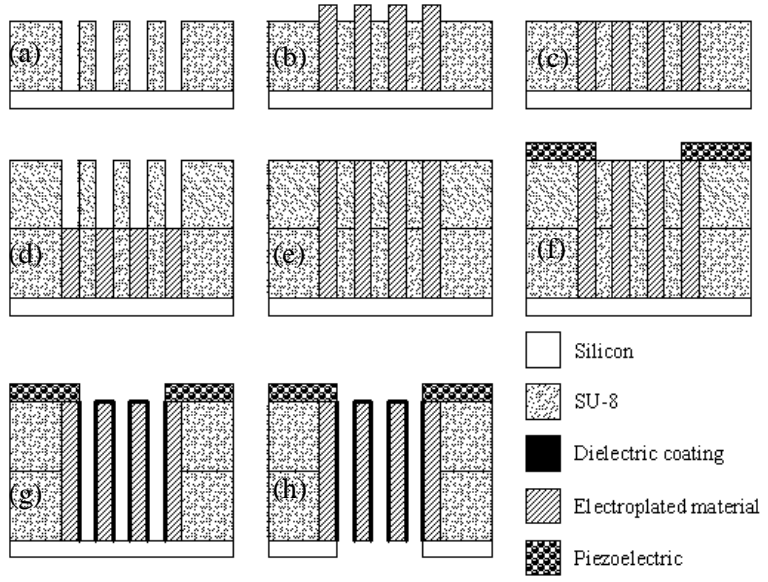
Figure 3.14 Cross section of flip-chip based process flow (a) SU-8 patterning, (b) electroplating, (c) CMP, (d) iterative SU-8, (e) iterative electroplating, (f) piezoelectric patterning, (g) dielectric deposition, (h) silicon etch release

3.4.1.2   On-chip MEMS Fabrication Plan

The ultimate form factor goal would be to fabricate the hybrid scavenger on the same wafer as the control electronics to minimize area and volume utilization via integration as depicted in Figure 3.15. All MEMS processing would be done in the center of the ASIC controller die. A significant hurdle in attempting this level of integration is the imposition of a thermal processing budget to avoid potential damage to the ASIC. The first step in this fabrication plan is to form the electrodes that comprise the electrostatic charge pump and supercapacitor. For this high-level of integration, the bulk silicon of the ASIC die is used as an electroplating mold. Figure 3.16(a-c) illustrates a cross-sectional view of the process flow for making the electrodes.

Initially, the silicon is anisotropically etched using either wet or dry techniques depending on the capability to create deep trenches (300-500μm) with narrow (5-20μm) sidewall structures. Once the trenches are complete, a conformal dielectric coating must be deposited to electrically isolate the sidewalls. This dielectric serves two purposes by facilitating bottom-up electroplating during fabrication and preventing electrical shorts between moving electrodes during operation.

The third major step in the fabrication sequence is the electroplating of the electrode material. It is necessary to provide a high quality, conductive material to minimize the internal resistance of the capacitor structures. Additionally, the electroplating process should be bottom-up to prevent keyholes, a voiding in the center of the trench, from forming that would decrease both mass and device reliability. Once the electroplating is complete a chemical mechanical polish (CMP)

process is used to planarize the wafer and remove excess metal deposits. At this point, the unreleased electrodes need to be mechanically and electrically connected with the piezoelectric springs. The final fabrication challenge is bonding and etching bulk piezoelectric materials, followed by a selective isotropic silicon etch to release the mass-spring system as shown in Figure 3.16(d-e) without damaging the metal.
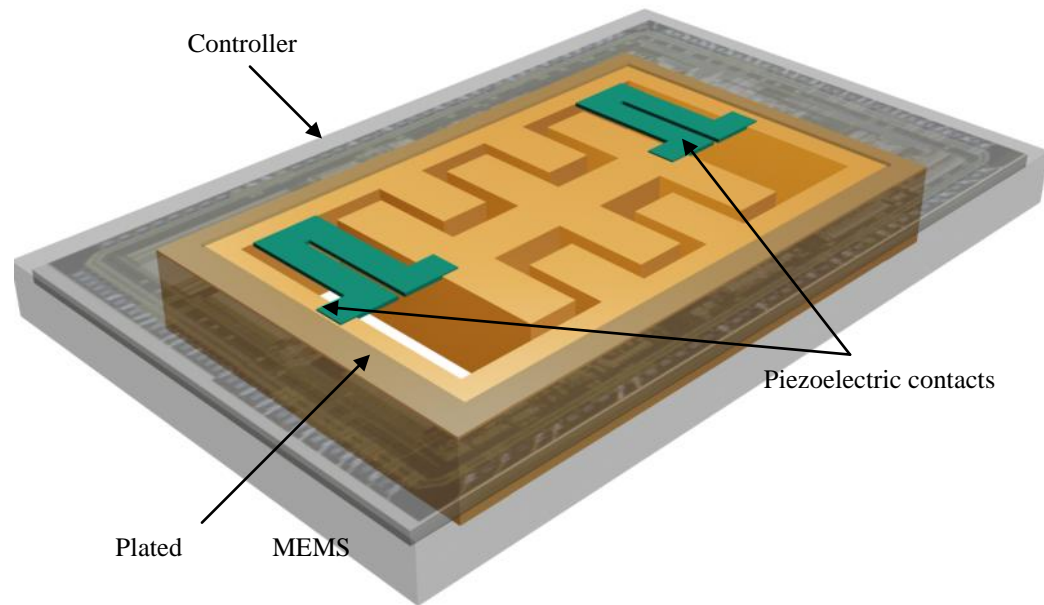
Figure 3.15 On-chip integration of the MEMS device within the controller ASIC
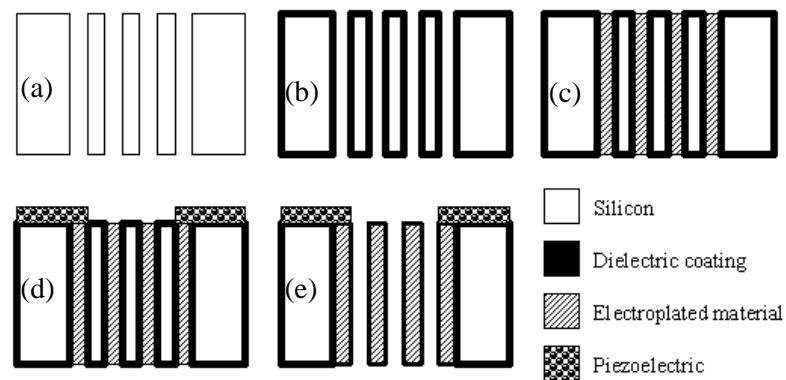
Figure 3.16 Cross section of on-chip integrated process flow (a) HAR etch, (b) dielectric coating, (c) HAR electroplating, (d) piezoelectric patterning, and (e) isotropic silicon release

3.4.2 Initial Fabrication Process Development – HAR Electrodes

Toward the realization of HAR interdigitated electrodes, unit process development was limited to the HAR etching of bulk silicon wafers to form an electroplating mold. This fabrication methodology was abandoned when transitioning from in-plane to out of plane designs; however, it would have been a path to ultimate system form factor. Despite this, the fabrication overhead and extreme cost would preclude adoption for prolific distribution. This section briefly describes the etch technologies explored and results for this work prior to being abandoned.

3.4.2.1 Magnetic=0 Resonant Induction Etch

Magnetic equals zero resonant induction (M0RI) is an etch technology that is similar to inductively coupled plasma (ICP) with the exception that the chamber is lined with both rare earth and electromagnets. This arrangement creates a plasma confinement that enables a two order-of-magnitude increase in the reactive ion density on the wafer surface. Traditionally, the etch technology has been used to fabricate HAR micro-vias for 3-dimensional integration work [49]. This etch technology is desirable for this application since the sidewall passivation is generated as the etch wave front propagates, resulting in nanometer-scale surface roughness. Additionally, previous work shows the presence of an electrically insulating dielectric coating of 20-50nm in thickness [50]. These characteristics would allow electrodes to come into intimate, with only 50-100nm separation; resulting in a remarkable increase in C_{max}. However, etch characterization demonstrates drawbacks in the use of M0RI for this specific HAR structure.

Careful balancing of the source and bias powers, as well as gas flows and chamber pressure, are needed to ensure the etch can propagate while coating the sidewall with the passivation layer for anisotropic etching. The M0RI platform used is primarily used for via etching and thus has a limited mass flow controller for SF_6, the primary reactive gas, and thus the silicon etch rate is low for large exposed areas such as the electrode pattern. These patterns are defined by a hard mask, usually tetraethyl orthosilicate (TEOS) or plasma enhanced chemical vapor deposition (PECVD) silicon dioxide (SiO_2), which is needed to prevent etching of the electrode gap regions. Furthermore, to facilitate sidewall passivation, O_2 and SiF_4 need to reach the etch wave front so that free Si^+ radicals can recombine on the surface to form SiO_2, so bias power needs to be balanced to get reactive ions to the etch wave front without etching the masking layer. Figure 3.17 illustrates some results from M0RI process development.
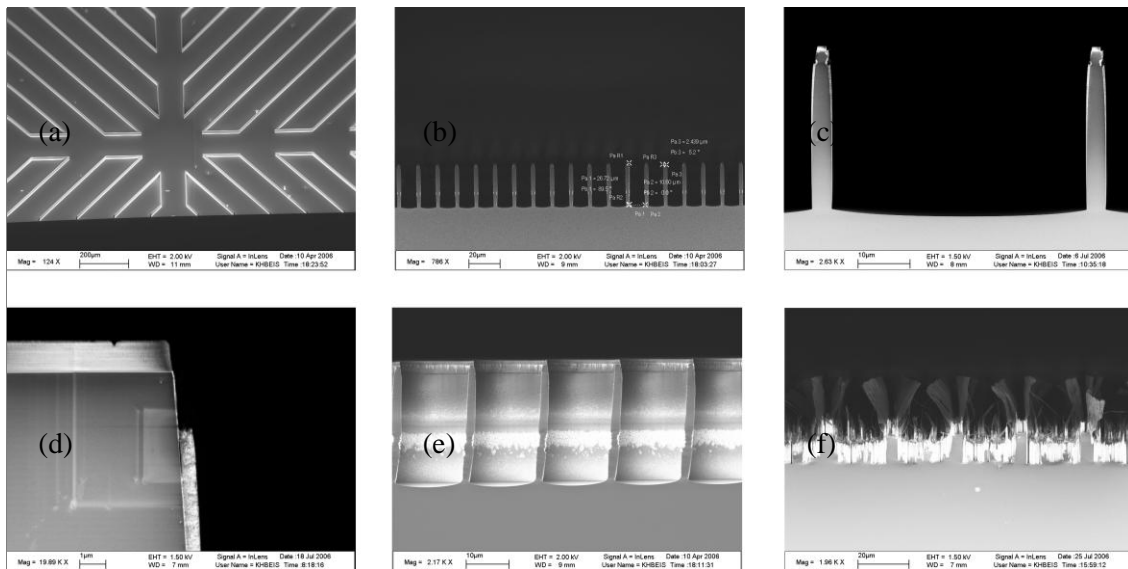
Figure 3.17 M0RI development SEM images (a) top view of Si mold, (b) cross section of mold, (c) re-entrant profile, (d) heavy sidewall passivation, (e) collapsing sidewalls, (f) failed hard mask

89

Figure 3.17(a-c) illustrates promising shallow etch results; however, (c) shows the beginning of a re-entrant etch profile. This indicates either the failure of passivation gasses from reaching the etch wave front or loss of directionality of energetic ion bombardment. Figure 3.17(d) shows the result of increased passivation gasses with a thick oxide deposition on the sidewall; thereby, enabling an etch depth of greater than 50μm. Despite this, as etch depth increases beyond 50μm, wall collapse and mask failure are the dominant failure modes shown in Figure 3.17(e-f). Several process changes and mask types were tested but it is apparent that a deep etch process on the current M0RI platform is not probable. New M0RI models have licensed Bosch technology for gas switching; however, an upgrade is more than $1M, so alternative means were pursued.

3.4.2.2 Deep Reactive Ion Etch

A common bulk micromachining technique known as Deep Reactive Ion Etch (DRIE) is an ICP etch module coupled with Bosch gas switching technology between SF_6 etchant and C_4F_8 for passivation. Benefits of DRIE include the use of photoresist masks and faster etch rates but induce higher cost overhead, sidewall scalloping, and re-entrant profiles for wide electrodes, shown in Figure 3.18. Etch depths to 300μm were achieved before abandoning the effort.
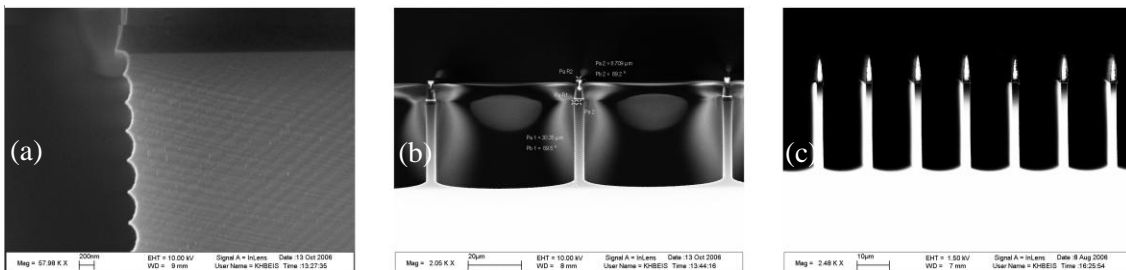
Figure 3.18 DRIE development SEMs images (a) sidewall scalloping, (b) re-entrant etch on large features, (c) minimal re-entrance on small features

3.4.2.3   Anodic Etching

Anodic etching was initially pioneered by Lehmann in the early 1990's in which pores were etched into *n*-type silicon substrates, initiating the field of micro-scale porous substrates (PS). When submerged in a weak hydrofluoric (HF) acid electrolytic solution, bulk silicon will not readily etch. However, when holes are generated at the surface and localized oxidation reaction occurs that is subsequently removed by the HF. Anodic etching requires the application of a bias and high current between the wafer, as the anode, and a top counter electrode. In *n*-type etching, hole generation is due to photon absorption [50]. However, *p*-type etching only requires a bias. Vertical structures, as shown in Figure 3.19 can be created using anodic etching by forming sharp dislocation points through KOH etch. At these points, holes accumulate and are attracted to the cathode by the electric field. The sidewalls are therefore passivated by hole depletion [52],[53],[54].

A custom anodic etch tool was designed and constructed for etching an electrode plating mold in 150mm *p*-type silicon wafers. However, the system testing was plagued with challenges in sealing and preventing leaking around the periphery of the wafer. Ultimately, due to safety concerns of HF liquid/vapor the effort was halted.
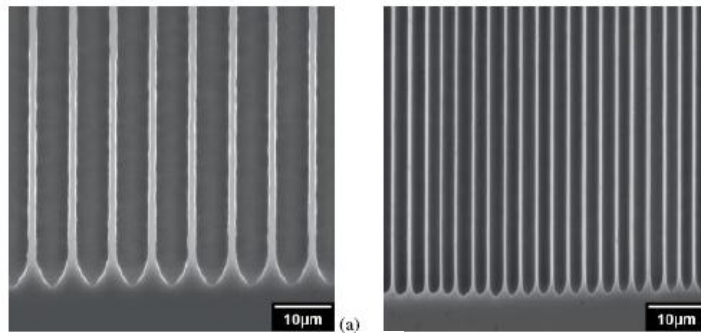
Figure 3.19 Cross sections of porous silicon [53].

91

3.4.3   Choice of Materials

The proof mass for the simplified, out-of-plane scavenger system is a solid block for ease of manufacturing, assembly, and testing. While non-ideal, it provides the basic functionality to prove the theoretical behavior of the system. This section discusses material selection for the electrostatic electrode/proof mass structure.

3.4.3.1   Proof Mass

Regardless of preclusion due to in-plane design deficiencies and immense fabrication challenges, both initially proposed HAR electrode fabrication plans are flawed by a limitation in material selection.   Both approaches assume a HAR electroplating capability. Apart from a major effort in electrochemistry and plating of novel materials, the MEMS fabrication would rely on commonly electroplated materials. The problem is that materials such as copper (Cu) and nickel (Ni) have relatively low densities; 8.96 g/cc and 8.912 g/cc respectively. Gold (19.3 g/cc) and platinum (21.45 g/cc) have substantially high density but would be cost prohibitive due to the relatively large volume required to obtain a large mass at a market value of approximately $40 and $55 USD per gram respectively.

In order to be economically viable, a common, low cost, high density material that can be easily processed is essential to obtaining a feasible proof mass. Tungsten also has a density of 19.3 g/cc at an industrial market value of $0.035 USD per gram. Furthermore, tungsten bar stock can be readily obtained and is easily machined using standard mechanical techniques and is therefore the most suitable material for the system proof mass.

3.4.3.2   Attach

The tungsten proof mass must be reliably attached to the electrostatic dedicated gold electrode on the piezoelectric beam. Initial attempts to coat the tungsten with a solderable metal were unsuccessful due to the inherent strong native oxides that form on tungsten. HF etching was attempted immediately prior to gold evaporation; however, due to ambient oxygen exposure during transfer and pump down of the CHA Mark-40, native oxides formed and precluded good adhesion. Alternative, methods, such as plating were not pursued due to lack of availability and penalties in cost and fabrication overhead. Instead, the tungsten is directly attached to the electrode via a physical contact and secured into place with cyanoacrylate. This ensures both a good electrical contact and strong mechanical bond. Furthermore, use of cyanoacrylate eases beam exchanges since all that is required for removal a razor to scrape off the old beam and an acetone rinse to prepare the electrostatic proof mass for connection to the new beam.

3.4.4   <u>Fabrication Process Flow</u>

The basic fabrication process for the electrostatic proof mass is low cost and well defined. A milling machine is used to obtain the desire lateral dimensions of a tungsten ingot. Next, a band saw is used to cut the slices of tungsten block into segments that are 0.5mm greater than the target.

For initial work, a target thickness of 1mm is desired for the final product, so the slices are 1.5mm to allow removal of 250µm from each side via lapping. This lapping process removes machining artifacts and ensures smooth mating surfaces with the counter electrode. Lapping of the tungsten is performed on a Logitech PM5

tool. The tool provides an in-situ process monitor to ensure that lapping remains flat throughout the process by continuously shaping the lapping plate. Tungsten blocks are mounted onto a 100mm glass carrier using Aquabond 80 as shown in Figure 3.20.
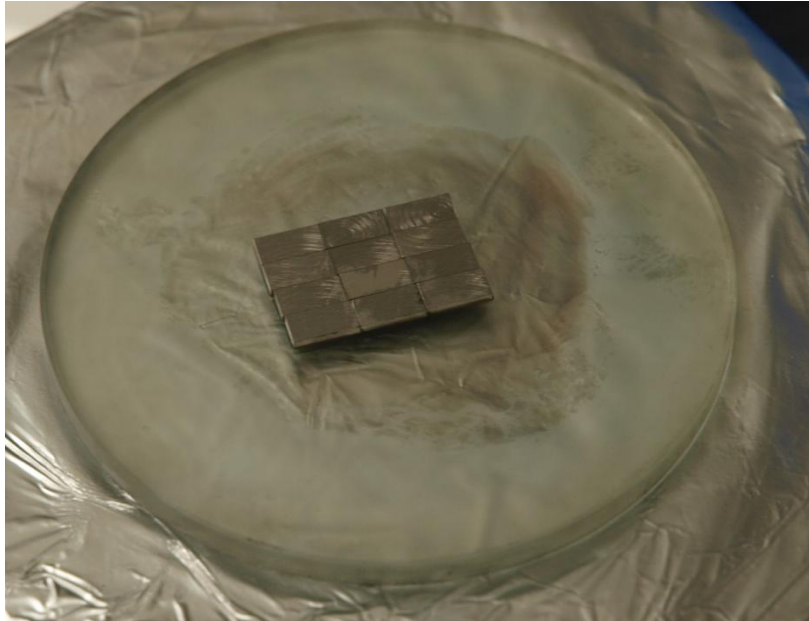
Figure 3.20 Tungsten block mounted onto 100mm glass carrier in preparation for lapping.

Figure 3.21 Lapping of tungsten blocks on Logitech PM5 tool.

Shown in Figure 3.21, the glass plate with attached blocks is loaded onto a PP6 lapping jig so that removal amount can be monitored. The jig force is set to 2.5kg at maximum plate speed of 70 rpm. Two abrasive grits are used to obtain the optimal surface finish. For the first 200μm a 9μm alumina abrasive is used to remove machining artifacts. For the final 50μm, a 1μm abrasive is used to obtain a smooth surface finish. Upon completion, the blocks are demounted, inverted, and polished on the opposing side to prepare them for system integration.

Once polished, the block center is measured and a scratch is induced to provide a guide mark for center mounting the piezoelectric beam. A small drop of cyanoacrylate is placed on the block and the beam is applied and held with manual force for 5 minutes until the adhesive sets. Continuity is tested and additional cyanoacrylate is applied around the beam perimeter to ensure robust mechanical bonding; thereby, readying the hybrid transducer for testing on the PCB.

3.5 Electrostatic Counter Electrode

The original planned electrode was simply a square pad embedded on the PCB. However, it was rapidly realized that due to gravitational effects, the beam and electrode would not be parallel to the PCB surface. As a result, an adjustable counter electrode for the electrostatic component was essential. This critical component has evolved from a simple block to a tripod with 20nm resolution micrometers for precision alignment. This section will discuss material selection and fabrication.

3.5.1 Choice of Materials

Initial prototypes of this electrode were brass and aluminum blocks due to ease of machining. Once a design was physically tested for functionality, an oxygen-free copper electrode was produced. Copper is chosen over aluminum due to its ability to be directly soldered and inherently low resistance. However, copper does induce a significant increase the mass loading due to its higher density when compared to aluminum (2.7 g/cc). Standard thin wire and eutectic Sn/Pb solder paste is used for wiring connections.

3.5.2 Fabrication Process Flow

The electrode is machined using a precision computer numerical controlled (CNC) milling platform. CAD drawings are programmed into the system that makes the device using an end mill. The completed part is cleaned using solvent triple rinse and dried using nitrogen gun. Eutectic Sn/Pb solder paste is dispensed; wires are then attached and reflowed on a hotplate to form the lead to the PCB. During reflow the copper electrode readily oxidizes, providing a thin, but unreliable insulating layer that can potentially reduce incidence of shorting. Assembly of the counter electrode onto the system test PCB has varied as experimental improvements were attempted and the architecture of the electrode has evolved to increase testability or static tuning of the electrode position to improve electrostatic performance. This evolution and the electrodes integration into the system will be discussed in the following section that explains PCB assembly.

3.6   Printed Circuit Board

The system PCB is the common platform for the entire electromechanical system. The PCB houses both diagnostic and operational/power conditioning circuits while also providing the rigid base for connecting mechanical components like the transducer beam clamp. When possible, mechanical clamps performed dual roles as mechanical and electrical contacts to enhance packing density and obtain a minimally sized PCB. Furthermore, the PCB is designed for mechanical connections to the electrodynamic shaker platform. Through several generations of evolution, the circuit components were strategically floorplanned to ease connections to external sources and diagnostics platforms while avoiding interference with essential mechanical components. Finally, when possible, surface mount technology (SMT) is utilized to minimize PCB volume. For example, jumper connections using 0402 surface mount devices (SMD) with 0Ω resistors are placed to allow maximum reconfiguration of circuit topography during the testing phase that is discussed in Chapters 4 and 5. This section discusses the assembly processes associated with creating the electromechanical system on the PCB.

3.6.1   Fabrication Services and Materials Selection

As mentioned in Section 2.5.3, EAGLE software is used to implement the circuit schematic into a physical layout with proper floor-planning and routing. This board design is converted into a Gerber machine format that is sent to Advanced Circuits for standard 4-layer PCB fabrication.   Electronic and mechanical components and assemblies utilize eutectic Sn/Pb solder paste for all solder joints, unless otherwise noted.
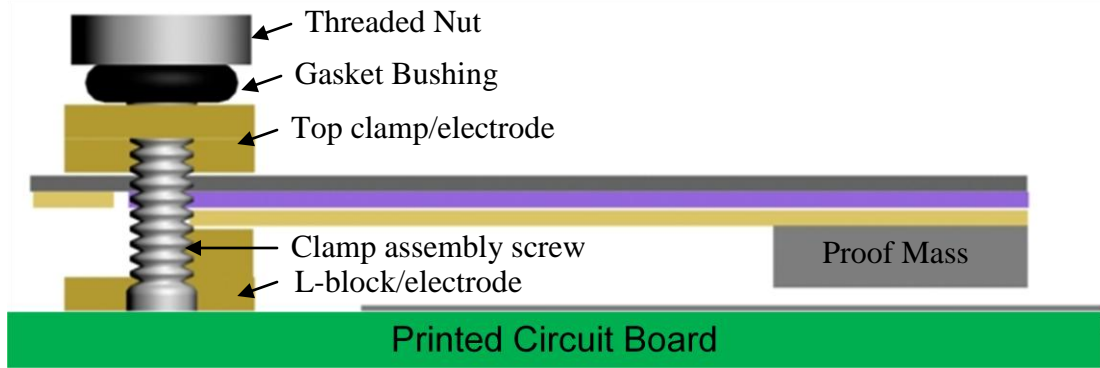
Figure 3.22 Cross-section diagram of transducer assembly on PCB.

3.6.2 Fabrication Process Flow

Once a fabricated board is received, it is inspected for any variations from the design. Next, the large base "L-block", shown in Figure 3.22, is solder attached via hotplate reflow to the PCB pad for the electrostatic electrode. This metal block has duality as the mechanical platform for the transducer beam and the physical compression electrical intermediate contact for routing the DC rail connection from the PCB to the beam electrode for the electrostatic proof mass. The "L-block" is attached first, as it requires the entire PCB to be at an elevated temperature that would result in reflow, causing misalignment or damage of other components.

Following attachment of the "L-block", the electrical circuits are assembled. The PCB is mounted onto the electrodynamic shaker platform to hold the system in place during soldering operations. Through-hole connectors are attached and soldered using a fine-tip iron and reel of solder. These connectors enable diagnostic testing of sub-circuits as the PCB is populated and facilitates early detection of PCB defects. Sub-circuits are assembled and tested in the following order: external power conditioning, stand alone on-board diagnostics (e.g. accelerometer), transducer power conditioning and rectification, analog signal processing (OPAMPs), digital processing, and power

98

switching/control. When available, SMDs are utilized to reduce PCB dimensions. Leadless components are attached using manual solder paste dispense and hot air gun reflow or solder iron tip if pads are sufficiently large. Leaded components are soldered one contact at a time to minimize incidence of solder bridging. SMD passives utilize soldering tweezers for making the solder joints.

Following circuit assembly and testing, the assembled transducer beam is clamped via screws that penetrate from the bottom of the PCB and hold the beam using the top clamp/electrode assembly with threaded nuts, as illustrated in Figure 3.22. As shown, rubberized o-rings can be used as bushings to provide some spring force and avoid over-clamping and fracturing the piezoelectric beam; however, these tend to compress over time and become ineffective, resulting in reduced clamping force that induces poor electromechanical performance.

Finally, the last electromechanical component, the electrostatic counter electrode, is connected to provide electrostatic charge that is applied to the variable capacitor that is comprised of the gap between the proof mass and the counter electrode. As mentioned previously, the electrode has evolved significantly through the duration of experimental testing. Clearly, from the discussion of electrostatic scavenging theory in Section 2.4.2, it is essential to ensure that high capacitance changes are available.

Initially, as shown in Figure 3.23a, the counter electrode was simply a pad on the PCB; however, the displacement of the beam and proof mass due to gravity results in a lack of parallelism to the PCB; resulting in immeasurable capacitance values. The next embodiment of the counter electrode was a metal block that was adjusted by using shim stock and cyanoacrylate with a wire to the PCB. Despite efforts, this

coarse adjustment did not suffice for obtaining alignment to the displacement of the proof mass to obtain measurable capacitance. The next iteration included an elongated block with fine pitch screws arranged in a tripod configuration as shown in Figure 3.23b. The tripod is held on by a threaded plastic screw used to hold the PCB into the test platform. Although an improvement, the coarse alignment of the threaded screws precludes fine adjustments needed to achieve a sub-micron gap. The requirement of precision alignment leads to integration of a complex tripod integrating 20nm resolution micrometers. Shown in Figure 3.23c, even the smallest micrometers require a large counter electrode platform. While providing enhanced alignment capabilities that are sufficient for verification of the theory of operation, the design is not feasible due to immense mass loading, large volume requirements, and spring attachments to the PCB that result in higher order resonant vibration frequency modes. These limitations are discussed and addressed in detail in Section 6.2.2.1 as part of ongoing efforts.

3.7 Summary

This chapter describes the process development efforts are required to obtain low cost, mass producible manufacturing of hybrid energy scavenger systems. Multidisciplinary technology development toward this goal spans from cutting edge MEMS-based microfabrication, incorporating new structural materials, to adapting traditional back-end operations such as dicing and solder attach to be compatible with piezoceramic processing limitation. When possible, low cost machining is exploited with surface lapping to obtain suitable interfaces for testing. Finally, a manual SMT-

centric PCB assembly provides a complete system that is ready for testing and characterization as discussed in Chapters 4 and 5.
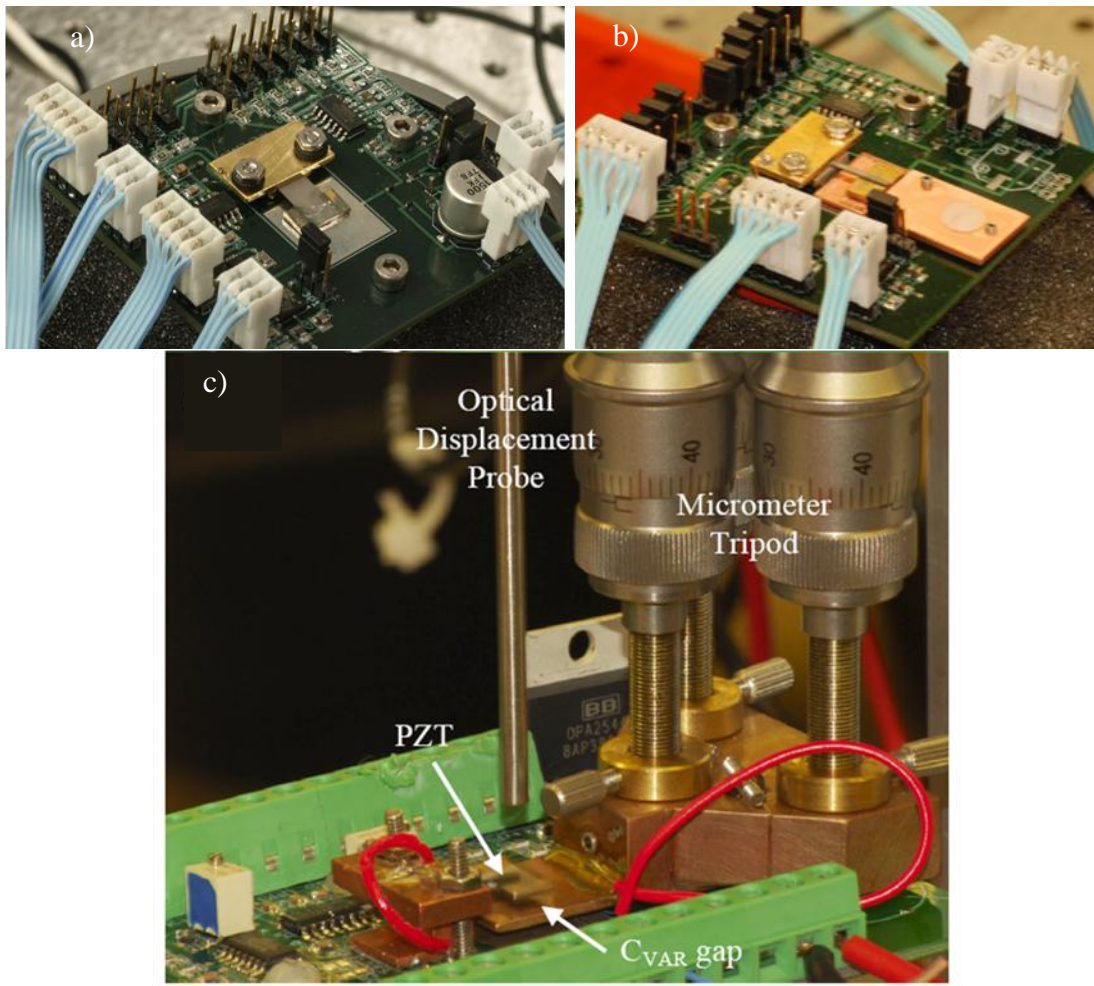
Figure 3.23 Evolution of counter electrode from PCB pad (a) to fine screw tripod (b) and micrometer tripod (c).

4 Chapter 4: Piezoelectric Scavenger Testing

4.1 Introduction

The piezoelectric beam transducer is the fundamental enabler of the hybrid energy scavenger system. The piezoelectric transducer simultaneously provides DC power to operate the conditioning electronics and an inherent AC signal that describes the position of the beam tip during operation; thereby, enabling synchronous electrostatic energy scavenging to augment the piezoelectric energy without substantially increasing volume. This chapter introduces the experimental laboratory test bed that is established for characterizing the vibration energy scavenging system. Additionally, the mechanical and electrical characterization of differing starting materials that comprise the piezoelectric beams to determine how much power can be sourced for running the system is discussed. Finally, monitoring and signal processing of the inherent feedback signal to determine electrostatic synchronization is summarized.

4.2 Experimental Setup

A comprehensive test bed is established for the purpose of evaluation and characterization of the hybrid energy scavenger system and its sub-components in a laboratory environment. Shown in Figure 4.1, the test bed is centralized around a vibration isolation floating table. The table is selectively floated by enabling a nitrogen bottle feed when seeking to eliminate ambient vibration noise from the surround building infrastructure. Hard mounted to the vibration isolation table is a Labworks Inc. ET-126B electrodynamic shaker table, shown in Figure 4.2, that

provides controlled vibration excitation to the entire energy scavenging PCB that is mounted directly on top of the shaker platform.
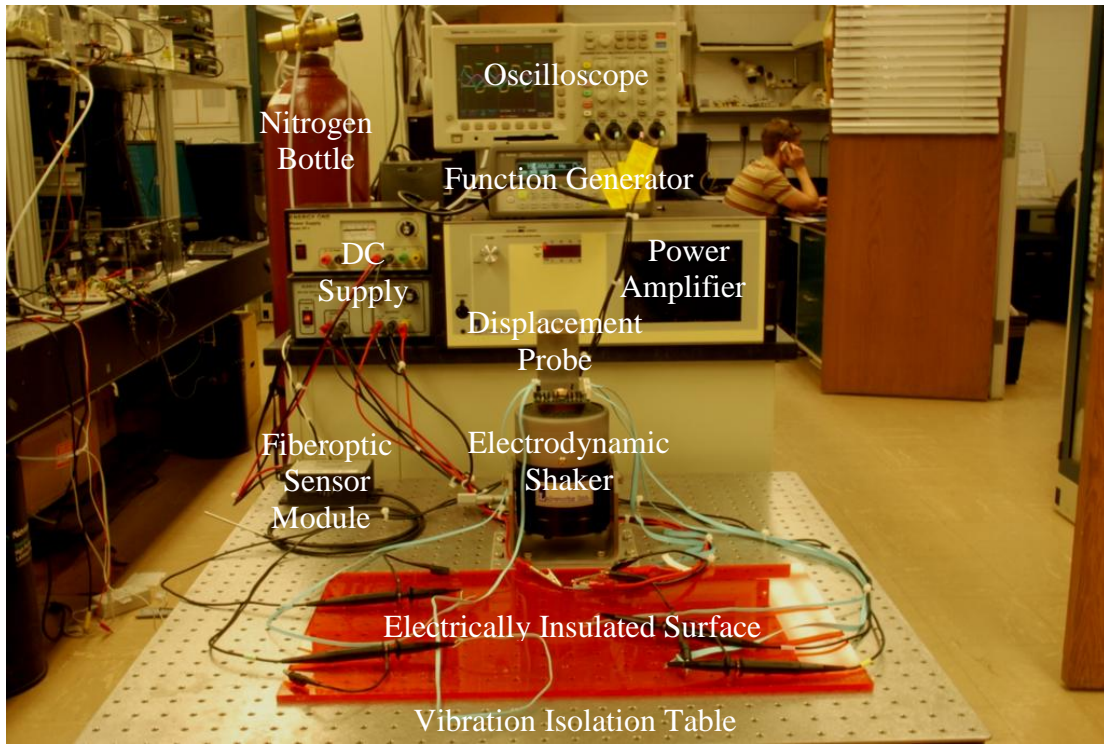
Figure 4.1 Laboratory test bed for characterization of vibration scavenging.
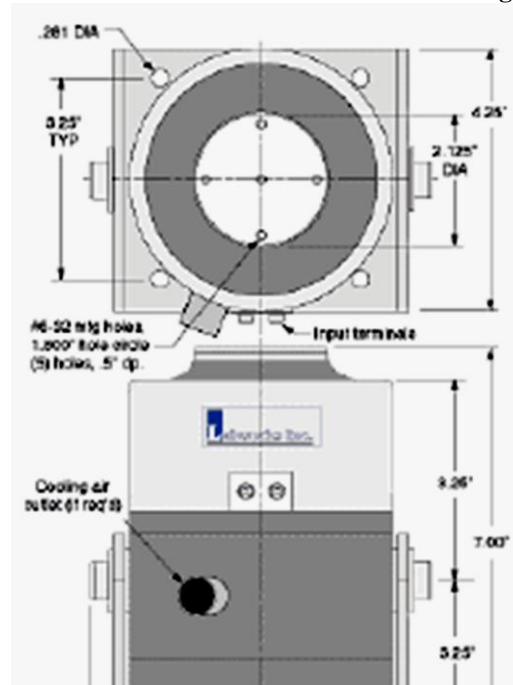
Figure 4.2 Schematic of Labworks ET-126B electrodynamic shaker.

Instrumentation is collocated on an adjacent independent table to provide proximal access to the system via cables without transmitting vibration from the chassis, such as fan noise.   A Labworks Inc. PA-141 power amplifier is utilized to drive the shaker with the signal provided by an Agilent 33220A 20MHz Function / Arbitrary Waveform Generator with the high current required to operate the ET-126B.   The power amplifier is set to a predetermined mark on its coarse analog control knob, allowing the waveform type, amplitude, and frequency of excitation to be precisely controlled by solely adjusting the digital settings of the function generator output.

Four independent DC power supplies are required for complete characterization of the system. One supply provides 5VDC to the independent on-board accelerometer (STMicroelectronics LIS3L02AL/LIS302SG 3-axis MEMS inertial sensor) circuit, shown in Figure 4.3, for measurement and verification of the amplitude and frequency of input vibration excitation from the ET-126B. This accelerometer signal is monitored via one of four channels on Tektronix TDS 3054 oscilloscope.
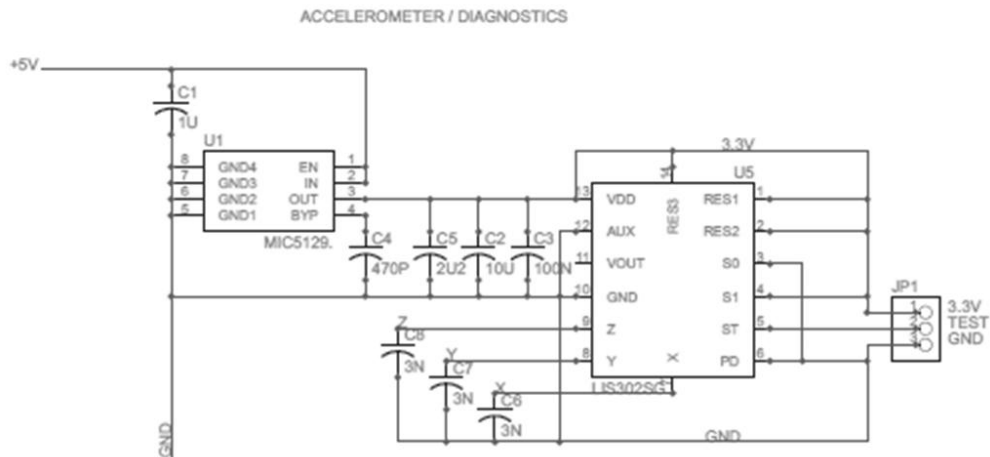
Figure 4.3 Schematic for independent accelerometer diagnostics circuit.

The second DC power supply provides a 12VDC source to power a PHILTEC Model D63 fiberoptic sensor for optical verification of beam tip displacement amplitude. The tip of the fiberoptic sensor probe is secured onto a 3-axis micrometer platform for precision alignment and calibration of the reflectance signal from the top surface of the proof mass/electrostatic electrode.

High power consuming COTS components such as OPA4350 and OPA4347 utilize the third DC power supply to obtain +/-2.5VDC rails. The OPA4350 is used in a voltage follower configuration to force the DC rail to the voltage level generated by the rectified piezoelectric signal but provides the high current feed for the OPA4347 operations such as active filtering and peak detection. This configuration enables diagnostics and circuit architecture modifications using COTS for testing and proof-of-concept purposes, and closely emulates a finished product; however, it is not feasible for deployable systems and is discussed and addressed using an ASIC-based system that is detailed in Section 6.2.3.

The final DC power supply is used to supply up to a +/-25VDC rail for an OPA2544 instrumentation amplifier for measuring the electrostatic operation without directly loading the circuit, as described in Section 5.2.1. Circuit operation is monitored and tested via a hand-held digital multi-meter (DMM) or additional channels on the Tektronix oscilloscope. Data is stored on disk and transferred to PC for post processing. A graphical overview of the entire vibration energy test platform is diagrammed in Figure 4.4.
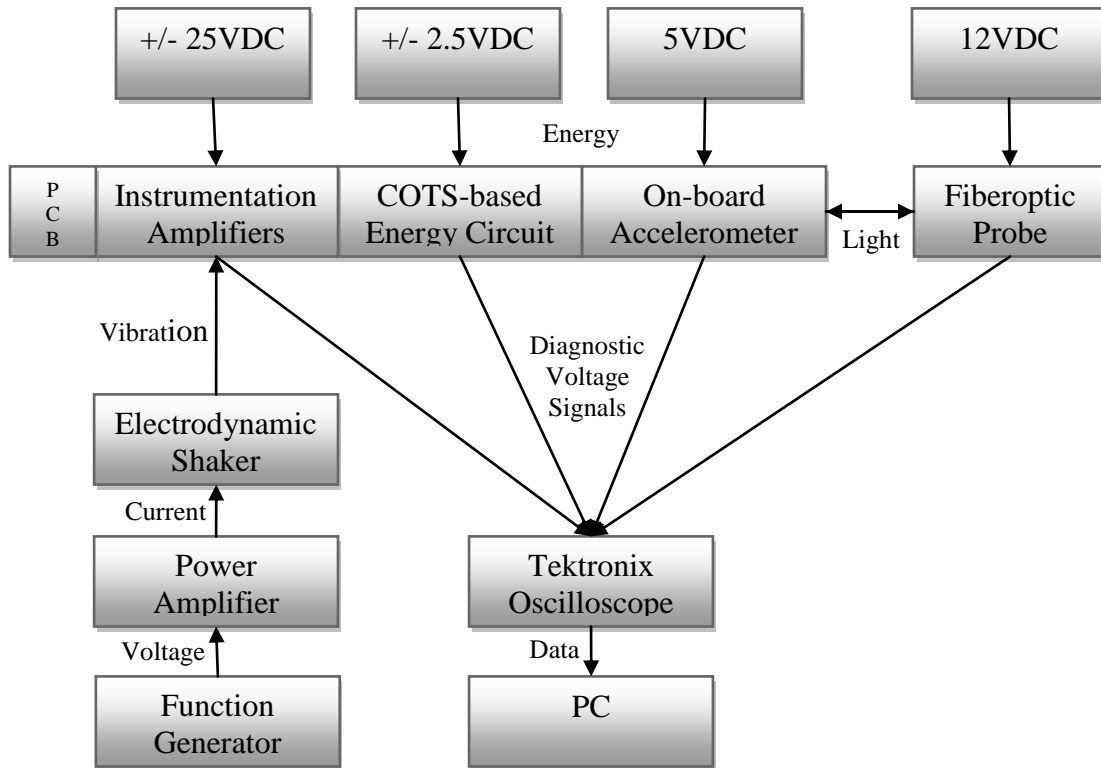
Figure 4.4 Diagram of characterization test bed.

4.3 Resonance Characterization

As a resonant system, ideally the vibration frequency should match the resonance of the transducer system. Based on the U of MD energy survey and prior work, discussed in Section 1.3.1, the ideal frequencies are harmonics of 50/60Hz noise due to operation of large-scale mechanical systems in commercial and industrial zones, so for the evaluation of the system, an input acceleration of 2.5m/s^2 at 120Hz is ideal. This section discusses the characterization and static tuning of system resonance to approach the ideal input conditions.

4.3.1 Measurement of Resonant Frequency

Mechanically, the transducer is designed to resonate at the fundamental frequency of 120Hz as described in Section 2.3.4.3. However, there are no considerations of

106

real-world variances in fabrication tolerance such as post-dicing beam dimensions or variations in mass loading. Finally, variability in experimental setup, such as beam clamping force and parallelism can have significant impact on resonance. As a result, the resonance frequency must be experimentally extracted.

For testing the beam, the piezoelectric voltage is monitored via an oscilloscope connection with 10MΩ impedance. Since the piezoelectric voltage is directly proportional to displacement, which is maximized at resonance, the peak piezoelectric voltage changes with frequency. With fixed acceleration amplitude of $2.5m/s^2$, the excitation frequency is swept on the function generator until the absolute maximum is detected. This is recorded as the mechanical resonant frequency of the beam as currently installed. Experimentally, the resonance of the single layer beam (4.87mm x 5.78mm x 0.127mm LxWxH) is measured to be 115.5Hz compared to the analytical model design of 5mm x 5.75mm x 0.125mm with a theoretical 120Hz resonance. Given a 3.75 percent error margin and the slight variance of physical dimensions, it can be said that the experimental results closely match the experimental model.

4.3.2 Manual Tuning

Despite this, other sources of resonance variability exist. The analytical model is ideal and does not consider effects of additional materials such as KMPR 1050 and cyanoacrylate on the structure. As a result, a completely processed beam is anticipated to have slightly lower resonance as the presence of KMPR should dampen mechanical response.

Fortunately, experimentally testing and manually tuning the device to obtain the desired resonance is simple. Using the theoretical model as a starting point, the

mechanical resonance is measured. The beam length can be adjusted by unclamping, and extending to lower resonant frequency (or conversely shortened to increase), then re-tested to confirm desired operation. While this provides a rudimentary tuning mechanism, it is only a partial solution as both the environment and system can dynamically shift resonance.

For example, electrical dampening has dramatic dynamic impact on behavior of the system. Electrical loading, both internally within the complex energy scavenging system and externally at the targeted load circuit, will vary over the differing states of operation (e.g. start-up versus steady state or periodic heavy loads for RF burst communication) and will shift resonance accordingly (measured shift of 3-5Hz). While a broad spectral response (low quality factor) would partially mitigate this, it also reduces maximum energy scavenging possible by reducing the peak response.

4.3.3   Quality Factor Measurements

The quality factor (Q factor) is a common dimensionless measure of a resonators damping. For a resonant energy scavenger system with absolutely certain input excitation, a high Q factor would be ideal; however, as discussed in the prior section, most energy scavenger systems will be subject to variability in electrical loading and input excitation and thus a lower Q factor may be preferred as it ensures some level of energy scavenging over a wider bandwidth.

For this work, Q factor measurements are experimentally determined by measuring the maximum voltage at the resonant frequency and then shifting frequency higher and lower until obtaining ½ of the peak voltage. Q factor is determined by

Equation 4.1 $Q\,factor = {f_0}/{\Delta f},$

where f_0 is the measured resonant frequency and Δf is the bandwidth (frequency difference between the upper and lower frequencies at ½ maximum piezoelectric voltage). As expected, the thin, single layer beam has a low Q factor of 16.04. However, the Q factor is also subject to variability in experimental setup. A measurement of a high performance, double layer beam produced a Q factor as low as 9.65. This unexpected result was attributed to poor mechanical clamping due to relaxation of the o-ring bushing that is discussed in Section 3.6.2. However, removal of the bushing improves clamping and increases Q factor dramatically, so clamping force can be used as a parameter to adjust bandwidth at the expense of peak power.

Experimentation with higher Q factor piezoelectric materials shows some clear indication of the proper regime for selection of specific piezoelectric beams. As shown in Table 3.1, Industry Type 5A4E material has a Q factor of 80; whereas, the Industry Type 5H4E only has a Q of 32. Composite bimorph beams of the same dimensions are compared experimentally. Electrically, the two beams performed similarly, with a 3.0V DC rail generated with the 5H4E and up to a 2.9V DC rail from the 5A4E using 2.5m/s^2 acceleration at resonance near 120Hz. The 5A4E is specified to have lower piezoelectric coupling coefficients; however, with similar excitation has higher displacement and stress induced due to higher mechanical Q factor, resulting in a negligible difference for DC operation. However, as expected, the operation drifts more than the 5H4E as the electrical loading of the system changes, thus consistent operation was elusive. Furthermore, at excitation as low as 5m/s^2, the high displacement of 5A4E beams induces critical fractures and are less resilient that the 5H4E for high amplitude transients. Therefore, the only viable use conditions for

higher Q factor beams are scenarios in which low amplitude, consistent vibration is expected. As a result of this limitation, all data reported in the remainder of this chapter is with use of 5H4E material.

4.4 Beam Displacement Measurements

An essential requirement of the hybrid energy scavenging system is synchronization of the displacement extrema with the charging cycle of the electrostatic scavenger component. As described in Section 1.2.2, the inherent feedback signal of the piezoelectric transducer can be used to track the displacement; however, from simulation, it is expected that the phase will differ. External tracking of displacement provides critical diagnostic information for establishing the correct synchronization of the piezoelectric signal as well as determining the magnitude of displacement that directly impacts the performance of electrostatic capacitance change.

As described in Section 4.2, for displacement measurements, an external fiberoptic probe (PHILTEC Model D63) is mounted to a 3-axis micrometer platform. The probe tip is aligned with the top of the electrostatic electrode/proof mass to measure tip displacement as closely as possible. For this measurement, it is essential that the electrode surface is smooth to reduce scattering effects. Calibration of the displacement sensor is performed by plotting the change in voltage as the probe tip is moved vertically using the Z-axis micrometer and is shown in Figure 4.5. The centroid of the linear region is targeted for the vertical position of the sensor tip. Using the slope of this region, the calibration of the sensor sensitivity is calculated to

be 25 mV/µm. Using this calibration data, the voltage signal from the sensor probe module, as measured by oscilloscope, is correlated to displacement amplitude.
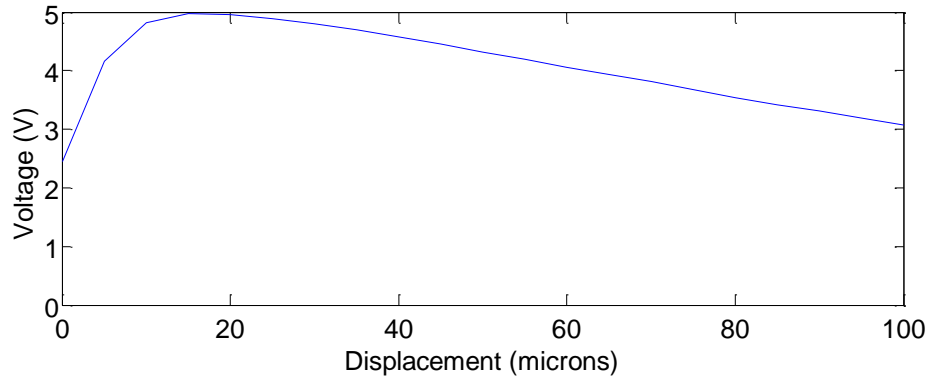
Figure 4.5 Calibration curve for the tip displacement of the proof mass.

4.5   Power Measurements

For piezoelectric transducers, the peak power is dependent on matching of the load resistance to obtain optimal power transfer. While circuit complexities may limit flexibility in optimal impedance matching, it is essential to determine the maximum power delivery of the standalone piezoelectric transducer. Furthermore, it is vital to predict the voltage and current output of the piezoelectric as many of the COTS components will not operate if provided insufficient inputs. This section details the electrical performance for three different Industry Type 5H beams.

4.5.1   Comparison of Differing Piezoelectric Beams

For the initial characterization, three different beams were designed for 120Hz resonance and compared for electrical performance. The beams consist of a single-layer, and two serially poled bimorphs with brass and composite center shims. Electrical characterization of the piezoelectric transducers consists of resistive loading of both the piezoelectric directly and the rectified DC rails in order to

111

determine if sufficient voltage and power is available to operate signal conditioning, peak detector, and electrostatic pre-charge circuits.

As shown in Figure 4.6, single layer beams produce insufficient voltage to operate analog COTS components that nominally require at least 2.5V to operate. In contrast, the serially poled bimorphs with brass and composite center shims that were tested produce substantially more voltage. However, in all cases, the composite beam had superior voltage output with the production of a 3.0-3.3V DC rail while the brass beam could not produce a DC rail (shown in bold) that would permit COTS op-amp operation due to the voltage drop of the rectifying Schottky diodes.

In addition to the voltage output, it is critical to determine the current capacity at the desired voltage levels. For a given piezoelectric beam, only a finite amount of energy can be extracted. Altering the poling configuration of the bimorph beam determines the voltage to current ratio. As shown in Figure 4.7, the current capacity of the tested piezoelectric beams is critically limited. Higher current capacity can be obtained by utilizing parallel poling (Y-poled) in lieu of serial poling (X-poled);
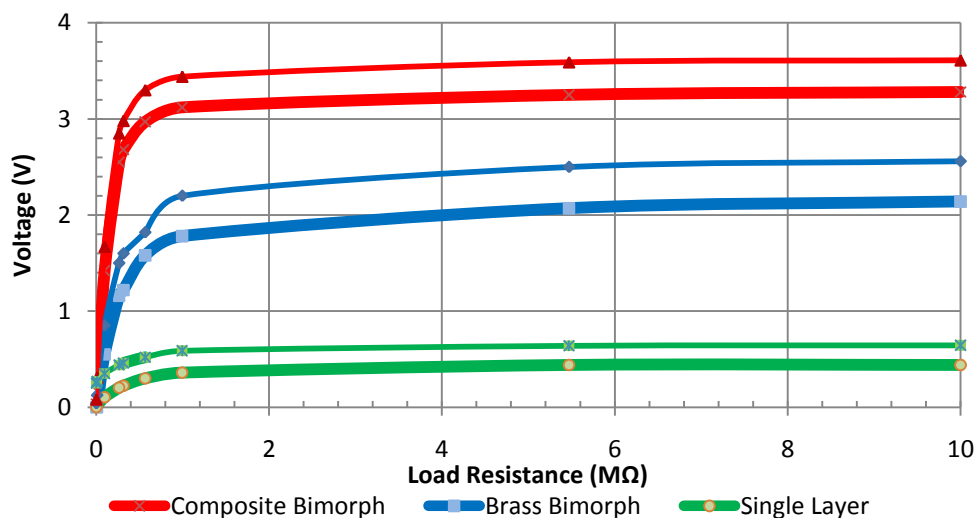
Figure 4.6 Comparison of 5H piezoelectric transducers rectified voltage (DC rail) in bold.

112
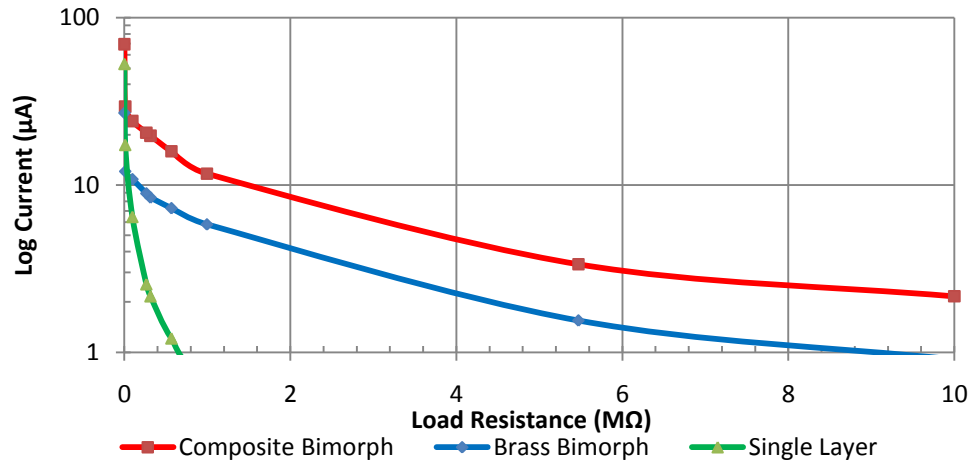
Figure 4.7 Logarithmic plot of current output of differing piezoelectric beams.
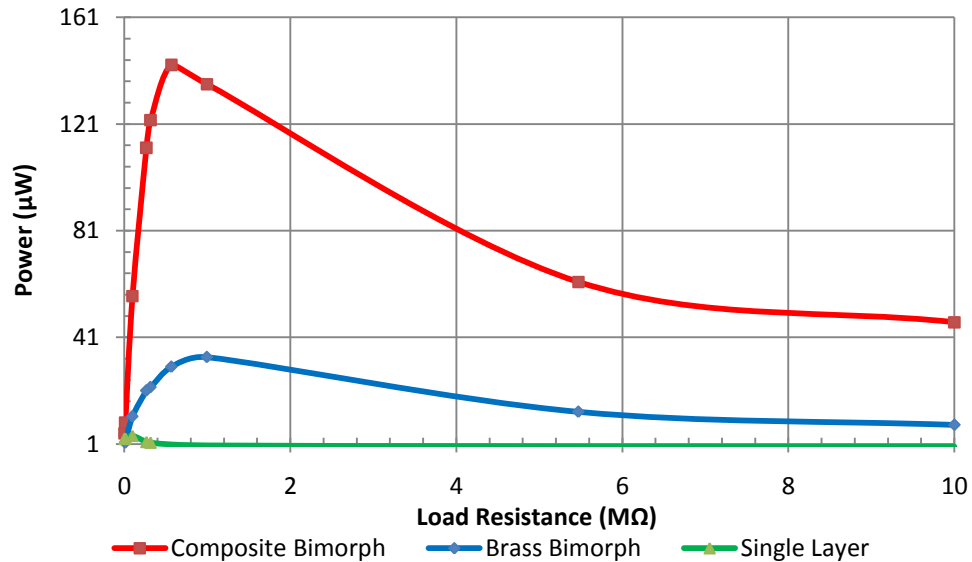
Figure 4.8 Output power of piezoelectric transducers with varying load resistance.

however, this is at the expense of design complexity as the parallel poled beam requires an internal contact while generating lower voltages. Since the necessary rail voltage is pre-determined by the utilization of COTS components, implementation of parallel poling would only compromise the testing of the system; however, if an application specific integrated circuit (ASIC) is designed to operate at lower voltage

levels, then higher current capacity could be achieved and is discussed as a potential optimization parameter in Section 6.2.1.

Graphed in Figure 4.8, the peak power corresponds to an optimal load resistance. From experimentation on a single beam, the maximum power output measured for the composite bimorph beam was 145μW. Given a transducer volume of 0.054cm^3, this corresponds to an optimal power density of 2.68mW/cm^3. With the power capacity of the system identified, the test circuits could be simulated, fabricated, and evaluated.

4.6 Piezoelectric Circuit Operation

Ideally, for linear systems, an optimal load circuit design would be impedance matched to ensure maximum power transfer; however, in the hybrid system, the use of dynamic switching for synchronization and charge transfer to the electrostatic results in dynamic loading conditions. As a result, the circuit is not designed for impedance matching, but instead seeks to minimize current paths between power rails for the rectification, synchronization, and charge control circuits, so that maximum current can be applied to the electrostatic transducer without dropping the DC rail below critical values and detrimentally impacting either the control circuits or displacement feedback signal from the piezoelectric.

The first stage of the system circuit, shown in Figure 4.9, enables selective configuration for testing the piezoelectric directly for diagnostic measurements, as described in the prior section, or generation of the DC rail voltage. Jumpers are placed to connect the piezoelectric terminals, denoted *PZT+* and *PZT-* to *GND* and *RAIL* terminals. Although it should be irrelevant which terminals of the piezoelectric

are connected to the rectifier, it was experimentally determined that the electrode

under the KMPR dielectric should be grounded to eliminate capacitive coupling

between the piezoelectric and electrostatic transducers. Once connected, the

piezoelectric utilizes Schottky diodes to charge a pair of 100μF capacitors to positive

and negative rail, denoted *VEE* and *VSS* respectively. Schottky diodes are selected to

minimize the forward bias voltage drop while the capacitor values are chosen to

minimize charging time while providing sufficient capacity to prevent DC rail ripple

when dynamically loaded. Two of the four opamps of the OPA4350 are connected in

a voltage follower configuration to track the *VEE* and *VSS* values, while providing

higher current output on DC rails denoted *V+* and *V-* for operation of high power

COTS components in the other circuit stages. This effectively emulates a finished

product while permitting the flexibility of COTS components.
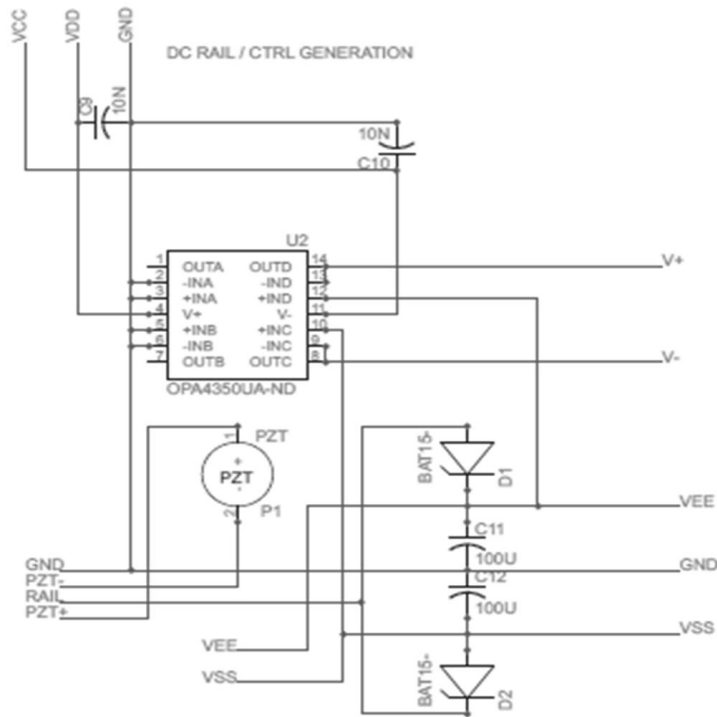
Figure 4.9. Circuit schematic for piezoelectric DC rail generation and voltage follower.

The second stage of the piezoelectric circuit contains the pre-conditioning and peak detectors for tracking of the displacement and is shown in Figure 4.10. Pre-conditioning circuits include a voltage divider to reduce the piezoelectric voltage; thereby protecting the COTS opamp by ensuring that the inputs do not exceed the DC rail values. A phase shifter was originally included for tuning purposes but is not utilized as explained in the following section. The peak detector circuits are simple as the opamp is used as a comparator between the piezoelectric input signal, denoted *CTRL*, and the DC rail reference voltages stored on capacitors *C17* and *C18*. When the piezoelectric voltage meets or exceeds the reference voltages, peak detection pulses, denoted *PEAK+* and *PEAK-* are emitted. The corresponding MOSFETs are simultaneously triggered during this pulse to keep the reference capacitors charged to either *VEE* or *VSS*. The voltage dividers used to reduce the opamp input to half of the reference voltage also provide high impedance discharge paths for the bleeding the reference capacitors should the rail voltage drop due to lower vibration excitation. This ensures the peak detectors will function in dynamic environmental conditions.
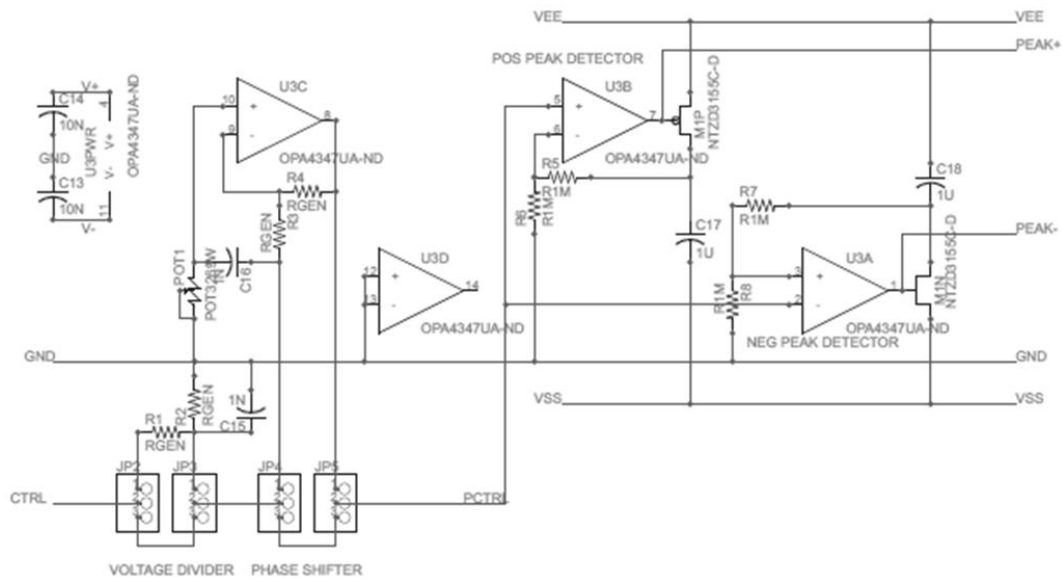
Figure 4.10 Circuit schematic for signal conditioning and peak detectors.

4.7 Displacement Feedback Signal Characterization

Arguably, the most novel aspect of the hybrid energy scavenger system is the utilization of the piezoelectric transducer to overcome the limitations of charge-based electrostatic energy scavengers.   More specifically, the piezoelectric provides the electrostatic pre-charge and operational power for synchronization circuits as well as the signal that drives the synchronization without the requirement of power hungry timing circuits like voltage controlled oscillators (VCOs) that have been demonstrated to consume an excess of 85 percent of generated power. For this work, system-level characterization of interdependencies and evolution of the circuit to obtain proper synchronization is a dominant concern and is addressed in this section.

4.7.1   Correlation with Displacement

Piezoelectric voltage is produced when a change in stress is applied. As a result, motion of the cantilever produces a voltage response that can be monitored, as shown in the example of vibration induced by typing on a keyboard in Figure 4.11. Therefore, relative amplitude and frequency of displacement from vibration excitation can be extracted and correlated to produce an acoustic sensor for dual utility.

This sensor function is applied to permit synchronization with the capacitance of the electrostatic transducer that follows displacement. In agreement with simulation, measured piezoelectric output is 90-degrees out of phase with the beam displacement, shown in Figure 4.12. However, deviating from simulation, the measured signal is attenuated at the peaks. This anomaly is attributed to excess current draw when forward biasing the rectifying Schottky diodes and applying current to the DC rail capacitors. This limitation has an adverse effect on the originally designed system.

117
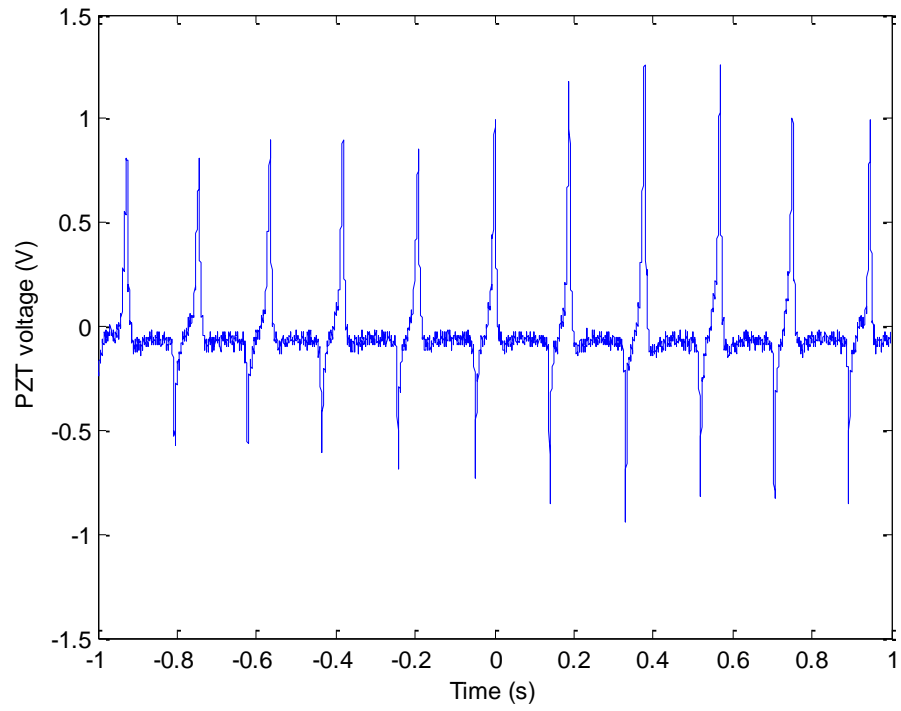
Figure 4.11 Piezoelectric voltage response to typing on nearby keyboard.
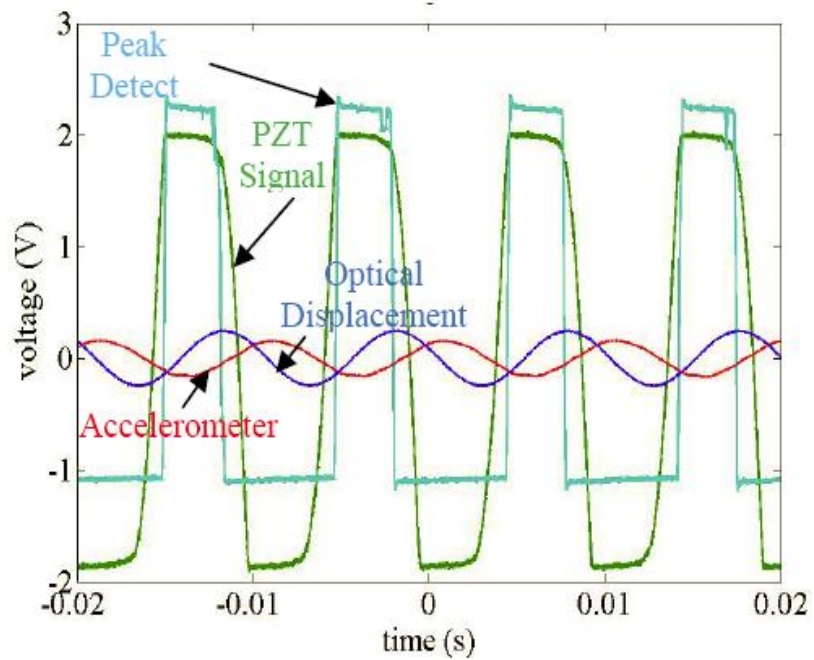
Figure 4.12 Oscilloscope plot of displacement and piezoelectric output.

118

Clipping of the piezoelectric signal broadens the peak detector output from the COTS circuit that is discussed in the prior section. If this broad peak is used to control charge transfer to and from the electrostatic energy scavenger component, little power will be generated as there will be immeasurable capacitance change in the inactive region between charge and discharge signals. Furthermore, due to the phase difference, the displacement peaks actually occur on the falling edge of the peak detector signals. As a result, a simple circuit alteration can provide proper timing signals for charge transfer.

4.7.2   Required Circuit Modifications – Edge Trigger

Fortunately, the critical displacement positions at the maximum and minimum align with the falling edge of the broad peak generated by the peak detector circuit. Given this scenario, a simple addition to the peak detector circuit enables proper synchronization triggering for optimal charge transfer. Shown in Figure 4.13, a COTS SN74LV123A, dual retriggerable monostable multivibrator with Schmitt-trigger inputs is used to send control pulses on the falling edge of both positive and negative peak detection signals. The outputs of the multivibrator are fed into two multiplexers, with outputs denoted *CHARGE* and *DISCHARGE*. This permits flexibility in selection and routing of the appropriate control signals for operation of the electrostatic scavenger at the time of testing. The SN74LV123A output pulse widths are controlled by setting the external reference capacitors (*C21* and *C22*) and potentiometers (*POT2* and *POT3*). Using this feature, the pulse width can be adjusted to ensure that the electrostatic component fully charges during a single charge control trigger. In spite of enabling the proper operation, shown in Figure 4.14, the

multivibrator only operates at a rail in excess of 2V, but requires a constant current draw of 50mA. In summary, the COTS component's power consumption of 100mW is approximately 3 orders of magnitude higher than the scavenged energy and is not feasible for real systems. Despite this, it is viable for demonstration of the proof-of-concept operation of the hybrid system by enabling the essential charge control.
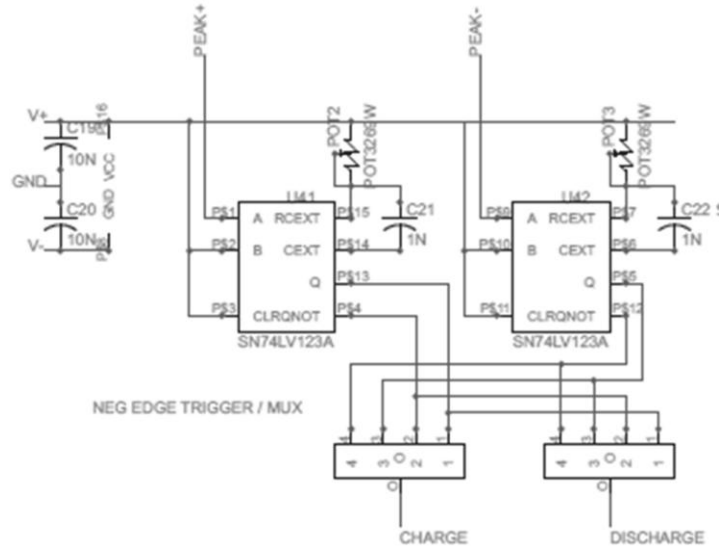
Figure 4.13 Schematic of circuit including monostable retriggerable multivibrator.
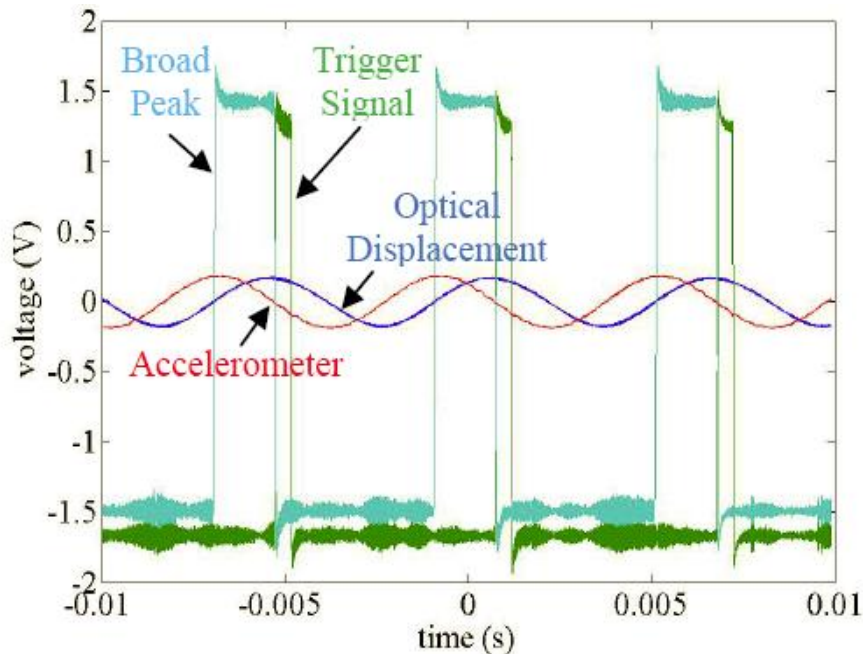
Figure 4.14 Resulting trigger signal by utilizing monostable retriggerable multivibrator.

4.8 Long Term Reliability Testing

As mentioned previously, initial beam characterization efforts focused on a thin single layer beam in order to minimize the proof mass volume ($0.05cm^3$) while maintaining low frequency operation. However, the single layer beam had poor electrical performance. Furthermore, the single layer beam experienced plastic deformation even under static loading. In addition, single layer beams experience stress induced fracturing at the clamp interface after less than 500,000 cycles. In contrast, both brass and composite bimorph structures are tested to be mechanically and electrically stable to over 30 million cycles of steady state operation and +/-2g of external shock testing, making them suitable for field applications.

Even though the bimorph beams are robust for long-term and overdrive conditions, they have an identified primary failure mechanism. If the tip of the proof mass strikes the electrostatic counter electrode, the impact force induces microfracturing within the piezoceramic material that comprises the beam. Microfractures result in a degradation of the beam's electromechanical coupling that does not noticeably manifest itself in lower voltages. Instead, even though the voltage signals appear unaffected, the current capacity is dramatically diminished. Excessive loading on a degraded beam will induce voltage droop during switching and peak detection circuit operation. This droop can inadvertently result in false triggering of the peak detection circuit and impede operation of the electrostatic energy scavenger. This susceptibility to microfracturing from impact shock is a critical limitation in the hybrid system as the gap between the electrostatic electrodes is ideally minimized to obtain substantial

peak capacitance values. Therefore, any increase in excitation amplitude has the potential of destroying the system and must be addressed by protecting the system using either mechanical shock absorbers or detuning the device to avoid the high amplitude displacement. Alternatively, the piezoelectric material can be replaced with different materials that can handle shock (e.g. Sol-gel, PVDF); however, these materials have historically suffered from poor coupling coefficients that would provide substantially less power and voltage.

4.9 Discussion

As the cornerstone of the hybrid energy scavenger system, the piezoelectric transducer element provides the initial energy for operation of the system, as well as the signal that tracks displacement for synchronous timing of the electrostatic scavenger component. Experimental results in beam resonance testing indicate that analytical models closely match the actual performance, with deviations attributed to manufacturing tolerances and material layers that are not considered by the ideal model. A manual, static tuning regiment is adopted to ensure that the beam is mechanically tested at the target frequency of 120Hz; however, in actual operation resonance can drift dynamically due to mechanical fatigue or changes in electrical loading conditions. Industry 5H beams are selected over 5A piezoceramics due to higher coupling coefficients and lower Q factor (wider bandwidth) to ensure that adequate power is provided despite small dynamic changes in resonance. Despite the intrinsic Q factor of the material, impact of relaxation of the clamping mechanism and force can result in lower than intended Q factor measurements and has direct impact on output voltage. As a result, it is critical to ensure rigid clamping without cracking

the beam and is highly dependent on technique of the persons performing the assembly.

Electrical power capacity (Figure 4.8) and, more critically, rectified rail voltages are measured and presented in Figure 4.6. As shown, the serially poled Industry 5H composite bimorph transducer is the only tested beam that produces sufficient voltage to operate the COTS opamps used in the peak detector circuit and thus is used exclusively for system testing.

When connected to the system circuit, the piezoelectric element produces a voltage output that closely tracks the displacement from vibration, as shown in Figure 4.11. In this mode, the device can be used as an acoustic sensor. Since the voltage output is the derivative of the beam displacement, the response curve, shown in Figure 4.12, exhibits a 90-degree phase shift as expected from the simulation results in Figure 2.14. However, the clipping of piezoelectric signal due to current loading of the rectifier circuit was not anticipated and results in a broad response peak from the analog peak detector circuits. Fortunately, the trailing edges of the peak detector output pulses correspond to the displacement peaks; thereby facilitating the use of a trailing edge detector to provide the correct triggering timing without necessitating the use of a power-hungry phase shifter to correct for the offset. Furthermore, the use of a monostable retriggerable multivibrator for trailing edge detection provides flexibility in the electrostatic switching circuits in both trigger pulse polarity and response width so that optimal charging profiles can be obtained.

Finally, upon attaining proper system behavior, the piezoelectric beam is tested for extended operation to identify long-term failure mechanisms. While single layer

piezoceramics exhibit fatigue from both static and dynamic mechanical loading, the composite bimorph was shown to be resilient and free from operational drift over an excess of 30 million cycles. While long-term operation under normal conditions is satisfactory, it is apparent that the primary mechanical failure mechanism is microfracturing from impact shock in the presence of overdrive conditions. This limitation is revealed via power capacity degradation immediately following short duration striking conditions and must be accounted for in further design considerations.

4.10 Summary

This chapter discusses the evaluation and characterization of the piezoelectric transducer as the cornerstone of the hybrid energy scavenger system. Attaining the sufficient DC voltage rails and proper timing signals is arguably the second most critical aspect of enabling collocated electrostatic energy scavenging, with the exception of maximizing capacitance change discussed in Chapter 5. Provided with these conditions, the second phase of experimental testing and systematic electromechanical design revisions is permissible. In light of this, Chapter 5 addresses the experimental testing, design modifications, and demonstration of rudimentary hybrid energy scavenging.

5 Chapter 5: Electrostatic Scavenger Testing

5.1 Introduction

Inclusion of an electrostatic energy scavenger to form a hybrid energy scavenger enables utilization of the normally wasted volume of the proof mass and area beneath the piezoelectric transducer. Given the pre-charge and synchronization signals from the piezoelectric, all external requirements for charge-based electrostatic energy scavenging are met. The purpose of the tests described in this chapter is to confirm the theory of operation for hybrid piezoelectric/electrostatic vibration energy scavenging. To this end, the initial focus of testing is not optimization of the energy production and overhead conservation, as evidenced by the utilization of COTS components. Instead, efforts to simplify the design and focus on ease of testing were paramount in discovering the critical limitations in both the electrical and mechanical domains as an enabling task for future scaling and optimization. This chapter defines the initial evolution of the electrostatic components for testability, proper charge transfer control architecture, and addressing current capacity limitations and confirmation of failure mechanisms of the serially poled composite bimorph piezoelectric transducer that is characterized in the preceding chapter.

5.2 Experimental Setup

As the second phase of system testing, the experimental setup utilized for characterization of the electrostatic component is identical to the laboratory environment detailed in Section 4.2. This section describes modifications to the

mechanical system and test PCB to accommodate proper characterization of electrostatic transduction.

5.2.1   Alignment of Electrostatic Counter Electrode

For simplicity in fabrication and testing, the electrostatic variable capacitor consists of a parallel plate structure with a variable air gap. This structure was chosen to preclude the requirement of precision alignment in 3 axes of motion. Despite this design decision, the challenge of obtaining an optimal capacitance profile using coarse adjusted mechanical system is significant. As measured by the optical displacement probe, at the target excitation of 2.5m/s^2 at 120Hz, the Type 5H4E composite bimorph displacement, relative to the PCB displacement is only 4.54µm. Given perfect parallelism and a 100nm (assuming a deposited dielectric hardstop) gap, the capacitance profile would be as depicted in Figure 5.1. As can be seen, the optimal change in capacitance occurs at gaps between 0.1 and 0.5µm, while beyond this range, the capacitance change is fractional.
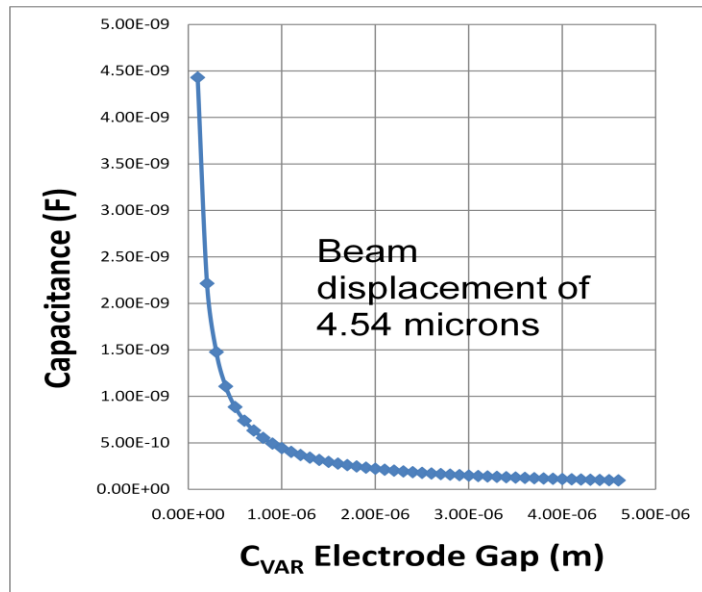
Figure 5.1 Ideal capacitance profile, assuming perfect parallelism and 100nm minimum gap.

126

The first generation systems did not possess an adjustable electrode assembly on the test PCB as the primary focus was on evaluation of the piezoelectric performance that was discussed in Chapter 4. Once the control architecture for synchronization was successfully tested, the focus shifted onto enabling hybrid scavenging via electrostatic transduction. Due to gravity and large proof mass to obtain low frequency resonance, the electrostatic electrode/proof mass is not parallel to the PCB.
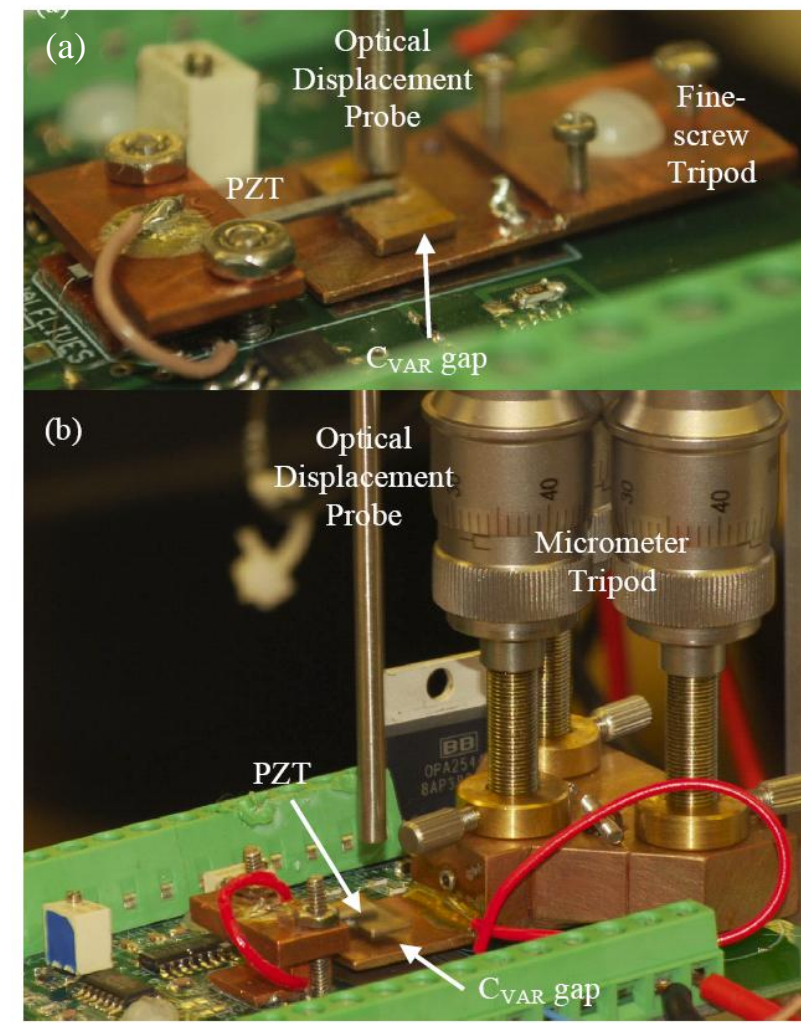
Figure 5.2 Evolution of adjustable electrode assemblies from (a) fine screw to (b) 20nm resolution micrometer.

The first attempt to create an adjustable electrode is shown in Figure 5.2(a), incorporating fine pitch screws in a tripod configuration, the center of the tripod is clamped to the PCB via a plastic screw that penetrates through the PCB and is used to secure the system to the electrodynamic shaker head. This screw applies the opposing force from the tripod adjustment screws. While providing some semblance of adjustability, the coarseness of the screws precluded obtaining sufficiently small gap and parallelism to obtain measureable capacitance changes.

The second revision to create an adjustable platform resolved the limitations of the threaded screws; however, induced numerous additional artifacts. Shown in Figure 5.2(b), three DM10A differential micrometers from ThorLabs are integrated onto a common copper block electrode assembly. The DM10A has 8mm of coarse travel with 1μm resolution, and an additional 300μm of fine travel with 20nm resolution. The DM10A are selected as they provided the finest adjustment capability within a relatively small package. Despite this, the addition of these three micrometers along with the massive Cu assembly that forms the tripod/counter electrode induces significant mass loading and volumetric increases to the test board. The tripod is affixed to the test PCB by two stiff springs to permit maximum adjustability. While this does provide an adjustable platform, the addition of the mass and stiff springs induce higher order resonant modes that result in high frequency vibration as measured by the accelerometer. Furthermore, the 20mm diameter of the micrometers require increasing the length of the copper tripod assembly, shown in Figure 5.3. With this design, using the front micrometer as a pivot point, the calculated 20nm adjustment resolution corresponds to 24.75nm movement, theoretically.
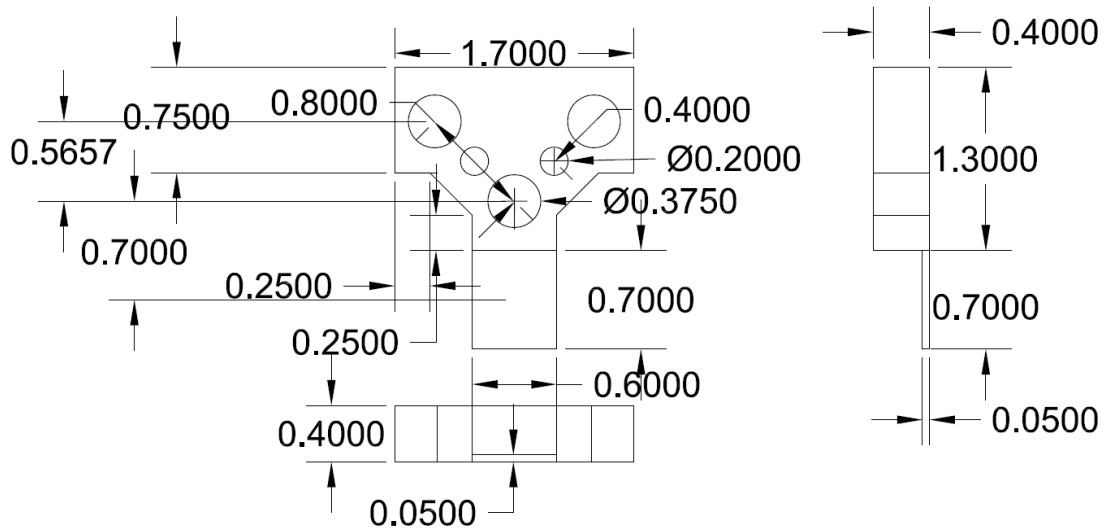
Figure 5.3 Engineering drawing for Cu tripod electrode (units in inches).

Of course, the fine resolution parameters, even if achievable, only account for alignment in one direction. Unfortunately, the tripod configuration is a poor design choice as it adds the complexity of pitch changes in along the perpendicular axis. While this provides the ability to match skew of the proof mass if not perfectly mounted, it dramatically increases the complexity of alignment and adjustment of the counter electrode.

Using this design, it is not possible to statically adjust the parallelism between the electrodes without an elaborate exsitu measurement capability. In lieu of this, the adjustment of electrode is performed during dynamic operation. While running, the voltage across the electrostatic transducer is monitored. The micrometers are adjusted until a noticeable voltage signal is achieved. Of course, with three independent micrometers, changing the position of one affects the electrode pitch. In addition, it is difficult to know when the gap is minimized. Using trial and error, the micrometers are individually adjusted until striking occurs and are then backed off.

5.2.2   Introduction of Instrumentation Amplifier

For simplicity of fabrication and testing, the variable capacitor denoted *CVAR*, which is comprised of the variable gap between the proof mass/electrostatic electrode and the counter electrode, is a simple parallel plate configuration. As described in Section 3.5, this simplification eliminates the complexity of precision multi-axis alignment at the expense of low capacitance (ideal maximum capacitance of 4.5nF). With this low capacitance, the circuit is directly perturbed through the utilization of standard 10MΩ oscilloscope probes; thereby, precluding the ability to measure the effective charge cycling of *CVAR*. As shown in Figure 5.4, the inclusion of an OPA2544 instrumentation amplifier provides the sufficiently high impedance of 1TΩ to measure the charging of *CVAR* and *CSTOR* without directly impacting the operation of the system. This essential diagnostics capability of monitoring charge transfer, as provided by the OPA2544 induces the overhead of an additional external +/-25V DC power supply on the laboratory test bed platform and adds substantial volume to the test PCB. However, charge transfer monitoring is not required in a final implementation of a hybrid scavenger system PCB and can thus be moved to an alternate diagnostics PCB with breakout probe points.
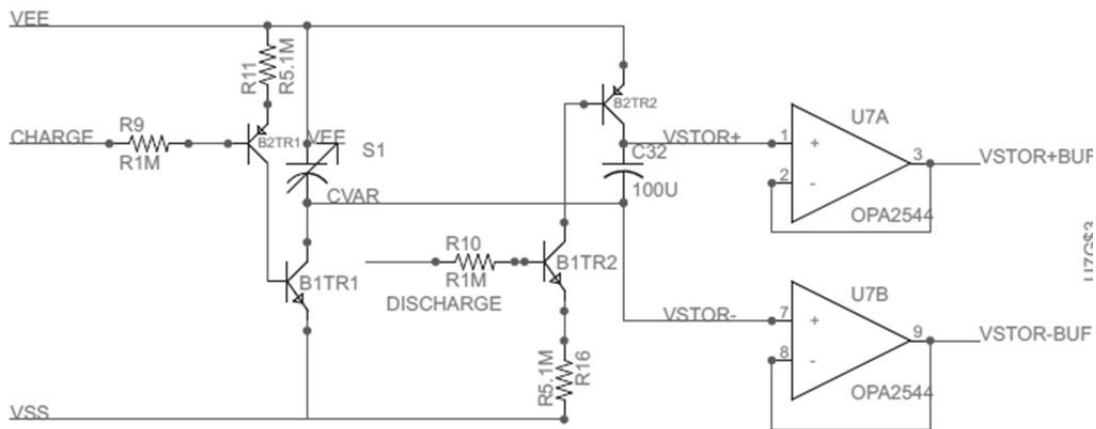
Figure 5.4 Schematic of the charge control circuit using instrumentation amplifiers.

5.3 Charge Transfer Synchronization

Once the charge transfer control architecture was changed from MOSFET based to a BJT configuration, as described in Section 2.5.2.2, the voltage across the variable capacitor, designated $VVAR$, is able to exceed the DC rails, VEE and VSS. The top electrode is held at VEE while the counter electrode is allowed to float except at the time of charging (when C_{VAR} is at the maximum value C_{max}), when it is pulled to VSS. Therefore, since charge is constant, the voltage across the variable capacitor is defined by

Equation 5.1 $$VVAR = \frac{C_{max}}{C_{VAR}}(VEE - VSS).$$

As mentioned in Chapter 4, the piezoelectric transducer is severely current limited. In light of this, charging of the variable capacitor is the singular case in which the small capacitance of the parallel plate configuration is advantageous as current draw is minimal.

Originally, 1MΩ resistors, $R9$ and $R10$, were added to minimize current injection into the circuit from the COTS opamps; however, the utilization of BJTs creates multiple current paths between VEE and VSS through the base of the control devices. If unchecked, these conduction paths essentially short circuit the DC rails instead of charging and discharging the variable capacitor. As shown in Figure 5.4, discrete 5.1MΩ resistors $R11$ and $R16$ are added to limit the collector-emitter currents to prevent shorting of the respective rails.

Despite efforts to minimize the current paths between the DC rails, as a piezoelectric transducer degrades, the current capacity becomes critically limited. As illustrated in Figure 5.5, the piezoelectric signal, V_{PZT}, suffers from droop in the

center of both positive and negative peaks. This is attributed to current draw during operation of the peak detector, that bleeds some current through the voltage divider (see Figure 4.10) while charging the DC rail reference capacitors. At a certain critical failure point, the current capacity of the piezoelectric will induce sufficient droop that is registered by the monostable retriggerable multivibrator as a trailing edge. Resulting false control pulses induce charge transfer at incorrect times and can only be corrected by replacing the piezoelectric transducer.
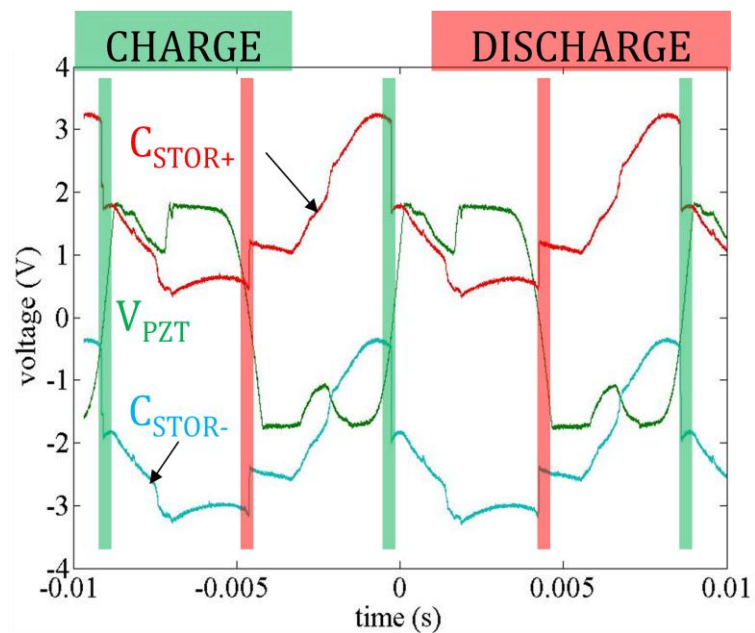
Figure 5.5 Oscilloscope plot of the C_{STOR} charge cycle with synchronization from piezoelectric.

Using the charge control circuit configuration in Figure 5.4, successful charging of the storage capacitor, C_{STOR} is achieved and shown in the oscilloscope plot in Figure 5.5. Synchronized with the trailing edge of the negative piezoelectric voltage signal, V_{PZT}, the counter electrode of variable capacitor, designated C_{STOR-}, is charged to VSS. The electrodes are then allowed to float during the capacitance change until the maximum displacement peak (and resulting minimum capacitance) as indicated by

132

the trailing edge of the positive V_{PZT} peak. At this point, the storage capacitor electrode, C_{STOR+} is connected to *VEE* thereby closing the circuit and allowing partial charge transfer from the variable capacitor to the storage capacitor.

5.4 Voltage Amplification Measurements

Over time, the excess voltage (*VVAR*) generated from operation of the electrostatic transducer is manifested on the storage capacitor, C_{STOR}, and is monitored by simply measuring the potential across the capacitor via the instrumentation amplifier output. In Figure 5.6, the voltage across C_{STOR} is 4.02V in contrast to the DC rail voltage of 3.35V, corresponding to an increase of 19.82 percent in the output voltage despite sub-optimal beam conditions.

Furthermore, as shown in both Figure 5.5 and Figure 5.6 there is an unexpected peak inversion when the capacitance should be minimized. Originally, thought to be
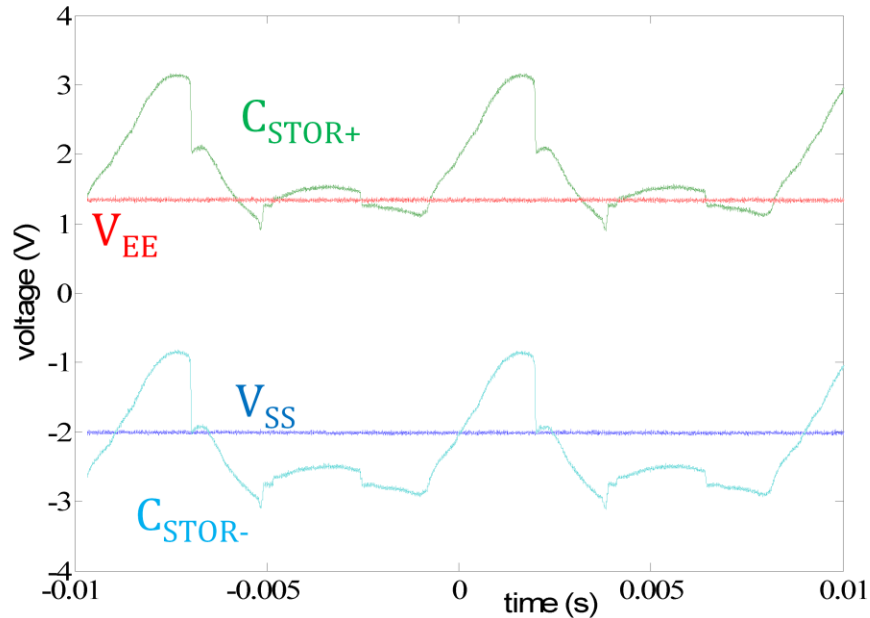
Figure 5.6 Oscilloscope trace of voltage amplification in excess of DC rails.

133
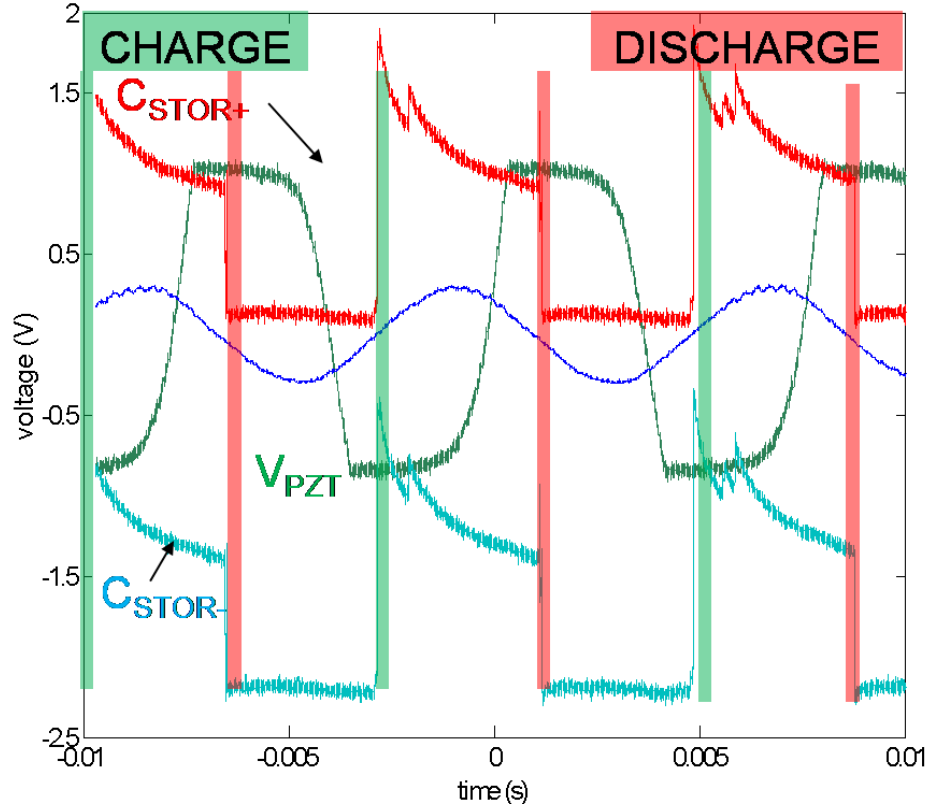
Figure 5.7 Proper operation of hybrid energy scavenging after beam replacement.
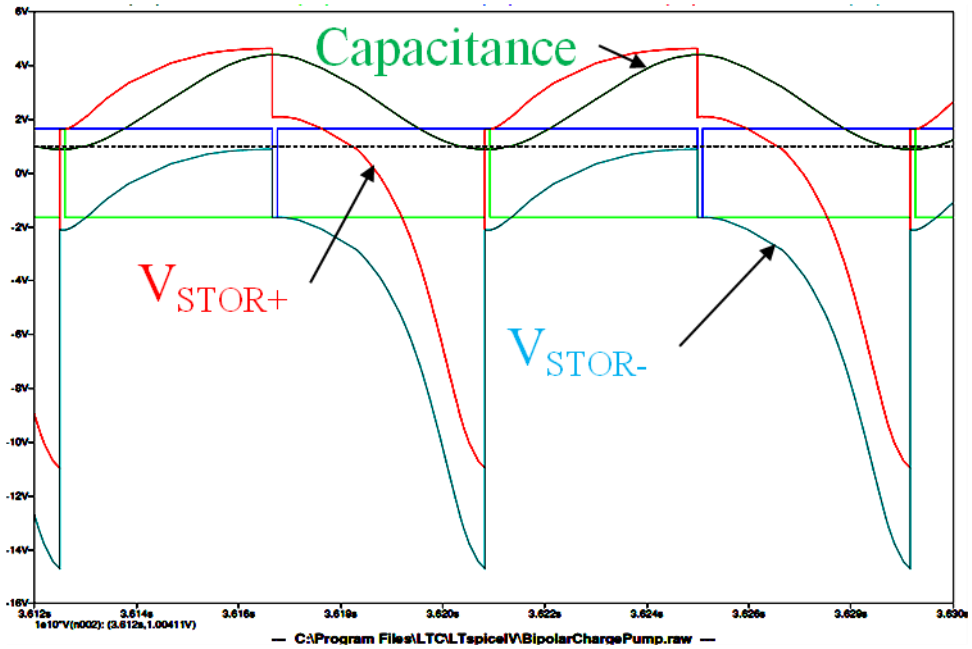
Figure 5.8 SPICE simulation result assuming proper 100nm electrostatic gap.

134

the effect of higher order resonant modes, it is clear via optical displacement measurements that this is not the case. Instead, it is attributed to circuit effects due to excessive current draw on the damaged piezoelectric beam that results in improper operational states.

As shown in Figure 5.7, a new beam does not suffer from the current capacity limitations of the microfractured beam. The operation closely resembles the ideal operation, as simulated by LTSPICE, that is depicted again in Figure 5.8. Although, the capacitance profile is not ideal, it is clear that hybrid energy scavenging is occurring. Furthermore, the system operates correctly even when the piezoelectric voltage is not ideal. For the example in Figure 5.7, the system is run slightly off resonance, as indicated by the shift between piezoelectric response and accelerometer signal. The result is a lower piezoelectric voltage and corresponding DC rail voltage of 1.707V while the voltage across the storage capacitor on the output of the electrostatic scavenger is 2.314V, a 35.29-percent voltage gain above the DC rail.

5.5 Power Measurements

Given the extremely low capacitance of the system, there is very little current capacity on the output of the electrostatic scavenger. This makes DC power measurements on the output of system challenging as extremely high resistances are required. Therefore using experimental measurement techniques is not useful as the electrostatic power levels are well below 1μW. However, the estimated energy levels can be extrapolated as discussed in the next section.

5.6 Discussion

The primary figure of merit for the HALF-LIVES system is the energy transfer per half cycle to the capacitor, ΔE is then commonly known as

Equation 5.2 $\quad \Delta E = \dfrac{1}{2} V_{IN} V_{OUT} \left(C_{max} - C_{min} \right).$

Given the known displacement of the piezoelectric beam of 4.54µm and resulting voltage increase of 35.29-percent beyond the DC rails, an approximation of electrostatic energy production can be calculated. Using the ideal parallel capacitance model, and the relationship given in Equation 5.1, the gap and resulting capacitance parameters can be approximated, as shown in Figure 5.9. This corresponds to a minimum capacitance of 25.46pF, maximum capacitance of 34.34pF, which by Equation 5.2 corresponds to 17.5pJ or 2.1nW of additional DC power. While the power output of the electrostatic energy scavenger is fairly negligible in comparison to the piezoelectric voltage generation, voltage amplification by the electrostatic transducer clearly indicates that hybrid energy scavenging is conceivable.
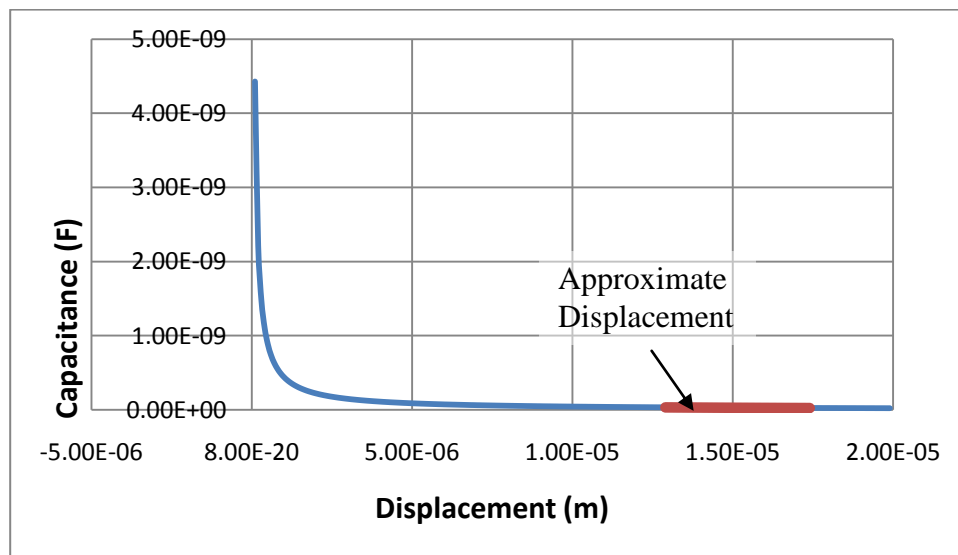
Figure 5.9 Approximation of actual displacement/capacitance profile.

5.7 Summary

This chapter discusses the evaluation and characterization of the electrostatic transducer as a secondary power source within the volume of the hybrid energy scavenger system. Attaining the sufficient change in capacitance is arguably the most critical aspect of enabling collocated electrostatic energy scavenging. Limitations of the current system are due to mechanical design limitations, and lack of optimization of the variable capacitor that is formed between the proof mass and adjustable counter electrode. Given the ability to resolve the alignment and parallelism limitations, using the simple parallel plate structure, with a minimum gap of 100nm, a theoretical maximum of 0.88µJ of energy could be produced per cycle, resulting in a constant power output of 100µW of additional power. Increasing capacitance further using novel structures could substantially improve performance, but considerations in impacting the cost must be considered. Chapter 6 closes this body of work with a summary of accomplishments, power and fiduciary cost analysis, and description of continuing and future efforts to make hybrid energy scavenging feasible for real-world applications.

6 Chapter 6: Conclusions

6.1 Summary

This dissertation presents the design, simulation, fabrication, testing, and evolution of the first published mass producible hybrid vibration energy scavenger system that exploits both piezoelectric and electrostatic transductions simultaneously on a common MEMS transducer. As global energy demands surge and fossil fuel sources dwindle, a dramatic shift toward alternative energy sources is eminent. Despite expansion of renewable energy sources, environmental energy densities and availability are lower than fossil fuel or nuclear sources, resulting in higher costs that limit renewable sources as only a partial solution to meeting increasing energy demands. Given that energy is wasted in converting electricity to heat, light, and vibration through operation electromechanical infrastructure equipment, wasted energy can be harnessed to operate low power sensor systems for health monitoring and optimization of critical infrastructure. The device presented in this dissertation is the first step in realization of a low cost method of recycling mechanical vibration energy in a self-sustained hybrid transducer system that can survey while obtaining sufficient power to operate digital systems for extended durations. Toward this goal, cost minimization and operational longevity are paramount.

This work has shown that a single hybrid vibration scavenger device can source sufficient voltage and power levels to run the majority of low power electronic components. However, further optimizations will be necessary to power more complex systems such as distributed sensor network nodes. Integration as part of a

multi-source hybrid power system, that incorporates light, heat, electromagnetic and vibration coupled with energy aware computation, will lend to flexible sensor platforms able to scavenge energy from the dominant source while utilizing the inactive scavengers as sensors for data acquisition. For example, it has been demonstrated that the vibration scavenger can behave as an acoustic sensor when not operating as the energy source.

This chapter summarizes the current state of the effort to use a common transducer platform to obtain both piezoelectric and electrostatic energy conversion. By exploiting the piezoelectric, charge-based synchronous electrostatic energy scavenging without an external battery source and synchronization circuits is possible. However, critical challenges in enabling feasible hybrid vibration energy scavenging are identified. The later portion of this chapter addresses on-going and future work that is being conducted toward realization of a deployable system.

6.1.1 Piezoelectric Scavenger

The piezoelectric beam forms the spring of the resonant mass-spring transducer for converting vibration excitation into an AC electrical output. A serially poled, composite shim, piezoelectric bimorph produces the highest output rectified voltage of over 3.3V and power output of 145μW using ¼ g vibration acceleration at 120Hz. Considering solely the volume of the piezoelectric beam and tungsten proof mass, the volume is 0.054cm^3, resulting in a power density of 2.68mW/cm^3.

While this is by no means the first piezoelectric transducer used as a vibration-excited generator, it is the first demonstration of the piezoelectric forming a hybrid structure with the electrostatic transducer. It is also the first demonstration of the use

of a piezoelectric beam to produce the electrostatic pre-charge and displacement tracking signal necessary for optimal charge-based electrostatic energy scavenging.

The tested piezoelectric beam has a relatively low Q factor that is highly dependent on the material and quality of mechanical clamping. The wider bandwidth provided by low Q factor is preferred in environments where the dominant frequency may shift slightly and maintains operability during changing electrical loading (as the storage capacitor saturates). However, as an engineering tradeoff, the wider frequency response results in lower displacement and voltages at resonance.

The single layer beam is shown to experience plastic deformation even with static gravitational loading. However, the composite bimorph is mechanically robust and a single beam has been tested to an excess of 30 million cycles in multiple intervals that span several months. While this does not constitute comprehensive testing of long-term continuous duty operation, it does show that plastic deformation and long term static loading do not appear to be primary failure mechanisms. The most significant failure mechanism is microfracturing that is induced by striking of the proof mass on the electrostatic counter electrode. Current capacity of the piezoelectric beam is rapidly diminished even after a few seconds of striking conditions; however, the voltage output is not as rapidly impacted. The drop in current capacity severely impacts the performance of the circuit as the rails are not sustained during peak loading conditions and can only be resolved by beam replacement. Given these limitations, future potential enhancements in the design and operation of piezoelectric beam are discussed later in this chapter.

6.1.2 Electrostatic Scavenger

The electrostatic energy scavenger is utilized as a secondary power generator from the common excitation. Traditional charge-based electrostatic vibration energy scavengers require a pre-charge and charge synchronization to operate properly. Most of these devices consume over 50 percent of the generated power to achieve synchronization and require a battery for pre-charging. The hybrid approach investigated in this thesis uses the piezoelectric transducer to eliminate the need for the batter and greatly reduces the power overhead for synchronization.

Since the electrostatic structure is intended to be simple (parallel plate) structure for testing purposes, it suffers from low capacitance. However, it is fairly trivial to increase the capacitance by introducing interdigitated electrodes. The challenge is maintaining parallelism and alignment for relative displacements of 4.54 microns at ¼ g 120Hz. This required significant effort to maintain fine alignment of the electrostatic counter electrode and resulted in several design revisions to enable observation of electrostatic energy scavenging. The addition of fine-pitch micrometers to adjust the gap and parallelism results in a substantial addition of mass to the system that induces additional vibration modes. Despite this, initial results show a 19.82 to 35.29 percent increase in voltage beyond the piezoelectric generated DC rails. This corresponds to approximately 2.1nW generation from the electrostatic scavenger component which is a far cry from the theoretical 100µW possible with the current parallel plate geometry. The limitations of the current electrostatic mechanical design are actively being addressed and potential solutions are discussed in Section 6.2.2.

6.1.3 <u>System Circuit</u>

The system circuit utilizes COTS components to enable rapid prototyping and system modifications and use of custom on-board diagnostics and measurement circuits. As testing progressed, it was determined that active signal filtering/conditioning is not required. However, clipping artifacts from utilizing the piezoelectric voltage for DC rail generation and displacement feedback simultaneously results in broad peak detection response. Fortunately, given the low frequency operation, the displacement peak detection signal trailing edges correlate to the measured displacement peaks. As a result, a monostable retriggerable multivibrator component enables synchronous charge transfer by clocking on the trailing edge. With the development of proper synchronization and inclusion of instrumentation amplifiers for measuring charge transfer via high impedance paths, basic hybrid energy scavenging from a shared piezoelectric/electrostatic transducer is demonstrated. Despite this, the COTS power requirements are orders of magnitude in excess of the scavenger power output. A report of the power requirements of the COTS devices is provided in the following section and identifies the current roadblocks to self-sustained operation. Reducing the COTS overhead is discussed later in this chapter as part of the on-going and future work section.

6.1.3.1 COTS power consumption analysis

First, it should be pointed out that a COTS energy scavenging system is inefficient and unable to provide a net positive energy system. As simulated and discussed in Section 2.5.2.3, optimized ASIC circuits will prevent this case in future work as they will be suitable efficient to enable real energy scavenging with minimal overhead.

Manufacturer typical specifications provide the ability to perform a rudimentary power consumption calculation for active components on the system PCB. The results are summarized in Table 6.1. As shown, the diagnostics components, strictly for measurement or current buffering applications, consume 92.3 percent of the total system power. Furthermore, the operation of these components requires three separate external power supplies. The majority of the 132mW of power is consumed by the quad operational amplifier (only half of which is actually utilized for peak detection) and the monostable multivibrator. Considering the piezoelectric generator only produces 145μW at ¼g at 120Hz, it is critical to replace the op-amp and multivibrator components with suitable low power alternatives. This is discussed in Section 6.2.3.

Table 6.1 Typical power and voltage requirements of active COTS components.

MANUFACTURER	PART#	PART DESCRIPTION	PURPOSE	PWR (mW)	VOLTAGE(V)
Texas Instruments	OPA2544T	IC OPAMP GP 1.4MHZ TO-220-11	DIAGNOSTICS	1056.0000	20V
Micrel Inc	MIC5219-3.3YMM	IC REG LDO 500MA 1% 3.3V 8-MSOP	DIAGNOSTICS	455.0000	5V
Texas Instruments	OPA4350UA	IC HS CMOS OPAMP (35MHZ)14-SOIC	DIAGNOSTICS	99.0000	>2.7V
STMicroelectronics	LIS302SG	ACCELEROMETER TRPL AXIS 14-LGA	DIAGNOSTICS	2.1450	3.3V
Rohm Semiconductor	IMX8T108	TRANS DUAL NPN 120V 50MA SOT- 457	OPERATION	0.0015	<120V
Rohm Semiconductor	IMT4T108	TRANS DUAL PNP 120V 50MA SOT- 457	OPERATION	0.0015	<120V
Texas Instruments	SN74LV123ADR	IC MONO MULTIVIBRATR DUAL 16SOIC	OPERATION	30.0000	2V-5.5V
Texas Instruments	OPA4347UA	IC QUAD RAIL-RAIL OPAMP 14-SOIC	OPERATION	102.0000	>2.3V
ON Semiconductor	NTZD3155CT1G	MOSFET N+P 20V 430MA SOT-563	OPERATION	0.0075	<20V

6.1.4   Cost Analysis

While initial prototype cost is anticipated to be high, the cost of distributed energy scavenging systems must be inconsequential in order to be practical. Therefore, cost amortization via mass production is a key factor to realizing a deployable system. Considerable effort is taken to minimize fabrication overhead and component counts as an initial step toward the goal of cost minimization. This section reports the cost of the current prototype system. It should be noted that the prices reported reflect the cost basis at the time of acquisition (2nd and 3rd quarters of 2009) not the current market rates. Generally speaking, the prices of discrete components from Digikey have increased by approximately 10-20 percent in one year. The prices of discrete active components are listed in Table 6.2. Passive components are not reported since bulk prices and low component counts have negligible contribution to the total cost of the system.   The diagnostics and test components consume 89.8 percent of the component cost overhead for the prototype. With the exception of the quad op-amp, all essential component costs are fractions of a dollar in low quantities and even less when purchased in bulk.   However, component price is not the only factor that impacts overall system cost. The area of the components also drives up the cost by increasing PCB dimensions. Not considering the area required for routing signals passive components, and mechanical assemblies, the diagnostics components consume 76.6 percent of the system PCB area. The current cost of a single PCB prototype is $82.42, but this cost is dramatically reduced by ordering bulk quantities. While efforts to minimize PCB area will result in a cost basis that could be acceptable for low volumes; it does not compare to the cost amortization that is realized by

migrating the architecture to an ASIC. Therefore, for large-scale deployment, an ASIC is the only viable option and is discussed further in Section 6.2.3.

Table 6.2 Cost and area consumption of active COTS components.

MANUFACTURER	PART#	PART DESCRIPTION	PURPOSE	DIM (mm)	QTY	COST (USD)
Texas Instruments	OPA2544T	IC OPAMP GP 1.4MHZ TO-220-11	DIAGNOSTICS	20.3 x 17.6	1	$ 18.0000
Micrel Inc	MIC5219-3.3YMM	IC REG LDO 500MA 1% 3.3V 8-MSOP	DIAGNOSTICS	3.1 x 5.1	1	$ 2.2300
Texas Instruments	OPA4350UA	IC HS CMOS OPAMP (35MHZ)14-SOIC	DIAGNOSTICS	8.8 x 6.2	1	$ 8.0600
STMicroelectronics	LIS302SG	ACCELEROMETER TRPL AXIS 14-LGA	DIAGNOSTICS	3.0 x 5.0	1	$ 5.8320
Rohm Semiconductor	IMX8T108	TRANS DUAL NPN 120V 50MA SOT- 457	OPERATION	2.8 x 2.9	1	$ 0.3124
Rohm Semiconductor	IMT4T108	TRANS DUAL PNP 120V 50MA SOT- 457	OPERATION	2.8 x 2.9	1	$ 0.3124
Texas Instruments	SN74LV123ADR	IC MONO MULTIVIBRATR DUAL 16SOIC	OPERATION	10.0 x 6.2	1	$ 0.3600
Texas Instruments	OPA4347UA	IC QUAD RAIL-RAIL OPAMP 14-SOIC	OPERATION	8.8 x 6.2	1	$ 2.5700
ON Semiconductor	NTZD3155CT1G	MOSFET N+P 20V 430MA SOT-563	OPERATION	1.6 x 1.6	1	$ 0.3168
TOTAL						**$ 37.9936**

Despite limitations in cost amortization due to adoption of COTS parts for the prototype system circuit, efforts to minimize transducer cost overhead have yielded promising results. Table 6.3 show that the estimated amortized cost of a single prototype beam is $2.76. This cost can be substantially reduced by purchasing piezoelectric material in bulk, resulting in a cost of $2.33. Further reductions can be obtained by switching to 150mm diameter wafers of piezoelectric material, since the consumption of KMPR and labor cost would not increase.

Table 6.3 Cost amortization schedule of prototype piezoelectric beams.

COMPONENT	COST / UNIT	AMORITIZED COST	COMMENTS
Piezoelectric Material (prototype)	$115/sheet	$ 1.1500000	503 sheet is 31.8mm x 63.5mm
Piezoelectric Material (bulk)	$72/sheet	$ 0.7200000	Yields 100 beams per sheet
KMPR 1050 (prototype)	$1471/L	$ 0.0735500	5cc per wafer w/ 1 sheet/wafer
Gold	$40/g	$ 0.0043425	19.3g/cc @ $40/g for 5.625E-6cc
Tungsten	$0.035/g	$ 0.0337750	19.3g/cc @ $0.035/g for 0.05cc
Labor	$15/hr	$ 1.5000000	Loaded labor rate of $15/hr for 10hrs
TOTAL		**$ 2.7616675**	
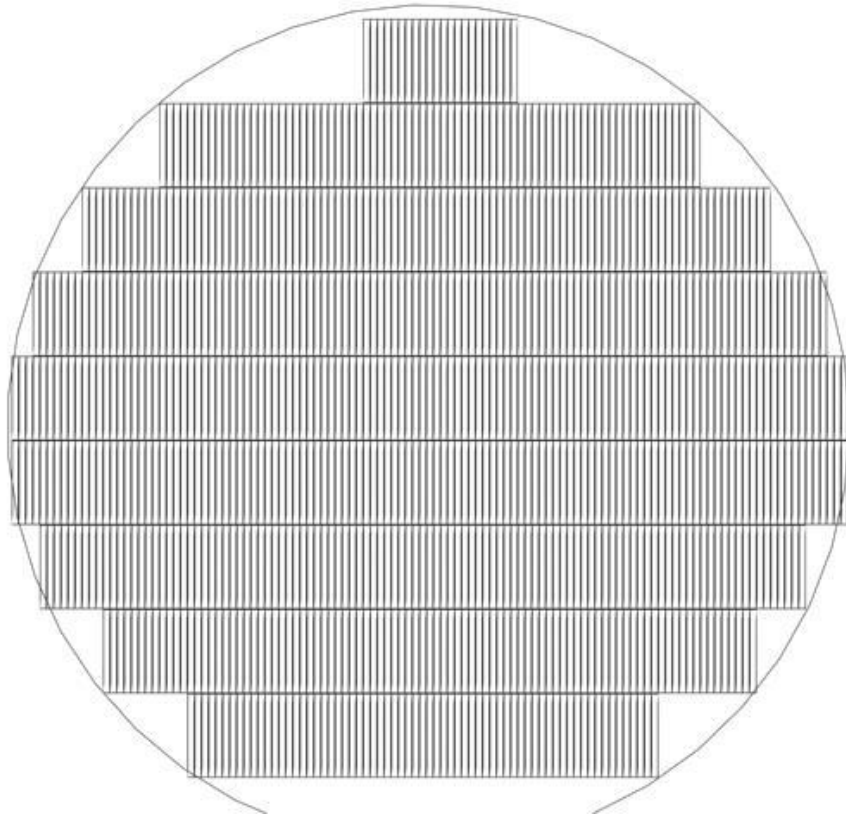
Figure 6.1Proposed layout of 150mm diameter wafer.

A die per wafer (DPW) estimation, using the formula

Equation 6.1 $$DPW = d\pi \left(\frac{d}{4S} - \frac{1}{\sqrt{2S}} \right),$$

where d is the wafer diameter in millimeters and S is the beam area, yields 865 beams. However, the dicing profile, shown in Figure 6.1, will result in only 815 transducer beams. Since budgetary quotation for a 150mm piezoelectric wafer from Piezo Systems is not readily available, a cost per unit area estimation yields an approximate cost of $630 per wafer. Table 6.4 shows the amortized cost is $0.773 per beam. However, substantial cost savings are realized for labor resulting in a cost of $1.004 per transducer if only a single wafer per 10 hour shift is produced. In reality, mass production of piezoelectric wafers would substantially reduce the labor

146

overhead so that the cost of purchasing piezoelectric wafers dominates the overhead. This overhead would certainly be reduced as commercial demand increases production capacity. Finally, the simplicity of fabrication process ensures extremely high yields with current prototype fabrication yields of above 95 percent.

Table 6.4 Cost amortization schedule for a single 150mm wafer.

COMPONENT	COST / UNIT	AMORITIZED COST	COMMENTS
Piezoelectric Material (150mm wafer)	$630/wafer	$ 0.7731192	Yields 815 beams per wafer
KMPR 1050 (prototype)	$1471/L	$ 0.0090245	5cc per wafer w/ 1 sheet/wafer
Gold	$40/g	$ 0.0043425	19.3g/cc @ $40/g for 5.625E-6cc
Tungsten	$0.035/g	$ 0.0337750	19.3g/cc @ $0.035/g for 0.05cc
Labor	$15/hr	$ 0.1840491	Loaded labor rate of $15/hr for 10hrs
TOTAL COST / BEAM		$ 1.0043103	

6.2 Future Work

This work has demonstrated rudimentary hybrid vibration energy scavenging using piezoelectric and electrostatic energy transduction at the system level with symbiotic interdependencies. While this demonstrates the viability of utilizing the piezoelectric as an initial charge, primary power, and synchronization source, the overall power production is negative. The power requirements of the COTS timing circuit exceeds the power generation. This section briefly describes current and future work to develop a deployable hybrid vibration energy scavenger.

6.2.1 Piezoelectric Optimization

Standard rectilinear piezoelectric beams are utilized in this work for the ease of manufacturing as well as design and simulation. While this beam geometry provides

acceptable voltage and power levels, it is suboptimal from a performance standpoint. Better geometries like trapezoidal piezoelectric beams that improve stress distributions are described elsewhere [31]. These could be easily incorporated into the existing fabrication process, but it would decrease the DPW and hence increase system cost significantly since the piezoelectric material is the current driver of transducer overhead.

Another limitation of the experimental piezoelectric transducer architecture is low current densities as a tradeoff for higher voltages. Given eventual reductions in working voltage requirements by COTS circuit modification or application specific integrated circuit (ASIC) integration, parallel poled piezoelectric beams could be used to generate higher current capacity. However, it should be noted that parallel poled piezoelectric beams would increase the wiring complexity as they require a third internal connection.

Finally, the continuous operation testing for robustness was only for intervals of 30 million cycles. At 120Hz that only corresponds to approximately 3 days of continuous operation and long-term trials are necessary. Environmental tests under different temperature and humidity conditions are also required before systems can be fielded en-masse.

6.2.2 Electrostatic Scavenger Optimization

One of the most obvious ways to improve the energy production from the electrostatic transducer is to maximize capacitance change by incorporating interdigitated electrodes via standard MEMS processing. This was not done here in order to avoid introducing two additional degrees of freedom that would require

precision alignment. The increase in surface area will also exacerbate viscous damping from squeeze film effects from the presence of air. While hermetic packaging in vacuum could eliminate the viscous damping between the electrodes, it could be detrimental to the overall robustness of the system as the squeeze film effect may be a valuable source of electrode strike protection. Clearly, a balance between maximizing the capacitance and enhancing mechanical robustness is required and could be specific to differing sources and environments.

6.2.2.1 Improvements in Counter Electrode Control – Self Alignment

Currently, the most challenging obstacle to obtaining efficient hybrid energy scavenging is the inability to obtain precision gap and parallelism between the electrostatic electrodes. A self-aligned counter electrode is being pursued by measuring the displacement, locking the beam into place at the displacement minima, placing the counter electrode into physical contact, and securing in place with solder. This is actively being addressed in the 2nd generation hybrid energy system as a mid-step progression toward volume and power minimization.

6.2.3 <u>Circuit Optimization – Power and Volume Reduction</u>

The reported hybrid energy scavenger system utilizes COTS components to facilitate rapid prototyping and measurements of conditions that are not expected by ideal SPICE simulation, but induce significant power overhead. As described in Section 6.1.3.1, two operational COTS components consume more power than the hybrid energy scavenger system is able to produce. With the exception of diagnostics (e.g. accelerometer) sub-circuits, the 2nd generation system should be independent of external power supplies. Low Power COTS, such as the National Semiconductor

149

LMV291 low power comparators that only consume 15µW are being incorporated to replace the high power operational amplifiers. However, a low power variant of the monostable retriggerable multivibrator remains elusive. While the dynamic power dissipation is low due to the inherent low frequency operation of the hybrid energy system, all commercial parts require 200-500mW static power. To mitigate this, an implementation using either low power discrete COTS parts or low power Application Specific Integrated Circuit (ASIC) is required. Given that more power savings can be realized by implementing the low power designs described in Section 2.5.2.3, an ASIC will give the low overhead electrical performance, facilitate incorporation of load electronic systems, and minimize volume of the electrical circuits.

ASIC integration will require volume reduction of mechanical fixture overhead that introduces new challenges. Modifications include solder attach of constantan wire for both sides of the piezoelectric and the use of an electromechanical copper support peg, shown in Figure 6.2, for making the electrical contact for the electrostatic proof mass/electrode to the board while simultaneously providing the mechanical support for the beam. The piezoelectric will require an additional gold coating on the back side to facilitate the additional wire solder attach as the pre-coated nickel coating is too thin for solder attach. Similar to the tungsten proof mass assembly, the copper support peg will be attached to the piezoelectric beam using cyanoacrylate and to the PCB using eutectic Sn/Pb solder. While using cyanoacrylate has been proven to be robust for vibration scavenging operation in the low frequency, low amplitude regime, there is no data on the robustness of the solder for mechanical

purposes. This may require additional cyanoacrylate to secure the copper peg to the PCB, but will complicate beam exchanges significantly and eliminate the ease of adjusting resonance by changing the beam length. Furthermore, the cyanoacrylate will have more compliance and material shrink than the copper and may adversely limit the piezoelectric performance. Therefore, the volume reductions in the mechanical assembly must be characterized and tested for robust operation on a PCB implementation before proceeding to the ASIC integration phase.

Figure 6.2 Concept rendering of volume reduction by using a Cu mounting peg.

6.2.4   Dynamic Frequency Tuning

There is low probability of static dominant vibration sources at a particular resonant frequency in remote sensing. Therefore, dynamic frequency tuning is required as small deviations from the transducer resonance will impede operation. Currently a topic of investigation in single transducer vibration scavengers, much of the research is applicable to the hybrid scavenger. One possible tuning mechanism is electrostatic adjustment of the spring constant by incorporating multiple variable capacitor structures (one for scavenging and others for tuning) on the end of the piezoelectric cantilever. Despite this, volume and power overhead will dominate the feasibility of resonant tuning.

151

6.3   Conclusion

This dissertation is the first demonstration of hybrid energy scavenging using both piezoelectric and electrostatic transduction mechanisms within a shared volume. The symbiotic relationship between the piezoelectric and electrostatic, in which the piezoelectric provides a pre-charge and synchronization for the electrostatic scavenger, while the electrostatic electrode serves as a large proof mass greatly reduces the problems experienced by previous electrostatic approaches. While more effort is required to improve the efficiency of the electrostatic component and develop suitably efficient ASICs, this work demonstrates the principle of low cost hybrid vibration scavenging. It is hoped that further development will enable the deployment of auxiliary, long-term power sources for remote sensing microsystem-based sensor networks that monitor critical infrastructure such as bridges and enable efficient operation of the power grid.

7 Appendix A: In-Plane Electrostatic Models

This appendix provides the derivations for in-plane operation as the initial design that is described in Section 2.4.4.2. This appendix will provide analytic models for the proof mass/electrostatic charge pump, energy transfer, and damping functions.

7.1 Generic Vibration-to-Electric Conversion Model

In 1995, Williams and Yates proposed modeling a vibration harvester as a spring, mass, dash-pot system as illustrated in Figure 7.1 [47].
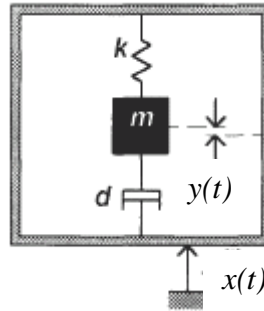
Figure 7.1 Spring, mass, dash pot model of a generic vibration harvester

In this model, $x(t)$ is the input (external) displacement applied by a vibration source while $y(t)$ is the internal mass displacement. This vibration harvester system is described by

Equation 7.1 $\quad -m\ddot{x} = m\ddot{y} + (b_e + b_m)\dot{y} + ky$

where m is the proof mass in (kg), b_e is the electrical damping coefficient, b_m is the mechanical damping coefficient, and k is the spring constant in (F/m). However, the damping coefficients are not necessarily dependent on velocity, so the model is

Equation 7.2 $\quad -m\ddot{x} = m\ddot{y} + f_e + f_m + ky$

where f_e is the electrically induced damping force function in (*N*) and f_m is the mechanically induced damping force function in (*N*). These functions are composites of the electrostatic, piezoelectric, and circuit damping functions as depicted in

Equation 7.3 $\quad f_e = f_{e_{electrosta\ tic}} + f_{e_{piezoelect\ ric}} + f_{e\ circuit}$

Equation 7.4 $\quad f_m = f_{m_{electrosta\ tic}} + f_{m_{piezoelect\ ric}}$

7.2 Electrostatic Energy Conversion Model

This section applies a specific implementation, using the electrostatic charge pump to the generic energy conversion model.

7.2.1 Shuttle Mass Model Variables

L_s – **length of shuttle (m)**

L_f – **length of fingers (m)**

L_o – **length of overlap (m)**

W_s – **width of shuttle (m)**

W_f – **width of fingers (m)**

h – **height of shuttle (m)**

N_g – **number of gaps**

ρ_s – **density of shuttle (kg/m^3)**

d – **initial gap between electrodes (m)**

7.2.2 Shuttle Mass Model

The shuttle mass is a straight forward calculation based on the geometry and material properties of the electrodes that comprise the structure shown in Figure 7.2. The mass of the center shuttle is defined by

Equation 7.5 $\quad m_{shuttle} = \rho_s \left(L_s \cdot W_s \cdot h \right),$

while the total mass of all electrode fingers is

Equation 7.6 $m_{fingers} = \rho_s \left(\left(N_g + 2 \right) \left(L_f \cdot W_f \cdot h \right) \right).$

This is combined for the total mass of

Equation 7.7 $m_{total} = \rho_s h \left(L_s \cdot W_s + \left(N_g + 2 \right) \left(L_f \cdot W_f \right) \right).$
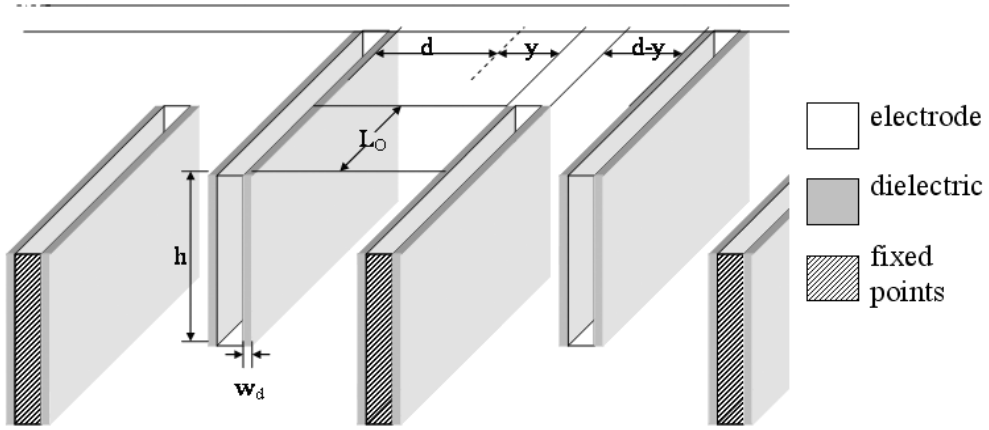
Figure 7.2 Geometry of electrostatic proof mass electrodes
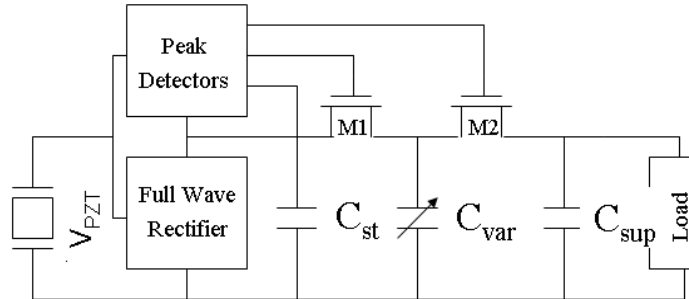
Figure 7.3 Hybrid electrostatic energy conversion system

7.2.3   Electrostatic Converter Model

In Figure 7.3, C_{var} is the variable capacitor that is comprised of the shuttle mass and the surrounding electrodes, C_{par} (not shown) is the parasitic capacitance, C_{st} is the temporary storage capacitor across which the V_{PZT}, the piezoelectric input voltage, is used for pre-charge, and C_{sup} is the storage supercapacitor.

155

Initial charge is supplied to the variable capacitor when the capacitance reaches the maximum value, denoted C_{max}, and is defined by

Equation 7.8 $\quad Q = (C_{max} + C_{par})V_{PZT}$.

Charge is fixed while C_{var} approaches C_{min}, at which point the voltage output is

Equation 7.9 $\quad Q = (C_{min} + C_{par})V_{OUT}$.

Equations A.8 and A.9 are related to the fixed charge by

Equation 7.10 $\quad Q = (C_{max} + C_{par})V_{PZT} = (C_{min} + C_{par})V_{OUT}$

that is rearranged to solve for V_{OUT} to be

Equation 7.11 $\quad V_{OUT} = \dfrac{C_{max} + C_{par}}{C_{min} + C_{par}} V_{PZT}$.

Mechanical work is done to move the variable capacitor between minimum and maximum capacitance values, so the change of energy per cycle is

Equation 7.12 $\quad \Delta E = \dfrac{1}{2}(C_{min} + C_{par})V_{OUT}^2 - \dfrac{1}{2}(C_{max} + C_{par})V_{PZT}^2$.

Substituting equation A.11 into A.12 yields

Equation 7.13 $\quad \Delta E = \dfrac{1}{2}(C_{min} + C_{par})\left(\dfrac{C_{max} + C_{par}}{C_{min} + C_{par}}\right)^2 V_{PZT}^2 - \dfrac{1}{2}(C_{max} + C_{par})V_{PZT}^2$.

Simplifying results in

Equation 7.14 $\quad \Delta E = \dfrac{1}{2}V_{PZT}^2(C_{max} + C_{par})\left(\dfrac{C_{max} - C_{min}}{C_{min} + C_{par}}\right)$

that can alternatively be expressed as

Equation 7.15 $\quad \Delta E = \dfrac{1}{2}V_{PZT}V_{OUT}(C_{max} - C_{min})$.

7.3 Variable Capacitance Model

The key result of the previous section is that the scavenged energy is dependent on the change in capacitance of the variable capacitor structure. This section explores two models for capacitance.

7.3.1 Variable Capacitor with Air Gap and Mechanical Stops

Common variable capacitor structures use mechanical hard stops to prevent electrode shorting. This section models this type of device.

The capacitance of a parallel plate is defined by

Equation 7.16 $$C = \frac{\kappa \varepsilon_0 A}{d},$$

where A is the surface area, d is the distance between the plates, ε_0 is the permittivity of free space that is defined to be 8.854e-12 F/m, and κ is the dielectric constant that is defined to be 1.0005 for air.

In the electrostatic component, the model for variable capacitance is two parallel, parallel plate capacitors for each gap. The total variable capacitance is defined by

Equation 7.17 $$C_{var} = N_g \kappa \varepsilon_0 L_o h \left(\frac{1}{d-y} + \frac{1}{d+y} \right)$$

that is simplified to be

Equation 7.18 $$C_{var} = 2 N_g \kappa \varepsilon_0 L_o h \left(\frac{d}{d^2 - y^2} \right).$$

Capacitance is at its minimum when $y=0$ and is described by

Equation 7.19 $$C_{min} = \frac{2 N_g \kappa \varepsilon_0 L_o h}{d}.$$

Using this architecture, the y travel must be restricted by mechanical stops to prevent shorting of the parallel electrodes, therefore, the maximum travel is defined by

Equation 7.20 $y_{max} = d - w_{stop}$,

where w_{stop} is the width of the mechanical stop, resulting in a maximum capacitance of

Equation 7.21 $C_{max} = 2N_g \kappa \varepsilon_0 L_o h \left(\dfrac{d}{2dw_{stop} - w_{stop}^2} \right)$.

7.3.2   Variable Capacitor with Air Gap and Dielectric Coating

A novel version of the variable capacitor uses a dielectric coating on the electrodes in lieu of mechanical hard stops to prevent electrical shorting. This permits the electrodes to come in close proximity. The total variable capacitance is defined by

Equation 7.22 $C_{var} = N_g \varepsilon_0 L_o h \left(\dfrac{1}{(d-y)+2w_d\left(\dfrac{1-\kappa}{\kappa}\right)} + \dfrac{1}{(d+y)+2w_d\left(\dfrac{1-\kappa}{\kappa}\right)} \right)$

where w_d is the width of the dielectric coating. This is simplified to be

Equation 7.23 $C_{var} = 2N_g \varepsilon_0 L_o h \left(\dfrac{d + 2w_d\left(\dfrac{1-\kappa}{\kappa}\right)}{d^2 - y^2 + 4w_d\left(\dfrac{1-\kappa}{\kappa}\right)\left(d + w_d\left(\dfrac{1-\kappa}{\kappa}\right)\right)} \right)$.

The capacitance is at its minimum when $y=0$ and is described by

Equation 7.24 $C_{min} = 2N_g \varepsilon_0 L_o h \left(\dfrac{1}{d + 2w_d\left(\dfrac{1-\kappa}{\kappa}\right)} \right)$.

Using this architecture, the y travel must be restricted by dielectric coatings to prevent shorting of the parallel electrodes; therefore, the maximum travel is defined by

Equation 7.25 $y_{max} = d - 2w_d$,

resulting in a maximum capacitance of

Equation 7.26 $C_{max} = N_g \varepsilon_0 L_o h \left(\dfrac{1}{\dfrac{2w_d}{\kappa}} + \dfrac{1}{2d + 2w_d \left(\dfrac{1 - 2\kappa}{\kappa} \right)} \right)$.

7.4 Electrostatic Component Loss Models

The electrostatic component losses must be modeled and factored into the system level model. This section models both mechanical and electrical loss functions.

7.4.1   Mechanical Damping Force Functions

Fluid damping is the primary mechanical damping for the electrostatic shuttle. Couette-flow damping is the drag caused by air between two parallel plates moving in parallel to each other and is represented by

Equation 7.27 $F_{couette} = \dfrac{\mu A}{d_s} \dot{y} = \dfrac{\mu L_s W_s}{d_s} \dot{y}$,

where μ is the viscosity of air with a value of *18μPa*s* and d_s is the distance between the shuttle and the substrate. Another fluid damping mechanism is the squeeze film damping induced by the electrostatic finger parallel plates. This phenomenon is generically described by

Equation 7.28 $F_{squeeze\_film} = \dfrac{16\,\mu L W^3}{y^3} \dot{y}$

that has been adapted for this device to be

Equation 7.29 $\quad F_{squeeze\_film} = 16 N_g \mu L_o h^3 \left(\dfrac{1}{(d-y)^3} + \dfrac{1}{(d+y)^3} \right) \dot{y}$.

The mechanical damping force function for the electrostatic component is

Equation 7.30 $\quad f_{m_{electrosta\ tic}} = \left(\dfrac{\mu L_s W_s}{d_s} + 16 N_g \mu L_o h^3 \left(\dfrac{1}{(d-y)^3} + \dfrac{1}{(d+y)^3} \right) \right) \dot{y}$.

7.4.2 Electrical Damping Force Functions

The electrical damping component for the electrostatic component is a result of the

charge stored on the variable capacitor. The electrostatic force is defined by

Equation 7.31 $F_{electrosta\ tic} = \dfrac{-\partial U}{dy}$,

where U is the stored electrostatic energy on the variable capacitor and is defined by

Equation 7.32 $\quad U = \dfrac{1}{2} CV^2 = \dfrac{Q^2}{2C_{var}}$.

Since the energy conversion is charge constrained, the later form of A.32 is

utilized. Using the definition of C_{var} from A.23, the stored electrostatic energy is

Equation 7.33 $\quad U = \dfrac{Q^2 \left(d^2 - y^2 + 4 w_d \left(\frac{1-\kappa}{\kappa} \right) \left(d + w_d \left(\frac{1-\kappa}{\kappa} \right) \right) \right)}{4 N_g \varepsilon_0 L_o h \left(d + 2 w_d \left(\frac{1-\kappa}{\kappa} \right) \right)}$.

Taking the derivative with respect to the y displacement results in the electrostatic

electrical damping function as defined by

Equation 7.34 $\quad f_{e_{electrosta\ tic}}( ) = \dfrac{-\partial U}{dy} = \dfrac{Q^2}{2 N_g \varepsilon_0 L_o h \left(d + 2 w_d \left(\frac{1-\kappa}{\kappa} \right) \right)} y$.

8   Appendix B: In-Plane Piezoelectric Models

The electrostatic proof mass is suspended by several piezoelectric springs. These springs are comprised of beams that make a folded flexure beam structure as illustrated in Figure 8.1.
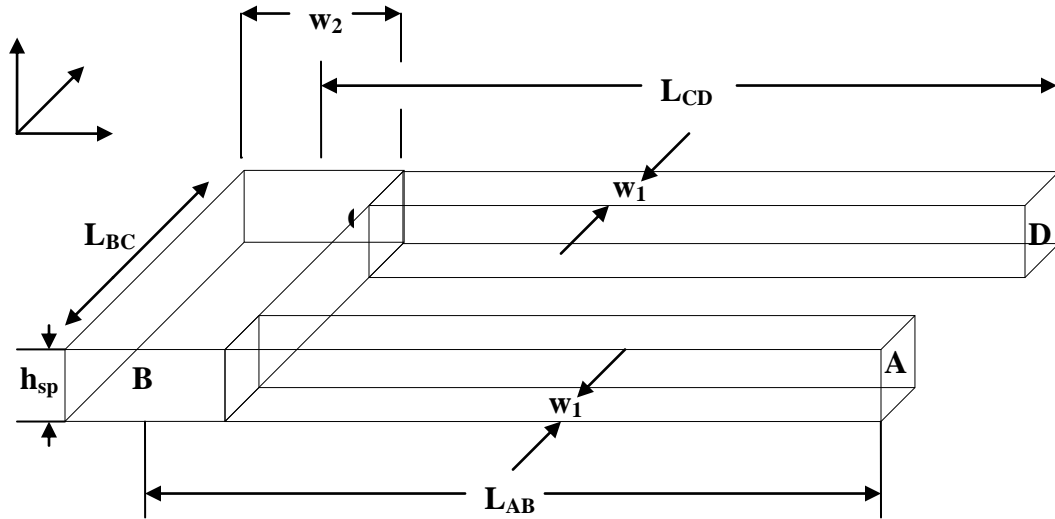
Figure 8.1 Model diagram of single folded spring

8.1   Piezoelectric Spring Displacement Model

The initial model for the piezoelectric spring addresses the displacement within the spring due to movement of a proof mass [43]. The displacement due to the movement of the proof mass by an applied force can be determined using Castigliano's 2nd theorem and internal energies. Castigliano's 2nd theorem describes a method for calculating displacement at a point in a body with respect to the strain energy stored in the body that applies to linearly elastic materials at a constant temperature. These conditions are assumed to be met by the piezoelectric materials used for the spring in the hybrid vibration scavenger.

8.1.1 Castigliano's Second Theorem

Castigliano's theorem states that if a body is subjected to external forces, then the external work as a function of the external forces, W_e is equal to the internal strain energy of the body, U_i as defined by

Equation 8.1 $\quad U_i = W_e = W_e(F_1, F_2, ..., F_n)$.

If one of the forces is increased by dF_k, the work and therefore the internal strain energy will also increase as described by

Equation 8.2 $\quad U_i + dU_k = W_e + dW_k = U_i + \dfrac{\partial U_i}{\partial F_k} dF_k$.

To achieve applied force order independence, $\triangle_k$ is introduced as the total displacement in the direction of F_k of the body due to all of the forces and is defined in

Equation 8.3 $\quad dU_k = dF_k \Delta_k = \dfrac{\partial U_i}{\partial F_k} dF_k$.

Therefore, the displacement can be defined by

Equation 8.4 $\quad \Delta_k = \dfrac{\partial U_i}{\partial F_k}$.

8.1.2 Internal Strain Energies, U_i

The internal strain energy of a beam, U_i is comprised of several strain energy components. These are strain energy components are due to axial loading, bending moment, transverse shear, and torsion moment and can be combined as described by

Equation 8.5 $\quad U_{int\,ernal} = U_{AxialLoadi\,ng} + U_{BendingMom\,ent} + U_{Transverse\ Shear} + U_{TorsionMom\,ent}$.

The strain energy due to axial loading of a beam of length L, is defined by

Equation 8.6 $U_{AxialLoading} = U_{AL} = \int_0^L \frac{N^2}{2AE} dx$,

where N is the axial force (load), A is the cross sectional area, E is the modulus of elasticity (Young's modulus), and L is the length of the beam.

The strain energy due to bending moment in a beam of length L, is determined by

Equation 8.7 $U_{BendingMoment} = U_{BM} = \int_0^L \frac{M^2}{2EI} dx$,

where M is the bending moment and I is the area moment of inertia for the beam cross section.

The strain energy due to transverse shear loading in a beam of length L, is

Equation 8.8 $U_{Transverse\ Shear} = U_{TS} = \int_0^L \frac{k_{y,z} \cdot V^2}{2GA} dx$,

where $k_{y,z}$ is the shape factor of 1.20 for a rectangle, V is the shear force, and G is the shear modulus that is defined by

Equation 8.9 $G = \frac{E}{2(1 + \upsilon)}$

where υ is Poisson's ratio.

The strain energy due to torsion moment in a beam of length L, is defined by

Equation 8.10 $U_{TorsionMoment} = U_{TM} = \int_0^L \frac{T^2}{2GJ} dx$,

where T is the torque of the beam and J is the polar moment of inertia for the beam cross section.

163

8.1.3 Internal Strain Energy for a Folded Flexure Spring

Since the superimposition principle applies to this problem, the components of the spring can be logically parsed into separate beams, forming three beams denoted as AB, BC, and CD. The internal strain energies and therefore displacement, by Castigliano's 2nd theorem, can be determined for each beam individually and then be superimposed for the final solution as described by

Equation 8.11 $U_i = U_{AB} + U_{BC} + U_{CD}$.

8.1.4 Reaction Forces and Moments

The first step to solving for the internal strain energies is to define the reaction forces and associated reaction moments within the beam or folded flexure spring. To begin, the structure is considered to be at equilibrium. To be at equilibrium, the structure must satisfy the two conditions of equilibrium, translational and rotational.

In translational equilibrium, the structure will not experience linear acceleration; therefore, the vector sum of all external forces must be zero as shown in

Equation 8.12 $\sum F_x = 0$,

Equation 8.13 $\sum F_y = 0$,

Equation 8.14 $\sum F_z = 0$.

In rotational equilibrium, the sum of the torques (bending moments) acting on any point in the structure must be zero as described in

Equation 8.15 $\sum M_x = 0$,

Equation 8.16 $\sum M_y = 0$,

Equation 8.17 $\sum M_z = 0$.

To solve the static equilibrium problem, the following methodology will be used:

Step 1: Draw free body diagram (FBD) of entire structure showing external forces

Step 2: Resolve all forces into axial components

Step 3: Apply the equilibrium conditions and solve for unknown forces and moments

Step 4: Draw a FBD of a member(s) of the structure of interest and repeat Steps 1-3.

8.2   Reaction Forces and Moments for Folded Flexure

A free body diagram for the entire folded flexure is illustrated in Figure 8.2.
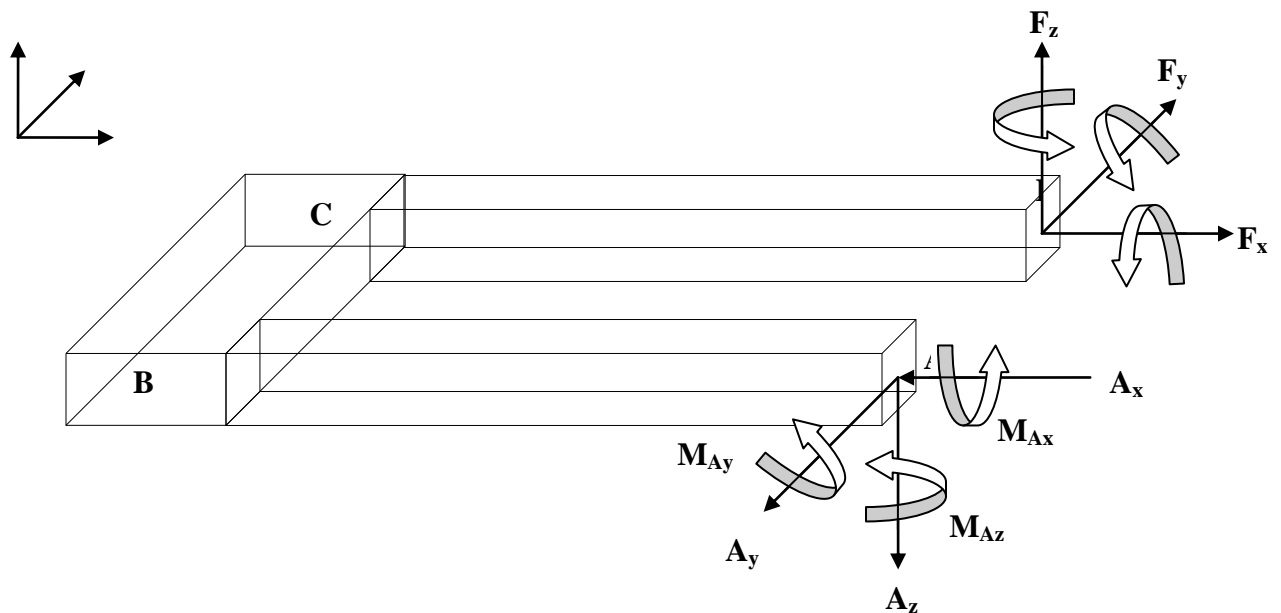
Figure 8.2 3-axis free body diagram (FBD) of folded flexure structure

The structure is supported (anchored) at point *A* and has the resulting forces and moments as listed. The proof mass is connected at point *D* with the resulting forces and moments as shown. It is assumed that the movement of the mass is linear and does not experience any rotation and is rigidly connected to point *D*.

In order to accurately define the moments of the structure, the FBD is projected into two-dimensional drawings for simplicity. Also, to reduce confusion, the

165

following sign conventions are maintained when working from the left side of the structure:

(1) Shear force is considered positive if it tends to bend the beam section clockwise.

(2) Bending moment is positive if it tends to bend the beam section concave (facing upward).

The sign of the forces and moments are labeled in the projection figures. Finally, the moments are defined by the magnitude of the force multiplied by the perpendicular distance from the pivot point.
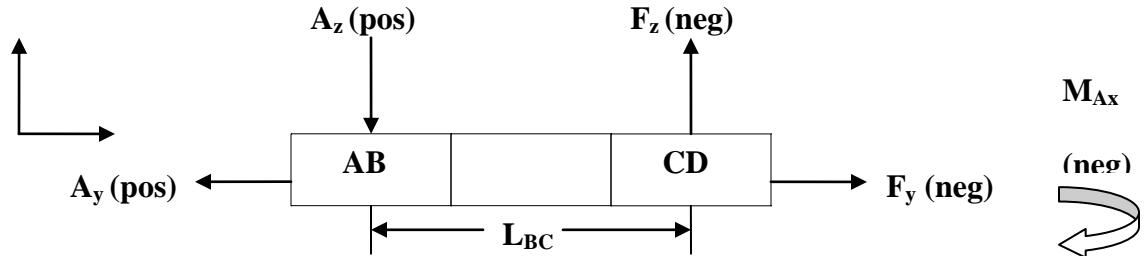
Figure 8.3 X-projection of free body diagram of folded spring

In Figure 8.3, the pivot point is *A* since the folded flexure is anchored at that point. The static equilibrium force and moment relations for Figure 8.3 are provided in

Equation 8.18 $\Sigma F_z = 0 = A_z - F_z$,

Equation 8.19 $F_z = A_z$,

Equation 8.20 $\Sigma F_y = 0 = A_y - F_y$,

Equation 8.21 $F_y = A_y$,

Equation 8.22 $\Sigma M_{xA} = 0 = A_y 0 - F_y 0 + A_z 0 - F_z (L_{BC}) - M_{Ax}$,

Equation 8.23 $M_{Ax} = -F_z L_{BC}$.
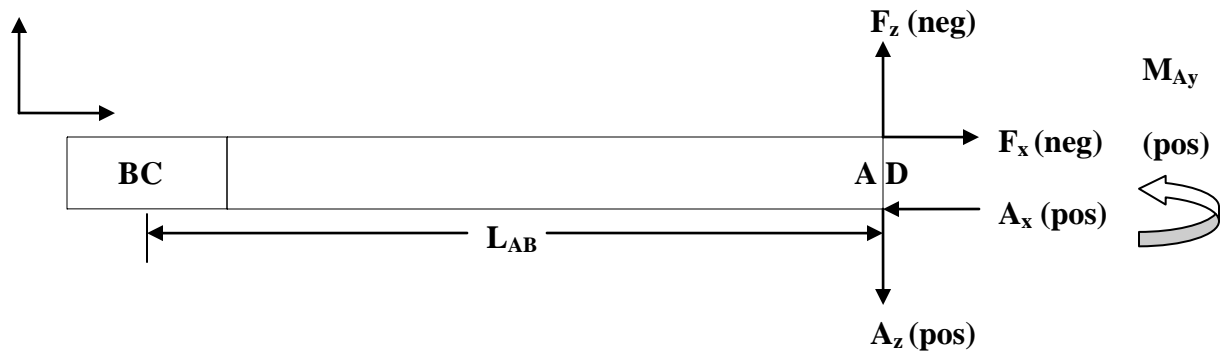
Figure 8.4 Y-projection of free body diagram of folded spring

In Figure 8.4, it is important to note that L_{AB} does not necessarily equal L_{CD} and thus the delta of the lengths does have some effect on the moments. The static equilibrium force and moment relations for Figure 8.4 are provided in

Equation 8.24 $\quad \sum F_x = 0 = A_x - F_x$,

Equation 8.25 $\quad F_x = A_x$,

Equation 8.26 $\quad \sum M_{yA} = 0 = A_x 0 - F_x 0 + A_z 0 - F_z \left(L_{CD} - L_{AB} \right) + M_{Ay}$,

Equation 8.27 $\quad M_{Ay} = F_z \left(L_{CD} - L_{AB} \right)$.
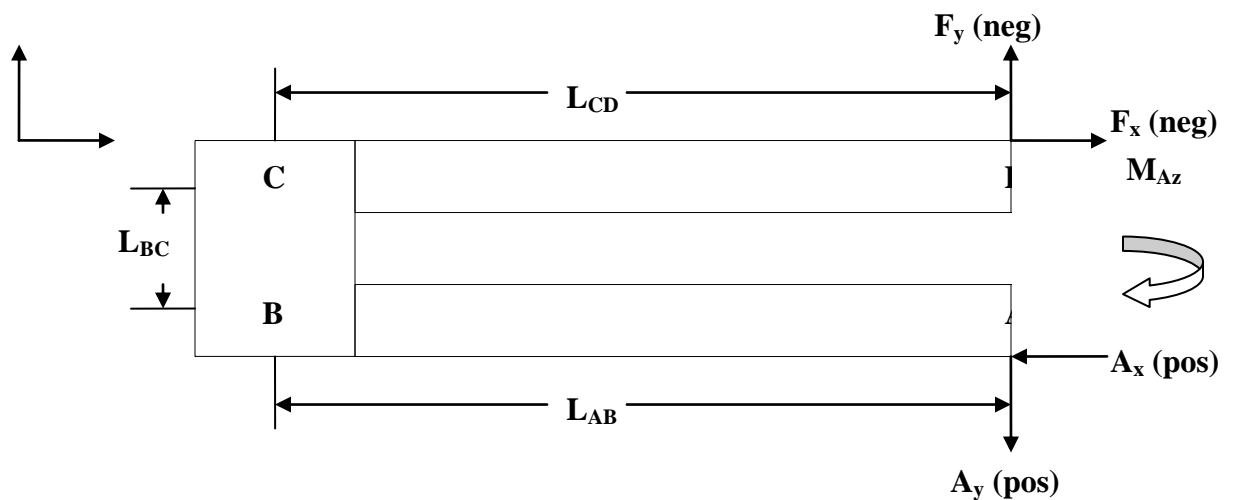
Figure 8.5 Z-projection of free body diagram of folded spring

The static equilibrium force and moment relations for Figure 8.5 are provided in

Equation 8.28 $\quad \sum M_{zA} = 0 = A_x 0 - F_x L_{BC} + A_y 0 - F_y \left(L_{CD} - L_{AB} \right) - M_{Az}$,

Equation 8.29 $\quad M_{Az} = -F_x L_{BC} + F_y \left(L_{AB} - L_{CD} \right)$.

8.3 Displacement at Point B

To determine the displacement at point *B*, the forces and moments for section *AB* and the member of section *AB* must be determined. This will provide the essential relationships to derive the displacement via Castigliano's theorem.

8.3.1 Reaction Forces and Moments for Section AB

To determine the displacement of point *B*, one must define the reaction forces and moments in effect at the point of interest. Figure 8.6 is the free body diagram for the entire beam that is the section *AB*.
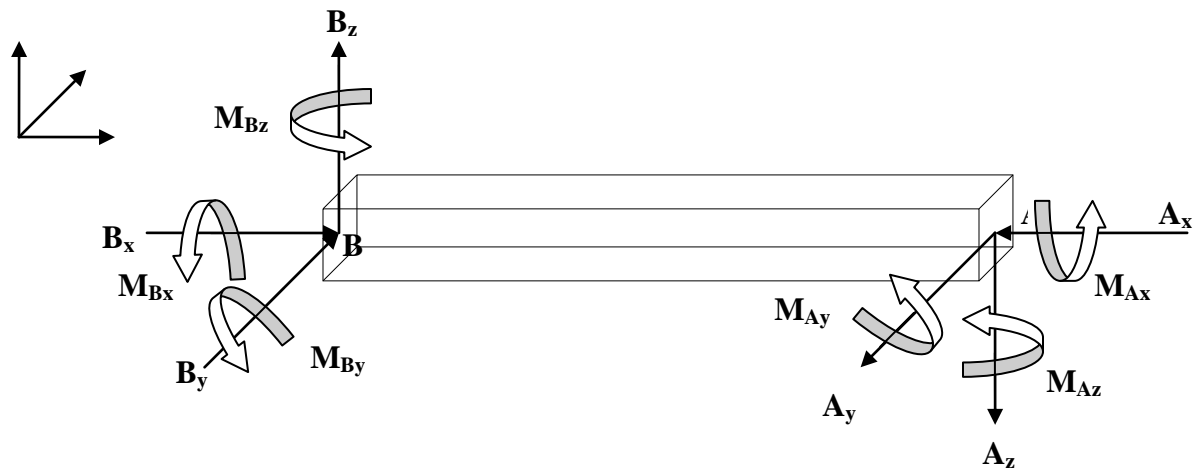
Figure 8.6 3-axis free body diagram for section AB

Analogous to Section B.2, the free body diagrams are projected to two-dimensions to assist in the proper determination of reaction forces and moments and the associated sign conventions.
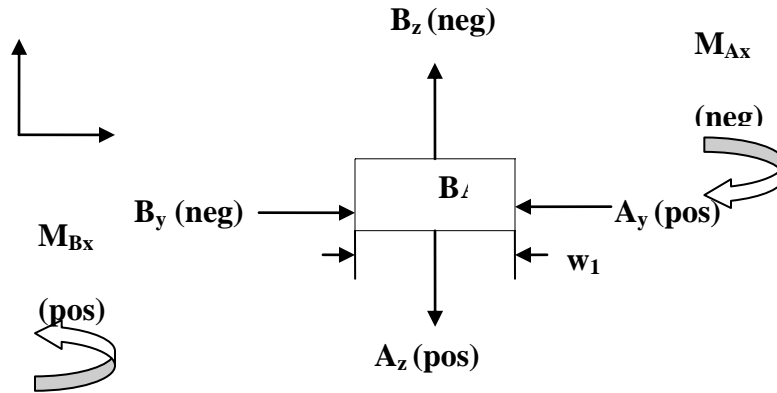
Figure 8.7 X-projection of free body diagram of section AB

In Figure 8.7, point *B* becomes the pivot point. From the projected free body diagram, the reaction forces and moments are derived as shown in

Equation 8.30 $\sum F_z = 0 = A_z - B_z$,

Equation 8.31 $B_z = A_z = F_z$,

Equation 8.32 $\sum F_y = 0 = A_y - B_y$,

Equation 8.33 $B_y = A_y = F_y$,

Equation 8.34 $\sum M_{xB} = 0 = M_{Bx} + A_y 0 - B_y 0 + A_z 0 - B_z 0 - M_{Ax}$,

Equation 8.35 $M_{Bx} = M_{Ax} = -F_z L_{BC}$.
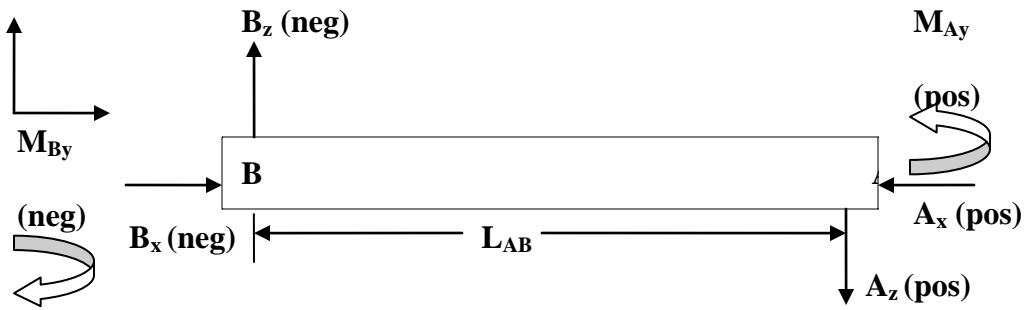
Figure 8.8 Y-projection of free body diagram of section AB

From the projected free body diagram in Figure 8.8, the reaction forces and moments are derived as shown in

Equation 8.36 $\Sigma F_x = 0 = A_x - B_x$,

Equation 8.37 $B_x = A_x = F_x$,

Equation 8.38 $\Sigma M_{yB} = 0 = -M_{By} + A_x 0 - B_x 0 + A_z L_{AB} - B_z 0 + M_{Ay}$,

Equation 8.39 $M_{By} = M_{Ay} + A_z L_{AB} = F_z L_{CD}$.
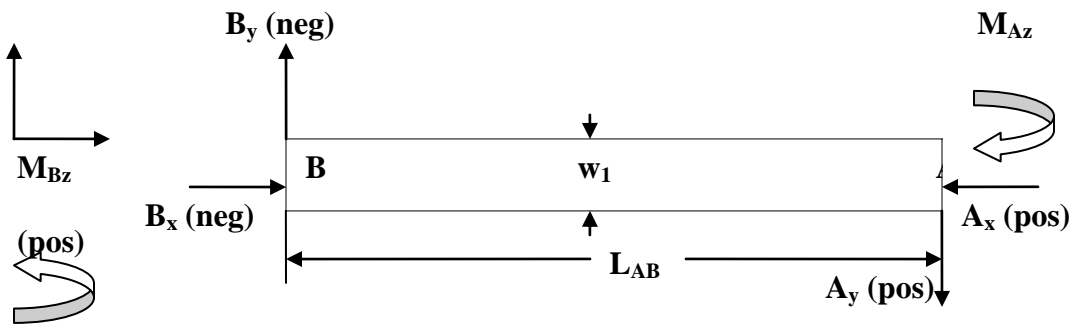
Figure 8.9 Z-projection of free body diagram of section AB

Finally, from the projected free body diagram in Figure 8.9, the remaining reaction forces and moments are derived as shown in

Equation 8.40 $\Sigma M_{zB} = 0 = M_{Bz} + A_x L_{AB} - B_x 0 + A_y 0 - B_y 0 - M_{Az}$,

Equation 8.41 $M_{Bz} = M_{Az} - A_x L_{AB} = -F_x L_{CD} - F_y L_{BC}$.

8.3.2   Reaction Forces and Moments for a Member of Section AB

To determine the displacement of point *B*, one must define the reaction forces and moments in effect all points along the entire length of the beam. Figure 8.10 is the free body diagram for a member of beam that is contained within the section *AB* that is arbitrarily cut at some length *x*.
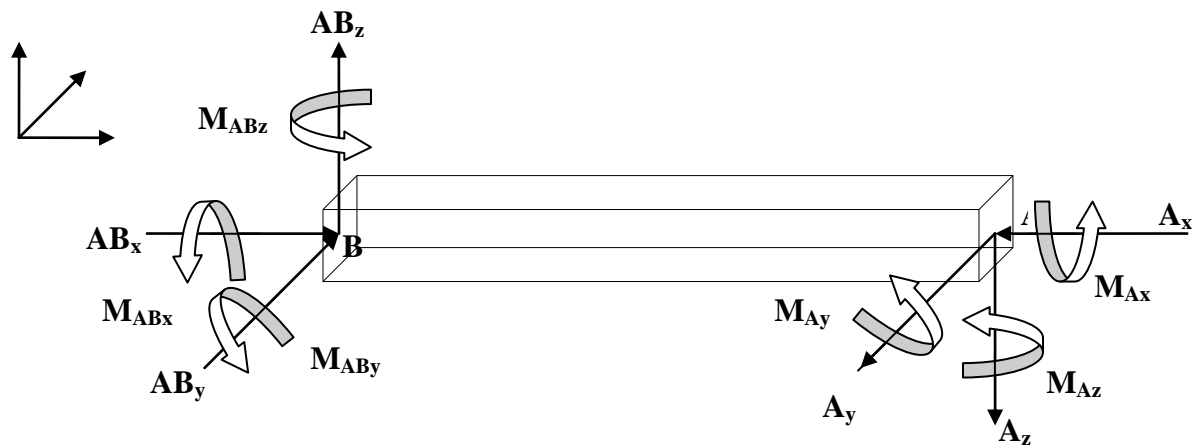
Figure 8.10 3-axis free body diagram for a member of section AB

Using the identical approach presented in Section B.2 and B.3.1, the reaction forces and moments are defined by projections of the free body diagram in Figure 8.11 through Figure 8.13.

In Figure 8.11, point *AB* becomes the pivot point of interest. From the projected free body diagram, the reaction forces and moments are derived as shown in

Equation 8.42 $\Sigma F_z = 0 = A_z - AB_z$,

Equation 8.43 $AB_z = A_z = F_z$,

Equation 8.44 $\Sigma F_y = 0 = A_y - AB_y$,

171

Equation 8.45 $AB_y = A_y = F_y$,

Equation 8.46 $\Sigma M_{xAB} = 0 = M_{ABx} + A_y 0 - B_y 0 + A_z 0 - B_z 0 - M_{Ax}$,

Equation 8.47 $M_{ABx} = M_{Ax} = -F_z L_{BC}$.
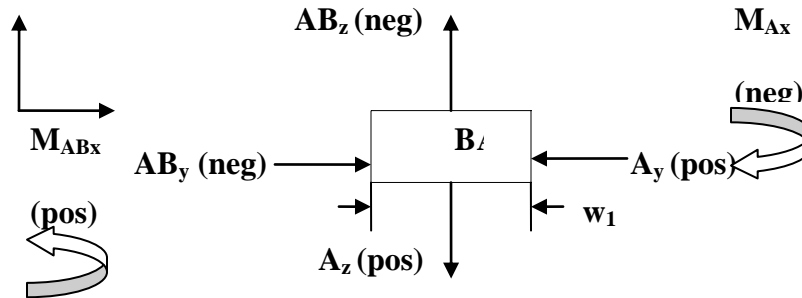
Figure 8.11 X-projection of free body diagram of member of section AB
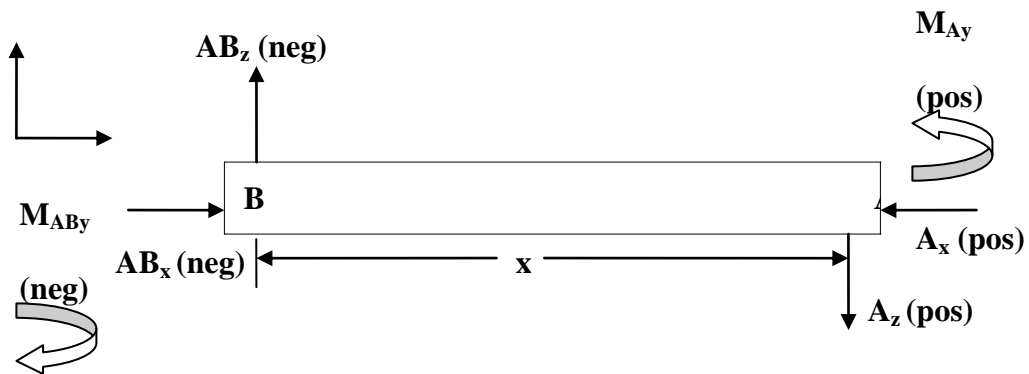
Figure 8.12 Y-projection of free body diagram of member of section AB

From the projected free body diagram in Figure 8.12, the reaction forces and moments are derived as shown in

Equation 8.48 $\Sigma F_x = 0 = A_x - AB_x$,

Equation 8.49 $AB_x = A_x = F_x$,

Equation 8.50 $\Sigma M_{yAB} = 0 = -M_{ABy} + A_x 0 - AB_x 0 + A_z x - AB_z 0 + M_{Ay}$,

Equation 8.51 $M_{ABy} = M_{Ay} + A_z x = F_z \left(L_{CD} - L_{AB} + x \right)$.

172
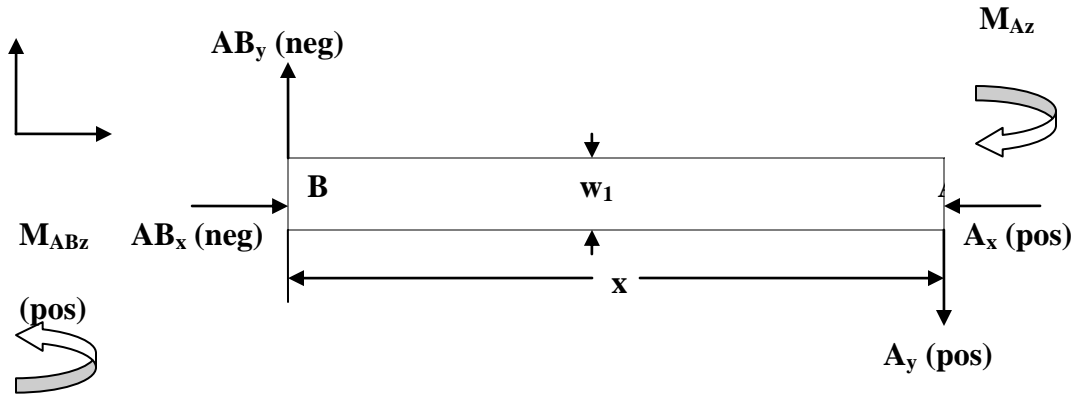
Figure 8.13 Z-projection of free body diagram of member of section AB

Finally, from the projected free body diagram in Figure 8.13, the remaining reaction forces and moments are derived as shown in

Equation 8.52 $\quad \Sigma M_{zAB} = 0 = M_{ABz} + A_x 0 - AB_x 0 + A_y x - AB_y 0 - M_{Az}$,

Equation 8.53 $\quad M_{ABz} = M_{Az} - A_y x = -F_x L_{BC} + F_y (L_{AB} - L_{CD} - x)$.

8.3.3 Summary of Reaction Forces and Moments of Interest

A summary of derived reaction forces and moments that are utilized for calculating the various strain energies for section *AB* are shown in

Equation 8.54 $\quad N_{AB} = AB_x = F_x$,

Equation 8.55 $\quad M_{ABy} = F_z (L_{CD} - L_{AB} + x)$,

Equation 8.56 $\quad M_{ABz} = -F_x L_{BC} + F_y (L_{AB} - L_{CD} - x)$,

Equation 8.57 $\quad V_{ABy} = AB_y = F_y$,

Equation 8.58 $\quad V_{ABz} = AB_z = F_z$,

Equation 8.59 $\quad T_{AB} = M_{ABx} = -F_z L_{BC}$.

8.3.4   Derivation of the Deformations at Point B

The strain energy within the section AB is defined by

Equation 8.60

$$U_{AB} = \int_0^{L_{AB}} \frac{N_{AB}^2}{2A_bE}dx + \int_0^{L_{AB}} \frac{M_{ABy}^2}{2EI_{bz}}dx + \int_0^{L_{AB}} \frac{M_{ABz}^2}{2EI_{bz}}dx + \int_0^{L_{AB}} \frac{6V_{ABy}^2}{10GA_b}dx + \int_0^{L_{AB}} \frac{6V_{ABz}^2}{10GA_b}dx + \int_0^{L_{AB}} \frac{T_{AB}^2}{2GJ_b}dx \;).$$

The displacement in the x-direction at point B due to force F_x is defined by Castigliano's 2nd theorem in

Equation 8.61 $\dfrac{\partial}{\partial F_x} U_{AB} = \Delta_{Bx}$.

Combining B.60 and B.61 and taking the partial derivative results in

$$\Delta_{Bx} = \int_0^{L_{AB}} \frac{N_{AB}}{A_bE}\left(\frac{\partial}{\partial F_x}N_{AB}\right)dx + \int_0^{L_{AB}} \frac{M_{ABy}}{EI_{bz}}\left(\frac{\partial}{\partial F_x}M_{ABy}\right)dx + \int_0^{L_{AB}} \frac{M_{ABz}}{EI_{bz}}\left(\frac{\partial}{\partial F_x}M_{ABz}\right)dx +$$

Equation 8.62 $\int_0^{L_{AB}} \dfrac{6V_{ABy}}{5GA_b}\left(\dfrac{\partial}{\partial F_x}V_{ABy}\right)dx + \int_0^{L_{AB}} \dfrac{6V_{ABz}}{5GA_b}\left(\dfrac{\partial}{\partial F_x}V_{ABz}\right)dx + \int_0^{L_{AB}} \dfrac{T_{AB}}{GJ_b}\left(\dfrac{\partial}{\partial F_x}T_{AB}\right)dx$,

which can be further simplified to

Equation 8.63 $\Delta_{Bx} = \int_0^{L_{AB}} \dfrac{F_x}{A_bE}(1)dx + \int_0^{L_{AB}} \dfrac{-F_xL_{BC} + F_y(L_{AB} - L_{CD} - x)}{EI_{bz}}(-L_{BC})dx$ ..

Finally, by integrating over the length of section AB, the displacement is

Equation 8.64 $\Delta_{Bx} = \dfrac{F_yL_{AB}}{A_bE} + \dfrac{F_xL_{BC}^2L_{AB}}{EI_{bz}} - \dfrac{F_yL_{BC}}{2EI_{bz}}\left(L_{AB}^2 - 2L_{CD}L_{AB}\right)$.

Similarly, the displacement in the y-direction at point B due to force F_y is defined by Castigliano's 2nd theorem in

Equation 8.65 $\dfrac{\partial}{\partial F_y} U_{AB} = \Delta_{By}$.

Taking the partial derivative results in

$$\Delta_{By} = \int_0^{L_{AB}} \frac{N_{AB}}{A_b E}\left(\frac{\partial}{\partial F_y}N_{AB}\right)dx + \int_0^{L_{AB}} \frac{M_{ABy}}{EI_{bz}}\left(\frac{\partial}{\partial F_y}M_{ABy}\right)dx + \int_0^{L_{AB}} \frac{M_{ABz}}{EI_{bz}}\left(\frac{\partial}{\partial F_y}M_{ABz}\right)dx +$$

Equation 8.66

$$\int_0^{L_{AB}} \frac{6V_{ABy}}{5GA_b}\left(\frac{\partial}{\partial F_y}V_{ABy}\right)dx + \int_0^{L_{AB}} \frac{6V_{ABz}}{5GA_b}\left(\frac{\partial}{\partial F_y}V_{ABz}\right)dx + \int_0^{L_{AB}} \frac{T_{AB}}{GJ_b}\left(\frac{\partial}{\partial F_y}T_{AB}\right)dx$$

,

which can be further simplified to

Equation 8.67
$$\Delta_{By} = \int_0^{L_{AB}} \frac{-F_x L_{BC} + F_y\left(L_{AB} - L_{CD} - x\right)}{EI_{bz}}\left(L_{AB} - L_{CD} - x\right)dx + \int_0^{L_{AB}} \frac{6F_y}{5GA_b}dx \quad ..$$

Finally, by integrating over the length of section *AB*, the displacement is

Equation 8.68
$$\Delta_{By} = -\frac{F_x L_{BC}}{2EI_{bz}}\left(L_{AB}^2 - 2L_{CD}L_{AB}\right) + \frac{F_y}{3EI_{bz}}\left(L_{AB}^3 - 3L_{CD}L_{AB}^2 + 3L_{CD}^2 L_{AB}\right) + \frac{6F_y L_{AB}}{5GA_b}\quad.$$

Finally, the displacement in the *z*-direction at point *B* due to force F_z is defined by Castigliano's 2nd theorem in

Equation 8.69 $\dfrac{\partial}{\partial F_z}U_{AB} = \Delta_{Bz}$,

Taking the partial derivative results in

$$\Delta_{Bz} = \int_0^{L_{AB}} \frac{N_{AB}}{A_b E}\left(\frac{\partial}{\partial F_z}N_{AB}\right)dx + \int_0^{L_{AB}} \frac{M_{ABy}}{EI_{by}}\left(\frac{\partial}{\partial F_z}M_{ABy}\right)dx + \int_0^{L_{AB}} \frac{M_{ABz}}{EI_{by}}\left(\frac{\partial}{\partial F_z}M_{ABz}\right)dx +$$

Equation 8.70

$$\int_0^{L_{AB}} \frac{6V_{ABy}}{5GA_b}\left(\frac{\partial}{\partial F_z}V_{ABy}\right)dx + \int_0^{L_{AB}} \frac{6V_{ABz}}{5GA_b}\left(\frac{\partial}{\partial F_z}V_{ABz}\right)dx + \int_0^{L_{AB}} \frac{T_{AB}}{GJ_b}\left(\frac{\partial}{\partial F_z}T_{AB}\right)dx$$

which can be further simplified to

Equation 8.71
$$\Delta_{Bz} = \int_0^{L_{AB}} \frac{F_z\left(L_{CD} - L_{AB} + x\right)}{EI_{by}}\left(L_{CD} - L_{AB} + x\right)dx + \int_0^{L_{AB}} \frac{6F_z}{5GA_b}(1)dx + \int_0^{L_{AB}} \frac{-F_z L_{BC}}{GJ_b}\left(-L_{BC}\right)dx \quad.$$

Finally, by integrating over the length of section *AB*, the displacement is

Equation 8.72
$$\Delta_{Bz} = \frac{F_z}{3EI_{by}}\left(L_{AB}^3 - 3L_{CD}L_{AB}^2 + 3L_{CD}^2 L_{AB}\right) + \frac{6F_z L_{AB}}{5GA_b} + \frac{F_z L_{BC}^2 L_{AB}}{GJ_b}\quad.$$

8.4 Displacement at Point C

Analogous to Section B.3, the derivation of the displacement of point C considers the bending of section BC.

8.4.1 Derivation of the Deformations at Point C

The strain energy within the section *BC* is defined by

$$\text{Equation 8.73} \quad U_{BC} = \int_0^{L_{BC}} \frac{N_{BC}^2}{2A_cE}dy + \int_0^{L_{BC}} \frac{M_{BCx}^2}{2EI_{cz}}dy + \int_0^{L_{BC}} \frac{M_{BCz}^2}{2EI_{cz}}dy + \int_0^{L_{BC}} \frac{6V_{BCx}^2}{10GA_c}dy + \int_0^{L_{BC}} \frac{6V_{BCz}^2}{10GA_c}dy + \int_0^{L_{BC}} \frac{T_{BC}^2}{2GJ_c}dy \quad .$$

The displacement in the *x*-direction at point *C* due to force F_x is defined again by Castigliano's theorem and added to displacement of point *B* by superimposition in

$$\text{Equation 8.74} \quad \frac{\partial}{\partial F_x}U_{AC} = \frac{\partial}{\partial F_x}\left(U_{AB} + U_{BC}\right) = \Delta_{Bx} + \frac{\partial}{\partial F_x}U_{BC} = \Delta_{Cx} \quad .$$

Combining B.73 and B.74 and taking the partial derivative results in

$$\text{Equation 8.75} \quad \begin{aligned} \Delta_{Cx} = \Delta_{Bx} + &\int_0^{L_{BC}} \frac{N_{BC}}{A_cE}\left(\frac{\partial}{\partial F_x}N_{BC}\right)dy + \int_0^{L_{BC}} \frac{M_{BCx}}{EI_{cz}}\left(\frac{\partial}{\partial F_x}M_{BCx}\right)dy + \int_0^{L_{BC}} \frac{M_{BCz}}{EI_{cz}}\left(\frac{\partial}{\partial F_x}M_{BCz}\right)dy + \\ &\int_0^{L_{BC}} \frac{6V_{BCx}}{5GA_c}\left(\frac{\partial}{\partial F_x}V_{BCx}\right)dy + \int_0^{L_{BC}} \frac{6V_{BCz}}{5GA_c}\left(\frac{\partial}{\partial F_x}V_{BCz}\right)dy + \int_0^{L_{BC}} \frac{T_{BC}}{GJ_c}\left(\frac{\partial}{\partial F_x}T_{BC}\right)dy \end{aligned} \quad ,$$

which can be further simplified to

$$\text{Equation 8.76} \quad \Delta_{Cx} = \Delta_{Bx} + \int_0^{L_{BC}} \frac{F_x(y - L_{BC}) - F_yL_{CD}}{EI_{cz}}(y - L_{BC})dy + \int_0^{L_{BC}} \frac{6F_x}{5GA_c}(1)dy \quad .$$

Finally, by integrating over the length of section *BC*, the displacement is

$$\text{Equation 8.77} \quad \Delta_{Cx} = \Delta_{Bx} + \frac{F_xL_{BC}^3}{3EI_{cz}} + \frac{F_yL_{BC}^2L_{CD}}{2EI_{cz}} + \frac{6F_xL_{BC}}{5GA_c} \quad .$$

Similarly, the displacement in the *y*-direction at point *C* due to force F_y is defined by Castigliano's 2nd theorem and superimposition in

Equation 8.78
$$\frac{\partial}{\partial F_y} U_{AC} = \frac{\partial}{\partial F_y}\left(U_{AB} + U_{BC}\right) = \Delta_{By} + \frac{\partial}{\partial F_y} U_{BC} = \Delta_{Cy} .$$

Taking the partial derivative results in

Equation 8.79
$$\Delta_{Cy} = \Delta_{By} + \int_0^{L_{BC}} \frac{N_{BC}}{A_c E}\left(\frac{\partial}{\partial F_y} N_{BC}\right)dy + \int_0^{L_{BC}} \frac{M_{BCx}}{EI_{cz}}\left(\frac{\partial}{\partial F_y} M_{BCx}\right)dy + \int_0^{L_{BC}} \frac{M_{BCz}}{EI_{cz}}\left(\frac{\partial}{\partial F_y} M_{BCz}\right)dy +$$
$$\int_0^{L_{BC}} \frac{6V_{BCx}}{5GA_c}\left(\frac{\partial}{\partial F_y} V_{BCx}\right)dy + \int_0^{L_{BC}} \frac{6V_{BCz}}{5GA_c}\left(\frac{\partial}{\partial F_y} V_{BCz}\right)dy + \int_0^{L_{BC}} \frac{T_{BC}}{GJ_c}\left(\frac{\partial}{\partial F_y} T_{BC}\right)dy ,$$

which can be further simplified to

Equation 8.80
$$\Delta_{Cy} = \Delta_{By} + \int_0^{L_{BC}} \frac{F_y}{A_c E}(1)dy + \int_0^{L_{BC}} \frac{F_x(y - L_{BC}) - F_y L_{CD}}{EI_{cz}}(-L_{CD})dy \ ..$$

By integrating over the length of section BC, the displacement is

Equation 8.81
$$\Delta_{Cy} = \Delta_{By} + \frac{F_y L_{BC}}{A_c E} + \frac{F_x L_{BC}^{\,2} L_{CD}}{2EI_{cz}} + \frac{F_y L_{CD}^{\,2} L_{BC}}{EI_{cz}} .$$

Finally, the displacement in the z-direction at point C due to force F_z is defined by Castigliano's 2nd theorem and superimposition in

Equation 8.82
$$\frac{\partial}{\partial F_z} U_{AC} = \frac{\partial}{\partial F_z}\left(U_{AB} + U_{BC}\right) = \Delta_{Bz} + \frac{\partial}{\partial F_z} U_{BC} = \Delta_{Cz} .$$

Taking the partial derivative results in

Equation 8.83
$$\Delta_{Cz} = \Delta_{Bz} + \int_0^{L_{BC}} \frac{N_{BC}}{A_c E}\left(\frac{\partial}{\partial F_z} N_{BC}\right)dy + \int_0^{L_{BC}} \frac{M_{BCx}}{EI_{cx}}\left(\frac{\partial}{\partial F_z} M_{BCx}\right)dy + \int_0^{L_{BC}} \frac{M_{BCz}}{EI_{cx}}\left(\frac{\partial}{\partial F_z} M_{BCz}\right)dy +$$
$$\int_0^{L_{BC}} \frac{6V_{BCx}}{5GA_c}\left(\frac{\partial}{\partial F_z} V_{BCx}\right)dy + \int_0^{L_{BC}} \frac{6V_{BCz}}{5GA_c}\left(\frac{\partial}{\partial F_z} V_{BCz}\right)dy + \int_0^{L_{BC}} \frac{T_{BC}}{GJ_c}\left(\frac{\partial}{\partial F_z} T_{BC}\right)dy ,$$

which can be further simplified to

Equation 8.84
$$\Delta_{Cz} = \Delta_{Bz} + \int_0^{L_{BC}} \frac{F_z(y - L_{BC})}{EI_{cx}}(y - L_{BC})dy + \int_0^{L_{BC}} \frac{6F_z}{5GA_c}(1)dy + \int_0^{L_{BC}} \frac{F_z L_{CD}}{GJ_c}(L_{CD})dy .$$

Finally, by integrating over the length of section BC, the displacement is

Equation 8.85 $\Delta_{Cz} = \Delta_{Bz} + \dfrac{F_z L_{BC}^{\ 3}}{3EI_{cx}} + \dfrac{6F_z L_{BC}}{5GA_c} + \dfrac{F_z L_{CD}^{\ 2} L_{BC}}{GJ_c}$.

8.5   Displacement at Point D

To determine the displacement at point *D*, the forces and moments for section *CD* and the member of section *CD* must be determined. This will provide the essential relationships to derive the displacement via Castigliano's theorem.   By superimposition, the displacements of points *B* and *C* will be summed to determine the complete displacement of the spring.

8.5.1   Summary of the Deformations at Point D

The displacement of point *D* is defined by

Equation 8.86 $\Delta_{Dx} = \Delta_{Cx} + \dfrac{F_x L_{CD}}{A_b E}$,

Equation 8.87 $\Delta_{Dy} = \Delta_{Cy} + \dfrac{F_y L_{CD}^{\ 3}}{3EI_{bz}} + \dfrac{6F_y L_{CD}}{5GA_b}$,

Equation 8.88 $\Delta_{Dz} = \Delta_{Cz} + \dfrac{F_z L_{CD}^{\ 3}}{3EI_{by}} + \dfrac{6F_z L_{CD}}{5GA_b}$.

The expanded equations for the spring displacement at point *D* are

Equation 8.89 $\Delta_{Dx} = F_x\left(\dfrac{L_{BC}^{\ 3}}{3EI_{cz}} + \dfrac{L_{BC}^{\ 2}L_{AB}}{EI_{bz}} + \dfrac{6L_{BC}}{5GA_c} + \dfrac{L_{CD}}{A_b E}\right) + F_y\left(\dfrac{L_{BC}^{\ 2}L_{CD}}{2EI_{cz}} - \dfrac{L_{BC}}{2EI_{bz}}\left(L_{AB}^{\ 2} - 2L_{CD}L_{AB}\right) + \dfrac{L_{AB}}{A_b E}\right)$,

Equation 8.90
$$\Delta_{Dy} = F_x\left(\dfrac{L_{BC}^{\ 2}L_{CD}}{2EI_{cz}} - \dfrac{L_{BC}}{2EI_{bz}}\left(L_{AB}^{\ 2} - 2L_{CD}L_{AB}\right)\right) +$$
$$F_y\left(\dfrac{1}{3EI_{bz}}\left(L_{AB}^{\ 3} - 3L_{CD}L_{AB}^{\ 2} + 3L_{CD}^{\ 2}L_{AB}\right) + \dfrac{L_{CD}^{\ 3}}{3EI_{bz}} + \dfrac{L_{CD}^{\ 2}L_{BC}}{EI_{cz}} + \dfrac{6L_{CD}}{5GA_b} + \dfrac{L_{BC}}{A_c E} + \dfrac{6L_{AB}}{5GA_b}\right)$$,

Equation 8.91

$$\Delta_{Dz} = F_z \left(\begin{array}{l} \dfrac{1}{3EI_{by}}\left(L_{AB}{}^3 - 3L_{CD}L_{AB}{}^2 + 3L_{CD}{}^2 L_{AB}\right) + \\[2em] \dfrac{L_{CD}{}^3}{3EI_{by}} + \dfrac{L_{CD}{}^2 L_{BC}}{GJ_c} + \dfrac{6L_{CD}}{5GA_b} + \dfrac{L_{BC}{}^3}{3EI_{cx}} + \dfrac{L_{BC}{}^2 L_{AB}}{GJ_b} + \dfrac{6L_{BC}}{5GA_c} + \dfrac{6L_{AB}}{5GA_b} \end{array} \right) ,$$

where the cross-sectional area of sections *AB* and *CD*, denoted A_b is

Equation 8.92 $A_b = w_1 h_{sp}$,

and the cross-sectional area of section *BC*, denoted A_c is

Equation 8.93 $A_c = w_2 h_{sp}$.

The second moment of area, also known as the area moment of inertia for a rectangle is defined as

Equation 8.94 $I_x = \dfrac{bh^3}{12}$,

where *b* is the base in direction *x* and *h* is the height in the direction *z*. The polar moment of inertia is defined by

Equation 8.95 $J = I_x + I_y$.

Therefore the area and polar moments of inertia for sections *AB* and *CD* are

Equation 8.96 $I_{by} = \dfrac{w_1 h_{sp}{}^3}{12}$,

Equation 8.97 $I_{bz} = \dfrac{h_{sp} w_1{}^3}{12}$,

Equation 8.98 $J_b = \dfrac{w_1 h_{sp}{}^3 + h_{sp} w_1{}^3}{12}$.

Likewise, the area and polar moments of inertia for section *BC* are

Equation 8.99 $I_{cx} = \dfrac{w_2 h_{sp}{}^3}{12}$,

Equation 8.100 $I_{cz} = \dfrac{h_{sp} w_2^{\,3}}{12}$,

Equation 8.101 $J_c = \dfrac{w_2 h_{sp}^{\,3} + h_{sp} w_2^{\,3}}{12}$.

8.6   Bending Stress in a Cantilever Beam

Stress induced by bending of a cantilever beam is described by the Euler-Bernoulli beam equation is simply defined in

Equation 8.102 $\sigma_z = \dfrac{M_x\, y}{I_x}$,

where x is the location along the beam axis, y is the location perpendicular to beam and loading, z is the location perpendicular to the beam in the load plane with the axis origin at the centroid of the cross section, σ is the bending stress, M is the moment at the neutral axis, and I is the second moment of inertia about the neutral axis.

8.6.1   Bending Stress in a Cantilever Beam Section

Strain in a bending beam is defined by both the Euler-Bernoulli equation and the axial strain along the beam as described by

Equation 8.103 $\dfrac{\partial u_x}{dx} = \dfrac{F_x(x)}{EA}$,

where u_x is the deflection along the beam, F_x is the axial force, E is the elastic modulus, and A is the cross sectional area. Likewise, as previously defined the strain energy of the beam due to bending is defined as

Equation 8.104 $\dfrac{\partial^2 u_z}{dx^2} = \dfrac{M_y(x)}{EI_y}$.

Integration of the strain energy defines strain due to bending. Using the simple stress-strain relation defined by Hooke's law as $\delta E = \sigma$, where δ is the strain, E is the elastic modulus, and σ is the stress, results in the composite stress due to both axial and bending moments that is given in

Equation 8.105 $\quad \sigma_x(x, y, z) = \dfrac{F_x(x)}{A} + \dfrac{M_y(x)z}{I_y} + \dfrac{M_z(x)y}{I_z}$.

8.6.2 Bending Stress in a Cantilever Beam Section AB

Using the definition of composite normal stress presented in the previous section and definitions derived in section B.3, the bending stress in section AB is

Equation 8.106 $\quad \sigma_{xAB} = \dfrac{N_{AB}}{A_b} + \dfrac{M_{ABy} \cdot h}{I_{by}} + \dfrac{M_{ABz} \cdot w_1}{I_{bz}}$.

Average composite stress is simply derived by integrating the stress along the length of the beam and dividing by the length, depicted in

Equation 8.107 $\quad \overline{\sigma_{xAB}} = \dfrac{1}{L_{AB}} \int\limits_0^{L_{AB}} \sigma_{xAB} \, dx$,

that is solved to be

Equation 8.108 $\quad \overline{\sigma_{xAB}} = F_x\left(\dfrac{1}{A_b} + \dfrac{w_1 L_{BC}}{I_{bz}} \right) + F_y \dfrac{w_1}{I_{bz}}\left(L_{CD} - \dfrac{L_{AB}}{2} \right) + F_z \dfrac{h}{I_{by}}\left(L_{CD} - \dfrac{L_{AB}}{2} \right)$.

8.6.3 Bending Stress in a Cantilever Beam Section BC

Using the definition of composite normal stress presented in section B.6.1 and definitions derived in section B.3, the bending stress in section BC is

Equation 8.109 $\quad \sigma_{yBC} = \dfrac{N_{BC}}{A_c} + \dfrac{M_{BCx} \cdot h}{I_{cx}} + \dfrac{M_{BCz} \cdot w_2}{I_{cz}}$.

Average composite stress is simply derived by integrating the stress along the
length of the beam and dividing by the length, depicted in

Equation 8.110 $\quad \overline{\sigma_{yBC}} = \dfrac{1}{L_{BC}} \displaystyle\int_0^{L_{BC}} \sigma_{yBC}\, dy$,

that is solved to be

Equation 8.111 $\quad \overline{\sigma_{yBC}} = F_x\left(\dfrac{-w_2 \cdot L_{BC}}{2 I_{cz}} \right) + F_y\left(\dfrac{1}{A_c} - \dfrac{w_2 \cdot L_{CD}}{I_{cz}} \right) + F_z\left(\dfrac{-h \cdot L_{BC}}{2 I_{cx}} \right).$

8.6.4 <u>Bending Stress in a Cantilever Beam Section CD</u>

Using the definition of composite normal stress presented in Section B.6.1 and
definitions derived in section B.3, the bending stress in section *CD* is

Equation 8.112 $\quad \sigma_{xCD} = \dfrac{N_{CD}}{A_b} + \dfrac{M_{CDy} \cdot h}{I_{by}} + \dfrac{M_{CDz} \cdot w_1}{I_{bz}}.$

Average composite stress is simply derived by integrating the stress along the
length of the beam and dividing by the length, depicted in

Equation 8.113 $\quad \overline{\sigma_{xCD}} = \dfrac{1}{L_{CD}} \displaystyle\int_0^{L_{CD}} \sigma_{xCD}\, dx$,

that is solved to be

Equation 8.114 $\quad \overline{\sigma_{xCD}} = F_x\left(\dfrac{1}{A_b} \right) + F_y\left(\dfrac{-w_1 \cdot L_{CD}}{2 I_{bz}} \right) + F_z\left(\dfrac{h \cdot L_{CD}}{2 I_{by}} \right).$

8.6.5 <u>Bending Stress in Complete Folded Spring</u>

The complete average composite stress for the entire folded flexure is
approximated by the sum of the normal stresses of all sections, as described by

Equation 8.115 $\quad \overline{\sigma_{flexure}} = F_x\left(\dfrac{2}{A_b} + L_{BC}\left(\dfrac{w_1}{I_{bz}} - \dfrac{w_2}{2 I_{cz}} \right) \right) + F_y\left(\dfrac{1}{A_c} + \dfrac{w_1}{2 I_{bz}}(L_{CD} - L_{AB}) - \dfrac{w_2 L_{CD}}{I_{cz}} \right) + F_z\left(\dfrac{h}{2 I_{by}}(3L_{CD} - L_{AB}) - \dfrac{h L_{BC}}{2 I_{cx}} \right).$

8.7 Modeling Forces, Coefficients, and Constants

8.7.1 Spring Constant of Complete Folded Spring

The effective spring constant of a spring is generally defined as the force per displacement, therefore the spring constants are defined in

Equation 8.116 $\quad k_{SPx} = \dfrac{Fx}{\Delta_{Dx}}$,

Equation 8.117 $\quad k_{SPy} = \dfrac{F_y}{\Delta_{Dy}}$,

Equation 8.118 $\quad k_{SPz} = \dfrac{F_z}{\Delta_{Dz}}$.

8.7.2 Mechanical Damping Coefficient of Complete Folded Spring

The mechanical damping coefficient of the folded spring relates stress to displacement of the spring where the shuttle mass attaches. These relations are simply defined in

Equation 8.119 $\quad b_{mx} = \dfrac{\overline{\sigma_{flexure}}}{\Delta_{Dx}}$),

Equation 8.120 $\quad b_{my} = \dfrac{\overline{\sigma_{flexure}}}{\Delta_{Dy}}$,

Equation 8.121 $\quad b_{mz} = \dfrac{\overline{\sigma_{flexure}}}{\Delta_{Dz}}$.

8.7.3 Geometric Constants of Complete Folded Spring

Roundy *et al*, defines two geometric constants for determining piezoelectric behavior [1]. The first geometric constant relates force to stress and is denoted as b^{**}. These relations are defined in

183

Equation 8.122 $\quad b_x{}^{**} = \dfrac{F_x}{\overline{\overline{\sigma_{flexure}}}}$,

Equation 8.123 $b_y{}^{**} = \dfrac{F_y}{\overline{\overline{\sigma_{flexure}}}}$,

Equation 8.124 $\quad b_z{}^{**} = \dfrac{F_z}{\overline{\overline{\sigma_{flexure}}}}$.

The second geometric constant relates strain to displacement and is denoted as b^*. By Hooke's Law, the stress of the flexure is related to the strain by the elastic modulus resulting in the relationships defined by

Equation 8.125 $\quad b_x{}^* = \dfrac{\overline{\sigma_{flexure}}}{E\Delta_{Dx}} = \dfrac{\overline{\delta_{flexure}}}{\Delta_{Dx}}$,

Equation 8.126 $\quad b_y{}^* = \dfrac{\overline{\sigma_{flexure}}}{E\Delta_{Dy}} = \dfrac{\overline{\delta_{flexure}}}{\Delta_{Dy}}$,

Equation 8.127 $\quad b_z{}^* = \dfrac{\overline{\sigma_{flexure}}}{E\Delta_{Dz}} = \dfrac{\overline{\delta_{flexure}}}{\Delta_{Dz}}$.

8.7.4 Definition of Forces Acting on System

It is assumed that the vibration effect on the system is multidirectional. Therefore, input vibration acceleration is assumed to induce input forces in all 3 axes. For simplicity, all forces are assumed to be normal and have equal input acceleration, denoted *a(t)*. The force definitions are presented in

Equation 8.128 $\quad F_x = \dfrac{m\ddot{x}}{n_{sp}} = \dfrac{ma(t)}{n_{sp}}$,

Equation 8.129 $\quad F_y = \dfrac{m\ddot{y}}{n_{sp}} = \dfrac{ma(t)}{n_{sp}}$,

Equation 8.130 $\quad F_z = \dfrac{m\ddot{z}}{n_{sp}} = \dfrac{m\left(g + a(t)\right)}{n_{sp}}$,

where *g* is the gravitational acceleration and n_{sp} is the number of springs.

8.8 Piezoelectric Conversion Model

The piezoelectric mechanical to electrical conversion lumped parameter model is represented by Figure 8.14. Roundy *et al* details the model; however, in this section it has been modified for the 3-dimensional piezoelectric spring case.
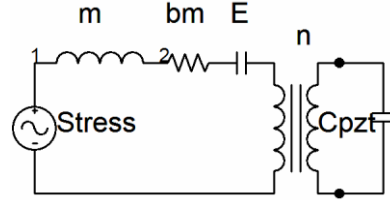
Figure 8.14 Piezoelectric converter lumped model

8.8.1 Mechanical Side of Transformer Model

On the mechanical side of the model, the analogous voltage parameter is stress while the parameter analogous to current is the derivative of strain. The transformer represents the conversion between mechanical and electrical domains. The input stress is defined by equation

Equation 8.131
$$\overline{\sigma}_{in} = \left(\frac{m\ddot{x}}{n_{sp}}\left(\frac{2}{A_b}+L_{BC}\left(\frac{w_1}{I_{bz}}-\frac{w_2}{2I_{cz}}\right)\right)+\frac{m\ddot{y}}{n_{sp}}\left(\frac{1}{A_c}+\frac{w_1}{2I_{bz}}(L_{CD}-L_{AB})-\frac{w_2 L_{CD}}{I_{cz}}\right)+\frac{m(g+\ddot{z})}{n_{sp}}\left(\frac{h}{2I_{by}}(3L_{CD}-L_{AB})-\frac{hL_{BC}}{2I_{cx}}\right)\right)\cdot$$

Displacements are then converted to strain parameters as shown in

Equation 8.132
$$\overline{\sigma}_{in} = \frac{m}{n_{sp}b_x^*}\ddot{\delta}\left(\frac{2}{A_b}+L_{BC}\left(\frac{w_1}{I_{bz}}-\frac{w_2}{2I_{cz}}\right)\right)+\frac{m}{n_{sp}b_y^*}\ddot{\delta}\left(\frac{1}{A_c}+\frac{w_1}{2I_{bz}}(L_{CD}-L_{AB})-\frac{w_2 L_{CD}}{I_{cz}}\right)+\frac{m}{n_{sp}b_z^*}\left(gb_z^*+\ddot{\delta}\left(\frac{h}{2I_{by}}(3L_{CD}-L_{AB})-\frac{hL_{BC}}{2I_{cx}}\right)\right)$$

.

The inertial loss term is due to gravitational forces and is represented by the inductor, denoted *m*, and is defined by.

Equation 8.133
$$\overline{\sigma}_m = \frac{m\ddot{z}}{n_{sp}} = \frac{m}{n_{sp}b_z^{**}b_z^*}\ddot{\delta}\cdot$$

185

The mechanical damping term is represented by a resistor, denoted b_m, includes both electrostatic and piezoelectric mechanical damping, and defined by

Equation 8.134 $\overline{\sigma_{bm}} = \dfrac{b_{mx}}{b_x^*}\dot{\delta} + \dfrac{1}{b_y^*}\left(b_{my} + \dfrac{\mu L_s W_s}{d_s} + 16 N_g \mu L_o h^3 \left(\dfrac{1}{(d-y)^3} + \dfrac{1}{(d+y)^3}\right)\right)\dot{\delta} + \dfrac{b_{mz}}{b_z^*}\dot{\delta}$.

Finally, the stiffness term is represented by the capacitor, denoted E, and is Hooke's Law and the electrical damping force of the electrostatic component defined in

Equation 8.135 $\overline{\sigma_E} = \left(E + \dfrac{1}{b_y^*}\dfrac{Q^2}{2 N_g \varepsilon_0 L_o h\left(d + 2w_d\left(\dfrac{1-\kappa_{SiO_2}}{\kappa_{SiO_2}}\right)\right)}\right)\delta$.

The transformer represents the mechanical to electrical conversion and is represented by the piezoelectric constitutive equations in

Equation 8.136 $\delta = \dfrac{\sigma}{E} + dE_{field}$,

Equation 8.137 $D = \kappa_{pzt} \varepsilon_0 E_{field} + d\sigma$,

where d is the piezoelectric coupling coefficient (d_{31}), E_{field} is the electric field, and D is the electrical displacement. Transformer functions relate stress to electric field with zero strain, and electrical displacement to strain at zero electric field, resulting in

Equation 8.138 $\sigma_{transformer} = -dEE_{field}$,

Equation 8.139 $D_{transformer} = -dE\delta$.

Using these relations, the turns ratio for the transformer, n is equal to $-dE$. Assuming the electrodes cover the top and bottom of the spring structure, the charge and voltage of the piezoelectric spring are defined by

Equation 8.140 $q = a\left(w_1\left(L_{AB} + L_{CD}\right) + w_2 L_{BC}\right)D$,

Equation 8.141 $\quad V = \dfrac{2E_{field}\,h_{sp}}{a}$,

where a is equal to 1 if the electrodes are wired in series and 2 if the electrodes are wired in parallel. Given the definitions for charge and voltage, the current and voltage of the primary (mechanical) side of the transformer are defined by

Equation 8.142 $\quad \dot{q}_t = -dEa\left(w_1(L_{AB} + L_{CD}) + w_2 L_{BC}\right)\dot{\delta}$,

Equation 8.143 $\quad \sigma_t = \dfrac{-dEa}{2h_{sp}}V$.

The application of Kirchhoff's Voltage Law, on the mechanical side of the transformer results in

Equation 8.144 $\quad \sigma_{in} = \sigma_m + \sigma_{bm} + \sigma_E + \sigma_t$.

8.8.2   Electrical Side of Transformer Model

The electric side of the piezoelectric transformer model is comprised of the capacitance of the piezoelectric spring and the load circuitry. Generally, the load is comprised of a full wave rectifier and storage capacitor. As depicted in Figure 8.15, there are five stages of operation.
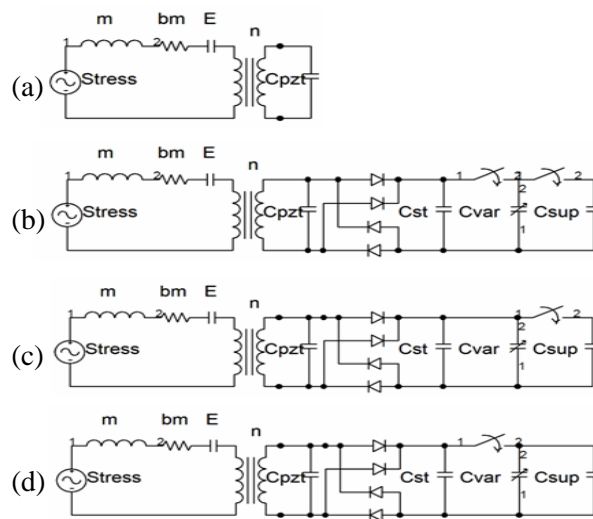
Figure 8.15 Multi-stage lumped system model (a) Stage 0 – disconnected, (b) Stages 1/3 – charging Cst, (c) Stage 2 – charging C_{var}, and (d) Stage 4 – charge transfer to C_{sup}

Assuming ideal diodes, there are five stages of normal operation. Stage 0 occurs when the piezoelectric output voltage is below the voltage stored across the storage capacitor, C_{st}. In this case, the diodes will not conduct. Therefore the current, of the electrical side of the circuit, flows through the piezoelectric capacitor as defined by Kirchhoff's Current Law (KCL) in

Equation 8.145 $\quad \dot{q}_t = \dot{q}_{C_{pzt}} = C_{pzt} \dot{V}$.

The piezoelectric capacitance, C_{pzt} is defined by

Equation 8.146 $\quad C_{pzt} = \dfrac{a^2 \kappa_{pzt} \varepsilon_0 \left(w_1 \left(L_{AB} + L_{CD} \right) + w_2 L_{BC} \right)}{2 h_{sp}}$,

resulting the voltage versus strain relationship shown in

Equation 8.147 $\quad \dot{V} = \dfrac{-2 dE h_{sp}}{a \kappa_{pzt} \varepsilon_0} \dot{\delta}$.

Stages 1 and 3 begin when the piezoelectric voltage output exceeds the voltage on C_{st}, the diodes conduct and begin charging the storage capacitor resulting in a change in the KCL equation that is reflected in

Equation 8.148 $\quad \dot{q}_t = \dot{q}_{C_{pzt}} + \dot{q}_{C_{st}} = \left(C_{pzt} + C_{st} \right) \dot{V}$,

Equation 8.149 $\quad \dot{V} = \dfrac{-dEa \left(w_1 \left(L_{AB} + L_{CD} \right) + w_2 L_{BC} \right)}{\left(C_{pzt} + C_{st} \right)} \dot{\delta}$.

At the piezoelectric voltage peak, the peak detector circuit switches in the variable capacitor that has a value of C_{max} that is given in Appendix A. This initiates stage 2 that alters the KCL equation resulting in

Equation 8.150 $\quad \dot{q}_t = \dot{q}_{C_{pzt}} + \dot{q}_{C_{st}} + \dot{q}_{C_{max}} = \left(C_{pzt} + C_{st} + C_{max} \right) \dot{V}$,

Equation 8.151 $\quad \dot{V} = \dfrac{-dEa\left(w_1\left(L_{AB} + L_{CD}\right) + w_2 L_{BC}\right)}{\left(C_{pzt} + C_{st} + C_{max}\right)}\dot{\delta}$.

When the shuttle in the center; the variable capacitance should be minimized. At this time, the variable capacitor should be switched to the storage supercapacitor; however, the piezoelectric circuit should not see this since it will be disconnected from the variable capacitor. As the shuttle moves in the opposite direction, the voltage will reverse and repeat the stages on the negative cycle.

9 Appendix C: MATLAB simulation code

This appendix contains the MATLAB simulation code used to estimate system behavior. While abandoned when moving to the out-of-plane design, it provided insight on what the hybrid system behavior should look like.

```
function S = simulate(S)
if(nargin < 1),
    S = [];
end

% Excitation Parameters

if(~isfield(S, 'AccelOffsetX')),
    % Constant X Acceleration (m/s^2)
    S.AccelOffsetX = 0;
end
if(~isfield(S, 'AccelOffsetY')),
    % Constant Y Acceleration (m/s^2)
    S.AccelOffsetY = 0;
end
if(~isfield(S, 'AccelOffsetZ')),
    % Constant Z Acceleration (m/s^2)
    S.AccelOffsetZ = 0;
end
if(~isfield(S, 'AccelAmplitudeX')),
    % Amplitude of Time-Variant X Excitation (m/s^2)
    S.AccelAmplitudeX = 1;
end
if(~isfield(S, 'AccelAmplitudeY')),
    % Amplitude of Time-Variant Y Excitation (m/s^2)
    S.AccelAmplitudeY = 1;
end
if(~isfield(S, 'AccelAmplitudeZ')),
    % Amplitude of Time-Variant Z Excitation (m/s^2)
    S.AccelAmplitudeZ = 1;
end
if(~isfield(S, 'AccelPhaseX')),
    % Phase Shift of Time-Variant X Excitation (Radians)
    S.AccelPhaseX = 0;
end
if(~isfield(S, 'AccelPhaseY')),
    % Phase Shift of Time-Variant Y Excitation (Radians)
    S.AccelPhaseY = 0;
end
if(~isfield(S, 'AccelPhaseZ')),
    % Phase Shift of Time-Variant Z Excitation (Radians)
    S.AccelPhaseZ = 0;
end
```

```
% Circuit Parameters
if(~isfield(S, 'Rload')),
    % Load on supercapacitor (Ohms)
    S.Rload = Inf;
end
if(~isfield(S, 'Cst')),
    % Temporary Storage Capacitance (Farads)
    S.Cst = 1e-6;
end
if(~isfield(S, 'Csup')),
    % Output Storage Capacitance (Farads)
    S.Csup = 1e-11;
end
if(~isfield(S, 'Cpeak')),
    % Peak Detector Capacitance (Farads)
    S.Cpeak = 2e-11;
end
if(~isfield(S, 'Crail')),
    % Control Electronics Rail Capacitance (Farads)
    S.Crail = 1e-11;
end
if(~isfield(S, 'Ipeak')),
    % Current consumed by the peak detector (Amps)
    S.Ipeak = 1e-12;
end
if(~isfield(S, 'VpeakThreshold')),
    % Minimum operating voltage of the peak detector (Volts)
    S.VpeakThreshold = 2;
end
if(~isfield(S, 'IpeakCharge')),
    % Peak Detector Charge Current (Amps)
    S.IpeakCharge = .9e-9;
end
if(~isfield(S, 'IpeakDischarge')),
    % Peak Detector Discharge Current (Amps)
    S.IpeakDischarge = .1e-9;
end
if(~isfield(S, 'IzeroCharge')),
    % Zero Detector Charge Current (Amps)
    S.IzeroCharge = .1e-9;
end
if(~isfield(S, 'IzeroDischarge')),
    % Zero Detector Discharge Current (Amps)
    S.IzeroDischarge = .9e-9;
end
if(~isfield(S, 'RpeakMin')),
    % Minimum On resistance of Peak Detector Switches (Ohms)
    S.RpeakMin = 1;
end
if(~isfield(S, 'Idsat')),
    % Saturation current of diodes (Amps)
    S.Idsat = 1E-10;
end
if(~isfield(S, 'Rrectify')),
    % Series resistance of rectifying diode (Ohms)
    S.Rrectify = 1;
end
```

```matlab
if(~isfield(S, 'Irectify')),
    % Maximum current for rectifying diode (Amps)
    S.Irectify = 0.1;
end
if(~isfield(S, 'Rswitch')),
    % On resistance of current pump switches (Ohm)
    S.Rswitch = 10;
end
if(~isfield(S, 'Gswitch')),
    % Transconductance gain of current pump switches (A/V)
    % Note: This controls the maximum current (Imax = (Vrail -
Vth)*G)
    S.Gswitch = 1E-10;
end
if(~isfield(S, 'Vdth')),
    % Thermal voltage of diodes (Volts)
    S.Vdth = 0.026 * 1;
    % (The one is an ideality constant)
end


% Variable Capacitor Properties
%if(~isfield(S, 'CapShuttleLength')),
    % Legnth of Shuttle (Meters)
%    S.VarCapHeight = 10E-3;
%end
%if(~isfield(S, 'CapFingerLength')),
    % Length of Fingers (Meters)
%    S.CapFingerLength = 4E-3;
%end
%if(~isfield(S, 'CapOverlapLength')),
    % Legnth of Overlap (Meters)
%    S.CapOverlapLength = 4E-3;
%end
%if(~isfield(S, 'CapShuttleWidth')),
    % Legnth of Overlap (Meters)
%    S.CapShuttleWidth = 1E-3;
%end
%if(~isfield(S, 'CapFingerWidth')),
    % Length of Fingers (Meters)
%    S.CapFingerWidth = 5E-6;
%end
%if(~isfield(S, 'CapShuttleHeight')),
    % Length of Fingers (Meters)
%    S.CapShuttleHeight = 500E-6;
%end
%if(~isfield(S, 'CapGaps')),
    % Number of Gaps
%    S.CapGaps = 312;
%end
%if(~isfield(S, 'CapInitialGap')),
    % Initial gap between electrodes (Meters)
%    S.CapInitialGap = 5E-6;
%end
%if(~isfield(S, 'CapMinimumGap')),
    % Minimum gap between electrodes (Meters; Hard Stop)
%    S.CapInitialGap = .5E-6;
%end
```

```matlab
%if(~isfield(S, 'CapDensity')),
    % Density of Shuttle (kg/m^3)
%    S.CapDensity = 19300; %Gold
%end
% define shuttle mass and electrostatic structure parameters
if(~isfield(S, 'maxShuttleSize'))
   S.maxShuttleSize = 5e-3; % size limitation on max shuttle size
per side
end
if(~isfield(S, 'heightShuttle'))
   S.heightShuttle = 500e-6; % height of shuttle (process dependent)
(m)
end
if(~isfield(S, 'widthShuttle'))
   S.widthShuttle = S.maxShuttleSize; %500e-6; % width of shuttle
(material dependent) (m)
end
if(~isfield(S, 'lengthShuttle'))
   S.lengthShuttle = S.maxShuttleSize; %-500e-6; % length of shuttle
(material dependent) (m)
end
if(~isfield(S, 'rhoShuttle'))
   S.rhoShuttle = 19300; % density in kg/m^3
end
if(~isfield(S, 'kappaElectrostatic'))
   S.kappaElectrostatic = 3.9; %25; % dielectric constant of
dielectric coating
end
if(~isfield(S, 'coated'))
   S.coated = 1; % boolean value for using dielectric coating for
mechanical stops
end
%if(~isfield(S, 'lengthFingers'))
%   S.lengthFingers = (S.maxShuttleSize-S.widthShuttle)./2; % length
of electrostatic fingers in m
%end
%if(~isfield(S, 'widthFingers'))
%   S.widthFingers = 10e-6; % width of electrostatic fingers in m
%end
%if(~isfield(S, 'lengthOverlap'))
%   S.lengthOverlap = S.lengthFingers - 20e-6; % length of
electrostatic finger overlap in m
%end

if(~isfield(S, 'mechanicalStop'))
   S.mechanicalStop = 0.1e-6; % width of mechanical stop or
dielectric coating in m
end
if(~isfield(S, 'initialGap'))
   S.initialGap = 1; % approximate width of initial gap in m
end
if(~isfield(S, 'numGaps'))
   S.numGaps = 1;
%2.*floor(S.maxShuttleSize./(2.*(S.widthFingers+S.initialGap))); %
number of parallel capacitor gaps
end
```

```matlab
% function to maximize electrodes and shuttle should go here
if(~isfield(S, 'Mass'))
S.Mass = massCalc(S);  % calculation of mass in kg
end


if(~isfield(S, 'VarBlockingSpring')),
    % Spring constant when impacting sidewall (N/m)
    % Note: Should not need to change this
    S.VarBlockingSpring = 150E9 * S.widthShuttle * S.lengthShuttle;
%S.lengthFingers * S.heightShuttle * 150E9 * S.numGaps;
end
if(~isfield(S, 'CapEpsilon')),
    % Dielectric Constant of Free Space (F/m)
    % Note: Should not need to change this
    S.CapEpsilon = 8.85418782E-12;
end
if(~isfield(S, 'CapCoatingEpsilon')),
    % Dielectric Constant of any coating (F/m; Set to CapEpsilon if
none)
    S.CapCoatingEpsilon = S.kappaElectrostatic * S.CapEpsilon;
end


% Spring Properties
if(~isfield(S, 'SpringLengthX')),
    % Length of spring in the x direction (Meters, Axis of Spring)
    S.SpringLengthX = 10e-3;
end
if(~isfield(S, 'SpringLengthY')),
    % Length of spring in the y direction (Meters, Direction of
Motion)
    S.SpringLengthY = 1e-3;
end
if(~isfield(S, 'SpringLengthZ')),
    % Length of spring in the z direction (Meters)
    S.SpringLengthZ = 140E-6;
end
if(~isfield(S, 'ElectrodeLengthX')),
    % Length of electrode in the x direction (Meters, Axis of
Spring)
    S.ElectrodeLengthX = S.SpringLengthX;
end
if(~isfield(S, 'ElectrodeLengthY')),
    % Length of electrode in the y direction (Meters, Axis of
Spring)
    S.ElectrodeLengthY = S.SpringLengthY;
end
if(~isfield(S, 'ShimThickness')),
    % Thickness of center shim layer (Meters)
    S.ShimThickness = 101.6E-6;
end
if(~isfield(S, 'ShimSpacing')),
    % Center-to-center spacing of shim and piezoelectric layers
(Meters)
    S.ShimSpacing = (S.ShimThickness+S.SpringLengthZ)/2;
end
```

```matlab
if(~isfield(S, 'SpringElasticModulus')),
    % Young's Modulus of Piezoelectric Layer (N/m^2, Axis of Spring)
    S.SpringElasticModulus = 7.1e10;
end
if(~isfield(S, 'ShimElasticModulus')),
    % Young's Modulus of Shim Layer (N/m^2, Axis of Spring)
    S.ShimElasticModulus = 7.1e10;
end
if(~isfield(S, 'ModulusRatio')),
    % Ratio of Young's Modulus (unitless)
    S.ModulusRatio = S.SpringElasticModulus / S.ShimElasticModulus;
end
if(~isfield(S, 'BeamMoment')),
    % Beam moment of inertia
    S.BeamMoment = 2 * (((S.SpringLengthY * (S.SpringLengthZ
^3))/12)+(S.SpringLengthY*S.SpringLengthZ*(S.ShimSpacing^2)))+((S.Mo
dulusRatio*S.SpringLengthY*(S.ShimThickness^3))/12);
end
if(~isfield(S, 'BStarStar')),
    % B** relates Force to Stress
    S.BStarStar =
(2*S.BeamMoment)/(S.ShimSpacing*((2*S.SpringLengthX)+S.lengthShuttle
-S.ElectrodeLengthX));
end
if(~isfield(S, 'BStar')),
    % B* relates Strain to Displacement
    S.BStar =
(((3*S.ShimSpacing)/(S.SpringLengthX^2))*((2*S.SpringLengthX+S.lengt
hShuttle-
S.ElectrodeLengthX)/((2*S.SpringLengthX)+(1.5*S.lengthShuttle))));
end
if(~isfield(S, 'SpringEpsilon')),
    % Dielectric Constant in the z direction (F/m)
    S.SpringEpsilon = 1730 * 8.85418782E-12;
end
if(~isfield(S, 'SpringNumber')),
    % Number of springs
    S.SpringNumber = 1;
end
if(~isfield(S, 'SpringPolling')),
    % Number of electrode sections in parallel: 1, 2, 4
    S.SpringPolling = 1;
end
if(~isfield(S, 'SpringCouple31')),
    % Electromechanical coupling coefficient d31 (m/V)
    S.SpringCouple31 = 274e-12;
end


if(~isfield(S, 'Cpzt')),
    % Equivalent Capacitance of PZT (Farads)
    %S.Cpzt = 0.5 * S.SpringPolling.^2 .* S.SpringNumber *
S.SpringEpsilon * S.SpringLengthX * S.SpringLengthY /
S.SpringLengthZ; %1 / 16 * S.SpringEpsilon * S.SpringLengthX *
S.SpringNumber ...
%        * S.SpringLengthZ * S.SpringPolling ^ 2 / S.SpringLengthZ;
% updated
```

```
    S.Cpzt = S.SpringNumber * S.SpringEpsilon * S.SpringLengthX *
S.SpringLengthY / S.SpringLengthZ / S.SpringPolling^2;
end
if(~isfield(S, 'SpringX')),
    % Effective Spring Constant in X axis (N/m)
    % Equal to b* b** E
    S.SpringX = (S.SpringElasticModulus * S.SpringLengthY ...
        * S.SpringLengthZ / S.SpringLengthX) * S.SpringNumber;
end
% correct
if(~isfield(S, 'SpringY')),
    % Effective Spring Constant in Y axis (N/m)
    % Equal to b* b** E
    %Iy = S.SpringLengthZ * S.SpringLengthY ^ 3 / 12;
    %S.SpringY = 12 * S.SpringElasticModulus / S.SpringLengthX ^ 3
...
    %     * S.SpringNumber * Iy;
    S.SpringY = (S.SpringElasticModulus * S.SpringLengthZ *
S.SpringLengthY ^ 3 / ((S.SpringLengthX ^3))) * S.SpringNumber;
% updated
end
if(~isfield(S, 'SpringZ')),
    % Effective Spring Constant in Z axis (N/m)
    % Equal to b* b** E
    %Iz = S.SpringLengthZ ^ 3 * S.SpringLengthY / 12;
    %S.SpringZ = 12 * S.SpringElasticModulus / S.SpringLengthX ^ 3
...
    %     * S.SpringNumber * Iz;
    S.SpringZ = (S.SpringElasticModulus * S.SpringLengthY *
S.SpringLengthZ ^ 3 ./ ((S.SpringLengthX ^3))) * S.SpringNumber;
% updated
end
if(~isfield(S, 'DashpotX')),
    % Effective Dashpot Constant in X axis (N*s/m)
    % Note: This should include Couette Term
    S.DashpotX = 0;
end
if(~isfield(S, 'DashpotY')),
    % Effective Dashpot Constant in Y axis (N*s/m)
    % Note: This should include Couette Term
    S.DashpotY = 0;
end
if(~isfield(S, 'DashpotZ')),
    % Effective Dashpot Constant in Z axis (N*s/m)
    S.DashpotZ = 0;
end
if(~isfield(S, 'VoltageForceX')),
    % Force/Voltage Coupling in X Axis (N/V)
    % Equal to -b** d E a / 2 / hsp
    S.VoltageForceX = 0;
end
if(~isfield(S, 'VoltageForceY')),
    % Force/Voltage Coupling in Y Axis (N/V)
    % Equal to -b** d E a / 2 / hsp
    %Iy = S.SpringLengthZ * S.SpringLengthY ^ 3 / 12;
    %S.VoltageForceY = S.SpringCouple31 * Iy *
S.SpringElasticModulus ...
```

```matlab
%      / (0.5 * S.SpringLengthZ) / (0.25 * S.SpringLengthY) ...
%      / (S.SpringLengthZ * 4 / S.SpringPolling) * S.SpringNumber;
    %S.VoltageForceY = 1/1.8e5;
    S.VoltageForceY = 0;
%updated
end
if(~isfield(S, 'VoltageForceZ')),
    % Force/Voltage Coupling in Z Axis (N/V)
    % Equal to -b** d E a / 2 / hsp
    %S.VoltageForceZ = S.SpringCouple31 * S.SpringElasticModulus *
S.SpringPolling * S.SpringLengthY * S.SpringLengthZ * S.SpringNumber
/ (12 * S.SpringLengthX);
    S.VoltageForceZ =
(S.SpringPolling*S.SpringCouple31*S.SpringElasticModulus*S.BStarStar
./(2*S.SpringLengthZ));
end
if(~isfield(S, 'VelocityCurrentX')),
    % Current/Velocity Coupling in X Axis (A*s/m)
    % Equal to -d E a (w1 (Lab + Lcd) + w2 Lbc) b*
    S.VelocityCurrentX = 0;
end
if(~isfield(S, 'VelocityCurrentY')),
    % Current/Velocity Coupling in Y Axis (A*s/m)
    % Equal to -d E a (w1 (Lab + Lcd) + w2 Lbc) b*
    %Iy = S.SpringLengthZ * S.SpringLengthY ^ 3 / 12;
    %S.VelocityCurrentY = S.SpringCouple31 * 0.25 * S.SpringPolling
...
%       * S.SpringLengthY * S.SpringLengthX * (0.5 *
S.SpringLengthY) ...
%       * (0.25 * S.SpringLengthX) / Iy * S.SpringY *
S.SpringNumber;
    %S.VelocityCurrentY = 1.5e-7;
    S.VelocityCurrentY = 0;
end
if(~isfield(S, 'VelocityCurrentZ')),
    % Current/Velocity Coupling in Z Axis (A*s/m)
    % Equal to -d E a (w1 (Lab + Lcd) + w2 Lbc) b*
    %S.VelocityCurrentZ = 0;
    %Iz = S.SpringLengthZ * S.SpringLengthY ^ 3 / 12;
    %S.VelocityCurrentZ = 15 * S.SpringPolling *
S.SpringElasticModulus * S.SpringCouple31 * (S.SpringLengthX ^2) *
S.SpringLengthY ...
%       * S.SpringLengthZ ./ ( 10 * (S.SpringLengthX ^2) + (3 *
S.SpringElasticModulus * S.SpringLengthZ ));
%updated
    S.VelocityCurrentZ =
(S.SpringPolling*S.ElectrodeLengthX*S.ElectrodeLengthY*S.SpringCoupl
e31*S.SpringElasticModulus*S.BStar);
end
if(~isfield(S, 'SqueezeFilm')),
    % Squeeze Film Dampening Coefficient (N*s*m^2)
    % 16*Ng*viscocity*Length*Height^3
    S.SqueezeFilm = 0; %16 * S.VarCapPairs * 16E-6 * S.VarCapWidth
...
%       * S.VarCapHeight ^ 3;
end
S.ResonantFreq = sqrt(S.SpringZ./S.Mass)/(2*pi);
```

```matlab
if(~isfield(S, 'Frequency')),
    % Excitation frequency in Hz
    S.Frequency = S.ResonantFreq;
end

% Scaling Term
S.Scaling = [ 1E-6 1E-6 1E-6 1E-6 1E-6 1E-6 1 1 ...
    CalcVarCap(0,0,0,S) 1 1 1 1E-6 1 ]';
% Maximum Y Displacement
%S.MaxYDisp = S.initialGap - S.mechanicalStop;
% Maximum Z Displacement
S.MaxZDisp = S.initialGap - S.mechanicalStop;

% For giving progress
if(~isfield(S, 'EndTime')),
S.EndTime = 10/S.Frequency;
end
global iterations;
iterations = 0;

% Solve system
options = odeset('MaxStep', .001/S.Frequency, 'AbsTol', 1E-10);
%options = odeset('MaxStep', .1/S.Frequency);
%options = odeset();
H = waitbar(0, 'Simulating...');
[S.T, S.V] = ode15s(@CalcStep, [0 S.EndTime], ...
    zeros(1, 14), options, S);
clear iterations;
%pack;
S.dVdt = CalcStep(max(S.T), S.V(length(S.T), :)', S) .* S.Scaling;

% Calculate some choice results
S.ResultX = S.V(:,1) * S.Scaling(1);
S.ResultY = S.V(:,3) * S.Scaling(3);
S.ResultZ = S.V(:,5) * S.Scaling(5);
S.ResultVpzt = S.V(:,7) * S.Scaling(7);
S.ResultVst = S.V(:,8) * S.Scaling(8);
S.ResultCvar = CalcVarCap(S.ResultX, S.ResultY, S.ResultZ, S);
S.ResultVvar = S.V(:,9) * S.Scaling(9) ./ S.ResultCvar;
S.ResultVsup = S.V(:,10) * S.Scaling(10);
S.ResultVpeak1 = S.V(:,11) * S.Scaling(11);
S.ResultVpeak2 = S.V(:,12) * S.Scaling(12);
S.ResultEnergy = S.V(:,13) * S.Scaling(13);
S.ResultVrail = S.V(:,14) * S.Scaling(14);

% Pretty plot
subplot(2, 1, 1);
plot(S.T, S.ResultVpzt, S.T, S.ResultVst, S.T, S.ResultVsup, ...
    S.T, S.ResultVpeak1, S.T, S.ResultVpeak2, S.T, S.ResultVvar, ...
    S.T, S.ResultVrail);
legend('V_{pzt}', 'V_{st}', 'V_{sup}', 'V_{peak1}', 'V_{peak2}', ...
    'V_{var}', 'V_{rail}', 'Location', 'Best');
subplot(2, 1, 2);
plot(S.T, S.ResultX, S.T, S.ResultY, S.T, S.ResultZ);
legend('X Position', 'Y Position', 'Z Position', 'Location',
'Best');
```

```matlab
% Final Cleanup
close(H);


function dVdt = CalcStep(t, V, S)
% Dependant Variables
%    V(1) - X Position
%    V(2) - X Velocity
%    V(3) - Y Position
%    V(4) - Y Velocity
%    V(5) - Z Position
%    V(6) - Z Velocity
%    V(7) - Voltage on PZT
%    V(8) - Voltage of Store Capacitor
%    V(9) - Charge on Shuttle (Variable Capacitor)
%    V(10) - Voltage on Supercapacitor
%    V(11) - Voltage on Peak Detector
%    V(12) - Voltage on Zero Detector
%    V(13) - Total Energy Harvested
%    V(14) - Voltage on Peak Detection Rail


% Update waitbar
global iterations;
iterations = iterations + 1;
if(iterations == 100),
    waitbar(t / S.EndTime);
    iterations = 0;
end
if(t > 0.04),
    disp('');
end

% Initialize differential and apply scaling
dVdt = zeros(size(V));
V = V .* S.Scaling;


% Excitation Forces
Scale = min(1, t * S.Frequency / 3) * S.Mass;
Fx = Scale * (S.AccelOffsetX + S.AccelAmplitudeX ...
    * sin(2 * pi * S.Frequency * t + S.AccelPhaseX));
Fy = Scale * (S.AccelOffsetY + S.AccelAmplitudeY ...
    * sin(2 * pi * S.Frequency * t + S.AccelPhaseY));
Fz = Scale * (S.AccelOffsetZ + S.AccelAmplitudeZ ...
    * sin(2 * pi * S.Frequency * t + S.AccelPhaseZ));


% Calculate Capacitance of Shuttle
Zdisp = V(5);
sidewall = false;
if(abs(Zdisp) > S.MaxZDisp),
    % Impacted Bottom
    %sprintf('impacted')
    Zdisp = sign(Zdisp) * S.MaxZDisp;
    sidewall = true;
end
% An X shift affects on side the opposite of the other, so no change
% A Y shift shows up in the gap changing
```

```
% A Z shift impacts overlap
[Cvar dCdX dCdY dCdZ] = CalcVarCap(V(1), V(3), Zdisp, S);

% Calculate Voltages on Capacitors
Vpzt = V(7);
Vst = V(8);
Vvar = V(9) / Cvar;
Vsup = V(10);
Vpeak = V(11);
Vzero = V(12);
Vrail = V(14);

% Trivial cases (second derivatives)
dVdt(1) = V(2); % dX = vX
dVdt(3) = V(4); % dY = vY
dVdt(5) = V(6); % dZ = vZ

% Peak Detectors
if(Vrail > S.VpeakThreshold),
    isPeak = (abs(Vpzt) > Vpeak);
    isZero = (abs(Vpzt) < Vzero);
else
    % Voltage to run to run peak detector
    isPeak = false;
    isZero = false;
end


% Electrical State
%    Current coming in from mechanical side unto Cpzt
dVdt(7) = dVdt(7) + S.VelocityCurrentX * V(2) ...
    + S.VelocityCurrentY * V(4) + S.VelocityCurrentZ * V(6);
%    Current from Cpzt -> Cst
%    This is two diodes in series
Id = Diode(.5 * (abs(Vpzt) - Vst), S.Idsat, S.Vdth, S.Rrectify);
Id = min(Id, S.Irectify);
dVdt(7) = dVdt(7) - sign(V(7)) * Id;
dVdt(8) = dVdt(8) + Id;
%    Current from Cst -> Crail
if(0),
Id = Diode(Vst - Vrail, S.Idsat, S.Vdth, S.Rrectify);
Id = min(Id, S.Irectify);
dVdt(8) = dVdt(8) - Id;
dVdt(14) = dVdt(14) + Id;
%    Current from Cst -> Cvar
%    This is one diode, charge at maximum capacitance
if(isPeak),
    Id = Diode(Vst - Vvar, S.Idsat, S.Vdth, S.Rswitch);
    Id = min(Id, (Vrail - S.VpeakThreshold) * S.Gswitch);
    dVdt(8) = dVdt(8) - Id;
    dVdt(9) = dVdt(9) + Id;
end
%    Current from Cvar -> Csup
%    This is one diode, discharge at minimum capacitance
if(isZero),
    Id = Diode(Vvar - Vsup, S.Idsat, S.Vdth, S.Rswitch);
    Id = min(Id, (Vrail - S.VpeakThreshold) * S.Gswitch);
```

```
        dVdt(9) = dVdt(9) - Id;
        dVdt(10) = dVdt(10) + Id;
        dVdt(13) = dVdt(13) + Id * Vsup;
    end
%    Current dissipated in Rload
dVdt(10) = dVdt(10) - Vsup / S.Rload;
%    Current dissipation of Peak Detector from Cst
if(Vrail > S.VpeakThreshold),
    dVdt(8) = dVdt(8) - S.Ipeak;
    if(isPeak),
        % If in peak, charge peak capacitor
        I = min(S.IpeakCharge, (Vrail - Vpeak) / S.RpeakMin);
        I = max(I, 0);
        dVdt(14) = dVdt(14) - I;
        dVdt(11) = dVdt(11) + I;
    else
        % If not in peak, discharge peak capacitor
        I = min(S.IpeakDischarge, Vpeak / S.RpeakMin);
        I = max(I, 0);
        dVdt(11) = dVdt(11) - I;
    end
    if(isZero),
        % If in zero, discharge zero capacitor
        I = min(S.IzeroDischarge, Vzero / S.RpeakMin);
        I = max(I, 0);
        dVdt(12) = dVdt(12) - I;
    else
        % If not in zero, charge zero capacitor
        I = min(S.IzeroCharge, (Vrail - Vzero) / S.RpeakMin);
        I = max(I, 0);
        dVdt(14) = dVdt(14) - I;
        dVdt(12) = dVdt(12) + I;
    end
end
end
% Equations of Motion
%    X Direction
dVdt(2) = (Fx - S.DashpotX * V(2) - S.SpringX * V(1) ...
    - S.VoltageForceX * Vpzt ...
    - .5 * V(9)^2 / Cvar^2 * dCdX) / S.Mass;
%    Y Direction.  Includes sidewall impact, electrostatics, and more
%SpringY = S.SpringY * V(3);
%if(sidewall),
    % If impacting wall, add a strong spring to arrest its motion
 %   SpringY = SpringY + S.VarBlockingSpring * sign(V(3)) ...
   %       * (abs(V(3)) - S.initialGap + S.mechanicalStop);
%end
dVdt(4) =  (Fy - S.DashpotY * V(4) - S.SpringY * V(3) ...
    - S.VoltageForceY * Vpzt ...
    - .5 * V(9)^2 / Cvar^2 * dCdY) / S.Mass;%(Fy - S.DashpotY * V(4)
- S.SpringY ...
    % - S.VoltageForceY * Vpzt ...
    % - S.SqueezeFilm * (1/(S.initialGap - Zdisp)^3 + 1/(S.initialGap
+ Zdisp)^3) * V(4) ...
    % - .5 * V(9)^2 / Cvar^2 * dCdY) / S.Mass;
%    Z Direction
SpringZ = S.SpringZ * V(5);
```

```
if(sidewall),
    % If impacting wall, add a strong spring to arrest its motion
    SpringZ = SpringZ + S.VarBlockingSpring * sign(V(5)) ...
        * (abs(V(5)) - S.initialGap + S.mechanicalStop);
end
dVdt(6) = (Fz - S.DashpotZ * V(6) - SpringZ ...
    - S.VoltageForceZ * Vpzt ...
    - S.SqueezeFilm * (1/(S.initialGap - Zdisp)^3 + 1/(S.initialGap
+ Zdisp)^3) * V(6) ...
    - .5 * V(9)^2 / Cvar^2 * dCdZ) / S.Mass;%(Fz - S.DashpotZ * V(6)
- S.SpringZ * V(5) ...
    %- S.VoltageForceZ * Vpzt ...
    %- .5 * V(9)^2 / Cvar^2 * dCdZ) / S.Mass;


% Adjust caps from current into voltage
dVdt(7) = dVdt(7) / S.Cpzt;
dVdt(8) = dVdt(8) / S.Cst;
dVdt(10) = dVdt(10) / S.Csup;
dVdt(11) = dVdt(11) / S.Cpeak;
dVdt(12) = dVdt(12) / S.Cpeak;
dVdt(14) = dVdt(14) / S.Crail;
% Cap our values to prevent NaN's and other mischeif
dVdt = max(min(dVdt ./ S.Scaling, 1E100), -1E100);


function [C, dCdx, dCdy, dCdz] = CalcVarCap(xPos, yPos, zPos, S)
% [C, dCdy] = CalcVarCap(X, Y, Z, S)
%
% Calculates the value of the variable capacitor and its spatial
% derivative as a function of the three displacements.
%A = S.NumGaps * S.CapFingerOverlap * (S.CapShuttleHeight - abs(Z));
%C = A / (S.CapMinGap / S.CapCoatingEpsilon + (S.CapGap - Y) /
S.CapEpsilon);
%C = C + A / (S.CapMinGap / S.CapCoatingEpsilon + (S.CapGap + Y) /
S.CapEpsilon);
permittivityFreeSpace = S.CapEpsilon;
if(S.coated == 0)%no dielectric coating
    kappa=1.00054; % air gap dielectric constant
    temp = kappa * permittivityFreeSpace * S.shuttleWidth *
S.shuttleLength;
    %C = temp.*(S.heightShuttle - abs(zPoz)).*(1./(S.initialGap -
yPos)+1./(S.initialGap + yPos));
    C = temp ./ (S.initialGap + zPos);
    % Independant of X to the first order
    dCdx = 0;
    % Inverse with Y to the first order
    %dCdy = temp.*(abs(zPos) -
S.heightShuttle).*(1/((yPos+S.initialGap)^2)-1/((yPos-
S.initialGap)^2));
    dCdy = 0;
    % Linear with Z to the first order
    dCdz = -1 * temp ./ ((S.initialGap + zPos).^2);
% done
elseif(S.coated == 1) %dielectric coating for mechanical stop
    temp = permittivityFreeSpace * S.widthShuttle * S.lengthShuttle;
    if(zPos==S.mechanicalStop)
        zPos = -1.* S.initialGap;
```

```
    %   sprintf('Calculated displacement exceeds mechanical stops on
electrostatic device!');
    end
%   % C = temp.*(1./((S.initialGap-zPos)+2.*S.mechanicalStop.*((1-
S.kappaElectrostatic)./S.kappaElectrostatic))+1./((S.initialGap+yPos
)+2.*S.mechanicalStop.*((1-
S.kappaElectrostatic)./S.kappaElectrostatic)));
    C = 1./((S.mechanicalStop./(temp .*
S.kappaElectrostatic))+(S.initialGap + zPos)./(temp));
    % Independant of X to the first order
    dCdx = 0;
    % Inverse with Y to the first order
    dCdy = 0; %temp.*(S.kappaElectrostatic.^2).*(abs(zPos)-
S.heightShuttle).*(1./((S.kappaElectrostatic.*yPos)-
2.*((S.kappaElectrostatic-1).*S.mechanicalStop-
0.5.*S.initialGap.*S.kappaElectrostatic).^2)-
1./((S.kappaElectrostatic.*yPos)+2.*((S.kappaElectrostatic-
1).*S.mechanicalStop-0.5.*S.initialGap.*S.kappaElectrostatic).^2));
    % Linear with Z to the first order
    dCdz = (-1 * (S.kappaElectrostatic.^2) *
temp)./(((S.kappaElectrostatic .* zPos)+(S.initialGap .*
S.kappaElectrostatic) + S.mechanicalStop).^2);
else
   sprintf('error capacitanceCalc function, please specify
mechanical stop type')
end
% Capacitance function complete

function I = Diode(V, Id, Vth, R)
% I = Diode(V, Id, Vth, R)
%
% Calculates the terminal relationship of a diode-resistor series
% component.  V is the voltage applied across the system (positive
is
% forward device), Id is the diode saturation current, Vth is the
thermal
% voltage (kT ~ 0.026), and R is the series resistance.
if(1),
    I = 0;
    if(V > 0.4),
        I = I + (V - 0.4) / R;
    end
else
if(V == 0),
    I = 0;
    return;
end

% Initial solver conditions
Vdmin = min(V, 0);
Vdmax = max(V, 0);
I = V / R;
err = abs(Vdmin - Vdmax) / max(abs(Vdmin + Vdmax), 1E-6);

% Iteratively solve
while(err > 1E-6),
```

```
    % Calculate currents
    Vd = 0.5 * (Vdmin + Vdmax);
    I = Id * (exp(Vd / Vth) - 1);
    IR = (V - Vd) / R;
    if(IR == I),
        % Helps eliminate issues at small currents
        return;
    end

    % Calculate new error and bounds
    err = abs(Vdmin - Vdmax) / max(abs(Vdmin + Vdmax), 1E-6);
    if(IR > I),
        Vdmin = Vd;
    else
        Vdmax = Vd;
    end
end
end


function m = massCalc(S)
% mass - calculates the mass of the shuttle proof mass
mShuttle =
S.rhoShuttle.*(S.lengthShuttle.*S.widthShuttle.*S.heightShuttle);
%mFingers =
S.rhoShuttle.*((S.numGaps+2).*(S.lengthFingers.*S.widthFingers.*S.he
ightShuttle));
m = mShuttle; %+mFingers;
```

10 Appendix D: References

[1]   S. Roundy, P.K. Wright, and J.M. Rabaey, Energy *Scavenging for Wireless Sensor Networks with Special Focus on Vibrations.* Boston, MA: Kluwer Academic Publishers, 2004.

[2]   K. Parker, "Harvesting power", *IEE Review*, vol. 45, no. 1, pp. 30, Jan. 1999.

[3]   S. Meninger, J.O. Mur-Miranda, R. Amirtharajah, A. Chandrakasan, and J.H. Lang, "Vibration-to-electric energy conversion" *IEEE Trans. on VLSI Systems*, vol. 9, no. 1, pp. 64-76, Feb. 2001.

[4]   S. Roundy, P. Wright, and J. Rabaey, "A study of low level vibrations as a power source for wireless sensor nodes", Computer Communications, vol. 26, no. 11, pp. 1131-1144, July 2003.

[5]   J. McGee, I. Ganelin, M. Khbeis, and R. Ghodssi, "Energy availability survey", *unpublished*, 2008.

[6]   R. Amirtharajah and A. Chandrakasan, "A micropower programmable DSP using approximate signal processing based on distributed arithmetic", *IEEE J. Solid-State Circuits*, vol. 39, no. 2, pp. 337-47, Feb. 2004.

[7]   A. Goetzberger, J. Luther, and G. Willeke, "Solar cells: past, present, future", *Solar Energy Materials and Solar Cells*, vol. 74, no. 1-4, pp. 1-11, Oct. 2002.

[8]   Spectrolab, CA "Boeing Spectrolab Terrestrial Solar Cell Surpasses 40 Percent Efficiency", Dec. 2006.

[9]   S.D. Allan, "Star Battery Unveiled at 50th Anniversary of Russian Science Center", May 2006.

[10]   M. Plett, private communication, Jun. 2005.

[11]   M. Strasser, R. Aigner, C. Lauterbachm, T.F. Sturm, M. Fanosch, and G. Wachutka , "Micromachined CMOS thermoelectric generators as on-chip power supply', *12th Int. Conf. on Solid State Sensors, Actuators, and Microsystems*, vol. 1, pp 45-48, 2003.

[12]   J.P. Fleurial, G.J. Snyder, J.A. Herman, P.H. Giauque, W.M. Phillips, M.A. Ryan, P. Shakkottai, E.A. Kolawa, and M.A. Nicolet, "Thick-film thermoelectric microdevices", *18th Int. Conf. on Thermoelectrics*, pp. 294-300, 1999.

[13]   E.E. Lawrence and G.J. Snyder, "A study of heat sink performance in air and soil for use in a thermoelectric energy harvesting device", *21st Int. Conf. on Thermoelectrics*, pp. 446-9, 2002.

[14]   J.P. Blanchard, "Radioisotope power sources for MEMS devices", *Trans. of the American Nuclear Society*, vol. 84, pp. 87-8, 2000.

[15]   T. Wacharasindhu, J.W. Kwon, D.E. Meier, and J.D. Robertson, "Liquid-semiconductor-based micro power source using radioisotope energy conversion," *Transducers 2009*, pp. 656-659, 2009.

[16]   E.V. Steinfelds, T.K. Ghosh, M.A. Prelas, R.V. Tompson, S.K. Loyalka, "The research and development of the radioisotope energy conversion system", *Trans. of the American Nuclear Society*, vol. 84, pp. 88-9, 2000.

[17]   J.P. Blanchard, D.L. Henderson, A. Lal, H. Li, H. Guo, and S. Santanam, "Radioisotope power for MEMS devices", *Trans. of the American Nuclear Society*, vol. 86, pp. 186-7, 2002.

[18]   A. Lal and J. Blanchard, "The daintiest dynamos", *IEEE Spectrum* vol. 41, no. 9, pp. 36-41, Sep. 2004.

[19]   M. Ghovanloo and K. Najafi, "Fully integrated power supply design for wireless biomedical implants" *2nd Annual Int. IEEE-EMBS Special Topic Conf. on Microtechnologies in Medicine & Biology*, pp. 414-19, 2002.

[20]   J.B. Burch, M. Clark, M. Yost, C. Fitzpatrick, A. Bachand, J. Ramaprasand, and J. Reif. "Radio Frequency Non-ionizing Radiation in a Community Exposed to Radio and Television Broadcasting", *Environmental Health Prospectives*, vol. 114, no. 2, Feb. 2006.

[21]   M.S. Khalaf, "Field Studies of RF & EMF in Bahrain", General Directorate of Environment & Wildlife Protection. Kingdom of Bahrain, 2005.

[22]   M. Fields, "Wireless Communications Facilities Position Paper", Washington State Department of Health.

[23]   T. Salter, K. Choi, M. Peckerar, G. Metze, and N. Goldsman, "RF Energy Scavenging System Utilizing a Switched Capacitor DC-DC Converter," *IET Letters on Electronics*, vol. 45, pp. 374-376, Mar. 2009.

[24]   C.B. Williams, C. Shearwood, M.A. Harradine, P.H. Mellor, T.S. Birch, and R.B. Yates, "Development of an electromagnetic microgenerator", *IEEE Proc. Circuits, Devices, and Systems*, vol. 148, no.6, pp. 337-42, Dec. 2001.

[25]   T. Galchev, H. Kim, and K. Najafi, "Non-resonant bi-stable frequency increased power scavenger from low-frequency ambient vibration" *Transducers 2009*, pp. 632-635, 2009.

[26]   V. Badilita, K. Kratt, T. Burger, J.G. Korvink, and U. Wallrabe, 3D high aspect ratio, MEMS integrated micro-solenoids and Helmholtz micro-coils" *Transducers 2009*, pp. 1106-1109, 2009.

[27]   F. Lu, H.P. Lee, SP Lim, "Modeling and analysis of micro piezoelectric power generators for micro-electromechanical-systems applications", *Smart Materials and Structures*, vol. 13, no. 1, pp. 57-63, Feb. 2004.

[28]   C. S. Lee, J. Joo, S. Han, and S. K. Koh, "Multifunctional transducer using poly (vinylidene flouride) active player and highly conducting poly (3,4-ethylenedioxythiophene) electrode: Actuator and generator", *Applied Physics Letters*, vol. 85, no. 10, pp. 1841-1843, Sept. 2004.

[29]   D. Han and V. Kaajakari, "Microstructured polymer for show power generation", *Transducers 2009*, pp. 1393-1396, 2009.

[30]   M. Renaud, P. Fiorini, R. van Schaijk, and C. van Hoof, "An impact based piezoelectric harvester adapted to low frequency environmental vibrations", *Transducers 2009*, pp. 2094-2097, 2009.

[31]   J. Baker, S. Roundy, and P. Wright, "Alternative geometries for increasing power density in vibration energy scavenging for wireless sensor networks," *3rd International Energy Conversion Engineering Conference*, pp. 5617, 2005.

[32]   J.C. park, D.H. Lee, J.Y. Park, Y.S. Chang, and Y.P. Lee, "Performance piezoelectric MEMS energy harvester based on D33 mode of PZT thin film on buffer-layer with PbTiO$_3$ inter-layer", *Transducers 2009*, pp. 517-520, 2009.

[33]   S. Meninger, J.O. Mur-Miranda, R. Amirtharajah, A. Chandrakasan, and J.H. Lang, "Vibration-to-electric energy conversion" *IEEE Trans. on VLSI Systems*, vol. 9, no. 1, pp. 64-76, Feb. 2001.

[34]   G. Despesse, T. Jager, J.J. Chaillout, J.M. Leger, and S. Basrour, "Design and fabrication of a new system for vibration energy harvesting", *2005 PhD Research in Microelectronics and Electronics*, vol. 1, pp. 225-8, 2005.

[35]   B.C. Yen and J.H. Lang, "A variable capacitance vibration-to-electric energy harvester", *IEEE Trans. on Circuits and Systems I: Fund. Theory and Applications*, vol. 53, no. 2, pp. 288-95, Feb. 2006.

[36] E. Halvorsen, E.R. Westby, S. Husa, A. Vogl, N.P. Ostbo, V. Leonov, T. Sterken, and T. Kvisteroy, "An electrostatic energy harvester with electrets bias", *Transducers 2009*, pp. 1381-1384, 2009.

[37] N. Sato, K. Ono, T. Shumamura, K. Kuwabara, M. Ugajin, S. Mutoh, H. Morimura, H. Ishii, J. Kodate, and Y. Sato, "Energy harvesting by MEMS vibrational devices with electrets", *Transducers 2009*, pp. 513-516, 2009.

[38] D. Miki, Y. Suzuki, and N. Kasagi, "Effect of nonlinear external circuit on electrostatic damping force of micro electrets generator", *Transducers 2009*, pp. 636-639, 2009.

[39] M. Khbeis, J. McGee, and R. Ghodssi, "Design of a hybrid ambient low frequency, low intensity vibration energy scavenger", *PowerMEMS 2006*, pp. 287-290, 2006.

[40] M. Khbeis, J. McGee, and R. Ghodssi, "Development of a simplified hybrid ambient low frequency, low intensity vibration energy scavenger system", *Transducers 2009*, pp. 525-528, 2009.

[41] M. Wischke, M. Masur, and P. Woias, "A hybrid generator for vibration energy harvesting applications", *Transducers 2009*, pp. 521-524, 2009.

[42] "Introduction to piezo transducers," [Online document], [cited 2009 Oct. 29], Available HTTP: http://www.piezo.com/tech2intropiezotrans.html

[43] V. Steward, "Modeling of a folded spring supporting MEMS gyroscope", M.S. thesis, Dept. Mech. Eng. Worcester Poly. Inst., Worchester, MA, Jun. 2003.

[44] L. Mateu and F. Moll, "Review of energy harvesting techniques and applications for microelectronics," *Proc. Of SPIE – The International Society for Optical Engineering,* v. 5837, pp. 359-373, 2005.

[45] J.B. Bates, G.R. Gruzalski, and C.F. Luck, "Rechargeable solid state lithium microbatteries", *Proc. IEEE Micro Electro Mechanical Systems*, pp. 82-6, 1993.

[46] Y. Ngu, M. Peckerar, N. Goldsman, M. Khbeis, and G. Metze, "An Electrochemical Cell with Capacitance-Enhanced Double Layer," *Electrochemical Society*, vol. 602, pp. 203, 2006.

[47] C.B. Williams and R.B. Yates, "Analysis of a micro-electric generator for Microsystems", *Sensors and Actuators A*, vol. A52, no. 1-3, pp. 8-11, Mar. 1996.

[48] G. De Geronimo, P. O'Connor, and A. Kandasamy, "Analog CMOS peak detect and hold circuits. Part 2. The two-phase offset-free and derandomizing configuration" *Nuclear Instr. and Methods in Physics Research A*, vol. 484, no. 1-3, pp. 544-56, May 2002.

[49] M. Khbeis, K. Powell, D. Thomas, A. Pentland, J. Hutchings, and G. Metze, "Profile control for deep silicon etch by sidewall passivation in high density plasma", presented at AVS 50th Int. Symposium, Baltimore, MD, Nov. 2003.

[50] M. Khbeis, C. Bles, G. Metze, and N. Goldsman, "Point-to-point 3-D interconnect fabrication using high pressure reflow of aluminum alloys", *VLSI Multilevel Interconnection Conf.*, Sept. 2006.

[51] M.D.B. Charlton and G.J. Parker, "Fabrication of high aspect ratio silicon microstructures by anodic etching," *J. of Micromechanics and Microengineering*, vol. 7, no. 3, pp. 155-8, Sept. 1997.

[52] S. Frey, M. Kemell, J. Cartensen, S. Langa, and H. Foll. "Fast pore etching." *Phys. Stat. Sol. A*, vol. 202, no. 8, pp. 1369-73, Jun. 2005.

[53] J. Zheng, M. Christophersen, and P.L. Bergstrom. "Thick macroporous membranes made of p-type silicon." *Phys. Stat. Sol. A*, vol. 202, no. 8, pp. 1402-6, Jun. 2005.

[54] J. Carstensen, M. Christophersen, S. Lolkes, E. Ossei-Wusu, J. Bahr, S. Langa, G. Popkirov, and H. Foll, "Large area etching for porous semiconductors." *Phys. Stat. Sol. C*, vol. 2, no. 9, pp. 3339-43, 2005.